Ilmenite megacryst-hosted melt inclusions from the Monastery kimberlite:

Implications for kimberlite origins

By:

Aiden Van Huyssteen

Supervisor:

Steffen Büttner

Co-supervisor:

Geoffrey Howarth

Thesis submitted in fulfilment of the requirements for the degree of:

Master of Science

In the Department of Geology, Rhodes University

2021

Abstract

Polymineralic inclusions encapsulating a daughter assemblage of crystalline phases (including silicates, oxides, and carbonates) and an amorphous glass phase, hosted in ilmenite megacrysts from the Monastery kimberlite, were investigated texturally and geochemically in order to constrain their melt origin, mode of formation, and evolution prior to quenching. The isolated nature of the melt inclusions within the ilmenite megacrysts provides an opportunity to study components of primary kimberlitic magma captured within the SCLM (4.5–6 GPa) that has been isolated from pervasive modifying processes that are common in kimberlites.

The common daughter phase assemblage within the melt inclusions comprises serpentine, phlogopite, calcite, spinel, kassite, perovskite, ilmenite, and glass. The glass is Si-Mg-Fe-rich, with low Al_2O_3 contents. It is also K_2O- and TiO_2-free, with variably depleted REE. In composition, serpentine forms a crystalline equivalent to the glass. However, these phases are optically distinct. Serpentine represents two modes of formation: (i) discrete euhedral grains set within a glass matrix that represent a primary phase, crystallising directly from the entrapped melts, and (ii) as patches of partially crystallised glass that represent a secondary phase formed by the devitrification of the glass. Spinel and phlogopite form along early kimberlitic evolutionary trends and record the depletion of the melt in TiO_2, Al_2O_3, and K_2O, which typically decreases from the core to the rim of the crystals. Volatile and alkali-bearing minerals (calcite, apatite, phlogopite) crystallised within the melt inclusions from the captured alkali-rich carbonated-silicate kimberlite melt. The daughter mineral assemblage initially crystallised as euhedral and subhedral grains with a uniform composition under equilibrium conditions. Subsequent crystallisation formed grains that exhibit magmatic zoning due to their crystallisation in a progressively depleted melt. Lastly, the crystallisation of skeletal oxide grains occurred under disequilibrium conditions, at a stage of magma ascent with rapidly changing variables including temperature, melt viscosity, and diffusivity. Prior to complete crystallisation, the residual Si-Mg-Fe melt of this crystallisation process was quenched to form the observed glass.

The phases that constitute the common daughter assemblage show large variations in modal proportions, forming a continuum from silicate-rich to carbonate-rich endmember inclusions, with certain daughter phases absent in some inclusions. This suggests that the melt was heterogenous at the time of capture and comprised immiscible silicic/oxidic and carbonate melts. Phase separation, therefore, may have started prior to capturing of magma batches as inclusions in ilmenite, but further segregation and crystallisation continued after these batches had become isolated from the megacryst matrix as melt inclusions. The immiscibility and co-existence of the silicic/oxidic and carbonate melts is preserved by textural features between calcite and glass, such as rounded globules of calcite grains set within a silicate glass matrix, calcite forming the matrix for euhedral silicate and oxide minerals, and calcite occupying the interior void of skeletal oxide grains set within a

silicate glass matrix. Furthermore, spherulitic globular domains of Ca- and Ti-rich glasses set within a matrix of the Si-Mg-Fe glass suggest that the silicic/oxidic melt underwent further segregation into oxide-rich (Ca-Ti) and silicate-rich (Si-Mg-Fe-Al-K-Ti) melts, potentially crystallising the oxide and silicate minerals of the daughter assemblage, respectively.

The abundance of incompatible trace elements and the Cr-poor composition of secondary low-Mg ilmenite as a daughter mineral within the melt inclusions (~1400 ppm Nb; <0.1 wt% Cr_2O_3; <0.1 wt% MgO), in addition to the Cr-poor composition of the other daughter phases within the inclusions (i.e. <0.1 wt% Cr_2O_3 for phlogopite and spinel), indicate that they crystallised from a similar melt as the Cr-poor, but high Mg-ilmenite megacrysts (~1400 ppm Nb; <0.1 wt% Cr_2O_3; ~10 wt% MgO). Furthermore, the melt inclusions are randomly distributed and no textural and/or geochemical evidence for melt infiltration of the ilmenite megacrysts was associated with the melt inclusions. These features are consistent with a primary origin for the melt inclusions which implies a cognate relationship between the megacrysts and the captured kimberlite melt.

Declaration:

All work in this thesis is the original work of the writer except where specific acknowledgement is made to the work of others.

Aiden Van Huyssteen

2021

Acknowledgements:

First and foremost, I would like to thank Dr Steffen Büttner for supervising this project and providing assistance and direction throughout its completion. Thanks must also be given to Dr Geoffrey Howarth for co-supervising this project.

Funding for this project was provided by DSI-NRF CIMERA (Centre of Excellence for Integrated Mineral and Energy Resource Analysis) in the form of a bursary awarded to the author.

I would like to thank Rhodes University for access to the Electron Microprobe (the purchase of which was partially funded by NRF National Equipment Program grant UID 74464) and Dr Deon van Niekerk for his assistance in data collection. Additional thanks must be given to the Rhodes University Microscopy Unit for providing access to EDS facilities and for their assistance in its use.

I would also like to extend my gratitude to the University of Cape Town. In particular, for providing access to the John J. Gurney Upper Mantle Research Collection, the use of microscopy facilities used in sample collection, and ICP-MS laser ablation facilities which were assisted by Dr Christel Tinguely.

Lastly, I would like to thank Sebastian Tappe and Trishya Owen-Smith for reviewing this project and providing insightful comments and suggestions.

Table of contents

List of Figures

List of Tables

Chapter 1: Introduction

1.1 Kimberlites

1.1.1 The formation and alteration of kimberlites

Kimberlites are formed during the rapid ascent of volatile-rich ultramafic potassic silicate-carbonate magma from the lower subcontinental lithospheric mantle (SCLM) through the lithosphere to their emplacement levels in the shallow crust (Mitchell, 1995a, 2008). During ascent, the primary kimberlite magma is subjected to a variety of processes that modify its original composition, such as metasomatism, assimilation, and contamination (Mitchell, 1995a; Price et al., 2000; Skinner and Marsh, 2004; Becker and le Roux, 2006; Mitchell, 2008; Moussallam et al., 2016). These processes complicate attempts to constrain primary kimberlite compositions and the conditions of kimberlite formation in the SCLM.

Entrained lithospheric xenocrysts and xenoliths interact with the primary kimberlitic melt to produce a heterogenous texture and composition that is not identical with the proto-kimberlitic magma that formed in the mantle source (Becker and le Roux, 2006; Moussallam et al., 2016). The resulting kimberlites emplaced at shallow crustal levels accordingly contain silicate and carbonate components inherited from the SCLM and secondary contamination acquired during ascent through the lithosphere (Mitchell, 1995a, 2008; Price et al., 2000; Skinner and Marsh, 2004). In addition, kimberlitic rocks are affected by late-stage hydrothermal alteration at emplacement levels where the loss of volatiles creates an environment that promotes deuteric alteration (Becker and le Roex, 2006; Moussallam et al., 2016). Because primary and secondary components cannot easily be separated in sample preparation, compositional data obtained from kimberlites are often difficult to interpret. This has initiated much debate surrounding the genesis of kimberlite magma as the observed data does not represent the primary parental magma. A contentious issue in the current literature regarding the composition of proto-kimberlite magma is whether it was initially a volatile-rich carbonated silicate melt (e.g. Nielson and Sand, 2008; Sparks et al., 2009; Howarth and Taylor, 2016; Stamm and Schmidt, 2017; Tappe et al., 2017; Howarth and Büttner, 2019) or a silicate-free carbonatitic melt that was contaminated by interactions with the silicate-rich lithosphere (Dawson, 1971; Dawson and Hawthorne, 1973; Kamenetsky et al., 2012; Russel et al., 2012; Soltys et al., 2016).

Kimberlites are classified into Group I and Group II kimberlites (Wagner, 1914; Smith et al., 1985). The distinction of Group I and II kimberlites is on the basis of radiogenic isotope signatures (Smith et al., 1985), which broadly correspond to early petrographical classifications (Wagner, 1914). Group I kimberlites are more basaltic (Wagner, 1914) and are less radiogenic in terms of Sr and more radiogenic in terms of Nd in comparison to Bulk Earth (Smith et al., 1985; Becker and le Roex, 2006). Group II kimberlites are more micaceous (Wagner, 1914) and are more radiogenic in terms of Sr isotopes in comparison to Bulk Earth (Smith et al., 1985; Becker and le Roex, 2006). Becker and le Roux (2006) provide estimations for primary magma compositions of Group I ($Mg / (Mg + Fe^{2+})$ = 0.81–0.87; MgO = 22–28 wt%; SiO_2 = 21–30 wt%; CaO = 10–17 wt%; K_2O = 0.2–1.7 wt%) and Group II (Mg /

(Mg + Fe^{2+}) = 0.86–0.89; MgO = ~23–29 wt%; SiO_2 = ~28–36 wt%; CaO = 8–13 wt%; K_2O = ~1.6–4.6 wt%) kimberlites. Other authors such as Harris et al. (2004) and le Roux et al. (2003) also provide similar estimations for compositions of primary kimberlite magmas.

Melting models indicate that the primary kimberlite magma was enriched in light rare earth elements (LREE) by ~10 x chondrite and heavy rare earth elements (HREE) by 0.8–2 x chondrite (Becker and le Roex, 2006). The similarities in isotope ratios and diagnostic trace element ratios of Group I kimberlites to ocean island basalts (OIB) suggest that Group I kimberlites originated from the melting of SCLM that has been enriched by OIB melts or fluids (Becker and le Roex, 2006). For South African kimberlites, these primary melts and fluids have been associated with Mesozoic upwelling of mantle plumes beneath southern Africa (le Roux et al., 2003; Becker and le Roux, 2006).

Other authors propose an alternative model for the formation of kimberlites on the basis of high-pressure experimental studies. Girnis et al. (2011) propose that kimberlites originated from the interaction of a modelled carbonated silicate parental melt with strongly depleted harzburgites at the base of the continental lithosphere. The composition of this parental melt was the average of estimations produced by Smith et al. (1985) and Price et al. (2000), similar to modelled compositions provided by Becker and le Roex (2006) described above. As a result of this interaction, the initial fluid-undersaturated melts were enriched in CO_2 and emplaced as kimberlites (Girnis et al., 1995). According to this model, the most probable source of kimberlites is from the partial melting of a carbonated garnet-harzburgite in the lithospheric mantle (6–8 GPa). This model produces a range of kimberlite-like compositions depending on the abundance of volatiles and degree of partial melting (Girnis et al., 2011).

However, the pre-emplacement contamination and syn/post-emplacement alteration of the primary proto-kimberlite melt complicate attempts to constrain primary kimberlite magma compositions (Becker and le Roux, 2006; Bussweiler et al., 2016; Moussallam et al., 2016). Due to the lack of fresh kimberlite magma, processes that modify the primary kimberlite melt, such as late stage alteration, assimilation, and contamination, need to be accounted for in order to constrain the composition of the proto-kimberlite magma. Kamenetsky et al. (2014b), however, suggest that the Udachnaya kimberlite located in Russia represents fresh unaltered kimberlite, with secondary serpentine almost absent, making it the only known occurrence of fresh kimberlite. This 'fresh' kimberlite contains up to 6.2 wt% Na_2O and Cl, with low H_2O contents. Kamenetsky et al. (2014b) propose that this represents the original kimberlite composition, as the lack of serpentine suggests the absence of syn- and post-magmatic aqueous fluids. Groundmass assemblages and melt inclusions contain alkali carbonate, chloride, and other Na- and Cl-bearing minerals, supporting a parental melt enriched in carbonate, chlorine, and sodium. The low sodium and high water contents usually associated with kimberlites are thus attributed to post-magmatic alteration. Kamenetsky et al. (2014b) suggest that the primary magma was unaltered during ascent and therefore preserves the original 'salty' carbonate composition. However, Kopylova et al. (2013) suggest that the unique composition of the Udachnaya kimberlite is a result of contamination by evaporite salts and brines during ascent.

Kimberlites observed at the emplacement level, and available for detailed study, are therefore composed of minerals from a variety of origins, including (i) minerals crystallised from the primary proto-kimberlite magma, (ii) entrained xenocrysts from the mantle and crust, and (iii) secondary minerals formed during post-magmatic alteration.

1.1.2 The origin of megacrysts hosted within kimberlites

Megacrysts, such as those seen in the Monastery kimberlite, are large mantle-derived minerals common in kimberlites. Megacrysts are also referred to as discrete nodules (Nixon and Boyd, 1973). The most common megacryst species in kimberlites are garnet, orthopyroxene, clinopyroxene, ilmenite, olivine, and less commonly zircon (e.g. Gurney et al., 1979). The origin of these megacrysts and their exact relationship to the surrounding kimberlite magma is still under debate.

A genetic relationship between the megacryst suite and the host kimberlite magma has been inferred on the basis of: i) the similarities in trace elements and isotopic trends between Cr-poor megacrysts and the host kimberlite (Nowell et al., 2004; Kopylova et al., 2009); ii) geochronological evidence of megacryst crystallisation occurring concurrently with entrainment into the transporting kimberlite magma (Kopylova et al., 2009; Kamenetsky et al., 2014a); iii) primary inclusions of kimberlitic material within megacrysts (e.g. Gurney et al., 1979; Howarth and Büttner, 2009); iv) the similarity in megacryst and kimberlite crystallisation temperatures (Kamenetsky et al., 2004).

Megacrysts form two broad compositional groups, Cr-rich and Cr-poor megacryst suites, which coexist in many kimberlites (e.g., Eggler et al., 1979). Megacrysts are coarse-grained (cm–dm) and show a range in crystallisation temperature (i.e. 1400–950 °C for Cr-poor megacrysts in the Monastery kimberlite) under effectively isobaric conditions (Boyd and Nixon, 1975; Gurney et al., 1979; Schulze, 1985; Moore, 1987). To account for this, Harte and Gurney (1981) propose that kimberlite liquid was injected into a fracture network and crystallised as coarse pegmatites down the temperature gradient in magmatic apophyses adjacent to the main kimberlite magma. The crystallisation of Cr-rich megacryst phases (garnet, clinopyroxene, and spinel) could result in Cr-depletion of this pegmatitic kimberlite magma in the source, resulting in subsequent megacrysts with a Cr-poor composition (e.g. Gurney et al., 1979), forming the Cr-rich and Cr-poor megacryst suites, respectively. Additionally, the main kimberlite magma body (essentially the same magma injected into the apophyses) may undergo different evolutionary trends. Moore (1987) notes that during the ascent of the main kimberlite magma, expansion of the olivine phase field at the expense of Cr-rich phases, such as garnet and clinopyroxene, would not deplete the main kimberlite body in Cr. This may account for the Cr_2O_3-rich composition of later crystallising groundmass grains (i.e. groundmass ilmenite). The Cr-rich and Cr-poor megacrysts, and the kimberlite groundmass are considered cognate according to this model (Moore and Belousova, 2005).

Other authors dispute a cognate relationship between the megacrysts and the host kimberlite. Merry and le Roex (2007) showed that quantitative modelling of REE patterns in

garnet and clinopyroxene megacrysts are more similar to crystallisation from an OIB parental magma instead of a primary kimberlite melt. The authors conclude that megacrysts crystallised from a melt that was compositionally distinct from the host kimberlite groundmass. Hence, they classify megacrysts as xenocrysts that were entrained in the kimberlite melt during ascent (Boyd and Nixon, 1973; Pasteris et al., 1979; Hops et al., 1992; Davies et al., 2001; Merry and le Roex, 2007).

1.1.3 Melt inclusions hosted within megacrysts

Melt inclusions, also termed 'polymineralic inclusions' or 'fully crystallised melt inclusions' in some studies, are common features within a variety of megacryst species hosted in kimberlites and have been described by a number of authors (e.g. van Achterbergh et al., 2002; 2004; Araújo et al., 2009; Pivin et al., 2009; Abersteiner et al., 2019; Howarth and Büttner, 2019). Recently, this body of literature has been compiled and reviewed by Bussweiler (2019). Melt inclusions have been described in ilmenite, olivine, garnet, and clinopyroxene megacrysts (see Bussweiler, 2019). The melt inclusions commonly host a daughter mineral assemblage of phlogopite, olivine, serpentine, spinel, garnet, ilmenite, perovskite, sulphides, and carbonate minerals (Bussweiler, 2019). The formation of the melt inclusions is attributed to the capture of an early proto-kimberlite melt which infiltrated the megacrysts at pressures corresponding to mantle depths (Abersteiner et al., 2019; Bussweiler, 2019). Howarth and Büttner (2019) attribute the formation of olivine megacryst-hosted melt inclusions from the Monastery kimberlite to the capture of primary kimberlite melt during crystallisation of the olivine megacrysts.

Along with the daughter mineral assemblage several authors have described a glass phase within polymineralic inclusions hosted in a variety of megacryst species and kimberlite localities. For example, van Achterbergh et al. (2004) described inclusions with concentric silicate glass–carbonate layers hosted in clinopyroxene xenoliths from the Slave Craton. These structures were interpreted to form from unmixing of the captured melt during ascent. Pivin et al. (2009) described a fresh glass phase hosted within garnet megacrysts from two kimberlite localities in the DRC. The authors noted that the glass is too silica rich and alkali poor to correspond with typical kimberlites. The glass is interpreted to result from the breakdown of an unknown original phase that equilibrated with the host garnet megacrysts (Pivin et al., 2009). Recently, Howarth and Büttner (2019) provided a detailed description and geochemical analysis of a fresh-to-devitrified glass phase within polymineralic inclusions hosted in olivine megacrysts from the Monastery kimberlite. The glass was interpreted to represent a residual melt that formed from the crystallisation of the daughter mineral assemblage, which was quenched during ascent.

Glasses may form under a variety of temperature, pressure, and compositional parameters which result in unique compositional and textural features of glass that reflect these conditions. Segregation or unmixing of silicate melts with distinct chemical compositions is referred to as liquid immiscibility and is common in many glass forming systems. It is generally preserved as globules of glass within a chemically distinct glass matrix (Shelley,

1993). The mechanisms and thermodynamics of phase separation and the resultant microscopic and macroscopic textures are further discussed in Chapter 1.3.

1.1.4 The evolution and co-existence of carbonate and silicate melts in the upper mantle

Experimental studies have been used to support the existence of carbonate in the upper mantle (Wallace and Green, 1988; Dasgupta and Hirschmann, 2010). Evidence for carbonate magma in the upper mantle has also been inferred on the basis of diamond inclusion studies (e.g. Weiss et al., 2015), through geochemistry of mantle-derived rocks (e.g. Yaxley et al., 1991), and inclusions in kimberlite xenoliths (Berg, 1986). Carbonate melts have previously been genetically linked to CO_2-bearing silicate melts, which may have separated through liquid immiscibility, crystal fractionation, and oxidation of carbon-bearing phases, such as diamond or graphite (Yaxley et al., 2019). Experimental studies indicate that the immiscibility between silicate and carbonate liquids may occur over pressures ranging from 0.2 to 2 GPa (Kjarsgaard and Hamilton, 1989). Dalton and Presnall (1998) determined experimentally that melt compositions in equilibrium show a systematic variation with temperature over a continuum from carbonatitic at the solidus through to kimberlitic at 70–100 °C above the solidus. The data are consistent with low-degree partial melting of garnet lherzolite at pressures of <10 GPa as an origin for Group I kimberlites. The carbonatite-kimberlite continuum supports petrogenetic links between carbonatites and kimberlites in the mantle source region.

However, the nature of this carbonate component and the origin of primary kimberlitic melt as a carbonatite melt or carbonated silicate melt is still highly debated. Experimental studies have indicated that carbonatitic melts are more likely to form at relatively low pressures (<3.5 GPa) whereas carbonated silicate melts form at higher pressures (>4 GPa) (e.g. Dalton and Presnall, 1998). Hence, kimberlites forming close to the bottom of the SCLM are more likely to derive from primary carbonated silicate melts (~4–6 GPa) (Gurney et al., 1979; Moore, 1986).

Textural evidence for liquid immiscibility between carbonate and silicate melts originating from the upper mantle is documented by various authors. For instance, Chalot-Prat and Arnold (1999) studied veinlets cross-cutting peridotite xenoliths from the lithospheric mantle. Mineralogical and textural relationships of carbonate patches included in a silicate matrix are consistent with an equilibrium liquid immiscibility origin and provide evidence that immiscibility occurred at mantle depths. Van Achterbergh et al. (2004) described concentric layers of silicate-carbonate globules in melt inclusions hosted in clinopyroxene from lherzolite xenoliths that were interpreted as a primary feature that formed from the unmixing of mantle-derived melts under disequilibrium conditions within the inclusion cavity, which were quenched during ascent. The inclusions are carbonate rich, with a groundmass composed of calcite that forms the matrix of an assemblage of euhedral phlogopite, olivine, spinel, perovskite, and sulphides (van Achterbergh et al., 2004). The authors also describe ‘silicate-rich’ inclusions where carbonate forms as discrete euhedral

crystals, colloform textures, or blebs in a silicate matrix (Bussweiler et al., 2016; van Achterbergh et al., 2004). Kjarsgaard and Peterson (1991) described globules in nephelinite lavas that were interpreted to be magmatic in origin, representing silicate-carbonate liquid immiscibility. Soltys et al. (2016) described carbonate-rich veins that transect garnet wehrlite xenoliths. The vein assemblage comprises a variety of Ca-Mg carbonates, sulphides, silicates, and apatite; the variable compositions indicate that they crystallised under disequilibrium conditions. Primary inclusions in the vein minerals and secondary inclusion trails host abundant alkali phases. The authors also noted that carbonates occur as droplet-like, globular segregations separated from a Si-rich phase by a thin meniscus of Mg-magnetite. These features were interpreted as representing immiscibility between carbonate and silicate melts that was preserved by quenching during ascent. The carbonate melt was interpreted to be the product of the reaction and assimilation of wehrlitic mantle wall rocks with the primary kimberlite melt. The presence of alkali carbonate inclusions in kimberlitic minerals has also been attributed to immiscible separation of silicate-oxide and carbonate phases from an initial proto-kimberlite melt near the lithosphere–asthenosphere boundary (Giuliani et al., 2013; Kamenetsky et al., 2014a; Kamenetsky and Yaxley, 2015).

Primary magmatic calcite is commonly reported as the major carbonate mineral phase in the groundmass of kimberlite rocks (e.g. Sparks et al., 2009). A primary origin for calcite is supported by experimental literature, which has determined that calcite ($CaCO_3$) is a stable phase at temperature and pressure conditions associated with the mantle (P > 10 GPa and T > 1000 K) (Biellmann et al., 1993). Calcite is also a common daughter phase in 'polymineralic' melt inclusions hosted within kimberlite minerals (e.g. Bussweiler, 2019; Howarth and Büttner, 2019).

Sparks et al. (2009) described an amorphous zone that surrounds serpentinised olivine pseudomorphs in kimberlites from Wesselton, South Africa. The authors interpreted this zone to represent serpentine that was produced by the replacement of calcite, as calcite is unstable in the serpentinising fluids. Late-stage serpentinisation is due to the infiltration of meteoric fluids near the surface. This alteration process results in an increase in SiO_2 and MgO and a decrease in CaO and CO_2 of the bulk compositions. This may result in over-estimations of SiO_2 and MgO when attempting to estimate primary magma compositions (Sparks et al., 2009).

1.1.5 Serpentine in kimberlites and melt inclusions

Serpentine forms a large component of hypabyssal kimberlites and also forms a major component within polymineralic inclusions. Its content of ~12 wt% structurally bound H_2O indicates a hydrous environment at the time of serpentine growth. The origin of serpentine in kimberlite is still contested. A major debate is whether the fluids that drive serpentinisation are deuteric or meteoric and whether serpentine is a primary phase (Mitchell, 2013, 2008; Fulop et al., 2018), or is a result of secondary alteration (Sparks, 2013; Gernon et al., 2019). Some authors suggest that the volatile content of serpentine is too high to originate form kimberlites (e.g. Gernon et al., 2019). However, the presence of

phlogopite as a megacryst and groundmass phase indicates that kimberlites are hydrous in nature (Sparks et al., 2009).

Skinner and Marsh (2004) suggest that groundmass serpentine in hypabyssal kimberlites may form as a product of the alteration of a kimberlitic glass. Similarly, Willcox et al. (2015) propose that circulating meteoric groundwater results in the serpentinisation of a reactive residual silicate glass, forming an Al-rich serpentine-like mineral, in the Igwisi Hills kimberlites. Howarth and Büttner (2019) highlight the compositional similarities of serpentine to fresh (and devitrified) glass within olivine megacryst-hosted melt inclusions and suggest that the glass may represent the kimberlitic glass inferred by Skinner and Marsh (2004) and Willcox et al. (2015). The preservation of the glass is due to the protection of the enclosing olivine megacrysts from meteoric water, which results in pervasive serpentinisation of the kimberlite groundmass (Howarth and Büttner, 2019). The presence of a glass phase may also explain the amorphous nature of isochemical serpentine patches described by Sparks et al. (2009).

1.1.6 Phlogopite in kimberlites and melt inclusions

Phlogopite is a common mineral in ultramafic-alkaline mantle-derived rocks, such as kimberlites (Mitchell, 1986, 1995b; Reguir et al., 2009) and is a common daughter mineral in megacryst-hosted melt inclusions (e.g. Bussweiler, 2019). Phlogopite is commonly partially replaced by serpentine during the pervasive serpentinisation process in kimberlites (Reguir et al., 2009). The high potential for substitutions on several structural sites, depending on the prevailing physio-chemical conditions, make phlogopite a useful tool in understanding the evolution of ultramafic melts (Mitchell, 1995b).

Kimberlitic micas, most commonly phlogopite, show two major evolutionary trends: the primary macrocryst trend (increasing Al and decreasing Mg) (Reguir et al., 2009) and the transitional macrocryst–groundmass trend (characterised by increasing Al and Mg; decreasing Fe, Ti, and Cr) (Mitchell, 1995b). Less commonly, phlogopites may trend towards Fe-rich, Al_2O_3-poor tetraferriphlogopite (>12 wt% FeO_T; $KMg_3FeSi_3O_{10}(OH)_2$) that contains ferric iron instead of Al in the tetrahedral site. Tetraferriphlogopite in kimberlites commonly forms as thin mantles on pre-existing Al-rich groundmass phlogopite grains (Mitchell, 1995b; Reguir et al., 2009). This abrupt compositional change is interpreted to form as a response to changes in the redox conditions of the system due to late-stage groundwater influx and/or CO_2 degassing during late-stage crystallisation (Lee et al., 2003). Recently, tetraferriphlogopite rims on groundmass phlogopite have been recorded in Group I kimberlites (Stamm et al., 2018; Dongre and Tappe, 2019), although this is generally uncommon in Group I kimberlites (Mitchell, 1995b).

1.1.7 Spinel in kimberlites and melt inclusions

Spinel forms a common component of kimberlites and polymineralic melt inclusions (Mitchell, 1986; Roeder and Schulze, 2008; Bussweiler, 2019). The majority of kimberlitic

spinels are classified as high-chromium chromite (Chr) or magnesio-ulvöspinel–magnetite (MUM) spinels. Chromite is interpreted to be a primary phase that crystallised from the kimberlitic melt during ascent from the upper mantle (Roeder and Schulze, 2008). Three zoning trends represent possible evolutionary trends away from early chromite compositions. Trend 1 is from a Chr to a MUM composition; this trend is unique to kimberlites. Spinel Trend 1 is a result of the evolution of carbon dioxide, rapid thermal changes, and crystallisation of other minerals (Roeder and Schulze, 2008). Roeder and Schulze (2008) suggest that CO_2 or carbonate potentially plays an important role in oxidising ferrous iron and maintaining relatively high Mg activity. This results in constant Fe^{2+}/ (Fe^{2+} + Mg) with increasing Fe^{3+}/ (Fe^{3+} + Al + Cr) that characterises Trend 1 (Roeder and Schulze, 2008). Spinel Trend 2 involves increasing Ti and Fe^{3+} and is interpreted to form as a result of the co-crystallisation of Mg and Al-rich silicate minerals such as olivine and phlogopite, which deplete the residual melt in these components (Roeder and Schulze, 2008). This results in increasing Fe^{2+}/ (Fe^{2+} + Mg) and increasing Fe^{3+}/ (Fe^{3+} + Al + Cr). Spinel Trend 3 is from a Chr to an Al-rich spinel composition and is interpreted to form as a result of rapid diffusion-controlled crystallisation of the spinel (Roeder and Schulze, 2008).

Bussweiler et al. (2016) note that chromites within polymineralic inclusions hosted in Cr-diopsides and Cr-pyropes plot along spinel Trend 2. Howarth and Büttner (2019) demonstrate that spinel as a daughter phase in olivine megacryst-hosted melt inclusions displays a MUM composition typical of kimberlites, plotting along spinel Trend 1. The variations in the composition of spinel within polymineralic inclusions has been attributed to fractional crystallisation of the co-existing daughter minerals and influences of the host megacrysts (Bussweiler, 2019).

1.1.8 Ilmenite in kimberlites and melt inclusions

Ilmenite is a common mineral present in Group I kimberlites. Ilmenite occurs as monomineralic megacrysts, inclusions/intergrowths with other megacrysts species, within sheared xenoliths, and as groundmass grains in kimberlite matrix (Shee, 1984; Schulze et al., 1995).

The majority of kimberlitic ilmenites are Mg-rich (Mg-ilmenite/picro-ilmenite/geikielite-rich ilmenite) and are part of the Cr-poor megacryst suite (>4 wt% MgO; <0.4 wt% Cr_2O_3 for ilmenites within on-craton South African kimberlites) (Schulze et al., 1995; Wyatt et al., 2004). Magnesian ilmenite uniquely occurs in kimberlites (Mitchell, 1973) and is therefore commonly used as an indicator mineral in kimberlite exploration. Wyatt et al. (2004) classified ilmenites in terms of “kimberlitic” and “non-kimberlitic” on the basis of MgO–TiO_2 compositions. MgO–TiO_2 relationships form a parabolic arc, with kimberlitic ilmenites plotting on the MgO-rich side of the curve. The position of this reference line varies between kimberlite localities, for ilmenites from South African on-craton kimberlites, such as the Monastery kimberlite, it lies between 4–16 wt% MgO and 40–58 wt% TiO_2.

The Mg-ilmenite megacrysts hosted in kimberlites commonly show a continuous range in composition, forming compositional zoning (Mitchell, 1973; Gurney et al., 1979).

Compositional zonation is present as an increase in the MgO and/or Cr_2O_3 composition in the outer 100–500 µm of the grain (generally the rims have ~1–4 wt% higher MgO contents than the cores of ilmenite megacrysts) (Haggerty et al., 1977; Schulze et al., 1995). This zonation is interpreted to represent late-stage crystallisation of ilmenite on pre-existing cores and/or partial re-equilibration with the Mg-rich host kimberlite (Haggerty et al., 1977; Pasteris et al., 1979; Shee, 1984).

Ilmenite megacrysts in contact with the kimberlitic host may also produce other reaction products along the grain boundaries, such as rims of rutile, Cr-spinel, titanomagnetite, perovskite, titanite, and MgO-poor ilmenite stricto (s.s.) ($FeTiO_3$) (Shee, 1984; Gurney et al., 1979; Golubkova et al., 2013; Peresetskaya et al., 2018). These products are formed by the reaction of ilmenite megacrysts with kimberlite groundmass fluids (Gurney et al., 1979).

Groundmass/matrix ilmenites are rare in kimberlites, but where present they occur as small (~10s of µm) unzoned, Mg-rich ilmenite grains (Boctor and Boyd, 1980; Moore, 1981). The unzoned nature of groundmass ilmenite grains suggest they formed over a short crystallisation period (Moore, 1981). The Mg-rich composition of groundmass ilmenites trends towards the composition of Mg-rich rims on ilmenite megacrysts of the same kimberlite (Boctor and Boyd, 1980). Ilmenite may be absent as a groundmass assemblage in some kimberlites due to the crystallisation of other Ti-bearing phases such as perovskite, which may be favoured due to the increase in the activity of Ca (a_{Ca}) in the magma resulting from a loss of CO_2 (Moore, 1981). Groundmass ilmenites are interpreted to have crystallised directly from kimberlitic melts and are generally Cr-rich relative to the ilmenite megacrysts, with a wide range in Cr_2O_3 contents (Moore, 1981). For example, Apter et al. (1984) reported Cr_2O_3 compositions of ~2–7 wt% for groundmass ilmenites in the Mayeng kimberlite sill complex.

However, Wyatt et al. (2004) note that a significant proportion of kimberlitic ilmenites fall into the low-MgO ("non-kimberlitic") field. These low-MgO ilmenite grains are most often, but not exclusively associated with groundmass ilmenites that show elevated MnO contents (Wyatt et al., 2004). Williams and Robey (1998) showed that kimberlitic ilmenites with near zero MgO contents showed elevated MnO compositions (4.5–5.4 wt%). This is attributed to replacement of MgO by MnO during alteration by Mn-bearing groundwater. Elevated MnO contents in Monastery ilmenites were attributed to late-stage carbonate and CO–CO_2 reactions (Haggerty, 1977; Wyatt et al., 2004). Nevertheless, the arc defined by MgO–TiO_2 has been chosen as a kimberlitic reference line as it correctly classifies ilmenites from a variety of sources (Wyatt et al., 2004).

Ilmenite as a daughter phase hosted within polymineralic inclusions has only been reported from olivine megacrysts (Haggerty and Boyd, 1975; Howarth and Büttner, 2019; Bussweiler, 2019). Compositionally, it is enriched in Mg in comparison to groundmass ilmenite (Bussweiler, 2019). As with spinel, Bussweiler (2019) notes that this may be a result of the interaction between the captured melt and the host Mg-rich olivine.

The position of ilmenite in the megacryst crystallisation sequence varies in different kimberlites, presumably reflecting the difference in compositions of primary magmas

(Moore, 1987). Ilmenite megacrysts from the Monastery kimberlite are further discussed in Chapter 1.2.

1.1.9 Perovskite in kimberlites

Perovskite is a ubiquitous accessory mineral and an important host of trace elements, particularly LREE, in SiO_2-undersaturated ultramafic and alkaline igneous rocks, such as kimberlites and carbonatites (Martins et al., 2014; Xu et al., 2018; Howarth and Büttner, 2019). Perovskite most commonly forms discrete crystals or crystal clusters within the kimberlite groundmass (Chakhmouradian and Mitchell, 2000). It crystallises simultaneously with MUM groundmass spinel, ceasing its crystallisation prior to the development of atoll spinel (Chakhmouradian and Mitchell, 2000).

However, primary magmatic perovskite is unstable in a CO_2-rich environment, such as during the emplacement of kimberlites, and as a result it is often replaced by other Ti-bearing minerals during subsolidus re-equilibration, metasomatism, and secondary alteration (Mitchell and Chakhmouradian, 1998). The interaction between perovskite and the CO_2-rich fluids results in progressive leaching of Ca^{2+} from the perovskite structure during initial stages of alteration and an increase in Fe^{2+} and Mn^{2+} in later stages of alteration (Mitchell and Chakhmouradian, 1998). The early product of perovskite replacement is kassite (reaction a below), further Ca^{2+} leaching eventually leads to the final products of perovskite replacement: anatase, calcite, and possibly ilmenite (reaction b). Therefore, kassite is an intermediate product of the alteration of perovskite to anatase (and/or calcite) and is favoured by lower rates of Ca^{2+} leaching (Mitchell and Chakhmouradian, 1998; Xu et al., 2018).

(a) $2CaTiO_3$ (perovskite) + CO_2 + H_2O → $CaTi_2O_4(OH)_2$ (kassite) + $CaCO_3$ (calcite)
(b) $CaTi_2O_4(OH)_2$ (kassite) + CO_2 → $2TiO_2$ (anatase) + $CaCO_3$ (calcite) + H_2O

Thermodynamic calculations indicate that the conversion of perovskite into kassite and, subsequently, anatase (and possibly ilmenite) initially requires high levels of $f(H_2O)$ in the system, followed by an increase in $f(CO_2)$ at either decreasing or constant temperature and $f(H_2O)$ (Mitchell and Chakhmouradian, 1998). Kassite only forms in a narrow range of $f(H_2O)$ and $f(CO_2)$ and its field of stability shrinks with increasing temperature (Mitchell and Chakhmouradian, 1998).

Perovskite replacement by late-stage oxide minerals, such as TiO_2 polymorphs and ilmenite, may also occur by the rearrangement of the TiO_6 octahedra (Banfield and Veblen, 1992). The replacement of perovskite by ilmenite in this process is possible due to the structural similarity of $CaTiO_3$ and $FeTiO_3$; tilting of the octahedra and cation exchange at larger cation sites of perovskite may result in the formation of ilmenite, with the absence of intermediate reaction products (Banfield and Veblen, 1992). However, whether alteration of perovskite to ilmenite (or other Ti-bearing oxides) in kimberlites occurs via octahedra rearrangement or by reabsorption and precipitation remains unclear.

This mechanism of alteration may result in Mg-poor ilmenite that forms a discontinuous reaction rim on the perovskite margins (Chakhmouradian and Mitchell, 2000). This is because the replacement of perovskite by ilmenite is dependent on the activities of the divalent species in the melt. Replacement of $CaTiO_3$ by geikielite ($MgTiO_3$) requires high activities of αMg^{2+} in the melt. The replacement of $CaTiO_3$ by ilmenite (s.s.) requires comparably lower activities of Fe^{2+} (and Mn^{2+}). Hence, even at high concentration of Mg^{2+}, replacement of perovskite by ilmenite will result in $FeTiO_3$-rich ilmenite compositions (Chakhmouradian and Mitchell, 2000).

Perovskite may also form as reaction rims on Ti-bearing oxide minerals of the kimberlite megacryst suite, typically on Mg-ilmenite that is Cr-Fe^{3+} enriched and Mn-poor (Smirnov 1959; Boctor and Boyd, 1980; Chakhmouradian and Mitchell, 2000). The perovskite rims (<60 μm) form as the reaction product between early Ti-bearing phases and the Ca-rich kimberlite magma (Chakhmouradian and Mitchell, 2000).

Accordingly, perovskite may crystallise in distinct generations from multiple origins that record the conditions of the system during crystallisation of a kimberlite. Perovskite may be a primary phase that crystallises directly from the kimberlite melt or form from the replacement of Fe-Ti oxides such as spinel or ilmenite, occurring along with calcite and serpentine, which is considered hydrothermal in origin (Chakhmouradian and Mitchell, 2000). Furthermore, perovskite may be replaced by other minerals, such as kassite, anatase, or ilmenite. For instance, Xu et al. (2018) identified two generations of perovskite in Indian kimberlites. The first generation is considered a primary magmatic mineral within the kimberlite groundmass that crystallised directly from the kimberlite magma and shows replacement by anatase or kassite. The second variety is considered hydrothermal in origin, replacing atoll spinel.

1.2 The Monastery kimberlite

The Monastery kimberlite is classified as a Group I kimberlite (Smith, 1983) and is located on the Kaapvaal Craton in South Africa, 80 km north of Maseru and 105 km east of Bloemfontein. The Monastery kimberlite is characterised by high Ti and Fe contents (Smith et al., 1985; Skinner, 1989) and a large (cm–dm) abundant megacryst suite, dominantly of the Cr-poor type, including olivine, ilmenite, clinopyroxene, orthopyroxene, garnet, phlogopite, and zircon (Gurney et al., 1979; Moore et al., 1992).

1.2.1 Megacrysts of the Monastery kimberlite

Megacrystic minerals, derived from the SCLM, are entrained and transported to emplacement levels by kimberlite magmas (e.g. Gurney et al., 1979). Gurney et al. (1979) identified a number of geochemical trends within the megacrystic suite at the Monastery kimberlite. The authors demonstrated: (i) strong linear trends in terms of Fe-Mg-Ca and the similar behaviour of Cr and Ti in Cr-poor silicate megacrysts (clinopyroxene (cpx), garnet (grt), and orthopyroxene (opx)); (ii) the correlation of MgO (wt%) in ilmenites with the Mg / Mg + Fe ratios in coexisting silicate megacrysts (cpx, grt, and opx); (iii) the similarity in the ranges of MgO (wt%) shown between ilmenites associated with cpx, grt, and opx; (iv) inclusions of megacryst phases within one another; (v) the Ca / Ca + Mg ratios in garnet megacrysts are consistent with crystallisation occurring in equilibrium with clinopyroxene and orthopyroxene megacrysts. These strong geochemical trends are consistent with a single igneous differentiation process under declining temperatures and isobaric conditions (~4.5 GPa), for garnet, clinopyroxene, orthopyroxene, and ilmenite megacrysts, and their inclusions (Gurney et al., 1979). Gurney et al. (1979) noted that the timing of crystallisation in the system from which megacrysts formed occurred over a 450 °C temperature decrease and therefore was likely to occur over a long period of time, potentially linked to Karoo volcanism produced by the breakup of Gondwanaland. This was followed by rapid exhumation through the crust to emplacement levels (Wartho and Kelley, 2003).

The age of the Monastery kimberlite has been constrained to ~90 Ma by U-Pb dating of zircon megacrysts (Davis et al., 1976; Kamenetsky et al., 2014a) and Rb-Sr dating of groundmass phlogopite (Allsopp and Barrett, 1975). A close temporal link exists between the crystallisation of the megacryst assemblage and the timing of entrainment in the kimberlite magma (Gurney et al., 1979). This, along with the presence of kimberlitic polymineralic inclusions hosted in the megacrysts, further supports a cognate origin between the megacrysts suite and the host kimberlite (Gurney et al., 1979; Kamenetsky et al., 2014a). Of the megacrystic suite entrained in the Monastery kimberlite, ilmenite, and the inclusions it hosts, is of particular interest in this study.

The Monastery kimberlite is characterised by abundant ilmenite megacrysts that occur as large crystals and as intergrowths with other phases of the megacryst suite (clinopyroxene, orthopyroxene, garnet, olivine, phlogopite, and zircon) (Haggerty et al., 1977; Jakob, 1977; Moore et al., 1992).

1.2.2 Ilmenite megacrysts of the Monastery kimberlite

The ilmenite megacrysts are dominantly part of the Cr-poor megacrystic suite (<0.4 wt% Cr_2O_3) (Gurney et al., 1979; Moore et al., 1992) with two minor Cr-rich populations (0.6–1.2 wt% Cr_2O_3) (Moore et al., 1992). On the basis of MgO compositions the Monastery ilmenite is classified as picro-ilmenite (10–15 wt% MgO) (Mitchell, 1973). The ilmenite megacrysts may define a trend towards Mg-richer compositions from core to rim (Haggerty et al., 1977), however, Gurney et al. (1979) noted that the majority of the ilmenite megacrysts are compositionally homogenous. Haggerty et al. (1977) identified four trends associated with ilmenite megacrysts: (1) the magmatic trend of the ilmenite megacrysts towards $MgTiO_3$; (2) the trend of ilmenite-pyroxene intergrowths towards $MgTiO_3$; (3) kimberlite reaction trend towards $FeTiO_3$; (4) formation of exsolution lamellae in ilmenite. According to Haggerty et al. (1977), the magmatic megacryst trend is a liquid interaction trend possibly due to a decrease in P_{total} and fO_2. The kimberlite reaction trend marks the onset of megacryst incorporation into the kimberlite.

Moore et al. (1992) demonstrated that the variations in trace element compositions of ilmenites from the Monastery kimberlite, most notably the systematic variations in elements relative to Nb, which behaves as an incompatible element, are consistent with a model of fractional crystallisation for their formation. Moore et al. (1992) identified 3 main ilmenite generations. Group 1 ilmenites are associated with the main silicate trend (MST: garnet, clinopyroxene, and orthopyroxene megacrysts) and are Cr-poor (<0.4 wt% Cr_2O_3). Group 2 ilmenites coexist with zircon and Fe-rich, Ni-poor olivine. Ilmenites in this group have higher Cr_2O_3 (>0.6 wt%) compositions and show a drop in Zr (600–1500 ppm) at constant Nb, followed by a rise in Nb contents (1200–1300 ppm). Group 3 ilmenites have high Cr_2O_3 (>0.6 wt%) and Nb (600–1200 ppm) with lower Zr (200–450 ppm) compositions and co-exist with phlogopite and calcic-clinopyroxene. The ilmenites analysed in the current study show trace element concentrations consistent with Group 1 and Group 2 ilmenites identified by Moore et al. (1992) (see Chapter 4.1).

The regular pattern of trace elements in Group 1 ilmenites suggests they crystallised from a uniform batch of magma with a simple fractionation history, where an increase in Nb correlates with the crystallisation of the co-existing megacrysts of the MST (Moore et al., 1992). The relationship between major and trace elements in Group 2 ilmenites is consistent with the fractional crystallisation of zircon, followed by the crystallisation of zircon and olivine (Moore et al., 1992). Group 2 ilmenites are primarily distinguished by higher Cr contents from Group 1 ilmenites. The trends of Group 1 and 2 ilmenites are interpreted to show crystallisation from the same batch of magma (Moore et al., 1992). However, magma mixing or wall rock assimilation is required to explain the increase in Cr from Group 1 to Group 2 ilmenites (Moore et al., 1992). Based on this model of fractional crystallisation, the sequence of crystallisation of the megacrystic suite at the Monastery kimberlite that formed Group 1 and 2 ilmenites was determined to be: (i) Fe-poor olivine + orthopyroxene + clinopyroxene + garnet; (ii) ilmenite + clinopyroxene + garnet + orthopyroxene; (iii) ilmenite + phlogopite; (iv) ilmenite + zircon + phlogopite; (v) ilmenite + zircon+ Fe-rich olivine +

phlogopite (Moore et al., 1992). Moore et al. (1992) estimate that during the fractional crystallisation process the increase in Nb (if Nb is assumed to be a perfect incompatible element) in Group 1 and 2 ilmenites reflects at least 90% crystallisation of the magma volume present at the beginning of ilmenite crystallisation. The lower Fe and Zn contents and higher Mg, Ni, and Cr contents of Group 3 ilmenites suggest that they formed from a more primitive magma, which was relatively Nb-rich, distinct from the magma that crystallised Groups 1 and 2 ilmenites (Moore et al., 1992).

Moore et al. (1992) demonstrated that ilmenite megacrysts coexist with a wide variety of megacryst phases at the Monastery kimberlite, implying that ilmenite precipitated late in the megacryst crystallisation history. The authors also note that ilmenite is a relatively small proportion of the cumulate megacryst assemblage in the fractionation sequence (Moore et al., 1992). This is in contrast with observations at the Monastery kimberlite where ilmenite is second in abundance only to olivine megacrysts (Moore et al., 1992). This suggest that ilmenite megacrysts, and therefore the melt inclusions hosted within them, have been preferentially preserved during transport (Moore et al., 1992).

The ilmenite megacrysts of the Monastery kimberlite show a variety of chemical modifications. The ilmenite megacrysts show chemical modifications along contacts with the host kimberlite matrix (up to <1 mm wide) (Haggerty et al., 1977; Kamenetsky et al., 2014a). The reaction assemblage that forms is composed of Ti-rich minerals, including Mg-Ti-Fe oxides, perovskite, Mn-ilmenite, kassite, and sphene (Haggerty et al., 1977; Kamenetsky et al., 2014a). Most of the chemical components required to form these secondary minerals are readily available. However, an external source is required for the Ca^{2+}, which is supplied by the carbonatite component of kimberlitic magma (Kamenetsky et al., 2014a). Ilmenites of the Monastery kimberlite also show pervasive orientated submicroscopic iron-rich exsolution lamellae, composed of magnetite and magnesian titanohematites that formed as a result of subsolidus reactions (Jakob, 1977; Kamenetsky et al., 2014a). Large ilmenite megacrysts (cm–dm) are irregular to ovoid in shape, suggesting that physical abrasion occurred during transport (Kamenetsky et., 2014a). Therefore, the chemical reaction between megacrysts and kimberlite melt occurred at emplacement level (Kamenetsky et., 2014a).

The chemical interaction of the ilmenite megacrysts and surrounding kimberlite melt (primarily characterised by a loss of Ti and an increase in Ca) indicates that the megacrysts were not in equilibrium with the kimberlite melt at the time of alteration (Kamenetsky et al., 2014a). The disequilibrium of the megacrysts and kimberlite melt at emplacement level suggests they are non-cognate (Kamenetsky et al., 2014a). However, the similarities in isotope characteristics and the crystallisation temperatures of the ilmenite megacrysts and the kimberlite matrix (Kamenetsky et al., 2004) are indicative of a similar source for the megacrysts and the host kimberlite magma in the lithospheric mantle (Kamenetsky et al., 2014a). To account for this discrepancy, Kamenetsky et al. (2014a) propose the unmixing of the carbonated-silicate proto-kimberlite into conjugate silicate-oxide and carbonate liquids under mantle conditions. Experimental studies indicate that carbonated-silicate compositions are expected for low-degree partial melts of carbonated peridotites at mantle

conditions, which has been proposed as a kimberlite source (Dalton and Presnall, 1998). These melts may separate into immiscible silicate and carbonate melts (Brooker and Kjarsgaard, 2011). Kamenetsky et al. (2014a) suggest that the silicate/oxide melt may separate into immiscible Si-rich and Si-poor (oxide-rich) melts, which crystallise the silicate and oxide megacryst species, respectively, whereas the carbonate component becomes the major liquid component of kimberlites and incorporates the megacrysts (Kamenetsky et al., 2014a). The immiscible separation of an early kimberlite-forming melt may account for the common depletion of kimberlites in HFSE relatively to REE (Price et al., 2000; le Roex et al., 2003; Harris et al., 2004) if HFSE are preferentially accommodated in the immiscible silicate melt (Kamenetsky et al., 2014a). Therefore, the disequilibrium of the megacrysts and kimberlite melt at emplacement level is attributed to changes in the kimberlite during exhumation rather than different sources (Kamenetsky et al., 2014a).

1.2.3 Megacryst-hosted melt inclusions from the Monastery kimberlite

Ilmenite and olivine megacrysts from the Monastery kimberlite host abundant melt inclusions. Early studies of megacryst-hosted melt inclusions reported an assemblage of calcite and an amorphous matrix material within the spherical melt inclusions (Nixon and Boyd, 1973; Haggerty et al., 1977; Jakob, 1977). It was also noted that the occurrence of melt inclusions in ilmenite megacrysts is restricted to individual ilmenite megacryst crystals that are not intergrown with other phases of the megacrystic suite (Nixon and Boyd, 1973; Jakob, 1977). However, this has not been extensively documented.

Haggerty and Boyd (1975) described spheroidal melt inclusions hosted in olivine megacrysts from the Monastery kimberlite. Jakob (1977) noted that the inclusions are a common feature of the olivine megacrysts. The melt inclusions host a daughter assemblage of kimberlitic minerals in a fine-grained translucent matrix that may be devitrified glass (Haggerty and Boyd, 1975; Jakob, 1977). The melt inclusions are associated with veinlets that run from the inclusion into the host olivine. The composition of the material within the melt inclusions and veinlets is similar to the composition of the phases in the kimberlite matrix (Jakob, 1977; Haggerty and Boyd, 1975). Similarly, Gurney et al. (1979) described a tubular inclusion in an olivine megacryst and noted that the inclusion has a similar composition to the kimberlite groundmass. Haggerty and Boyd (1975) favour an entrapped liquid hypothesis rather than infiltration by a later kimberlite-related melt. According to their model the liquids that formed the inclusions were present during crystallisation of the olivine megacrysts (Jakob, 1977).

Haggerty et al. (1977) described ovoid inclusions in ilmenite megacrysts composed of calcite, pyrrhotite, and pentlandite. These inclusions were interpreted as having reacted with the host ilmenite megacrysts to produce a reaction assemblage of magnetite at the contact and a reaction rim of zoned titaniferous-magnetite (1–4 wt% MgO), and a magnesium-depleted ilmenite enriched in Fe. Kirkley et al. (1986) showed that the carbonate component within melt inclusions hosted in ilmenite megacrysts from the Monastery kimberlite consists of calcite. Kirkley et al. (1986) noted that the calcite has

enriched $\delta^{13}C$ signatures that are similar to carbonates from the Monastery kimberlite groundmass and carbonatised xenoliths. This isotopic signature may be a function of ^{13}C isotopes being fractionated into CO_2 vapour and suggests that Monastery volatiles were particularly enriched in CO_2 in the source area (Kirkley et al., 1986). The isotopic similarities between the calcite within the inclusions and kimberlitic calcite imply that the kimberlitic and megacrystic systems had similar CO_2-rich compositions, which supports a close genetic affinity between kimberlite and the liquids from which megacrysts formed. Furthermore, the authors note that the inclusions appear to be primary and protected from alteration by the enclosing megacrysts (Kirkley et al., 1986).

More recently, Kamenetsky et al. (2014a) described an assemblage of alkali phases within melt inclusions hosted in ilmenite megacrysts from the Monastery kimberlite. These Na-K-bearing phases are present as silicates, carbonates, chlorides, sulphates, and phosphates. Although these phases are uncommon in kimberlites, they are expected to form a common component in low-degree partial melts, such as kimberlites (Kamenetsky et al., 2014a). Their absence in the kimberlite groundmass may be a result of late-stage alteration. The formation of these melt inclusions is attributed by Kamenetsky et al. (2014a) to the healing of fractures that formed during the infiltration of kimberlite magma, evident by their linear arrangement, that reacted with the host ilmenite megacrysts. Kamenetsky et al. (2014a) do not constrain the exact timing of fracture healing but consider a genetic link between the kimberlite melt, the infiltrating melt, and the mantle source of the Monastery kimberlite likely. Kamenetsky et al. (2014a) consider these melt inclusions to represent relics of the original alkali-carbonate melt that formed the Monastery kimberlite.

Howarth and Büttner (2019) described large circular to ovoid melt inclusions (3–10 mm) hosted in olivine megacrysts from the Monastery kimberlite. The melt inclusions host a daughter mineral assemblage similar to the surrounding kimberlite groundmass. Furthermore, the authors identified a Si-Mg-Fe-rich glass (occasionally showing localised devitrification), possibly representing the amorphous groundmass mentioned in earlier studies on melt inclusions hosted in megacrysts from the Monastery kimberlite (e.g. Haggerty and Boyd, 1975; Jakob, 1977).

Howarth and Büttner (2019) propose that these inclusions represent quenched components of the primary carbonated-silicate kimberlitic magma captured during rapid growth of the olivine megacrysts at the lithosphere-asthenosphere boundary. The variable proportions of calcite hosted in the inclusions are attributed to phase separation of the carbonate and silicate components prior to melt capture by the olivine megacrysts. Additionally, spherulite-like Ca-Ti globules indicate that the silicate component may have further segregated into silicate (Si-Mg-Fe) and oxidic (Ca-Ti) melts from which the silicate and oxide minerals of the daughter phase assemblage crystallised, respectively. Prior to complete crystallisation of the entrapped kimberlite magma, ascent resulted in strong undercooling and the formation of skeletal crystal shapes indicative of disequilibrium growth and the quenching of the residual melt to form the Si-Mg-Fe glass. The decrease in pressure during ascent of the kimberlite resulted in the formation of radial apophyses originating from the melt inclusions and extending into the host olivine megacrysts. The olivine megacrysts sheltered the glass and

mineral assemblages within the melt inclusions from late-stage alteration. Properties such as thermal conductivity may explain the ability of a particular megacryst species to preserve glass within melt inclusions (Bussweiler, 2019).

Howarth and Büttner (2019) provide trace element analyses for the glass and components of the common mineral assemblage (perovskite, phlogopite, and calcite) within olivine megacryst hosted-melt inclusions. The authors showed that the trace element signatures of the glass (i.e. Th/U) are strongly controlled by fractionation into perovskite, despite its low modal proportions (1–3 vol. %). The results indicate that perovskite-kimberlite melt partition coefficients may be underestimated (Howarth and Büttner, 2019). In addition, the low contents of Rb and Ba in the glass are likely the result of fractionation of these trace elements into phlogopite and the low Sr contents are due to calcite crystallisation (Howarth and Büttner, 2019). REE and trace element patterns, therefore, show partitioning from the residual melt (glass) into phlogopite, calcite, and mainly perovskite, during crystallisation of the daughter mineral components within the melt inclusions (Howarth and Büttner, 2019).

In general, the trace element abundances of the daughter phases within polymineralic inclusions from a variety of kimberlites overlap with their respective kimberlite hosts (e.g. van Achterbergh et al., 2004; Araújo et al., 2009). Bussweiler (2019) noted that trace element trends are similar to early stages of kimberlite differentiation trends. This supports the hypothesis that the entrapped melt represents early kimberlite melt trapped at mantle depths.

1.3 Textural features preserved in fast-cooling melts

1.3.1 Glass formation

If a magma is subject to rapid undercooling, such that the temperatures ideal for effective nucleation and growth are too brief to initiate the formation a crystal, the melt is quenched into a non-crystalline glass (e.g. Shelley, 1993). As a result, glass forms with an unordered atomic arrangement like that of a silicate melt but with the rigidity of a solid. Due to this unordered arrangement, glass is characterised by a short-range order, as opposed to the long-range order of atomic arrangements in crystalline minerals (Vernon, 2004). This gives glass its characteristic optical isotropy.

Due to the less ordered atomic arrangement of glass, it is in a higher energy state than a compositionally identical crystal. This results in the characteristic metastability of glass (Vernon, 2004). Due to this thermodynamic instability, glass tends to crystallise (devitrify) with time, under a variety of conditions (Marshall, 1961), but especially in the presence of water, often forming spherulitic or axiolitic aggregates (Vernon, 2004). Glass that has undergone this process will not be isotropic, due to a more ordered atomic arrangement formed during the (partial) crystallisation of a compositional crystalline equivalent to the glass (Vernon, 2004). This may result in glass (or patches of glass depending on the extent of devitrification) that displays birefringence and textural heterogeneity (Marshall, 1961; Vernon, 2004).

The high rate of undercooling required for the formation of glass may occur in a variety of environments and melt compositions. Commonly, glass may form during the rapid ascent and emplacement of magma, in the presence of water, or subsequent to impact melting (Vernon, 2004). Glasses may form by the quenching of a variety of melt compositions in these environments. However, silica-rich melts form glass more easily than mafic melts due to the higher degree of polymerisation of $[SiO_4]^{4-}$ tetrahedra in silicate melts (Vernon, 2004).

The criteria used to identify glass in the present study are the same as those used by Howarth and Büttner (2019): (i) fresh glass is optically isotropic with refractive indices between ~1.48 and ~1.62 (Tröger et al., 1982), (ii) glass forms coherent pools/patches, that when fresh are texturally and optically homogenous, and (iii) the formation of glass from strong undercooling of a melt means that it is associated with other textures that form in the same environment such as skeletal crystal growth or spherulitic textures. Spherulitic textures may form hemispherically into glass pools or as seams at the melt/glass interface if crystal surfaces serve as nucleation points (Büttner and Howarth, 2019).

In natural systems, the timing and degree of undercooling needs to be considered. A melt may experience varying degrees of undercooling resulting in phase separation or crystallisation prior to the formation of a glass (e.g. Swanson et al., 1989). This would result in textures that record the conditions the system was subject to, and thereby preserving the crystallisation history and the igneous processes acting on the system prior to quenching (e.g. Swanson et al., 1989).

1.3.2 Liquid immiscibility

In silicate melts, liquid immiscibility is the result of the interaction between the atomic arrangement of two types of structural cation components: network-formers (Si^{4+}) and network-modifiers (most other metal cations except Al^{3+} and Ti^{4+}) (Hudon and Baker, 2002). Network-formers (Si) bond to oxygen ions in bridging positions (Si-O-Si) forming tetrahedra. Network-modifiers (X) bond to oxygen ions in non-bridging positions (Si-O-X) forming polyhedra (Warren and Pincus, 1940; Galakhov and Varshal, 1973; James 1975; Hudon and Baker, 2002). In silicate melts, bridging oxygen ions are generally more abundant and as a result the randomly distributed network-modifying cations are not screened from one another by non-bridging oxygen ions (Hudon and Baker, 2002). Instead, they are surrounded by the more abundant bridging oxygen ions. Because the bridging oxygen ions are strongly bonded to Si^{4+}, coulomb repulsion forces build up between the individual network-modifying cations, causing unmixing and phase separation (Warren and Pincus, 1940; Galakhov and Varshal, 1973; James 1975; Hudon and Baker, 2002). Unmixing therefore results in two compositionally distinct phases, commonly an SiO_2-rich phase that is poor in network-modifying cations and an SiO_2-poor phase that is rich in network-modifying cations, in comparison to the initial bulk composition of the homogenous melt (Hudon and Baker, 2002). Thermodynamically, phase separation is a function of Gibbs free energy of mixing. The system will favour the melt structure (homogenous/unmixed) that yields the lowest free energy (Warren and Pincus, 1940; Galakhov and Varshal, 1973; James 1975; Hudon and Baker, 2002).

Phase separation from a homogenous melt into two coexisting compositionally distinct immiscible melt phases may occur as the result of two mechanisms: the nucleation and growth of melt globules or spinodal decomposition (Cahn, 1965). The mechanism by which phase separation occurs is dependent on the prevailing conditions of the system.

Phase separation through nucleation and growth is the unmixing of immiscible melts under equilibrium conditions. The nucleation of a separate melt domain involves an initial free energy barrier as microscopic clusters form nuclei, and these melt clusters then grow through diffusion. The composition of the growing phase is constant through time. This mechanism of phase separation results in spherical globules of one phase, set within a matrix of the conjugate immiscible liquid (Cahn, 1965).

Phase separation through spinodal decomposition forms when immiscible melts separate under disequilibrium conditions. No thermodynamic barrier is present in the region of spinodal decomposition as it occurs completely through diffusion (Cahn, 1965). Initially, chemical components in the melt begin to cluster, and these microscopic clusters may coalesce into single macroscopic phases (Cahn, 1965). Therefore, the composition and texture are time dependent. Spinodal decomposition initially results in diffuse separation of chemical components, followed by interpenetrating microscopic veinlets with a high connectivity, which gradually decreases through coalescence until macroscopic clusters are formed (Cahn, 1965; Siggia, 1979).

1.3.3 Crystallisation

Alternatively, if undercooling occurs sufficiently slow enough, a crystal may form. The development of a crystal is a function of nucleation, diffusion, and growth, all processes which are characterised by rates (Shelley, 1993). These rates vary according to the environmental conditions of the crystallising system, and the slowest of these rates generally acts as the controlling factor in crystallisation process (Shelley, 1993).

Another important factor in the crystallisation process is the saturation of the melt. Supersaturation refers to the concept that a melt contains more dissolved solid phases than it can typically accommodate at that temperature, which results in metastability, and equilibrium of the system is achieved through crystallisation (Shelley, 1993). Therefore, supersaturation is a prerequisite to the crystallisation of minerals from a melt and affects the nucleation, diffusion, and growth rates of a crystallising mineral (Ting and McCabe, 1934; Mullin, 1993).

Nucleation refers to the initial site in the formation of a crystal. Homogenous nucleation is the formation of nuclei at random within a melt or solution as atoms arrange into crystal patterns; it occurs more commonly as the degree of undercooling or supersaturation increases (Shelley, 1993). Heterogenous nucleation is initiated by a seed crystal or impurity and occurs more easily in comparison to homogenous nucleation (e.g. Shelley, 1993). For example, the wall of a magma chamber, existing crystal boundaries or other defects and impurities may function as nucleation sites. Potential sites of nucleation are characterised by a high surface energy, and when in combination with the high energy of the embryonic new phase, the nucleation energy barrier is overcome (Shelley, 1993). Seed crystals are a common initiator of heterogenous nucleation. The lattices of a seed crystal generally share certain structural elements with the nucleating phase (Shelley, 1993). The ability of one mineral to nucleate on the other, if they are sufficiently similar, is termed epitaxy. When the two crystals have an essentially parallel crystallographic orientation it is known as syntaxy (Powers, 1963; Nielsen, 1964; Shelley, 1993). The crystal grows as more atoms are added to the crystalline structure in homogenous and heterogenous nucleation.

As undercooling begins, nuclei start to form at random (Shelley, 1993). Initially the nucleation rate is low, but as undercooling increases so does the nucleation rate, until it reaches a maximum. If undercooling continues to a high degree, rates of nucleation decline from this maximum (Harker, 1909; Hawkes, 1967). This relationship is also applicable to growth rates of nucleated minerals, where the maximum growth rate is achieved at a particular degree of undercooling. These rates vary with different magma composition and are particularly sensitive to the presence of volatiles (water/alkalis) and viscosity (which inversely correlates with volatiles) (Shelley, 1993).

In order for crystals to grow, appropriate ions need to move to the site of nucleation/growth, this occurs through diffusion. The rate of diffusion is highest in melts/liquids, slower in glass, and slowest in crystals (Shelley, 1993). Equilibrium shapes are produced if diffusion rates are faster than crystal growth rates, forming simple faceted forms. This may occur, for example, in low-viscosity magma with slight undercooling. As

viscosity increases with higher degrees of undercooling, the nucleation and growth rates may also increase (Shelley, 1993). This may result in diffusion-controlled growth kinetics and the development of disequilibrium textures, such as skeletal, dendritic and spherulitic forms (Shelley, 1993).

The mobility of ions within a solid structure also occurs through diffusion, ultimately resulting in the unmixing of the solid phase and the formation of exsolution textures. The mobility of ions is limited in solid solution minerals and becomes more limited as temperatures decreases (Vernon, 2004). Therefore, the separating phases seldom form separate crystals and instead form exsolution lamellae. The lattices of the lamellae have a specific crystallographic relationship with the host. The less abundant phase generally forms crystallographically orientated planar bonds or exsolution lamellae in the more abundant host (Vernon, 2004). For example, ilmenite and hematite form a complete solid solution ($FeTiO_3$–Fe_2O_3) at more than 1050°C. With decreasing temperature, a miscibility gap develops and the solubility of hematite in ilmenite decreases. Exsolution of hematite in ilmenite forms when Ti^{4+} and Fe^{2+} are replaced by Fe^{3+}. A decrease in temperature therefore forms the commonly observed exsolution lamellae of hematite in ilmenite as the two solid solution phases undergo unmixing in the solid state (e.g. Deer et al., 2013).

The interplay between diffusion, nucleation, and growth is represented by the textural features preserved by a crystallising mineral. Slow rates of diffusion relative to growth rates are likely to result in skeletal or dendritic habit (Shelley, 1993). These crystals form crystallographically orientated hollows or voids, typically filled with groundmass material. This crystal shape forms as the chemical components necessary for crystal growth are not readily available at the site of nucleation, often resulting in preferential growth at crystal corners (Shelley, 1993; Vernon, 2004). Instead of a stable regular crystal, the crystal tends to reach out towards source material in a melt. Components of the melt not incorporated into the growing crystal are therefore concentrated around the crystal-melt interface, reducing the degree of supersaturation around the mineral interface, such that further crystal growth is only possible further away from the interface in undepleted melt (Gornitz, 1981; Shelley, 1993). This crystal form is indicative of rapid undercooling and supersaturation and represents a disequilibrium texture. This texture, and other disequilibrium textures, are often associated with glass, as they form in similar rapidly undercooled environments, such as in quenched volcanic rocks (Shelley, 1993; Vernon, 2004).

Euhedral crystals are bounded on all sides by well-developed crystal faces. This mode of crystal shape forms in melts that are not significantly undercooled and are suspended in a melt (Shelley, 1993). With subsequent crystallisation from these early formed minerals, they begin to fill the magma body and come into contact with one another, impeding some or all of the crystal faces, forming subhedral or anhedral crystal shapes, respectively (Shelley, 1993; Vernon, 2004). From this it is possible to form a sequence of crystallisation; euhedral crystals form first with more developed crystal faces and anhedral crystals form last filling interstitial spaces between euhedral crystals. However, it is important to note that well developed faces also depend on surface energy of the faces, and in some cases minerals

with a low surface energy may form euhedral crystals even in metamorphic rocks (Winter, 2013).

Equilibrium crystallisation occurs when elements between mineral phases and their coexisting melt are in equilibrium at all stages of the crystallisation process (Sha, 2012). Fractional (Rayleigh) crystallisation occurs when a newly formed mineral is isolated from the melt. This may be a result of a variety of mechanisms, including fractional crystallisation by removal, zoning, or entrapment (Sha, 2012). Newly formed crystals may be isolated from the melt by physical removal of the crystal from the system (i.e. crystal settling). Newly formed layers of a crystal may isolate the interior of the crystal from the melt and are evident as crystal zoning (Sha, 2012). This requires that the diffusion rates across the crystal zones are sufficiently slow enough, or the growth rates are sufficiently fast enough (common in a quenched environment and may also lead to skeletal crystal growth), so that there is no exchange of elements across the crystal zones (Sha, 2012). Crystals may also be isolated from the melt by entrapment as an inclusion in another phase (Sha, 2012).

1.4 Aims and objectives

A review of the literature reveals that many aspects of kimberlites, and in particular the polymineralic melt inclusions hosted in megacrysts, are still highly debated (Bussweiler, 2019). These melt inclusions may provide valuable information pertaining to the parental kimberlite melt compositions and the relationship between the megacryst-forming melt, the captured melt, and the kimberlite melt.

This project aims to better understand the genesis of the melt inclusions hosted in ilmenite megacrysts and the evolution of the melt prior to melt capture, and subsequently within the melt inclusion cavity. To achieve this, we propose to present evidence through textural, and major and trace element analyses of unaltered glass and related crystalline phases, which have been preserved in quenched silicate-carbonate primary melt inclusions hosted in ilmenite megacrysts from the Monastery kimberlite. The studied thin sections will be examined petrographically and the optical features of the glass and crystalline phases described. The samples will then be investigated geochemically, initially using EDS analysis, followed by more focused EPMA and ICP-MS analysis to collect major and trace element data on the ilmenite megacrysts and the mineral and glass daughter phase assemblage hosted within the melt inclusions. The observed features will be incorporated into the current body of literature regarding kimberlite evolution and the formation of melt inclusions in the Monastery kimberlite and kimberlites worldwide.

In many instances, this thesis requires the reader to refer to figures or tables presented in earlier chapters. For the convenience of the reader, find attached a separate document (Appendix 1) containing duplicates of all the figures and tables presented in this thesis. The purpose of this document is to aid the reader in navigating to the appropriate figure/table referred to in the text.

Chapter 2: Methodology

2.1 Sample acquisition

Thin sections of ilmenite and olivine megacrysts used in the current study were obtained from the John J. Gurney Upper Mantle Research Collection at the University of Cape Town. Samples were selected from the Monastery kimberlite material in the collection on the basis of the presence of well-preserved melt inclusions within the megacrysts identified using optical microscopy facilities at UCT. A total of 32 thin sections were obtained. The 32 thin sections were subjected to more detailed optical microscopy at Rhodes University and a further 16 were selected for EDS analysis; of these eight are used in the current study. Select samples of these eight were subjected to EPMA analysis and ICP-MS laser ablation trace element analyses.

2.2 EDS analytical techniques

Energy dispersive spectrometry (EDS) was used to identify and analyse glass, crystal phases of the common daughter assemblage, and the host ilmenite megacrysts. Results of EDS analyses were validated with a smaller number of EPMA results, which proved sufficiently similar. EDS analyses were conducted using an Oxford Instruments silicon-lithium detector attached to a TESCAN Vega TS 5136LM SEM at Rhodes University's Electron Microscopy Unit. The EDS detector is an INCA Pentafet-X3 Si (Li) detector with a $30mm^2$ detector crystal and a peak resolution better than 129 eV (MnKα). A cobalt standard was used for calibration. A 20 kV acceleration potential with 50–60% dead time on the processor and 60 net seconds of data acquisition was used for point analysis. Area analyses were recorded during 120–200 net seconds of data acquisition depending on area size.

2.3 EPMA analytical techniques

Quantitative mineral chemical analyses of ilmenite, serpentine, and glass were obtained by using four wavelength dispersive spectrometers on a JEOL JXA-8230 electron probe micro-analyzer at Rhodes University. The beam was generated by a tungsten cathode, and excited with 15 kV accelerating potential at 2 or 10 nA current depending on the sensitivity of the phases to beam damage. Beam sizes of 1–20 µm were used depending on the beam sensitivity of the material. CRM BIR-1G was used to validate the glass routine. All elements were measured on K-alpha peaks. Counting times on each of peak and total background measurements were 10 s for ilmenite and glass, and 15 s for serpentine. Overlap of Ti-Kβ on V-Kα was corrected for. Commercial "SPI" standards were used for intensity calibration. The standards were Kaersutite/Pyrope/Plagioclase (Al, Si, Mg), Magnetite/Pyrope (Fe), Albite (Na), Rhodonite/Mn-metal (Mn), Plagioclase (Ca), Orthoclase (K), Cr_2O_3 (Cr), Olivine/Ni-metal (Ni), Rutile (Ti), and V-metal (V). The data were collected with JEOL software (PC EPMA 1.9.2.0) and its ZAF matrix algorithm (Heinrich/Duncumb-Reed with FFAST-2005 MACs) was applied to correct for differential matrix effects. Oxygen was calculated by stoichiometry and H_2O by difference before the correction. Samples were polished down to 20 µm before analyses, and vacuum carbon coated to 25 nm (+/-5) thickness.

2.4 Trace element analytical techniques

Trace element analysis were performed using a New Wave UP213 solid-state laser ablation system attached to a ThermoFisher XSeries2 quadrupole ICP-MS (inductively coupled plasma mass spectrometer) at the University of Cape Town. The beam size ranged between 60 and 100 microns and spots were measured for 50 seconds. Calibration was achieved using NIST standards (NIST 610 and NIST 612).

2.5 Data processing

Stoichiometric calculations of cations and volatiles for EDS and EPMA analysis of minerals were made using the Rock Maker software (Büttner, 2012). The abundance of H_2O in phlogopite, serpentine, and kassite was iteratively determined for the optimal stoichiometric fit. The Fe^{3+}/Fe^{2+} ratio in the analysed minerals was also calculated iteratively to produce the optimal stoichiometric structural site fit and charge balance.

For phlogopite, H_2O was added to optimise the OH position to 2 anions. The Fe^{3+}/Fe^{2+} ratio was modified until the tetrahedron position was occupied by 4 cations and the octahedron position was occupied by 3 cations. For serpentine, H_2O was added to produce 4 OH molecules. The Fe^{3+}/Fe^{2+} ratio was modified to produce 3 cations in the octahedral position and 2 cations in the tetrahedral position. For kassite, H_2O was added to produce 2 OH molecules. The Fe^{3+}/Fe^{2+} was modified to optimise for 3 cations per 5 oxygen atoms.

For perovskite, the Fe^{3+}/Fe^{2+} proportion was optimised for 2 cations per 3 oxygen atoms. The cation distribution was optimised to 1 cation in the Ti site and 1 cation in the Ca (Na, Fe^{2+}) site. For ilmenite, the Fe^{3+}/Fe^{2+}ratio was optimised for 2 cations per 3 oxygen atoms. The cation distribution was optimised to 1 cation in the Ti (Zr + Si) site and 1 cation in the Fe (Mg + Mn + V + Cr) site. For spinel, the Fe^{3+}/Fe^{2+} ratio was optimised for 3 cations per 4 oxygen atoms. The spinel end-member compositions were determined by distributing Fe^{3+} to Fe^{2+} or Mg^{2+} endmembers.

The H_2O content of the glass was calculated by differences in EPMA oxide totals, which produced results of ~13 wt%. This volatile abundance was then assumed for EDS calculations.

EDS area scans were used to calculate bulk compositions using exposed modal proportions in 2-D with the Rock Maker software (Büttner, 2012). Modal proportions were calculated using BSE images and the ImageJ software. CO_2 content was calculated using modal proportions of calcite, assuming that calcite contains 44 wt% CO_2 and no other CO_2-bearing phase is present.

Chapter 3: Petrography

3.1 Sample material and rationale for petrography

The material described and analysed in this study has been selected from 32 thin sections of ilmenite megacrysts of the Monastery kimberlite obtained from the John J. Gurney Upper Mantle Research Collection at the University of Cape Town. Of the 32 thin sections, eight that show well-developed melt inclusions (MI) have been described petrographically and analysed micro-chemically. The Mantle Room collection does not possess the original thin section off-cuts or the sample material. This study is entirely based on polished thin section material.

The ilmenite crystals are, with one exception (ROM109 (C); Fig. 3.1), larger than the thin sections (~ 2.9 x 4.7 cm). Some samples show the margins and parts of the kimberlitic matrix; others show only the interior of the ilmenite crystals. One sample (S5251) is a mount of two centimetre-sized ilmenite fragments. The size of the original megacryst and the positions of the fragments within it are not known. In such samples it is not possible to determine the proximity of the investigated ilmenite domains or the melt inclusions with respect to the margins of the ilmenite megacrysts. Where the megacryst rim is exposed, the text will refer to the distance to the crystal margins where relevant.

The petrographic study of the selected eight thin sections has shown that the phase assemblage and the composition of these phases is similar in all melt inclusions. Also, the textures and compositional variations are similar across all ilmenite samples. Therefore, the focus of this chapter is to initially describe the thin section samples, followed by the general composition and textural features across all melt inclusions, avoiding the repetitive description of a large number of melt inclusions that in principle show identical textures and compositions. In that regard, the descriptions will make use of appropriate examples from the investigated material to describe general features. However, the presence of specific features that may be relevant to the understanding of the genesis or evolution of the trapped melt are always highlighted, even if such features are not ubiquitous, abundant, or common.

The ilmenite samples (and the number of melt inclusions studied within them) analysed in this study are:

1) PO15 (6 MI)
2) S5628 (6 MI)
3) S5626 (3MI)
4) S5251 (2 MI)
5) ROM 109 (C) (3 MI)
6) ROM112 (1 MI)

7) ROM31E (A) (2 MI)
8) ROM 264 (1 MI)

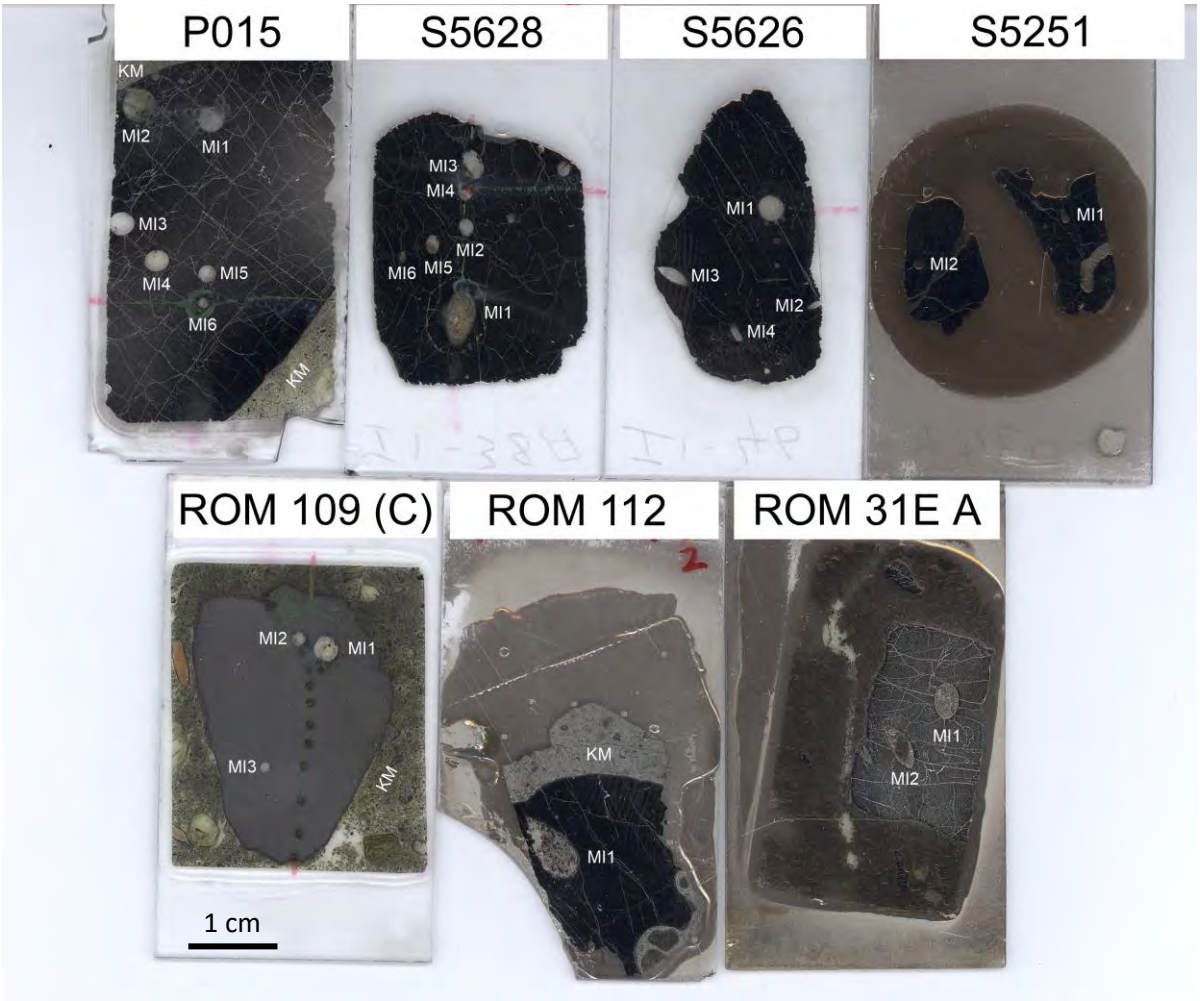

Fig. 3.1. Scanned thin sections used in the current study, showing the investigated ilmenites, their melt inclusions (MI), and the surrounding kimberlite matrix (KM).

3.2 Ilmenite megacrysts

The ilmenite megacryst are largely homogeneous in texture. Crystal inclusions, other than those contained in melt inclusions, appear to be rare in the investigated Monastery ilmenites. Among the 32 examined thin sections only one (S5679) contains two zircon crystal inclusions of 1.5 and 3 mm in their longest dimensions. This thin section, however, does not contain the commonly observed melt inclusions. Within the ilmenite megacrysts no variation in the BSE signal intensity or in the intensity of optical light reflection suggests significant compositional changes. A further remarkable feature of the ilmenite megacrysts are thin veins, of which two types are present. The first type contains phases similar to those present in the melt inclusions (calcite, perovskite, serpentine etc.). These veins are present in the proximity of melt inclusions from which they appear to emanate. Some can

be seen to pinch out nearby the melt inclusions within the ilmenite host. The second type are calcite-rich veins that may or may not transect melt inclusions. Since this type intersects the melt inclusions, they are interpreted as secondary structures that formed subsequent to the solidification of all phases in the melt inclusions. Both types of veins are further described below (Chapter 3.3).

3.3 Melt inclusions in ilmenite megacryst samples

The ilmenite megacryst-hosted melt inclusions range from 1 to 5 mm in size. In thin section they show either circular or oval cross-sections (Fig. 3.1), which is consistent with spherical to ellipsoidal melt inclusion shapes seen in X-ray tomography of similar ilmenite megacrysts from the Monastery kimberlite (pers. comm., Büttner, 2019). The distribution and abundance of melt inclusions within the ilmenite megacrysts appears to be random, with samples containing between 1 to 6 melt inclusions in thin sections (Figure 3.1). 3D tomography of 2–4 cm ilmenite megacrysts confirms this impression, with some crystals containing only few or no melt inclusions, whereas others show >20 inclusions (pers. comm., Büttner, 2019).

The melt inclusions commonly host a daughter mineral assemblage of calcite, ilmenite, spinel, phlogopite, serpentine, and perovskite, as well as a glass component. The textures of glass and mineral phases are described in detail across all melt inclusions in Chapter 3.4, their major-element compositions in Chapter 4, and trace element composition in Chapter 5. The variations in modal proportions of these minerals and glass are largely dependent on calcite proportions, which show the largest variability. In this context it is important to note that the melt inclusions in thin section represent a 2D slice, which may not fully represent the phase or modal compositions of the three-dimensional melt inclusions that are intersected. Table 1 shows the large variations in calcite modes in the exposed melt inclusions that range from 0.5 to 96.5% area cover, which impacts on the mode of other phases, such as silicates, oxides and glass. Oxide phases (perovskite, secondary ilmenite, spinel) are present in all melt inclusions in the study and range from fairly abundant (12.1%) to comprising a minimal component (0.5%). Glass is present in all but one inclusion and where present it varies greatly in abundance (1.4–95.1%). Serpentine is not present in all inclusions but where it does form it does not comprise less than 8% of the melt inclusion and forms up to 79%. Phlogopite forms a minor component; when present, phlogopite modes range from 0.5–9.0%. Calcite is commonly the most abundant phase, comprising >90% of some inclusions, but varies greatly, comprising only 0.5% of other inclusions. It is unclear to what extent such data represent true modal variations in the three-dimensional volume of melt inclusions (Howarth and Büttner, 2019).

Table 1. Modal proportions of phases in melt inclusions, determined from BSE images using ImageJ software

		Modal proportions (%)						
Sample	Melt Inclusion	Glass	Calcite	Oxides	Serpentine	Phlogopite	Apatite	Ca-Si (Harkerite)
P015	MI1	51	43	6	-	-	-	-
	MI3	19	79	2	-	-	-	-
	MI4	72	22	6	-	-	-	-
	MI5	36	60	4	-	-	-	-
	MI6	10	75	7	-	8	-	-
S5628	MI1	9	1	6	76	9	-	-
	MI2	1	97	2	-	-	-	-
	MI3	7	81	12	-	-	-	-
	MI4	14	78	8	-	-	-	-
	MI5	5	93	3	-	-	-	-
	MI6	9	83	9	-	-	-	-
S5626	MI1	52	14	2	34	-	-	-
	MI2	87	3	3	8	-	-	-
ROM 109 (C)	MI1	43	41	6	-	3	7	-
	MI2	57	35	8	-	-	-	-
	MI3	2	93	5	-	1	0.1	-
ROM 31-E(A)	MI1	25	72	3	-	1	-	-
	MI2	56	38	6	-	-	-	-
ROM264	MI1	74	7	2	-	-	-	-
ROM112	MI1	-	12	4	80	-	-	5
S5251	MI1	91	-	9	-	-	-	-
	MI2	95	-	5	-	-	0.5	-

3.3.1 S5626: MI1–MI4

Sample S5626 contains four main melt inclusions (Fig. 3.1) that are either circular or lenticular in cross-section and range from 1–3 mm in their largest exposed dimension. Three of them (MI1-MI3) have been analysed. All melt inclusions contain the commonly observed assemblage of glass, calcite, serpentine and oxide phases, but phlogopite is absent. MI1 (Fig. 3.2) is connected to one ~10–20 µm thick veinlet that extends about 1 cm into the host ilmenite. The vein material merges with the material that forms the interior of MI1, suggesting crystallisation from the same melt in the vein and in the inclusion. Other thin carbonate-rich veinlets transect the host ilmenite in orientations either parallel to the vein extending from MI1, at sub-parallel orientations, or at high angles (Fig. 3.1). Most are not connected to any melt inclusions. These veinlets contain mainly calcite but also minor amounts of silicates (serpentine) and perovskite. In one vein that transects the host ilmenite megacryst a small crystal of strontianite has been identified using EDS.

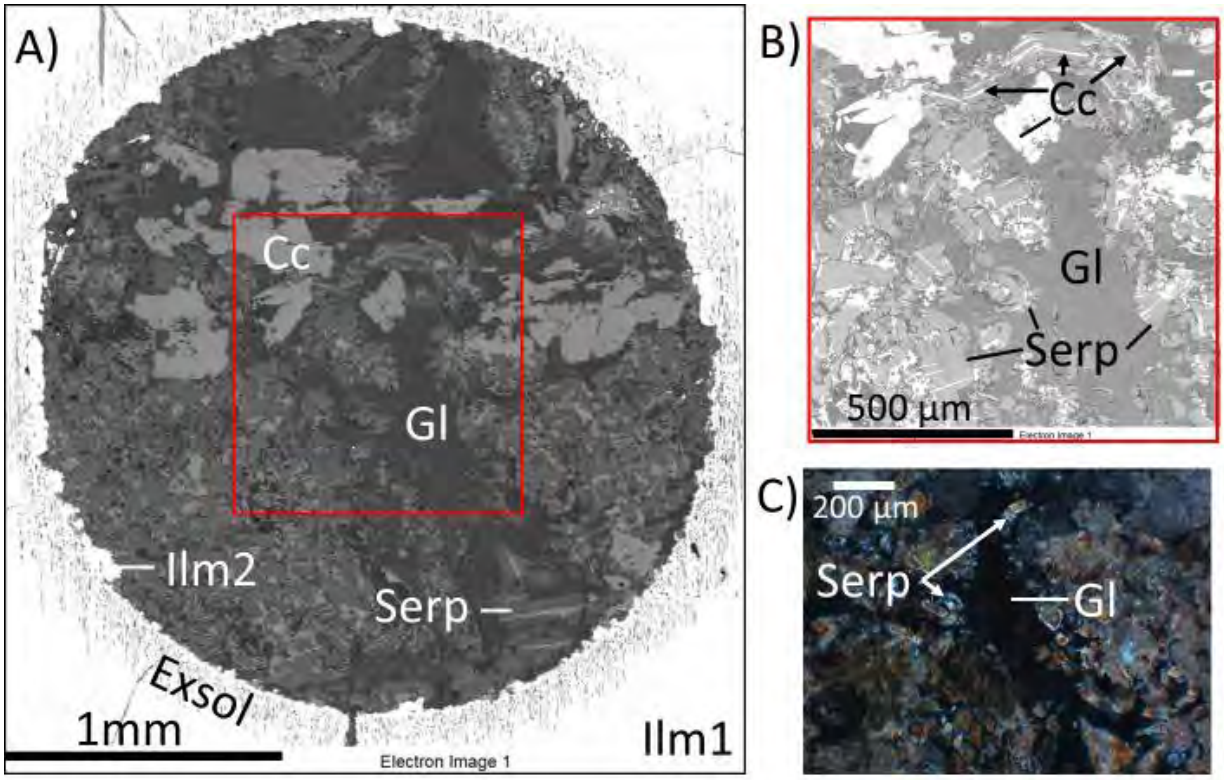

Fig. 3.2. Backscattered electron images (BSE) and cross-polarised light (XPL) photomicrographs of MI1 and the host ilmenite megacryst (Ilm1) in sample S5626. A) Spherical melt inclusion with secondary epitaxial ilmenite (Ilm2) on the melt inclusion interface with Ilm1. Exsolution textures (Exsol) extend about 250 µm into the host ilmenite. Fresh glass (Gl) forms large coherent central pools and occupies the space between serpentine (Serp) and calcite (Cc); B) Close-up view of large central glass pool (red square on figure A). Serpentine forms euhedral fan-shaped grains with calcite and occasionally glass between the radial crystals of the serpentine (arrows). Calcite (Cc) also forms large grains. C) Central glass pool in cross-polarised light showing the isotropic nature of fresh glass and radially arranged serpentine crystals (arrows).

The lenticular MI2 and MI3 (Fig. 3.3), and rhombohedral MI4, contain the same assemblage observed in MI1 (glass, calcite, serpentine, and oxide phases). Hence, sample S5626 shows melt inclusions with similar assemblages and textures but variable size and shape. The thin veinlets that are connected to these melt inclusions appear to be more calcite-rich but otherwise are similar in composition to the inclusions themselves. Within the ilmenite megacrysts immediately surrounding MI1, MI2, and MI3 is a zone of exsolution lamellae (~250 µm wide) (see Chapter 3.4).

Features seen in MI1 to MI4 are within the common range of textures and assemblages seen in the analysed eight thin sections and are covered in Chapter 3.4.

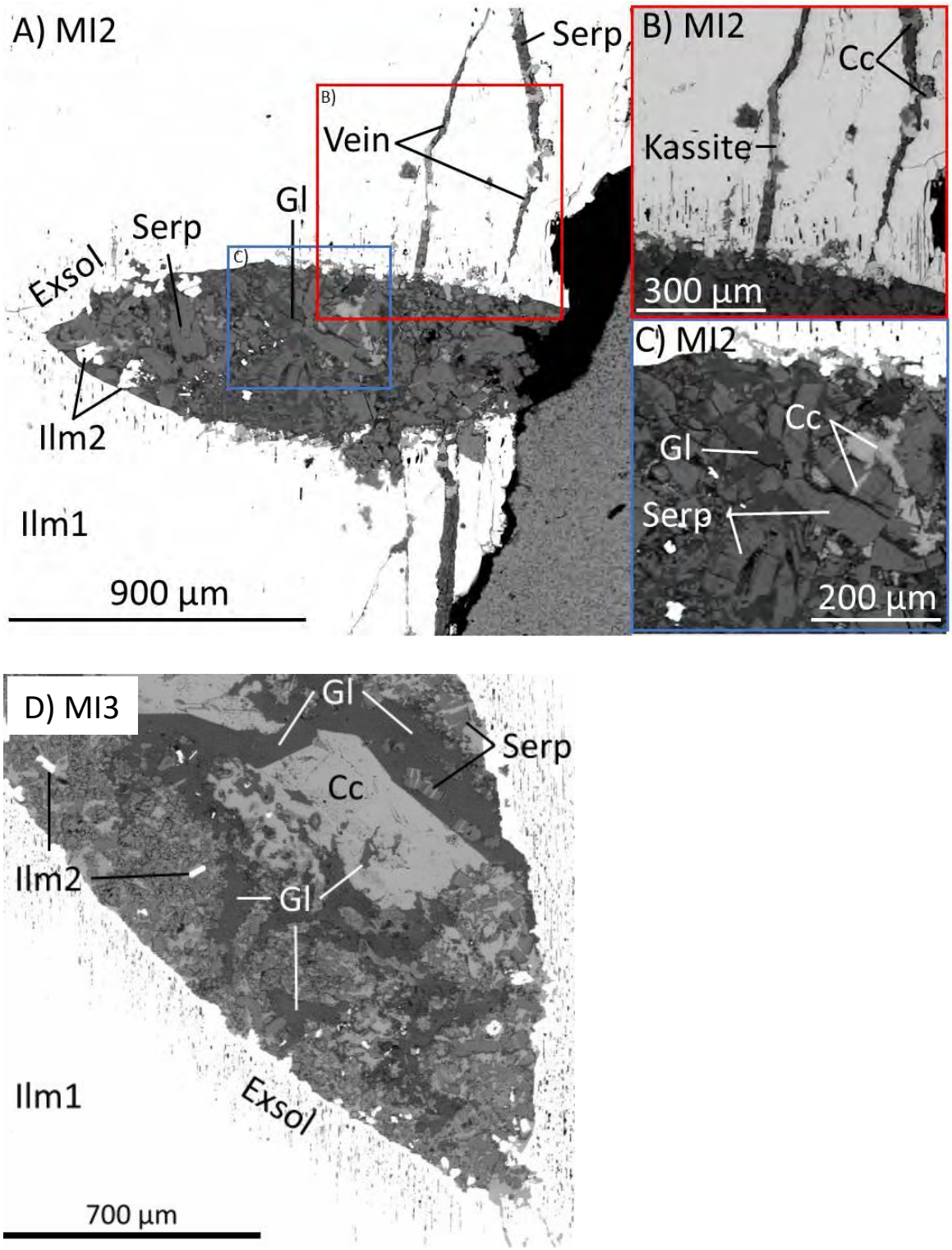

Fig. 3.3. BSE of sample S5626, melt inclusion 2 (A, B, and C) and melt inclusion 3 (D), hosted in an ilmenite megacryst (Ilm1). A) Lens-shaped MI2. The entirety of the inclusion is not visible as it occurs on the margins of the thin section. The host ilmenite megacryst (Ilm1) shows an exsolution pattern around the margin of the inclusion. Subhedral secondary ilmenite (Ilm2) occurs within the melt inclusion along with large subhedral serpentine (Serp), coherent glass (Gl) pools, and anhedral calcite (Cc). Three large veins extend into the ilmenite megacryst from the melt inclusion margin. The veins host material similar to the common mineral assemblage identified within the melt inclusions. B) Closer BSE image of 2 large veins that radiate from MI2 into the host megacryst. The veins host components of the common mineral assemblage within the melt

inclusion. Subhedral kassite and calcite occur within the veins. C) Close-up BSE image of the central coherent glass pool within MI2. The glass pool forms the matrix for fan-shaped subhedral and euhedral serpentine. Calcite is anhedral and occurs between the rays of the fan-shaped serpentine grains. D) Lenticular MI3 hosted within the ilmenite megacryst. Exsolution patterns occur around the margins of the melt inclusion within the megacryst. Secondary ilmenite forms subhedral and euhedral grains within the melt inclusion. Anhedral calcite is present between subhedral and euhedral fan-shaped serpentine. Calcite also occurs as large subhedral grains with well-developed crystal faces in the centre of the melt inclusion. Glass forms large coherent pools in which calcite and serpentine form with well-developed crystal faces.

3.3.2 P015: MI1–MI6

Sample P015 contains seven melt inclusions of which six have been analysed. All melt inclusions are circular in cross-section. Their diameters range from 0.7 to 3.3 mm. The melt inclusions appear to be randomly distributed. Two types of melt inclusions can be distinguished: two MIs adjacent to the ilmenite megacryst margin contain material indistinguishable from the kimberlitic matrix (Fig. 3.4), all other MIs, which are exposed within the ilmenite megacryst interior, contain the typical assemblage of calcite, oxides, silicate crystals and glass (Chapter 3.5).

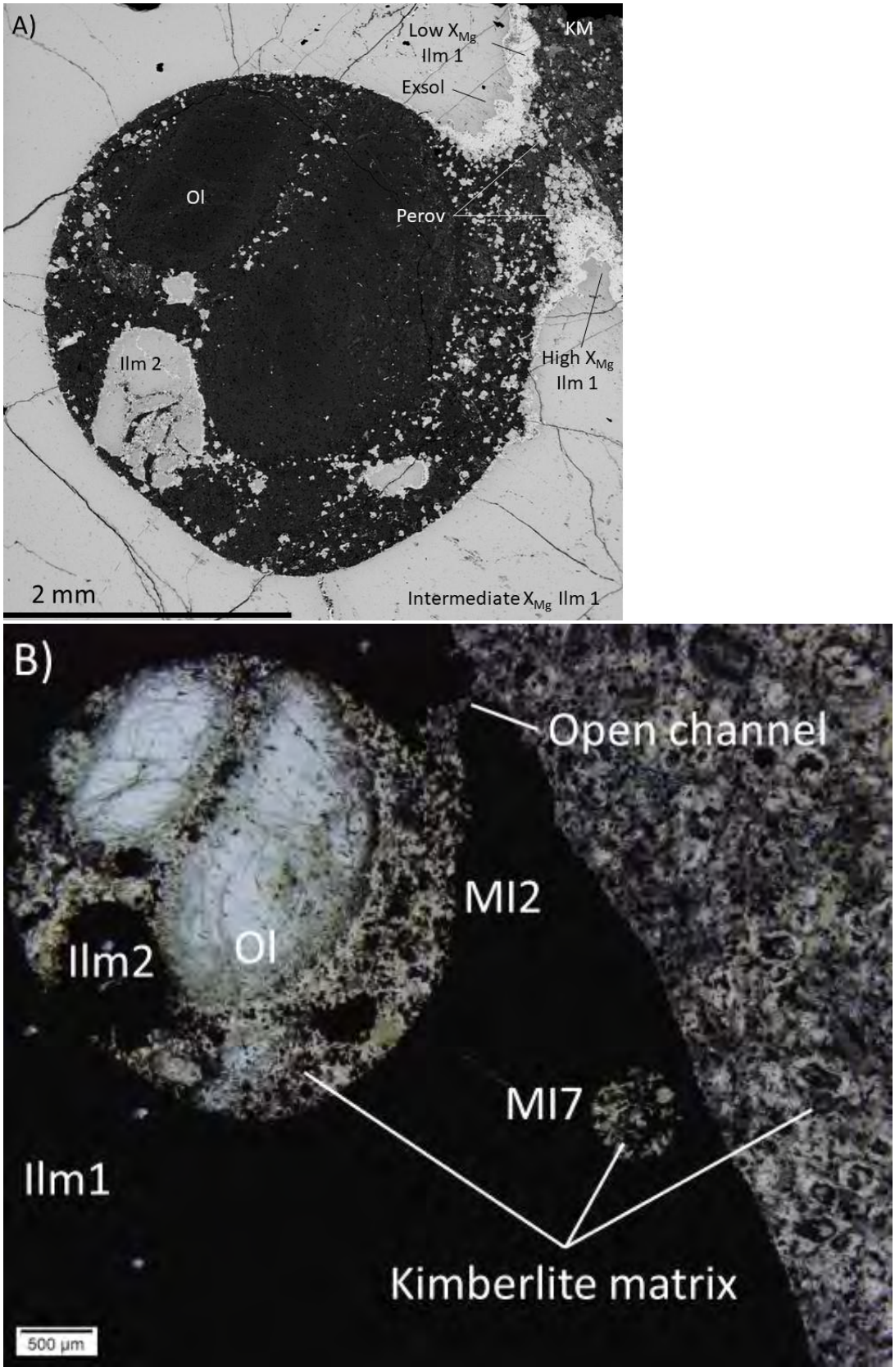

Fig. 3.4. BSE and PPL photomicrographs of sample P015 MI2 and MI7. A) BSE image of MI2 showing irregular secondary ilmenite (Ilm2) and serpentinised olivine (Ol). The host megacryst ilmenite (Ilm1) does not completely enclose the melt inclusion and the melt inclusion connects to the kimberlite matrix (KM). Perovskite (Perov) forms around the margins of the ilmenite megacryst near the opening to the surrounding

kimberlite matrix. A reaction zone of Mg-poor/Fe-rich ilmenite (Low X_{Mg} Ilm1: 0.03 X_{Mg}; Chapter 4.1) forms along the margin of the ilmenite megacryst in contact with the kimberlite matrix. Surrounding this reaction zone is a zone of Mg-rich/Fe-poor ilmenite (High X_{Mg} Ilm1: 0.6 X_{Mg}; Chapter 4.1). This zone also forms with exsolution lamellae (Exsol). The megacryst interior consists of an intermediate Mg/Fe composition (intermediate X_{Mg}: 0.3 X_{Mg}; Chapter 4.1). B) PPL image of MI2 and MI7 shows the similarity in texture of material hosted within the melt inclusions and kimberlitic matrix. MI2 hosts large serpentinised olivine crystals, which are larger in size than the connecting channel. A smaller melt inclusion (MI7) located near the rim of the ilmenite megacryst also hosts material similar in texture to the kimberlite matrix.

The largest melt inclusion, MI2 (Fig. 3.4), is positioned close to the ilmenite megacryst margin and is connected to the kimberlite matrix via a narrow channel. Its composition is markedly different from the commonly seen inclusions. Phases in the channel connecting MI2 with the matrix are essentially serpentine, perovskite, and minor spinel. Within the inclusion, two prominent large serpentine domains show relict olivine. In texture, composition, and size these crystals are identical to serpentinised olivine in the kimberlite matrix. This inclusion also contains large ilmenite crystals (Ilm2 in Fig. 3.4). The ilmenite and olivine contained in the melt inclusion are significantly larger than the exposed channel that connects the melt inclusion to the matrix. There is a textural and mineralogical continuum from the melt inclusion through the channel into the kimberlite matrix (Fig. 3.4). A small melt inclusion nearby (MI7; Fig. 3.1; Fig. 3.4) is similar in composition but appears to be entirely enclosed by the ilmenite megacryst. However, the inclusion is separated by an only ~200 µm thin rim of ilmenite megacryst from the kimberlite matrix (Fig. 3.4). Hence, it may be connected to the kimberlite matrix above or below the level exposed in thin section.

The inclusions in the interior of the ilmenite megacryst in sample P015 are texturally different from MI2 and MI7. MI1 and MI3–MI6 show variable amounts of calcite, oxides, and glass. Olivine or large secondary ilmenite grains are absent. In their compositions and textures these melt inclusions are similar to those seen in other samples and are described in the general descriptions in Chapter 3.4.

3.3.3 S5628: MI1–MI6

Sample S5628 contains nine melt inclusions ranging from circular to ellipsoidal and slightly irregular in shape. The size varies between 0.7 to 5.1 mm in their largest exposed dimension. All except MI1 show the commonly seen features with high calcite proportions, glass, oxides, but are phlogopite free. MI1 is the largest inclusion in sample S5628. It shows an oval cross-section of 5.1 x 2.7 mm. In contrast to the other melt inclusions, MI1 does not contain significant calcite in the exposed section and also has a relatively low proportion of glass. Its assemblage is serpentine, phlogopite, glass, ilmenite (secondary), kassite, and spinel. The most common among the oxides hosted within the inclusion appears to be spinel, and the least abundant is kassite.

Phlogopite forms a cluster around a glass pool in the centre of MI1 (Fig. 3.5B). The majority of MI1 is occupied by serpentine with glass in interstices. Few large spinel crystals appear to be randomly distributed or accumulate into aggregates. They commonly show some intergrowth with other oxide phases (Fig. 3.3B). Along the margin of MI1, a reaction zone of hemispherical bulges with a higher BSE intensity extends into the hosting ilmenite megacryst. EDS analysis determined this reaction zone to be Ca-rich (see Chapter 4.3.5). Surrounding this reaction zone, the ilmenite megacryst shows a thin zone of lower BSE intensity, suggesting decreasing iron contents toward the reaction zone (Fig. 3.5C). This texture suggests a chemical reaction between the melt inclusion and the hosting ilmenite megacryst forming this texture.

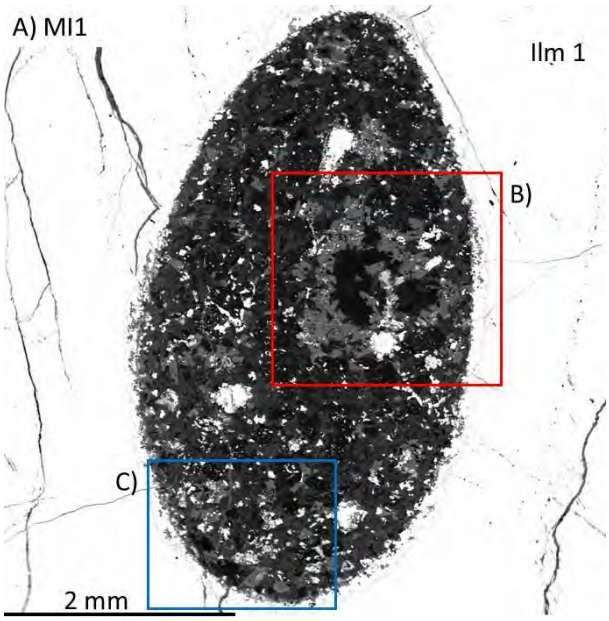

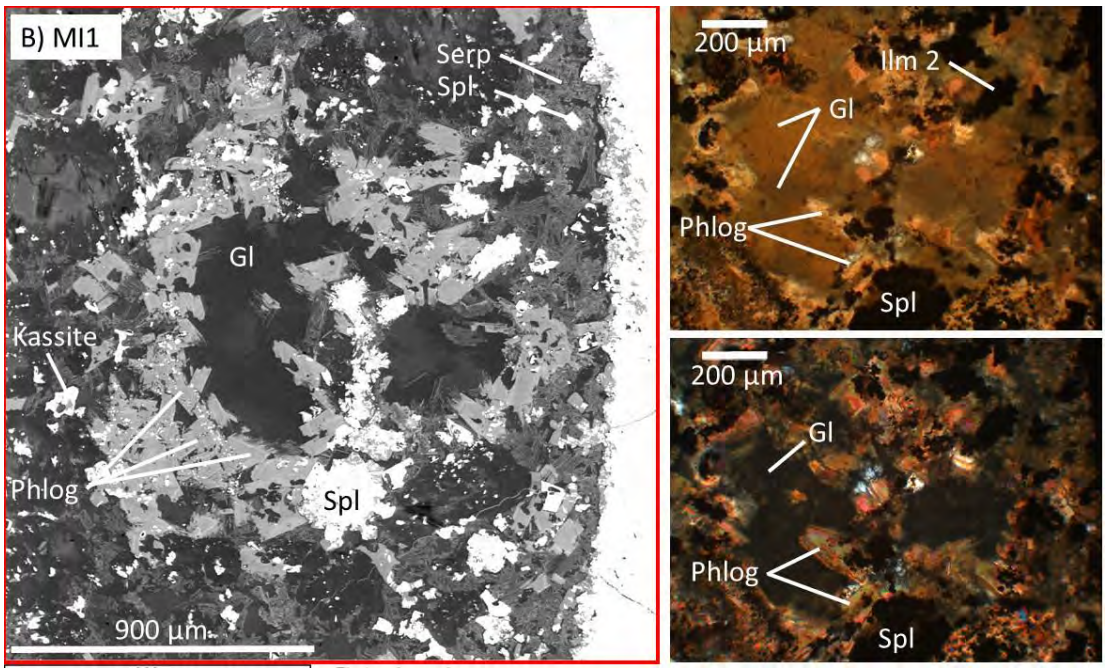

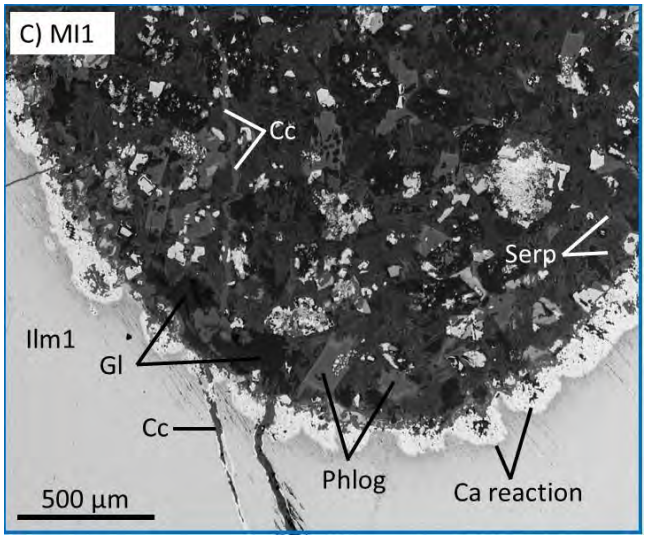

Fig. 3.5. BSE, PPL, and cross-polarised light (XPL) images of MI1, sample S5628. A) Ellipsoidal melt inclusion hosted in Ilm1. Bright BSE signals are spinel (Spl), secondary ilmenite (Ilm2) and kassite crystals. Phlogopite (Phlog) is light grey; serpentine (Serp) and glass (Gl) are BSE-dark. B) Close-up BSE, PPL, and XPL images of a large coherent glass pool surrounded by an aggregation of subhedral lath-shaped phlogopite and fine-grained serpentine. In PPL the glass has a light brown colour with areas that are darker in colour. In XPL, the glass is isotropic. Serpentine commonly shows glass in interstices. Fined-grained euhedral spinel forms single grains and clusters. Kassite forms small subhedral grains within the melt inclusion. C) A Ca-rich reaction zone (Ca reaction) of hemispherical bulges protruding into the host ilmenite megacryst (Ilm1), commonly containing BSE-dark small inclusions, presumably glass or serpentine. The ilmenite megacryst surrounding the Ca-reaction zone shows a slightly darker BSE colour, suggesting lower Fe contents. The interior of MI1 contains glass, serpentine, phlogopite, and oxide phases. A small vein of calcite (Cc) texturally overprints the mineral assemblage within the melt inclusions and therefore is interpreted to have formed after the solidification of the inclusion content.

3.3.4 S5251: MI1–MI2

Thin section S5251 contains two ilmenite fragments mounted together. It is unclear whether or not these fragments belong to the same ilmenite megacryst. Each fragment contains one main melt inclusion. The two melt inclusions host similar daughter phase assemblages and textures.

MI1 is a bottle-shaped melt inclusion that is ~1.3 x 0.6 mm in size (Fig. 3.6). It contains only glass, spinel, and secondary ilmenite. Perovskite, phlogopite, serpentine, and calcite are absent (Table. 1). Glass is always isotropic without signs of devitrification or alteration. Texturally the glass domain shows unusual features that are only observed in this thin section (in both MI1 and MI2). The glass pool is subdivided into isometric pale brown to yellow domains that are separated by thin linings of opaque particles with high BSE signal intensity, from a transparent and colourless glass matrix. The opaque particles are <1 µm and could not be analysed with the available instrumentation. The separate pale-brown glass domains are 20–40 µm in diameter. BSE images show no variation in signal intensity

between the pale-brown and colourless glass domains, suggesting roughly uniform composition (Fig. 3.6). This is confirmed by EDS analysis (Chapter 4.3.1). There is no clear indication what causes the different colours of these two different glass varieties. Where brown glass domains are in contact, the geometry formed by the small opaque particles resembles 120° triple-point junctions. The same geometry is formed in some euhedral and skeletal spinels that form only crystal faces with skeletal voids in the interior occupied by glass. Large euhedral spinels most commonly form near the margins of the inclusion.

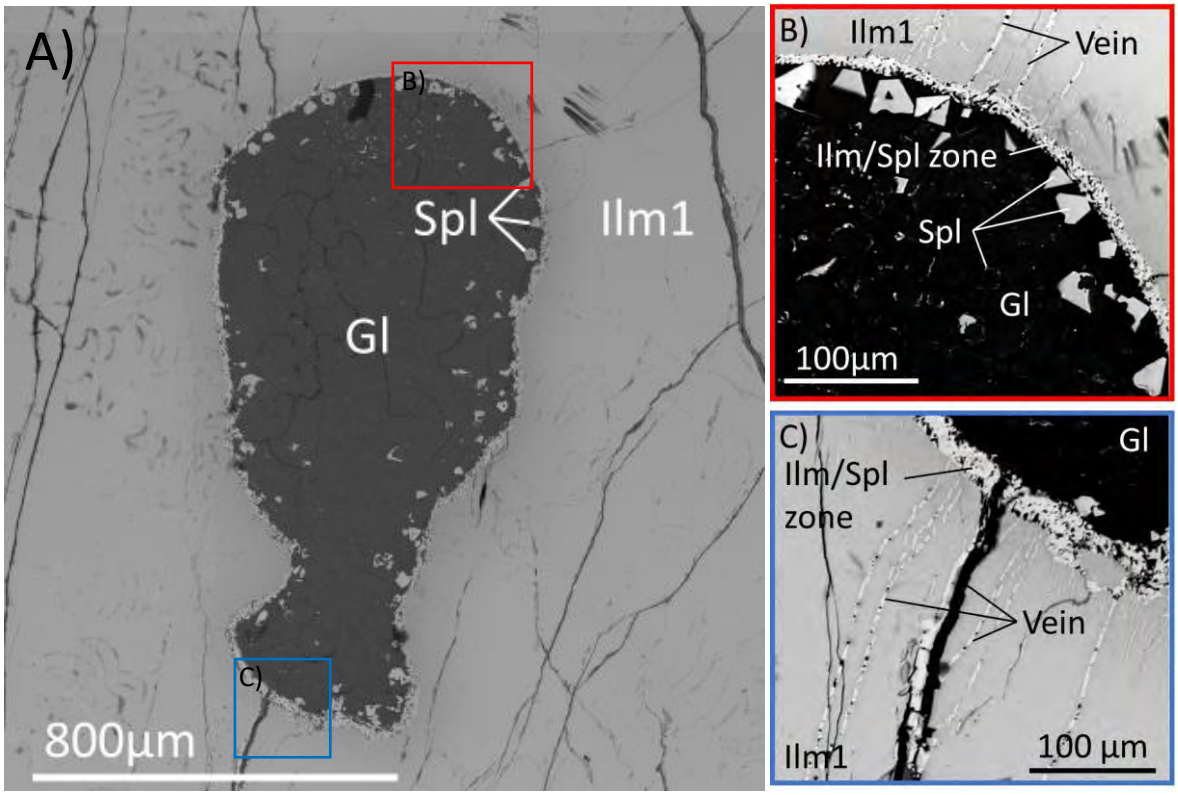

Fig. 3.6. A) BSE image of MI1 in sample S5251. The glass exhibits a uniform BSE signal intensity. Fine-grained <1 µm opaque minerals form within the glass. Large skeletal and euhedral spinel forms towards the margins of the inclusion. B) Close-up BSE image of the melt inclusion–megacryst interface showing large subhedral spinel and fine-grained spinel set within a glass matrix. Veins containing separate BSE-dark domains (similar to the glass within the melt inclusion) and BSE-bright oxide domains extend from the fine-grained poikilitic oxidic material along the rim of the melt inclusion (Ilm/Spl zone) into the host ilmenite megacryst. C) Close-up BSE image of the melt inclusion–megacryst interface with small oxide-rich veins that extend from the poikilitic oxidic material that is set within glass along the rim of the melt inclusion (Ilm/Spl zone) and a larger BSE-dark vein that extends from the melt inclusion interior.

MI2 is near circular with a diameter of 1 mm (Fig 3.7). It contains a large but heterogeneous glass proportion, abundant oxides that commonly form intergrowths of spinel and ilmenite and minor abundances of apatite. Calcite, serpentine, phlogopite, and perovskite are absent (Table. 3.1). The glass component contains a transparent and an orange-brown phase. The brown phase forms small isometric (20–50 µm) domains (Fig. 3.7; Gl (i)) within the transparent glass matrix (Fig. 3.7; Gl (ii)). At high optical magnification the boundary between the brown and the transparent glass appears irregular and dendritic, but sharp.

This geometry is not as prominent in the 2D BSE imagery (Fig. 3.7). EDS analysis reveals that the two glass varieties vary in Fe content. The brown isometric glass phase is Fe-rich in comparison to the Fe-poor transparent glass matrix (Chapter 4.3.1).

A prominent spinel grain contains brown glassy particles similar in size and optical characteristics to those forming the isometric glass component. In PPL these inclusions show their brown absorption colour (Fig. 3.7 D). This implies that during the growth of the large spinel crystal the brown isometric melt already existed as a separate phase.

Along the melt inclusion–megacryst interface of MI1 and MI2, a poikilitic reaction zone (up to 40 µm wide) composed of fine-grained ilmenite and spinel hosted in glass forms. Small oxide particles within the melt inclusion are mainly spinel. The spinels are present either as euhedral or skeletal crystals (Fig. 3.7). The transparent glass phase (ii) is isotropic but, in many places, shows devitrification that results in minor optical anisotropy. Prismatic domains of up to 200 µm long phyllosilicate crystals occupy the interstitial space, replacing the transparent glass matrix (Fig. 3.7D). These phyllosilicates have a composition similar to serpentine and are interpreted as secondary phases after the glass matrix or its precursor melt.

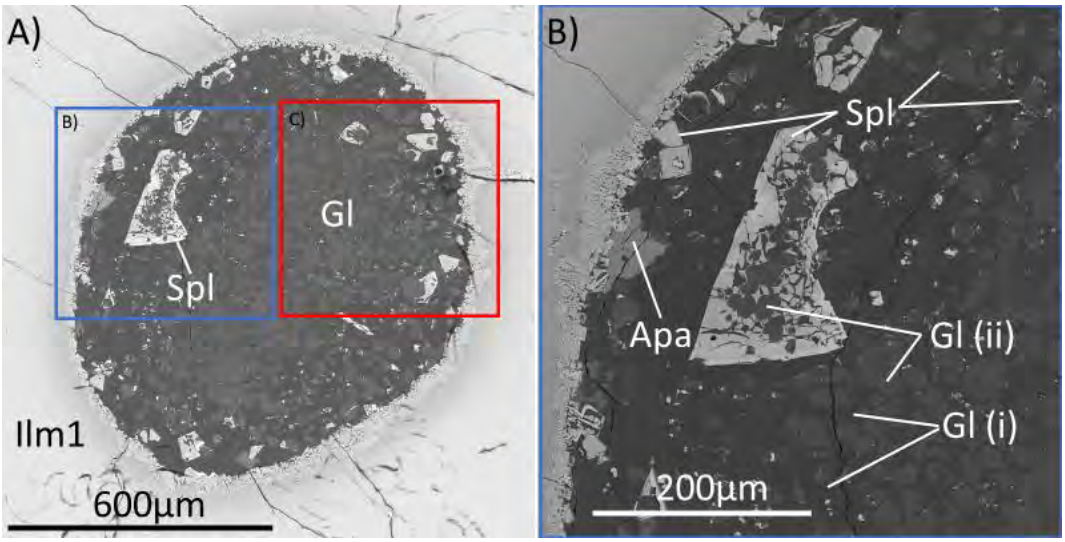

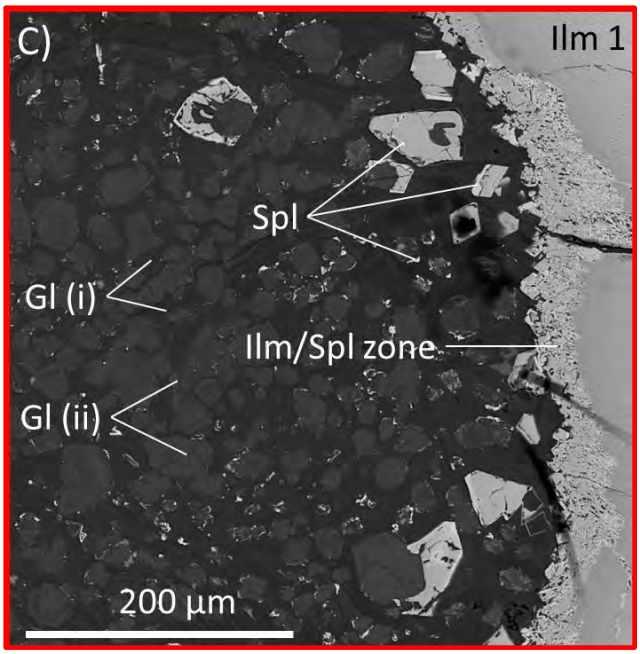

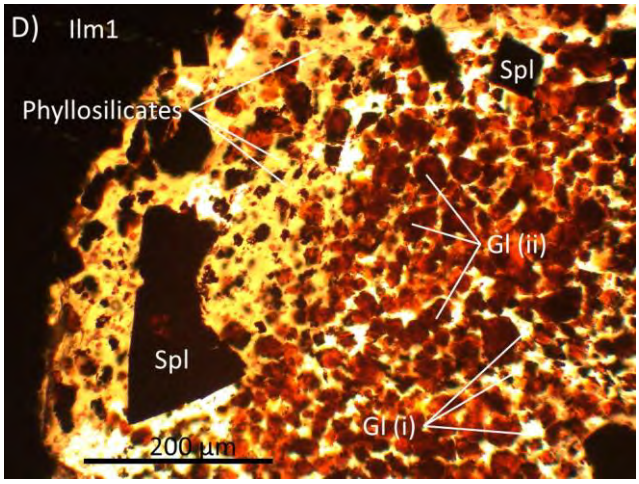

Fig. 3.7. A) BSE image of MI2 in sample S5251. The majority of the inclusion exhibits a low BSE signal intensity that is composed of glass (Gl) phases. Bright signals are spinel (Spl) and secondary ilmenite that are commonly intergrown with each other. The glass component shows lighter grey domains (Gl (i)) in a darker grey matrix (Gl (ii)). EDS analysis indicates that these domains correspond to glasses with different Fe-Mg ratios. The BSE-brighter domains (Gl(ii)) contain somewhat higher iron contents (Chapter 4.3.1). B) Close-up of (A), a large spinel grain containing brown glass particles. The spinel grain shows variations in BSE signal intensity; the rim of the grain displays a higher BSE signal intensity in comparison to the interior of the grain. C) Close-up of (A) with glass phases and subhedral and skeletal spinel phases. Along the interface with the melt inclusion and the hosting ilmenite megacryst, a poikilitic reaction zone (up to 40 µm wide) consisting of ilmenite and spinel is present (Ilm/Spl zone). D) PPL photomicrograph of MI2 showing red-brown isometric glass domains (Gl(ii)) set within a transparent glass matrix (Gl(i)). In some areas, phyllosilicate crystals replace the glass matrix. This feature is not visible in BSE images as these regions are composed of a similar composition to the glass.

3.3.5 ROM 112: MI1

Thin section ROM 112 contains a large (6.7 mm in length) tear-drop shaped melt inclusion (Fig. 3.8). The melt inclusion is situated near the margins of the ilmenite megacryst, which is surrounded by kimberlite matrix (Fig. 3.1). The melt inclusion hosts phases of the common mineral assemblage of serpentine, calcite, oxides (spinel, perovskite, kassite, and ilmenite), phlogopite, and uniquely an unidentified calcium-rich silicate that is possibly harkerite ($Ca_{12}Mg_4Al(BO_3)_3(SiO_4)_4(CO_3)_5 \cdot H_2O$) or afwillite ($Ca_3(SiO_3OH)_2 \cdot 2H_2O$). Glass was not identified in this melt inclusion.

Calcite occurs in irregular pools up to 0.5 mm in size. The calcite pools are surrounded by serpentine and phlogopite intergrowths. All calcite shares a common extinction position in cross-polarised light, suggesting that the pools are interconnected and consist of one large single crystal. Serpentine, and less commonly phlogopite, forms intergrown aggregates of euhedral and subhedral lath-shaped grains, the well-developed crystal faces of which often extend into the calcite (Fig. 3.8). Spinel occurs as small subhedral grains within the serpentine and phlogopite aggregates and is absent in calcite phases. Perovskite and kassite form anhedral grains along the interface with the host ilmenite megacryst and subhedral grains enclosed in calcite within the melt inclusion, commonly associated with the unidentified Ca-rich silicate phase. The unidentified Ca-rich silicate forms on the serpentine and phlogopite aggregates, within the calcite. The Ca-Si phase forms large (~100 μm) hexagonal skeletal crystals that are transparent in PPL, the interior void of which contains calcite and subhedral kassite (Fig. 3.8).

The host ilmenite megacryst forms Fe-rich exsolution lamellae immediately surrounding the inclusion in a 300 μm-wide zone. The Fe-rich lamellae appear to extend into the inclusion, suggesting the reabsorption of the low-Fe ilmenite in a reaction with the contents of the melt inclusion. The Fe-rich exsolved lamellae appear to have remained stable during this reaction (Fig. 3.8).

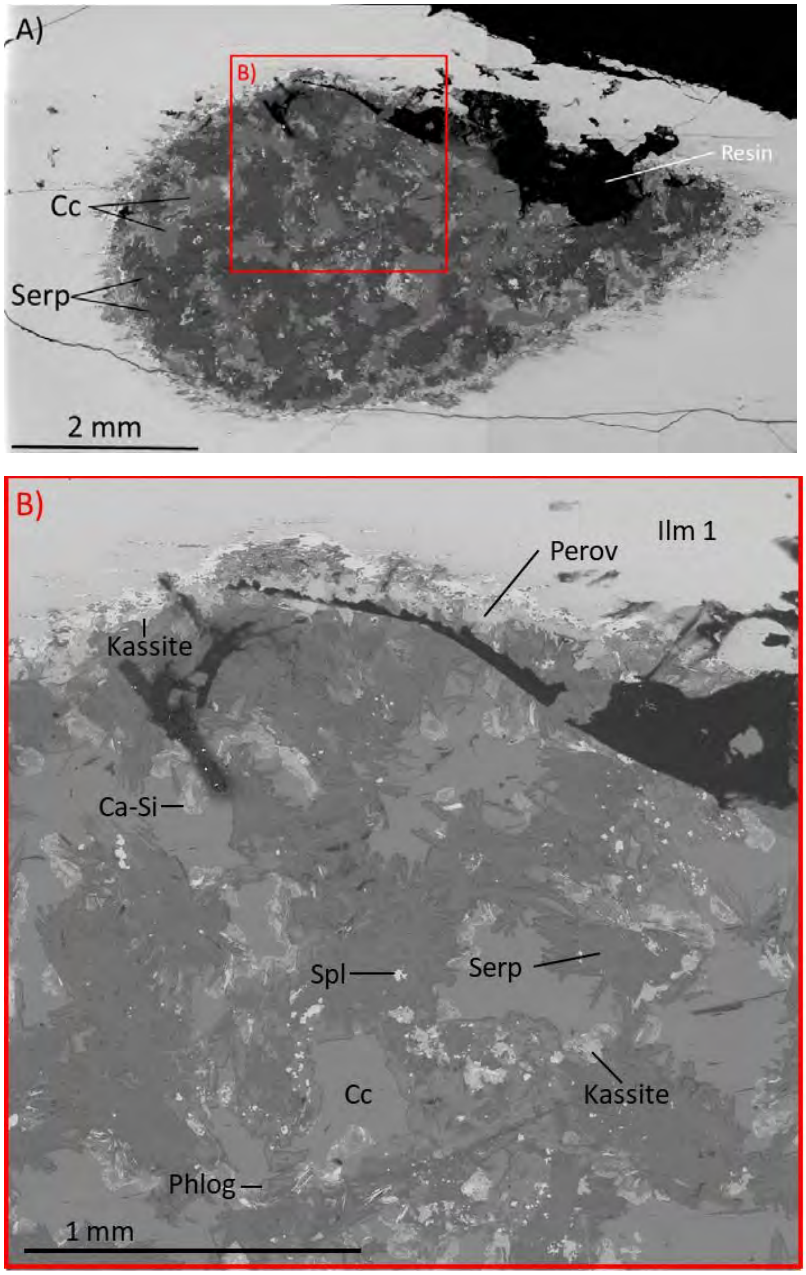

Fig. 3.8. BSE of sample ROM 112 MI1. A) Overview of a large teardrop-shaped inclusion that hosts anhedral calcite and interconnected aggregates of serpentine and phlogopite. Glass was not identified in this inclusion. B) Closer view of the interior of MI1 showing large anhedral calcite (Cc) and aggregates of euhedral serpentine (Serp) intergrown with phlogopite (Phlog), which host small anhedral grains of spinel (Spl). Kassite forms subhedral grains associated with an unidentified Ca-silicate (Ca-Si; possibly harkerite or afwillite), which displays skeletal crystal shapes. Kassite and perovskite (Perov) are intergrown on the margins of the melt inclusion.

3.3.6 ROM 109(C): MI1–MI3

Thin section ROM 109 (C) contains three melt inclusions that are all circular in cross-section and range from 1.1–2.6 mm in diameter (Fig 3.9A). The entire host ilmenite megacryst and

parts of the surrounding kimberlite matrix is visible in the thin section (Fig. 3.1). The melt inclusions host the commonly observed assemblage of calcite, glass, oxides, phlogopite and additionally apatite, but are serpentine free (Table 1).

Melt inclusion 1 (Fig 3.9 B) hosts unusually high proportions of apatite, which are present as skeletal or anhedral crystals in glass and calcite. Calcite forms large anhedral grains throughout the inclusion with irregular and dendritic boundaries with large glass pools. Phlogopite forms two large euhedral lath-shaped grains hosted within glass. Spinel forms the majority of oxide phases, which are present as either euhedral, anhedral or skeletal grains, growing either epitaxially along the melt inclusion margin or as isolated grains within the melt inclusion.

Glass is light brown in absorption colour and slightly devitrified in patches. BSE signal intensities of coherent glass pools are uniform in devitrified and fresh domains (Fig. 3.9 B), suggesting uniform major element composition (Chapter 4.3.1). A small proportion of glass is present in interstitial spaces between crystals or as inclusions in skeletal oxide phases.

Melt inclusion 2 (Fig 3.9 E) consists of calcite, glass and oxides (spinel, ilmenite and perovskite). Phlogopite, serpentine, and apatite are absent in this inclusion. Calcite forms in three different textural varieties: (i) large (400 µm) globular shapes; (ii) as inclusions in the interior of large skeletal spinel and ilmenite; and (iii) as a large poikilitic/colloform grain with a dendritic network of silicate glass. This texture of calcite displays a concave boundary to the central large glass pool (Fig. 3.9 E).

The large central glass pools show patches with variable BSE signals intensities, indicating variable compositions. EDS analysis (Chapter 4.3.1) indicates Fe-Mg contents as the main variable. Inclusions of glass in oxides and calcite are typically the BSE-darker glass variety (Fig. 3.9E).

Melt inclusion 3 (Fig. 3.9 F) is mostly composed of calcite. Oxides occur as large euhedral epitaxial spinel grains along the host ilmenite megacryst interface, with smaller anhedral ilmenite. Anhedral perovskite forms along the margins of the inclusion. Small (70 µm) lath-shaped phlogopite is present within small glass pools. Apatite comprises a minor component, forming small subhedral grains. The inclusion is transected by a thin vein that contains calcite and extends bilaterally into the host ilmenite (Fig. 3.9 F).

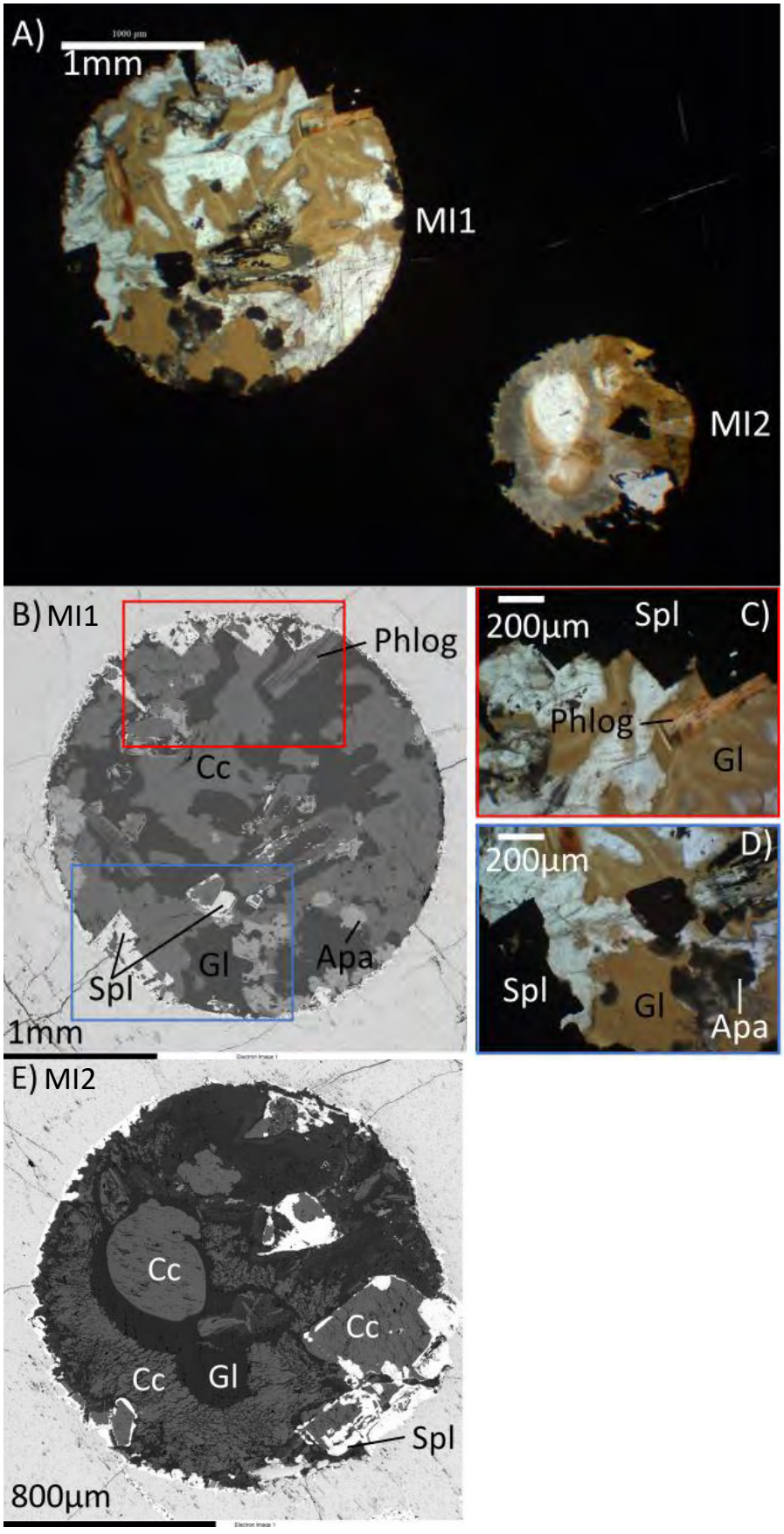
A)
1mm
MI1
MI2
B) MI1
Phlog
Cc
Gl
Spl
Apa
1mm
200µm
Spl
C)
Phlog
Gl
200µm
D)
Spl
Gl
Apa
E) MI2
Cc
Cc
Cc
Gl
Spl
800µm

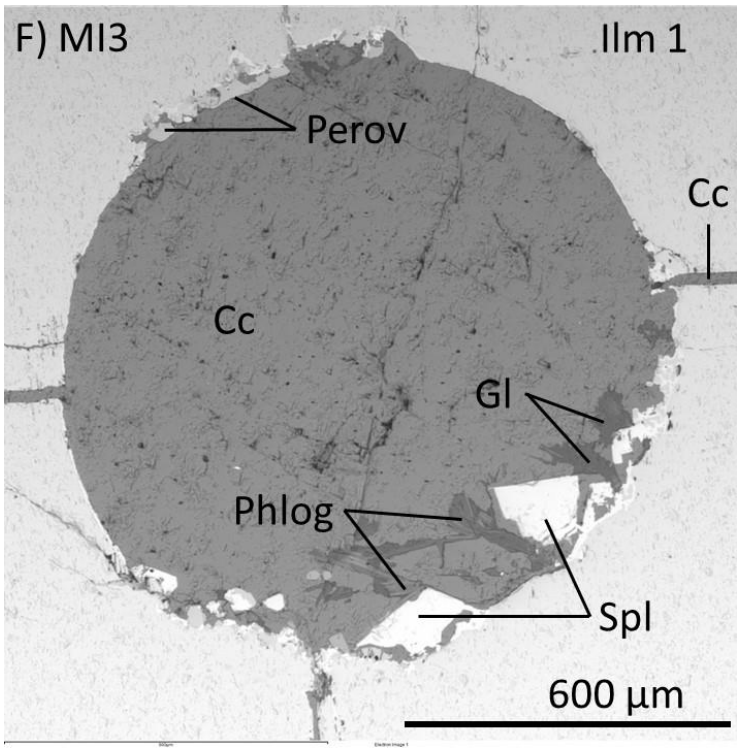

Fig. 3.9. PPL photomicrographs and BSE of three melt inclusions in sample ROM109(C) hosted in an ilmenite megacryst (Ilm1). A) PPL photomicrographs of two melt inclusions showing their close spatial relationship within the hosting ilmenite. B) BSE image of melt inclusion 1 (MI1) with large lath-shaped euhedral phlogopite (Phlog) and large euhedral spinel (Spl). Glass (Gl) shows a uniform BSE signal intensity. C) & D) PPL photomicrographs from melt inclusion 1 (B). Glass shows variation in absorption colour from a light to darker brown colour. It is associated with large euhedral spinel (Spl) and phlogopite (Phlog). E) BSE image of melt inclusion 2. Spinel forms large skeletal grains with calcite in the skeletal voids. Calcite also occurs as a large central globular grain or, along the margin of the melt inclusion, as a large poikilitic grain hosted in glass. The poikilitic calcite grain shows concave boundaries with the central glass pool. F) MI3 mostly consists of calcite. Large euhedral spinel and anhedral perovskite (Perov) forms near the margins of the inclusion. Lath-shaped phlogopite forms in coherent glass pools.

3.3.7 ROM 264: MI1

Thin section ROM 264 contains one melt inclusion that is circular in cross-section and ~2.8 mm in diameter. The ilmenite megacryst is transected by a 2.5 mm wide channel. This channel hosts kimberlite matrix-like material and runs from one end of the thin section to the other.

The melt inclusion displays a concentric distribution pattern of crystal and glass phases. The entire melt inclusion is not visible; however, the crystal and glass phases, and their textures hosted within it are characteristic of the common assemblages observed within enclosed melt inclusions. Calcite occupies the centre of the melt inclusion as an irregular anhedral grain (1 x 0.4 mm). Five glass varieties are present in the melt inclusion, three of which form

a concentric distribution pattern: (i) a 460 µm-wide zone of Si-Mg-Fe glass interconnected with carbonate veinlets (demonstrated by high resolution element maps produced in an honours project by Marima (2019) on the same sample) surrounding the inner calcite grain; (ii) the second variety of glass forms a low-Fe glass in a 150 µm-thick layer and is light-brown in absorption colour with a dark BSE signal intensity; (iii) the outer glass layer consists of a high-Fe glass, which is 350 µm thick. It is dark brown in absorption colour with a lighter BSE signal intensity (Fig 3.10 C and D). Spherulite-like globular glass structures are present along the host ilmenite margin, forming structures up to 180 µm in diameter (Fig 3.10 B and D). These structures also have a concentric distribution of phases, which host the other two varieties of glass. The interior of these circular globular structures is composed of kassite, surrounded by a concentric middle layer of a Ca-Ti glass (iv) and calcite (Fig 3.10 B and D). The outer layer, which is transparent in plane-polarised light, comprises a Ca-Ti-Si glass (v) (Fig 3.10 B and D) (Chapter 4.3.1). These structures are unique to thin section ROM 264.

A lath-shaped inclusion is in contact with MI1. It is composed of a central portion of euhedral and subhedral phlogopite grains and skeletal spinel. The interior voids of the skeletal spinel hosts devitrified glass and perovskite. The outer portion of the lath-shaped inclusion consists of devitrified glass that is transparent to greenish in absorption colour and has a composition similar to glass within MI1 (Fig. 3.10 C).

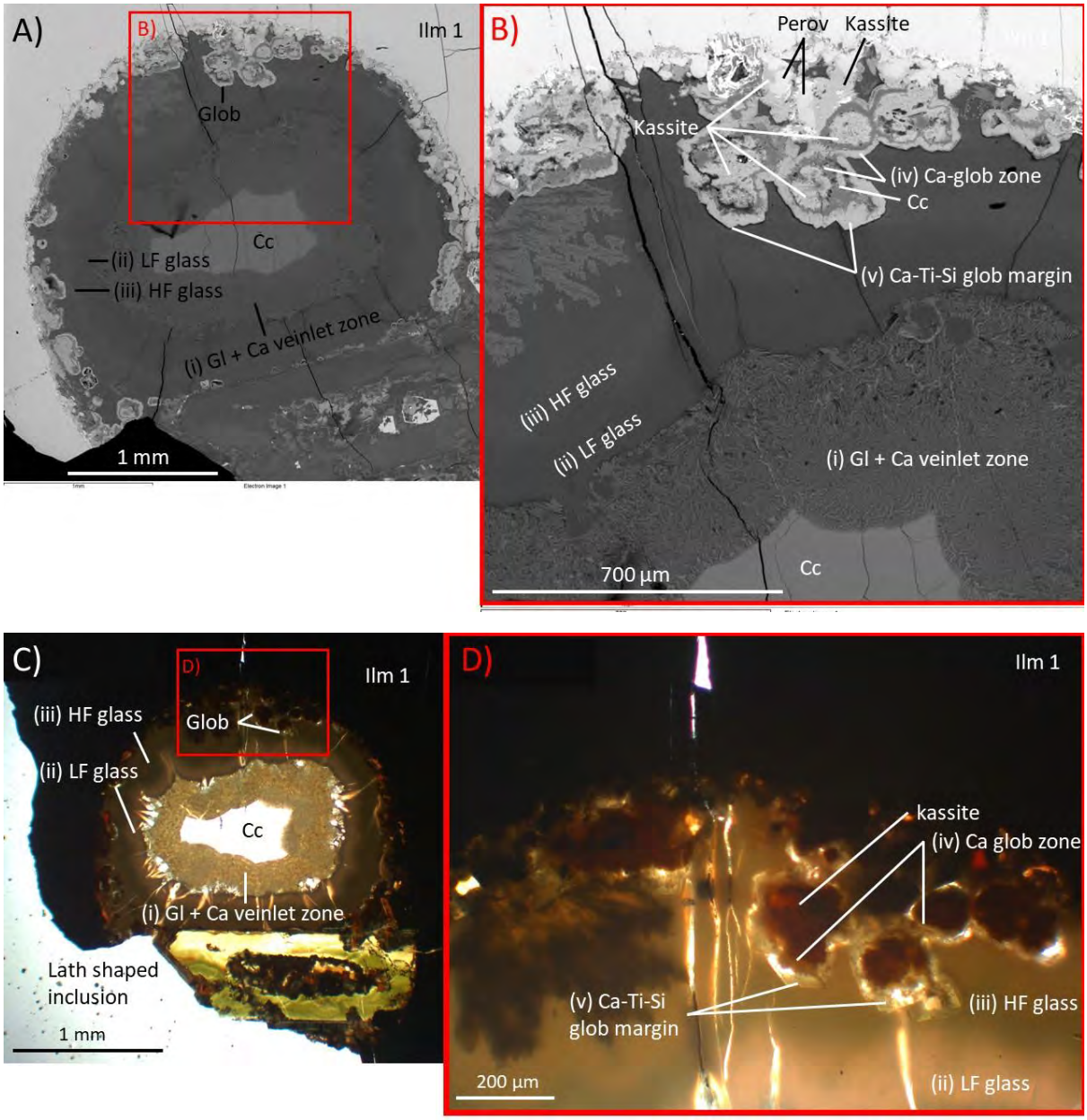

Fig. 3.10. PPL photomicrographs and BSE of melt inclusion 1 (MI1), thin section ROM264. A & C) PPL and BSE images of MI1, showing the concentric distribution of crystal and glass (Gl) phases. Calcite (Cc) occupies the centre of the melt inclusion, forming a large irregular grain. A zone consisting of silicate glass interconnected with carbonate veinlets surrounds the calcite grain ((i) Gl + Ca veinlets). Surrounding this is a glass that is commonly observed in other melt inclusions, which is differentiated into two varieties, an inner layer of light brown Fe-poor glass (LF glass (ii)) and an outer layer of dark brown Fe-rich glass (HF glass (iii)). B & D) PPL and BSE images of spherulite-like globular (Glob) structures form within the melt inclusion on the host ilmenite (Ilm1) megacryst. Globular glass and mineral structures show a concentric distribution of phases. The interior comprises a kassite grain, surrounded by an inner globule zone composed of a Ca-Ti glass (iv). The outer globule margin consists of a Ca-Ti-Si (v) glass.

3.3.8 ROM 31E (A): MI1–MI2

Sample ROM 31E (A) hosts two melt inclusions. MI1 is oval in cross section and 3 mm in its longest dimension (Fig. 3.11 A and B). The majority of the melt inclusions consist of calcite that forms a single large grain in the centre of the melt inclusion. Glass occurs as a coherent pool and a thin layer in between the host ilmenite megacryst and the large calcite grain (Fig. 3.11 B). The coherent glass pool hosts atoll spinel, the interior 'lagoon' of which is occupied by calcite and glass, euhedral lath- to needle-shaped phlogopite, and subhedral spinel (Fig 3.11 A). The glass pool commonly displays a dendritic concave boundary to the central calcite grain.

MI2 is lens-shaped and 4 mm in length (Fig. 3.11D). Glass forms a large central interconnected coherent pool. Calcite forms as small anhedral grains that show a sharp boundary with the glass or as large grains that show a dendritic boundary with the glass, that is commonly concave in shape (Fig. 3.11 C). A grain of strontianite is surrounded by calcite (Fig. 3.11 D). Subhedral secondary ilmenite is surrounded by glass and calcite. The ilmenite shows a zonation in BSE images (Fig. 3.11 C), where the interior has a lower BSE signal intensity in comparison to the rim, suggesting a compositional zoning of the secondary ilmenite (Fig. 3.11 C). EDS analysis shows Fe-Mg variations correlating with the BSE signals (Chapter 4.3.1).

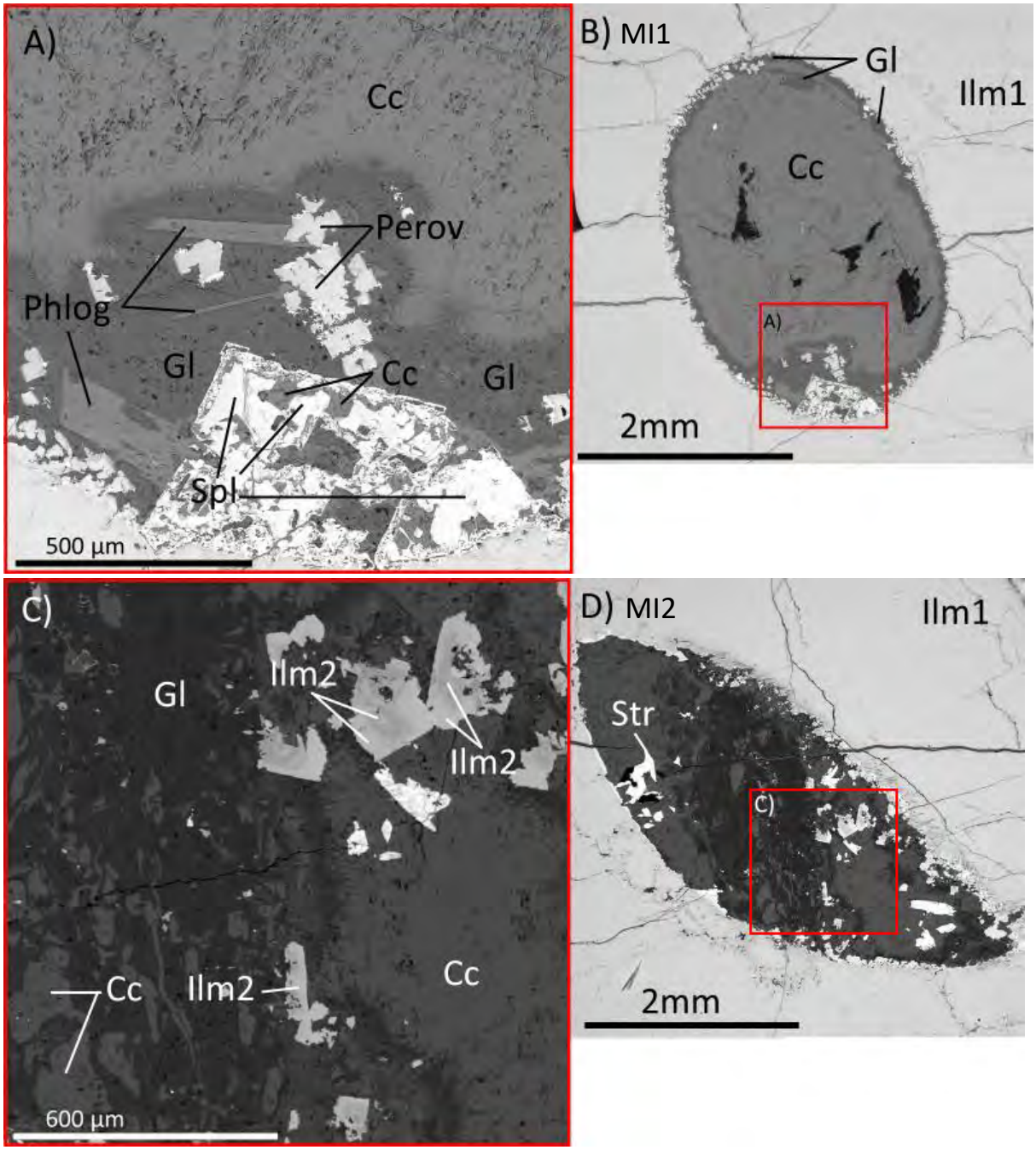

Fig. 3.11. BSE of sample ROM 31 E (A) MI1 and MI2. A) Close-up view of a large coherent glass (Gl) pool in MI1 that hosts skeletal spinel (Spl), euhedral phlogopite (Phlog) and subhedral perovskite (Perov). A large calcite grain has a concave dendritic boundary with the glass pool. B) An overview of MI1. A large calcite occupies most of the inclusion and contains an inclusion of glass. Glass surrounds the calcite grain in a thin layer. C) Close-up view of a central proportion of MI2. Glass occurs as a central coherent pool. Calcite forms small grains with a sharp boundary with glass and as a larger grain with a dendritic, commonly concave, boundary with glass. Secondary ilmenite is subhedral and surrounded by glass and calcite. BSE signal intensity shows a zoned compositional pattern in the secondary ilmenite. D) BSE image overview of the lens shaped MI2 showing a large strontianite grain (Str).

3.4 Reaction zones in ilmenite megacrysts

A common feature of the megacrysts are reaction seams along the interface between ilmenite megacrysts and melt inclusions as well as along the interface between ilmenite megacrysts and the kimberlite matrix. Such seams occur surrounding approximately half of the melt inclusions (10 out of 23 melt inclusions). In some samples (S5251, S5626, S5628, ROM112), all melt inclusions show such alteration zones. In other samples (P015, ROM31E (A), ROM109 (C)), only some or none of the melt inclusions show them. Furthermore, melt inclusions that display these reaction seams may show large variations in modal abundances and textural features. Hence there is no consistency, in regard to mineralogy and texture of the hosted daughter phases, as to whether or not melt inclusions may or may not show alterations seems.

Where ilmenite megacrysts are in contact with kimberlite matrix, such as along the channel that connects MI2 of P015 (Fig. 3.4 A), BSE images show zones of brighter signal intensity, which may form up to ~160 µm thick domains. These domains show irregular but sharp boundaries with the BSE-darker ilmenite megacryst that approximately follow the ilmenite-kimberlite interface. The ilmenite megacryst may show zones that are BSE-darker than both the reaction seam and the interior of the ilmenite megacryst. This suggests that the reaction seam formed by Mg-Fe diffusion between the kimberlitic matrix and the megacryst, producing a more iron-rich ilmenite as a reaction product. This was confirmed by EDS analysis (Chapter 4.1).

The most common type of reaction seam surrounding melt inclusions consists of lamellar Fe-rich domains. These lamellar domains consist of ~1 µm thick BSE-bright lamellae with a spacing of 5–10 µm alternate with domains that are somewhat BSE-darker than the unaltered ilmenite megacryst (Fig. 3.2; Fig. 3.3). The lamellae are uniformly oriented around different melt inclusions in a given ilmenite crystal, suggesting crystallographic control on their orientation. EDS analysis (Chapter 4.1) indicates that Fe-Mg substitution is an important process that has formed the BSE-bright lamellae and their BSE-darker matrix.

In the immediate vicinity of some melt inclusions, a reaction zone, ~150 µm thick, composed of fine-grained ilmenite and spinel shows abundant small inclusions with dark BSE signals, similar to the silicate material in the interior of the melt inclusions (Fig. 3.6; Fig. 3.7). In addition, the ilmenite megacryst immediately surrounding some melt inclusions shows variations in the Mg-Fe composition (sample P015, MI2) or a Ca-rich reaction zone (Fig. 3.5). These patterns suggest complex chemical interaction between the material in some melt inclusions and the hosting ilmenite. These processes will be discussed in Chapter 6.

3.5 Textural features of glass and crystal phases hosted in melt inclusions

This section describes the textural characteristics of the mineral and glass phases in ilmenite-hosted melt inclusions in detail. The phases are texturally similar throughout the melt inclusions and will be described per phase across all melt inclusions, with examples from specific melt inclusions where appropriate.

3.5.1 Glass

Glass forms a common component of the melt inclusions with modal proportions of up to 95% of the area exposed in thin section (Table 1), and only one inclusion devoid of glass (Sample ROM 112 MI1, Chapter 3.3.5). The fresh glass component of melt inclusions is typically transparent to orange brown in absorption colour, optically isotropic, and texturally homogenous (see glass identification criteria, Chapter 1.3). Occasionally it displays devitrification textures. Glass that displays devitrification (or patches of devitrification) is pleochroic (Fig. 3.9; Fig 3.12), and is texturally heterogenous. The glass is restricted to the interior of melt inclusions and was not identified in silicate or carbonate-rich veins.

Glass forms coherent pools, commonly towards the centre of melt inclusions. An example can be seen in sample S5628 MI1, where glass forms a large (620 x 300 µm) irregular central pool, with an adjacent equant glass pool (320 x 310 µm) (Fig. 3.5). The glass is light brown, with patches of darker brown glass in the central glass pool and is isotropic in cross-polarised light (Fig 3.5). The glass pools are surrounded by aggregates of subhedral lath-shaped phlogopite, up to 360 µm thick (Fig. 3.5). Similarly, sample S5626 MI1 hosts glass that forms as large central coherent pools (380 x 880 µm) that are interconnected (Fig. 3.2). Where present, large anhedral calcite grains commonly occupy the centre of the melt inclusions. In these inclusions glass occupies positions along the megacryst-melt inclusion interface, such as in MI1 of sample ROM 31E(A) and MI3 of sample P015, where glass forms coherent pools (0.65 x 1.23mm; 0.67 x 1.48mm, respectively) and thin films (44 µm; 82 µm wide) that line the ilmenite megacryst-melt inclusions interface (Fig. 3.11 B; Fig. 3.12 A & E).

Glass may form the matrix for skeletal and euhedral oxides and silicate crystals, or, where present, for euhedral calcite. Glass is also present in the voids of skeletal ilmenite and spinel, and around globular calcite domains.

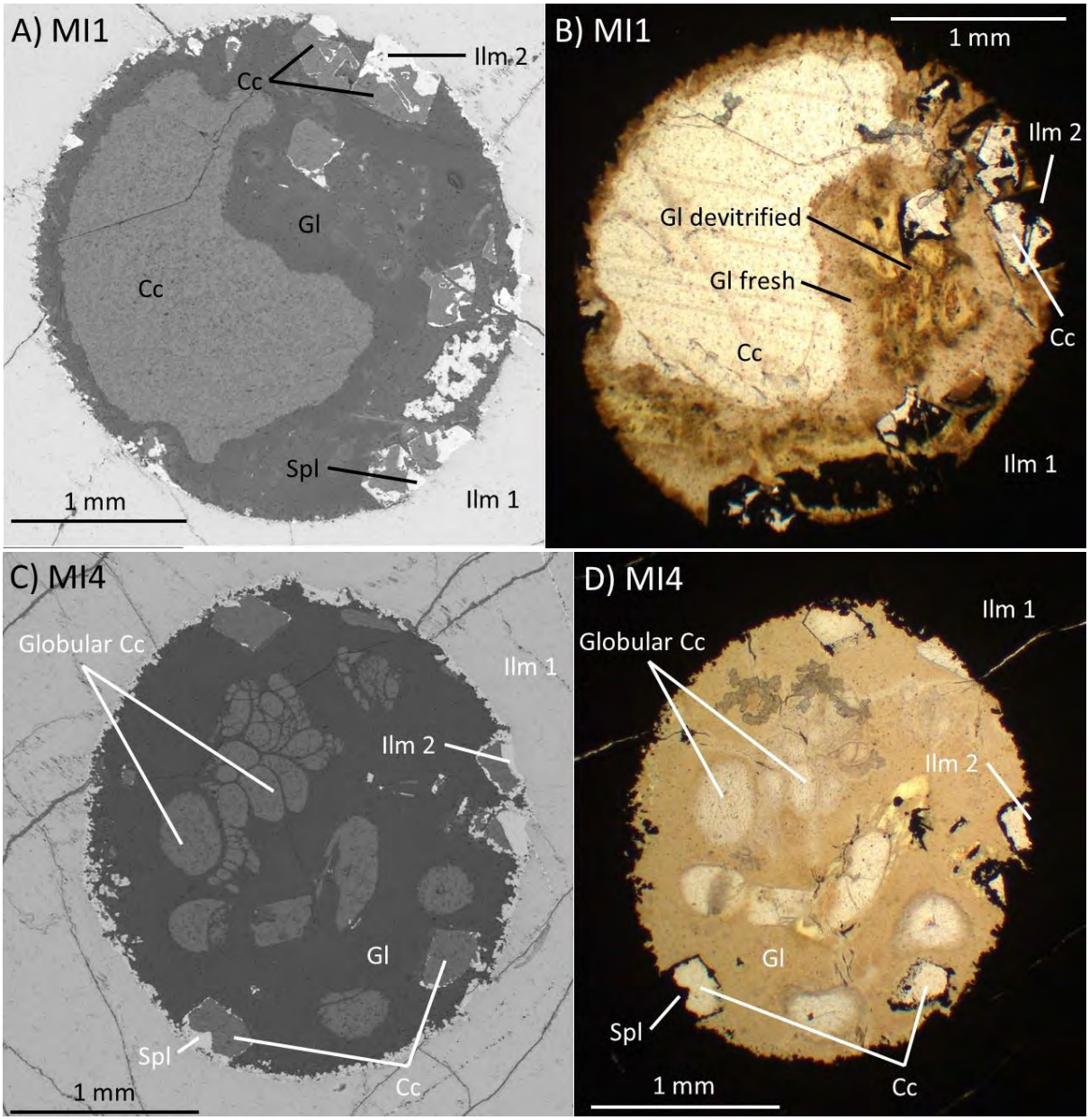
A) MI1
Ilm 2
Cc
Gl
Cc
Spl
1 mm
Ilm 1
B) MI1
1 mm
Ilm 2
Gl devitrified
Gl fresh
Cc
Cc
Ilm 1
C) MI4
Globular Cc
Ilm 1
Ilm 2
Gl
Spl
1 mm
Cc
D) MI4
Ilm 1
Globular Cc
Ilm 2
Gl
Spl
1 mm
Cc

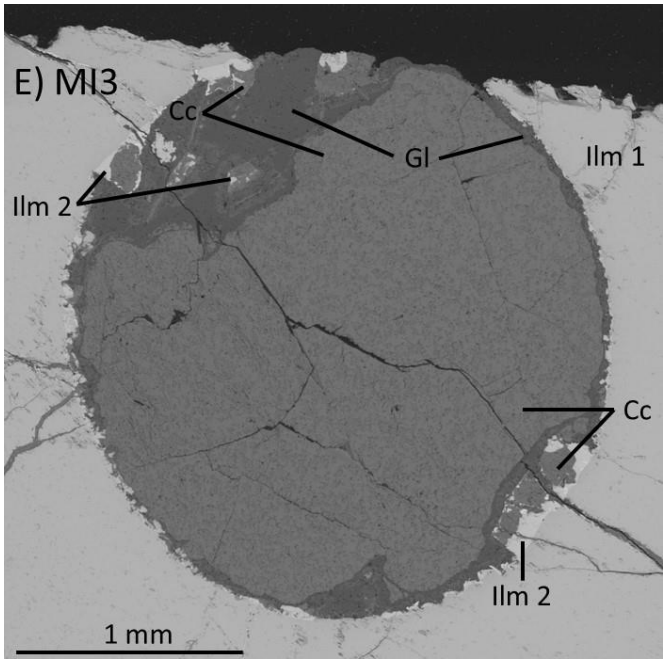

Fig. 3.12. BSE and PPL images of sample P015 MI 1, 3, and 4. A) BSE photomicrograph of MI1, which hosts a large anhedral calcite (Cc) grain surrounded by a large coherent glass (Gl) pool. The interior void of skeletal ilmenite (Ilm2) consists of calcite. B) PPL photomicrograph of MI1 showing the light brown absorption colour of the glass and areas of devitrified glass. C) BSE image of MI4, which hosts skeletal ilmenite and spinel. Calcite forms globular melt structures and fills the internal void of skeletal spinel and secondary ilmenite. A coherent glass pool occurs throughout the inclusion. D) PPL photomicrograph of MI4 showing the light-brown absorption colour of glass. E) BSE photomicrograph of MI3, consisting of a large central calcite grain surround by glass. Glass forms either as a coherent pool or a thin layer around the calcite grain. Calcite also forms in the interior voids of skeletal ilmenite, which form epitaxially or in interior positions within the melt inclusion and are surrounded by glass.

At higher modal proportions of glass (Table 1), it forms large interconnected coherent pools throughout the entire inclusion. For instance, sample P015 MI1 hosts a high glass proportion (~51%; Table 1). The glass forms a single coherent pool throughout the inclusion (Fig. 3.12 A). The glass forms the matrix for skeletal and euhedral secondary ilmenite and spinel. The glass also forms sharp but irregular boundaries with a large central anhedral calcite crystal which the glass surrounds (Fig. 3.12 A). A central patch of glass shows devitrification textures in PPL, evident as variations in absorption colour and texture; except for this devitrified domain the glass is optically homogenous (Fig 3.12 B). MI4 of the same sample (P015) also hosts a high proportion of glass which forms a single coherent pool throughout the inclusion and has a light-brown absorption colour (Fig 3.12 C & D). The glass in MI4 forms the matrix for skeletal ilmenite and spinel, and calcite, which forms 'tear-drop' shaped globular melt structures (Fig. 3.11 C). Similarly, sample ROM109 (C) MI1 hosts a high proportion of fresh glass which forms a coherent interconnected pool throughout the inclusion and separate large equant glass pools that may be connected above or below the exposed thin section (~550 µm) (Fig. 3.9 B).

Glass forms the matrix to skeletal and euhedral grains of the common mineral assemblage. For example, in sample S5626 (MI1–MI3) glass forms the matrix for subhedral and euhedral serpentine (Fig 3.2; Fig.3.3). Furthermore, the well-developed crystal faces of subhedral calcite in MI1 (Fig 3.2) and MI3 (Fig 3.3) of sample S5626 protrude into glass pools. An additional example in sample ROM 109 (C), which hosts euhedral phlogopite in glass (Fig 3.9 B & C). In sample P015 (MI1; MI3; MI4) (Fig. 3.12), glass surrounds skeletal oxides (secondary ilmenite and spinel), which form both in epitaxial positions on the host ilmenite megacryst and in interior positions within coherent glass pools. The interior voids of these skeletal oxides are occupied by calcite (Fig. 3.12).

Glass ranges in absorption colour from light brown to a darker brownish orange. The absorption colour of fresh glass may be uniform. For instance, MI4 of sample P015 hosts glass that displays a uniform light-brown colour (Fig. 3.12 D). Glass may also show variations in absorption colour within the same inclusion or glass pool. The variations in absorption colour correlate with a variation in BSE signal intensity, and therefore composition. For example, in sample S5628 MI1 a central coherent glass pool shows variations in absorption colour from light brown to darker brown (Fig. 3.5 B). BSE images show a variation in BSE signal intensity between glass varieties (Fig. 3.5 B). EPMA and EDS analysis show this variation is due to a difference in Fe–Mg between the glass varieties (section 4.3.1).

The occurrence and textures of glass described above are common in the analysed samples. However, a number of rare glass varieties were also identified. Sample ROM264 MI1 hosts the most varieties of glass in a single inclusion of the observed samples, some of which are unique to this sample. The glass forms five varieties, three of which form concentric layers of the general melt inclusion structure: (i) the inner layer of glass that surrounds a central calcite grain (up to 500 µm from the calcite) with a light-brown absorption colour and a microstructure of interconnected silicate glass and Ca-rich veinlets (Fig. 3.10 C); (ii) the middle layer of glass, which is brownish in absorption colour and 160 µm wide; (iii) the 280 µm-wide outer glass layer near the margins of the inclusion, which shows a darker-brown absorption colour (Fig. 3.10 C and D). Towards the margin of the melt inclusion, globular structures form on the interface of the host ilmenite megacryst (Fig. 3.10 D). These structures have a circular shape in thin section and a concentric internal structure (Fig. 3.10 A). The centre of these structures consists of kassite, which is surrounded by an inner glass layer (iv) and an outer BSE-bright glass layer (v) (Fig 3.10 B). Both the inner and outer glass layers are transparent in PPL (Fig 3.10 D). The different BSE signal intensities are related to variations in Si, Fe, Mg, Ca, and Ti content between the different glass varieties (see Chapter 4.3.1).

Another sample that hosts glass that forms as uncommon varieties is sample S5251 MI1 and MI2, which hosts glass textures unique to this sample. In MI1, glass forms two distinct varieties: (i) isometric pale brown to yellow domains and (ii) a transparent matrix. The two

glass varieties have roughly uniform compositions (Chapter 4.3.1) shown by EDS analysis and similar BSE signal intensities (Fig. 3.6). MI2 of the sample hosts similar glass textures, however, with a more compositionally heterogenous nature (Fig. 3.7). Glass in MI2 forms two varieties, similar to MI1: (i) a pale yellow-brown to transparent matrix and (ii) an orange-brown phase that forms isometric domains set within the matrix (20–50 µm) (Fig. 3.13). The second glass variety also forms as circular (presumably spherical in three dimensions) inclusions set within a large spinel grain (Fig. 3.7 B). EDS analysis (Chapter 4.3.1) associates the different BSE signal intensities of the two glass varieties with Fe-Mg variations. The boundaries between the two glass varieties are sharp with an irregular dendritic shape (Fig. 3.7 B & C).

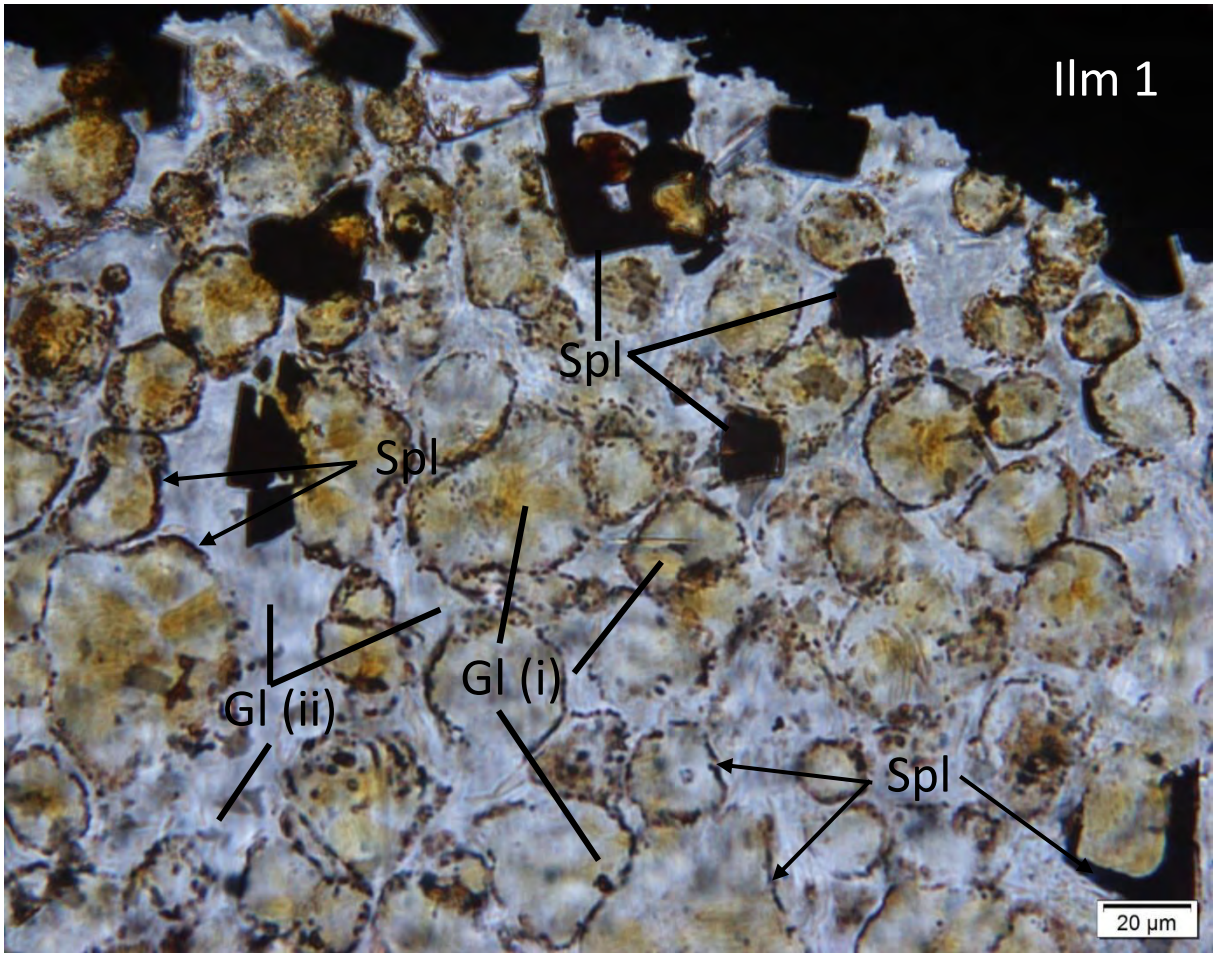

Fig. 3.13. PPL images of glass in sample S5251 MI1. Large euhedral spinel (Spl) crystals occur near the margins of the inclusion and are set in a glass matrix (Gl). Glass forms two distinct varieties of orange-brown globular domains (Gl (i)) set within a glass matrix (Gl (ii)). Spinel (arrows) forms on the sharp boundaries of the two glass varieties. These textures were investigated further using BSE imagery (Fig. 3.6) and element maps (see Chapter 4.3.1; Fig. 4.6).

3.5.2 Calcite

Calcite occurs in five distinct textural varieties, commonly co-existing in the same inclusion or sample: (i) globular melt structures; (ii) completely filling the interior void of skeletal ilmenite and spinel; (iii) subhedral grains with well-developed crystal faces that are in contact with glass; (iv) anhedral grains of varying sizes (0.01–2 mm), with an irregular, commonly concave, boundary with surrounding glass; (v) anhedral crystals occuping nearly the entire melt inclusion, forming the matrix of euhedral and skeletal shaped components of the common mineral assemblage. Calcite is variable in modal proportions, but it is typically the most abundant phase. In Sample S5628 MI1 it reaches 0.5% and in MI2 of the same sample it reaches 96.5% of the inclusions' area exposed in thin section (Table 1).

(i) Typical examples of globular calcite are present in sample P015 MI4, which hosts calcite as anhedral, circular to teardrop-shaped grains that range in size from 10 to 300 μm and are surrounded by glass (Fig. 3.12 C). A further example is ROM 109 (C) MI2 in which calcite forms a large poikilitic/colloform grain (1.09 x 0.26 mm) composed of small rounded globular calcite grains and an adjacent large (400 μm) rounded globular grain, within a glass matrix. The poikilitic calcite grain has a concave boundary with the adjacent central glass pool (Fig. 3.9 E).

(ii) Typical examples of calcite internal to skeletal grains can be observed in samples P015 (MI1, MI3, and MI4), where calcite is present as occupying the internal void of skeletal ilmenite or spinel (100–470 μm), located in epitaxial positions on the host ilmenite megacryst or within the melt inclusion interior (Fig. 3.12A, C & E).

(iii) Calcite forming subhedral grains in contact with glass is notable in sample S5626 MI1 and MI3. In MI3 calcite forms large (540 μm) subhedral grains, the well-developed crystal faces of these grains in contact with a large (184–493 μm) glass pool (Fig 3.3). The subhedral calcite grain also hosts small inclusions of glass (up to 80 μm in size) (Fig 3.3).

(iv) An example of irregular calcite grains is observed in sample P015 MI1 and MI3, where calcite forms as large (2–2.37 mm) anhedral grains, towards the centre of the melt inclusions, surrounded by glass (Fig. 3.12 A & E). An additional example of this textural variety of calcite is observed in ROM 31E (A) MI1. Calcite occupies the majority of this melt inclusion as a single large (2.5 mm) irregular shaped grain (Fig 3.11 B), commonly showing a concave grain boundary with a large coherent glass pool (Fig. 3.11 A). The calcite grain is surrounded by glass and hosts a large (430 μm) irregular inclusion of glass (Fig 3.11 B). Calcite may also form as small (5–10 μm) anhedral intergrowths with other minerals. In sample S5626 MI1 and MI3 calcite forms as anhedral intergrowths with subhedral and

euhedral serpentine, by forming along the serpentine crystal surface and between the individual 'rays' of the fan-shaped serpentine (Fig. 3.2; Fig. 3.3).

(v) An example where calcite forms the matrix for skeletal components of the common mineral assemblage is sample S5628 MI2 and MI3, where calcite occupies the majority of the melt inclusions and surrounds skeletal spinel that forms epitaxially on the host ilmenite megacryst. Calcite also occupies the interior of these skeletal grains (Fig. 3.14). In addition to skeletal grains, calcite may form the matrix for euhedral components of the common mineral assemblage. For instance, sample ROM 112 MI1 contains anhedral irregular patches of calcite (220 x 400µm), all of which share a common extinction position in cross-polarised light and the same addition and subtraction colours with inserted lambda plate. This indicates that these patches are connected above and/or below the exposed section and belong to a single large calcite crystal. Euhedral serpentine and phlogopite, and skeletal shapes of a Ca-Si rich phase (possibly harkerite or afwillite) extend into the calcite 'pools' (Fig 3.8). Another example of calcite forming the matrix of euhedral grains is sample ROM 109(C) MI3. Calcite occupies the majority of this inclusion and surrounds large euhedral spinel (142–180 µm) (Fig. 3.9F). Additionally, in MI2 and MI3 of sample S5628 calcite forms a matrix that hosts skeletal/euhedral oxides (Fig. 3.14).

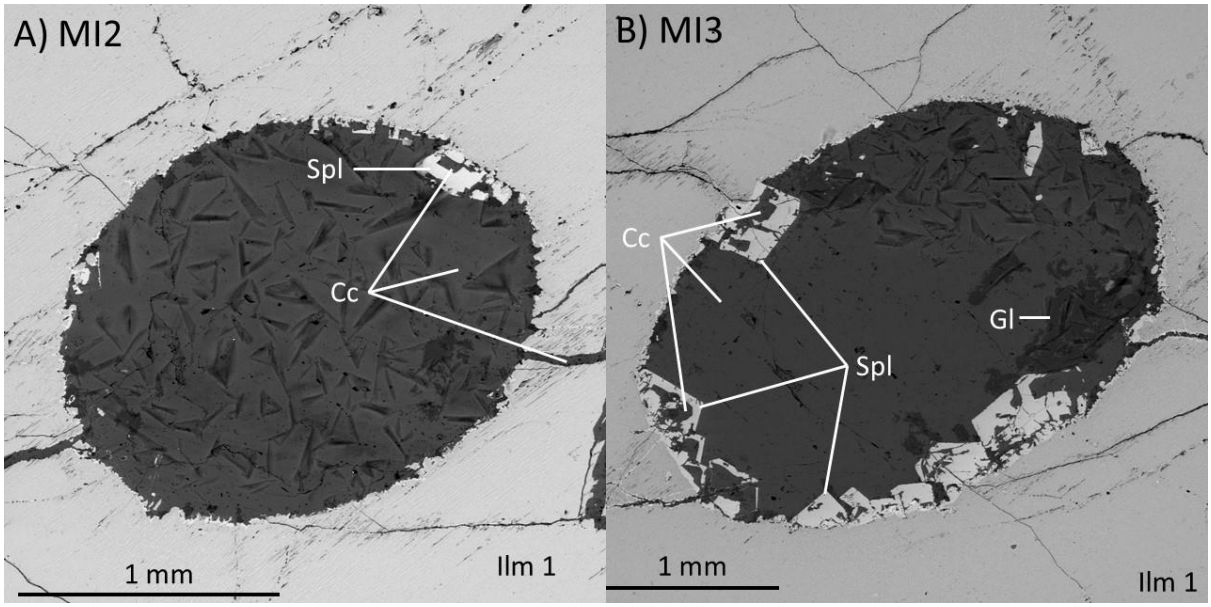

Fig. 3.14. BSE images of sample S5628 MI2 and MI3. Calcite (Cc) occupies the majority of the inclusions and a vein that bisects MI2 (A). Spinel (Spl) forms large euhedral and skeletal grains epitaxially on the host ilmenite megacryst (Ilm1) within a surrounding calcite matrix. Glass (Gl) forms small coherent pools within calcite and comprises a minor component of the melt inclusions.

3.5.3 Ilmenite

Secondary ilmenite is common throughout all samples, although it does not occur in significant modes (Table 1). Secondary ilmenite is present in a variety of textures: it forms epitaxially on the host ilmenite megacryst or as discrete crystals in interior positions within the melt inclusions. Crystal shapes of secondary ilmenite are commonly euhedral or skeletal. The interior voids of skeletal secondary ilmenite are filled with either silicate glass or, more commonly, calcite. Secondary ilmenite is commonly hosted in silicate glass, even if interior skeletal voids are filled with calcite. Secondary ilmenite also forms small anhedral irregular grains randomly distributed throughout the melt inclusions.

Skeletal ilmenite grains are observed in sample P015 (MI1; MI3; MI4; MI5), ROM 109 (C) (MI1; MI2), S5628 (MI2; MI3; MI4; MI6), and ROM 31 E(A) (MI1). A typical example is found in sample PO15 MI1 and MI4, where secondary ilmenite forms large skeletal grains (70–490 μm). The secondary ilmenite forms epitaxially on the host ilmenite megacryst, or occupies interior positions within the melt inclusion. The skeletal secondary ilmenite is surrounded by glass, and the interior voids are occupied by calcite (Fig. 3.12).

Secondary ilmenite also forms subhedral and euhedral crystal shapes, which are present in samples P015 (MI1; MI3; MI4; MI5; MI6), S5626 (MI3), S5628 (MI1; MI2; MI3; MI6), ROM 109(C) (MI1; MI2), and ROM 31E (A) (MI1). Sample P015 (MI6), for example, hosts secondary ilmenite that forms a large euhedral crystal (361 μm), epitaxially on the host ilmenite megacryst, surrounded by calcite (Fig. 3.15). Sample S5626 (MI3) hosts small subhedral secondary ilmenite (~51 μm), which forms in interior positions within the melt inclusion, and is surrounded by aggregates of serpentine microlites (Fig. 3.3 D).

Typical examples of irregular anhedral secondary ilmenite are observed within sample S5628 MI1 and S5626 MI2, where secondary ilmenite occurs as small (19–75 μm) anhedral grains throughout the inclusions that may accumulate into large aggregates (250 μm) (Fig. 3.5 B).

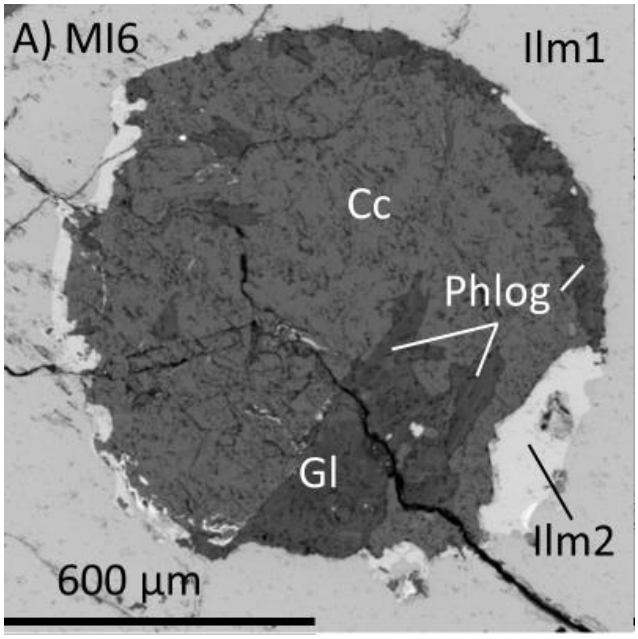

Fig. 3.15. BSE images of sample P015 MI6, showing large subhedral secondary ilmenite (Ilm2), which forms epitaxially on the host ilmenite megacryst (Ilm1). The majority of the inclusion consists of calcite (Cc). Glass (Gl) occurs as coherent pools. Glass also hosts lath-shaped subhedral phlogopite (Phlog).

3.5.4 Spinel

Spinel forms a common component of most melt inclusions and is present in the same textural varieties as secondary ilmenite, with which it is often intergrown. Spinel forms on either the host ilmenite megacryst, or in interior positions within the melt inclusion, generally surrounded by glass or calcite. Spinel forms with euhedral, subhedral, and skeletal crystal shapes and in varying sizes (10–491 µm).

Skeletal spinel is observed in samples ROM 109 (C) (MI1; MI2), P015 (MI1; MI3; MI4). In sample ROM 109 (C) MI1, for instance, it forms large skeletal crystals (40–180 µm), in both epitaxial positions and within the interior of the inclusion, within a calcite matrix. The interior void of these skeletal shapes is generally occupied by calcite (Fig. 3.9). Sample S5251 MI2 hosts a large spinel grain (231 µm) which encloses circular glass inclusions (5–30 µm). Spinel in this sample also forms as small (5–12 µm) grains along the boundary between the two glass varieties or as euhedral grains (25–40 µm) (Fig. 3.7; Fig. 3.13). Another example of euhedral spinel shaped grain is observed in sample ROM 109 (C) MI3, where spinel forms large euhedral crystals (40–180 µm) surrounded by a calcite matrix (Fig. 3.9).

3.5.5 Perovskite and kassite

Perovskite comprises a minor component of the common mineral assemblage and is commonly intergrown with, or forms in the same textural positions as kassite, so their textural features are described together. Perovskite and kassite are commonly absent, but where present typically form small (37–87 μm) grains that vary in shape from anhedral to euhedral, with subhedral grains being the most common.

A typical example of euhedral to subhedral kassite is observed in sample ROM 112 MI1. Kassite in this melt inclusion forms as large (45–80 μm) subhedral and euhedral grains within the melt inclusion. Kassite and perovskite also form anhedral grains on the margins of the melt inclusion and in the interior void of skeletal grains of a Ca-Si rich phase (possibly harkerite/afwillite) (Fig. 3.8). Similarly, in sample ROM 264, perovskite is intergrown with kassite on the margins of the melt inclusion. Kassite also forms as the interior (93–122 μm in diameter) of globular structures on the margins of the inclusion (Fig. 3.10) (Chapter 4.3.4). Perovskite forms as anhedral grains on the margins of ROM 109 (C) MI3 (Fig. 3.9 F). Perovskite in sample ROM 31 E(A) MI1 forms typical examples of subhedral and anhedral grains (31–80 μm), that occur within a large glass pool (Fig. 3.11). S5628 MI1 hosts kassite, which forms subhedral grains (up to 55.6 μm) that are randomly distributed throughout the inclusion. Sample S5626 hosts subhedral kassite (50 x 20 μm) that forms within large veins (17–25 μm) that extend laterally from MI2 (Fig. 3.3 A and B).

Perovskite also forms along the margins of the ilmenite megacryst in contact with the kimberlite matrix. Perovskite in sample P015 MI2 occurs as subhedral (<1–50 μm) grains that form aggregates that extend (~400 μm) from the ilmenite megacryst into the kimberlite matrix-filled channel (Fig 3.4 A).

3.5.6 Phlogopite

Phlogopite generally occurs in low modal proportions, up to 9 area%, and is absent in many inclusions (Table 1). Phlogopite is commonly surrounded by glass or less commonly calcite, with euhedral and subhedral lath-shaped grains, ranging in size from 25 to 570 μm.

The majority of phlogopite forms as lath- to needle-shaped grains of varying size (25–300 μm in length) within coherent glass pools (e.g. ROM 31 E (A) MI1; Fig. 3.11 A). For example, in sample S5628 MI1, which hosts the greatest abundance of phlogopite (9 area%; Table 1), phlogopite forms subhedral lath-shaped grains (25–170 μm) that concentrate around a central glass pool, up to 370 μm away from the glass pool, and in aggregates of up to 400 μm in width (Fig. 3.5 B). Phlogopite also forms large euhedral crystals (190 μm) dispersed throughout the melt inclusion (Fig 3.5 C).

The largest euhedral phlogopite occurs in sample ROM 109 (C) MI1. Phlogopite in MI1 forms two large euhedral grains (571–606 μm) set in a glass matrix. The phlogopite grains host small inclusions of glass towards their margins (25 μm) (Fig 3.9 C). The interior of the phlogopite has a weaker BSE signal intensity in comparison to the margins of the grain (Fig. 3.9 B). EDS analysis shows that BSE-bright rims consist of tetraferriphlogopite and the interior consists of a Al_2O_3, TiO_2-rich phlogopite (Chapter 4.3.5).

3.5.7 Serpentine

Serpentine is only present in five of the 23 analysed melt inclusions. Serpentine commonly forms as lath- to fan-shaped subhedral or euhedral grains that vary in size. Sample S5626 MI1, MI2, and MI3 host the same textural variety of serpentine. Serpentine in this sample forms large (up to 176 μm) euhedral and subhedral fan-shaped grains. The serpentine is associated with anhedral calcite, which forms between serpentine grains and in-between the 'rays' of individual fan-shaped serpentine grains (Fig. 3.2; Fig. 3.3). The fan-shaped serpentine forms around, and occasionally within, large coherent glass pools, with interstitial glass forming less commonly between the serpentine grains. The serpentine grains accumulate into large aggregates (Fig 3.2; Fig. 3.3). Euhedral crystal shapes often form in contact with coherent glass pools.

S5628 hosts fine-grained needle-shaped serpentine that forms throughout the inclusion, commonly radiating from euhedral phlogopite (Fig. 3.5 C). Sample ROM 112 hosts lath- to needle-shaped serpentine (up to 108 μm) that forms as large aggregates (up to 1 mm), commonly intergrown with phlogopite. The needle-shaped serpentine (24–128 μm) extends into anhedral calcite pools (Fig. 3.8).

3.5.8 Apatite

Apatite occurs in low modal proportions and is only observed in three melt inclusions within two of the selected thin sections (ROM 109 (C) MI1 and MI3, and S5251 MI1). Apatite forms subhedral grains, surrounded by either glass or calcite. MI3 of sample ROM 109 (C) hosts apatite as small (15–25 μm) subhedral laths surrounded by calcite (Fig 3.9). Sample S5251 also hosts minor amounts of apatite, which forms subhedral laths (~42 μm) near the margins of the inclusion, surrounded by glass (Fig 3.7 B).

At 6.9 area%, sample ROM 109 (C) MI1 contains the largest amount of apatite (Table 1), which is present in four textural varieties. Apatite forms (i) anhedral irregular grains (17–67 μm) surrounded by calcite or glass; (ii) skeletal (81–180 μm) grains surrounded by glass or calcite, with the interior voids occupied by either glass or calcite; (iii) large, rounded grains

(173 μm) set within glass; (iv) large subhedral grains (50–177 μm) set within glass or calcite (Fig. 3.9).

Chapter 4: Geochemistry

4.1 Major and minor elemental composition of the ilmenite megacrysts

The host ilmenite megacrysts exposed in thin section are largely compositionally homogenous. However, compositional variations are present as exsolution patterns immediately surrounding 10 out of the 23 melt inclusions analysed, as Mg-rich ilmenite rims surrounding the melt inclusions, and as Mg-poor reaction rims at the contact with kimberlite matrix. Minor compositional variations are present within the ilmenite megacrysts, but no major systematic compositional changes within a megacryst or between samples were identified. The Fe_2O_3 contents are uniform across the majority of samples (~10 wt%). However, in samples P015 MI4 (Table 4) and ROM 112 MI1 (Table 6) some analysis of the ilmenite megacryst in close proximity to the melt inclusions produced significantly higher Fe_2O_3 contents (22.9 wt% and 15.1–16.9 wt%, respectively). The high MgO contents (7.1–12.6 wt%) of the studied ilmenite megacrysts classify them as picro-ilmenites. The endmember compositions for ilmenite megacrysts are variable, but mainly consist of ilmenite *s.s* ($FeTiO_3$) and geikielite ($MgTiO_3$) (Table 2–Table 6).

Two EPMA point transects in sample P015 (Table 2–Table 3) and another EPMA point transect in sample S5628 (Table 6) show homogenous major and minor elemental compositions across the interior of the ilmenite megacrysts (Fig. 4.1 A and B). Furthermore, the ilmenite megacrysts of sample P015 and S5628 show similar X_{Mg} values (Fig. 4.1 A and B). However, in sample P015, the ilmenite megacrysts show an increase in X_{Mg} immediately surrounding the melt inclusions (up to 0.40) (Fig. 4.1 B), followed by a decrease in X_{Mg} with distance from the MIs (up to 150 µm from the MI), after which the composition remains uniform across the megacryst (X_{Mg} ~0.30). EPMA point analysis of ilmenite megacryst in sample P015 was also performed immediately surrounding MI3, MI4, and MI5 (Table 4). These analyses either show an increase in X_{Mg} (up to 0.39) or similar X_{Mg} (~0.30) compared to analyses performed in more interior positions within the ilmenite megacrysts (Table 4). The TiO_2 contents of the ilmenite megacrysts of sample P015 and S5628 are uniform and show no systematic spatial variations (~50 wt%) (Table 2–Table 6).

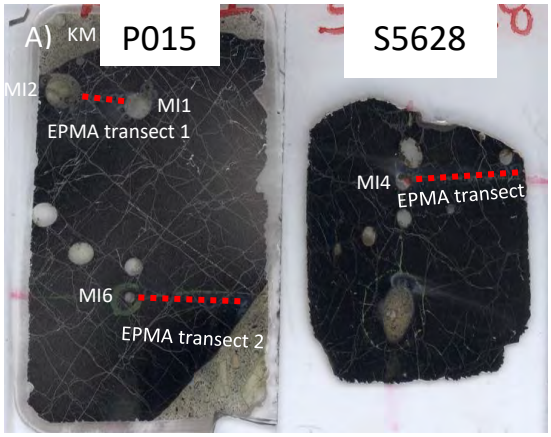

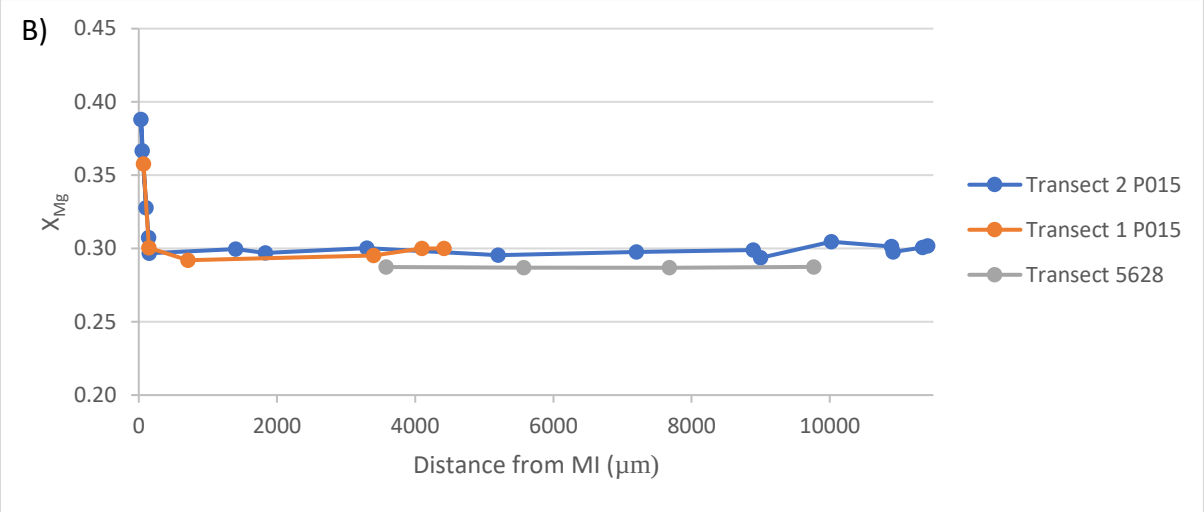

Fig. 4.1. A) Scan of samples P015 and S5628 showing EPMA transects (red dotted lines) across the host ilmenite megacryst (KM = kimberlite matrix, MI = melt inclusion). B) X_{Mg} of the ilmenite megacrysts versus distance of the analyses from the margins of the melt inclusions. Transect 1 and 2 performed within sample P015 show an increase in X_{Mg} (up to ~0.40) surrounding MI1 and MI6. The X_{Mg} decreases with distance from the MIs (up to 150 µm from the MI), after which the X_{Mg} remains constant (~0.30). A transect across the interior of S5628 produced similar X_{Mg} values (~0.30) to sample P015.

Table 2
EPMA transect 2 across ilmenite megacryst in sample P015 (from MI6 to margin of the megacryst; Fig. 4.1).

	mi6	mi6	mi6	mi6	mi6	mi6	mi6
Site	ilm6	ilm7	ilm1	ilm8	ilm9	ilm10	ilm11
SiO_2	0.03	0.02	0.05	0.00	0.17	0.04	0.00
Al_2O_3	0.37	0.53	0.57	0.53	0.62	0.53	0.59
Fe_2O_3	10.89	11.72	10.14	10.83	9.54	10.37	10.44
Cr_2O_3	0.07	0.05	0.00	0.09	0.03	0.05	0.00
TiO_2	50.81	50.25	50.23	49.81	50.23	49.76	49.85
FeO	27.91	28.53	30.55	30.86	32.29	31.25	31.46
MgO	9.94	9.27	8.36	7.69	7.65	7.50	7.46
MnO	0.23	0.25	0.15	0.19	0.18	0.20	0.20
CaO	0.02	0.04	0.01	0.00	0.02	0.00	0.02
NiO	0.02	0.00	0.04	0.00	0.02	0.02	0.04
Total	100.29	100.67	100.09	99.99	100.74	99.73	100.06
Cation proportions calculated for 3 O							
Si	0.00	0.00	0.00	0.00	0.00	0.00	0.00
Al	0.01	0.01	0.02	0.01	0.02	0.02	0.02
Fe^{3+}	0.19	0.21	0.18	0.19	0.17	0.19	0.19
Cr	0.00	0.00	0.00	0.00	0.00	0.00	0.00
Ti	0.90	0.89	0.90	0.89	0.90	0.90	0.90
Fe^{2+}	0.55	0.56	0.61	0.62	0.64	0.63	0.63
Mg	0.35	0.32	0.30	0.27	0.27	0.27	0.27
Mn	0.00	0.00	0.00	0.00	0.00	0.00	0.00
Ca	0.00	0.00	0.00	0.00	0.00	0.00	0.00
Ni	0.00	0.00	0.00	0.00	0.00	0.00	0.00
Total	2.00	2.00	2.00	2.00	2.00	2.00	2.00
X_{Mg}	0.39	0.37	0.33	0.31	0.30	0.30	0.30
Ti	0.90	0.89	0.90	0.89	0.90	0.90	0.90
Fe+Mg+Mn+Cr	1.10	1.11	1.10	1.10	1.10	1.10	1.10
Ilmenite	0.61	0.63	0.67	0.69	0.70	0.70	0.70
Pyrophanite	0.00	0.01	0.00	0.00	0.00	0.00	0.00
Geikielite	0.39	0.36	0.33	0.31	0.30	0.30	0.30

Table 2 continued

EPMA transect 2 across ilmenite megacryst in sample P015 (from MI6 to margin of the megacryst; Fig. 4.1).

Site	mi6 ilm12	mi6 ilm13	mi6 ilm14	mi6 ilm15	mi6 ilm16	mi6 ilm17	mi6 ilm18	mi6 ilm19	mi6 ilm20	mi6 ilm21
SiO_2	0.08	0.03	0.03	0.01	0.04	0.01	0.05	0.12	0.04	0.01
Al_2O_3	0.64	0.54	0.55	0.55	0.55	0.56	0.57	0.63	0.55	0.63
Fe_2O_3	10.51	9.93	9.88	10.54	10.06	10.96	9.95	9.97	10.45	9.89
Cr_2O_3	0.00	0.05	0.08	0.03	0.01	0.04	0.06	0.03	0.00	0.04
TiO_2	49.97	50.00	49.96	50.47	50.40	50.21	50.30	49.83	50.16	50.27
FeO	31.68	31.70	31.54	31.76	32.12	31.24	31.77	31.81	31.48	31.56
MgO	7.63	7.46	7.51	7.60	7.50	7.68	7.69	7.57	7.59	7.65
MnO	0.16	0.20	0.18	0.15	0.15	0.19	0.19	0.21	0.17	0.17
CaO	0.00	0.01	0.01	0.01	0.02	0.01	0.00	0.01	0.01	0.00
NiO	0.03	0.04	0.07	0.00	0.13	0.01	0.04	0.02	0.00	0.03
Total	100.71	99.95	99.81	101.12	100.96	100.91	100.62	100.20	100.44	100.24
Cation proportions calculated for 3 O										
Si	0.00	0.00	0.00	0.00	0.00	0.00	0.00	0.00	0.00	0.00
Al	0.02	0.02	0.02	0.02	0.02	0.02	0.02	0.02	0.02	0.02
Fe^{3+}	0.19	0.18	0.18	0.19	0.18	0.20	0.18	0.18	0.19	0.18
Cr	0.00	0.00	0.00	0.00	0.00	0.00	0.00	0.00	0.00	0.00
Ti	0.89	0.90	0.90	0.90	0.90	0.89	0.90	0.89	0.90	0.90
Fe^{2+}	0.63	0.63	0.63	0.63	0.64	0.62	0.63	0.64	0.63	0.63
Mg	0.27	0.27	0.27	0.27	0.26	0.27	0.27	0.27	0.27	0.27
Mn	0.00	0.00	0.00	0.00	0.00	0.00	0.00	0.00	0.00	0.00
Ca	0.00	0.00	0.00	0.00	0.00	0.00	0.00	0.00	0.00	0.00
Ni	0.00	0.00	0.00	0.00	0.00	0.00	0.00	0.00	0.00	0.00
Total	2.00	2.00	2.00	2.00	2.00	2.00	2.00	2.00	2.00	2.00
X_{Mg}	0.30	0.30	0.30	0.30	0.29	0.30	0.30	0.30	0.30	0.30
Ti	0.89	0.90	0.90	0.90	0.90	0.89	0.90	0.89	0.90	0.90
Fe+Mg+Mn+Cr	1.11	1.10	1.10	1.10	1.10	1.10	1.10	1.11	1.10	1.10
Ilmenite	0.70	0.70	0.70	0.70	0.70	0.69	0.70	0.70	0.70	0.70
Pyrophanite	0.00	0.00	0.00	0.00	0.00	0.00	0.00	0.00	0.00	0.00
Geikielite	0.30	0.29	0.30	0.30	0.29	0.30	0.30	0.30	0.30	0.30

Table 3
EPMA transect 1 across ilmenite megacryst in sample P015 (from MI1 to MI2; Fig. 4.1).

Site	mi1 ilm55	mi1 ilm50	mi1 ilm49	mi1 ilm56	mi1 ilm57	mi1 ilm58	mi1 ilm59	mi1 ilm60	mi1 ilm61
SiO_2	0.00	0.06	0.02	0.04	0.06	0.01	0.06	0.01	0.07
Al_2O_3	0.44	0.31	0.54	0.56	0.55	0.56	0.56	0.54	0.49
Fe_2O_3	10.65	8.88	11.03	10.04	9.48	9.88	9.98	10.84	9.77
Cr_2O_3	0.08	0.00	0.08	0.05	0.00	0.00	0.00	0.04	0.01
TiO_2	51.71	51.78	50.20	50.39	50.55	50.09	50.15	50.13	50.32
FeO	28.75	30.06	31.45	32.04	32.10	31.52	31.86	30.90	31.18
MgO	9.92	9.39	7.58	7.42	7.55	7.59	7.67	8.00	7.98
MnO	0.30	0.20	0.18	0.20	0.22	0.24	0.16	0.22	0.20
CaO	0.03	0.03	0.01	0.01	0.01	0.00	0.00	0.00	0.01
NiO	0.07	0.04	0.00	0.05	0.07	0.06	0.08	0.04	0.07
Total	101.94	100.75	101.08	100.79	100.59	99.94	100.52	100.72	100.09
Cation proportions calculated for 3 O									
Si	0.00	0.00	0.00	0.00	0.00	0.00	0.00	0.00	0.00
Al	0.01	0.01	0.01	0.02	0.02	0.02	0.02	0.01	0.01
Fe^{3+}	0.19	0.16	0.20	0.18	0.17	0.18	0.18	0.19	0.18
Cr	0.00	0.00	0.00	0.00	0.00	0.00	0.00	0.00	0.00
Ti	0.90	0.91	0.89	0.90	0.90	0.90	0.90	0.89	0.90
Fe^{2+}	0.56	0.59	0.62	0.64	0.64	0.63	0.63	0.61	0.62
Mg	0.34	0.33	0.27	0.26	0.27	0.27	0.27	0.28	0.28
Mn	0.01	0.00	0.00	0.00	0.00	0.00	0.00	0.00	0.00
Ca	0.00	0.00	0.00	0.00	0.00	0.00	0.00	0.00	0.00
Ni	0.00	0.00	0.00	0.00	0.00	0.00	0.00	0.00	0.00
Total	2.00	2.00	2.00	2.00	2.00	2.00	2.00	2.00	2.00
X_{Mg}	0.38	0.36	0.30	0.29	0.30	0.30	0.30	0.32	0.31
Ti	0.90	0.91	0.89	0.90	0.90	0.90	0.90	0.89	0.90
Fe+Mg+Mn+Cr	1.10	1.09	1.11	1.10	1.10	1.10	1.10	1.11	1.10
Ilmenite	0.62	0.64	0.70	0.70	0.70	0.70	0.70	0.68	0.68
Pyrophanite	0.01	0.00	0.00	0.00	0.00	0.01	0.00	0.00	0.00
Geikielite	0.38	0.36	0.30	0.29	0.29	0.30	0.30	0.31	0.31

Table 4
EPMA analysis of ilmenite megacryst around melt inclusion 3, 4 and 5 in sample P015.

	mi5	mi5	mi5	mi5	mi4	mi4	mi4	mi3	mi3	mi3
Site	ilm22	ilm23	ilm26	ilm29	ilm32	ilm33	ilm39	ilm40	ilm41	ilm45
SiO_2	0.06	0.01	0.07	0.00	0.09	0.05	0.01	0.00	0.07	0.02
Al_2O_3	0.45	0.39	0.41	1.11	0.59	0.47	1.26	0.61	0.48	0.51
Fe_2O_3	11.82	11.82	10.94	14.09	9.99	10.91	22.94	9.90	10.91	11.10
Cr_2O_3	0.04	0.04	0.08	0.00	0.10	0.11	0.05	0.07	0.05	0.01
TiO_2	50.13	50.44	50.69	49.12	50.33	50.00	45.13	50.70	50.26	50.19
FeO	28.76	28.76	28.03	26.94	31.89	31.08	22.37	31.58	29.46	29.98
MgO	9.09	9.31	10.04	9.58	7.72	7.73	10.19	7.75	8.92	8.36
MnO	0.21	0.25	0.29	0.37	0.20	0.25	0.35	0.20	0.23	0.18
CaO	0.01	0.02	0.05	0.03	0.00	0.02	0.02	0.02	0.03	0.01
NiO	0.00	0.06	0.04	0.05	0.01	0.02	0.00	0.02	0.10	0.00
Total	100.57	101.09	100.64	101.27	100.91	100.63	102.31	100.84	100.48	100.37
Cation proportions calculated for 3 O										
Si	0.00	0.00	0.00	0.00	0.00	0.00	0.00	0.00	0.00	0.00
Al	0.01	0.01	0.01	0.03	0.02	0.01	0.03	0.02	0.01	0.01
Fe^{3+}	0.21	0.21	0.19	0.25	0.18	0.19	0.40	0.18	0.19	0.20
Cr	0.00	0.00	0.00	0.00	0.00	0.00	0.00	0.00	0.00	0.00
Ti	0.89	0.89	0.89	0.86	0.90	0.89	0.78	0.90	0.89	0.89
Fe^{2+}	0.57	0.56	0.55	0.52	0.63	0.62	0.43	0.63	0.58	0.59
Mg	0.32	0.32	0.35	0.33	0.27	0.27	0.35	0.27	0.31	0.30
Mn	0.00	0.00	0.01	0.01	0.00	0.00	0.01	0.00	0.00	0.00
Ca	0.00	0.00	0.00	0.00	0.00	0.00	0.00	0.00	0.00	0.00
Ni	0.00	0.00	0.00	0.00	0.00	0.00	0.00	0.00	0.00	0.00
Total	2.00	2.00	2.00	2.00	2.00	2.00	2.00	2.00	2.00	2.00
X_{Mg}	0.36	0.37	0.39	0.39	0.30	0.31	0.45	0.30	0.35	0.33
Ti	0.89	0.89	0.89	0.86	0.90	0.89	0.78	0.90	0.89	0.89
Fe+Mg+Mn+Cr	1.11	1.11	1.11	1.14	1.10	1.11	1.22	1.10	1.11	1.10
Ilmenite	0.64	0.63	0.61	0.61	0.70	0.69	0.55	0.69	0.65	0.67
Pyrophanite	0.00	0.01	0.01	0.01	0.00	0.01	0.01	0.00	0.00	0.00
Geikielite	0.36	0.36	0.39	0.38	0.30	0.31	0.44	0.30	0.35	0.33

Table 5
EPMA analysis of ilmenite megacryst in sample S5628 (from MI4 to the margins of the ilmenite megacryst; Fig. 4.1).

	s5628	s5628	s5628	s5628	s5628	s5628	s5628	s5628
Site	ILM11	ILM2	ILM3	ILM7	ILM8	ILM9	ILM10	ILM15
SiO_2	0.03	0.04	0.00	0.02	0.12	0.03	0.00	0.10
Al_2O_3	0.36	0.57	0.48	0.50	0.42	0.43	0.46	0.36
Fe_2O_3	9.64	10.00	10.46	10.52	9.81	10.60	10.58	10.69
Cr_2O_3	0.07	0.00	0.02	0.05	0.06	0.01	0.11	0.05
TiO_2	50.23	49.85	49.77	49.65	48.46	49.76	49.73	49.15
FeO	32.66	31.90	31.52	31.71	31.31	31.94	31.88	32.22
MgO	7.09	7.39	7.35	7.18	7.07	7.21	7.22	7.00
MnO	0.19	0.25	0.18	0.16	0.18	0.19	0.18	0.20
CaO	0.02	0.02	0.02	0.00	0.01	0.01	0.01	0.01
NiO	0.03	0.06	0.01	0.00	0.03	0.04	0.02	0.04
Total	100.31	100.07	99.81	99.79	97.47	100.23	100.18	99.82
Cation proportions calculated for 3 O								
Si	0.00	0.00	0.00	0.00	0.00	0.00	0.00	0.00
Al	0.01	0.02	0.01	0.01	0.01	0.01	0.01	0.01
Fe^{3+}	0.17	0.18	0.19	0.19	0.18	0.19	0.19	0.19
Cr	0.00	0.00	0.00	0.00	0.00	0.00	0.00	0.00
Ti	0.90	0.90	0.90	0.90	0.90	0.90	0.90	0.89
Fe^{2+}	0.65	0.64	0.63	0.64	0.64	0.64	0.64	0.65
Mg	0.25	0.26	0.26	0.26	0.26	0.26	0.26	0.25
Mn	0.00	0.01	0.00	0.00	0.00	0.00	0.00	0.00
Ca	0.00	0.00	0.00	0.00	0.00	0.00	0.00	0.00
Ni	0.00	0.00	0.00	0.00	0.00	0.00	0.00	0.00
Total	2.00	2.00	2.00	2.00	2.00	2.00	2.00	2.00
X_{Mg}	0.28	0.29	0.29	0.29	0.29	0.29	0.29	0.28
Ti	0.90	0.90	0.90	0.90	0.90	0.90	0.90	0.89
Fe+Mg+Mn+Cr	1.10	1.10	1.10	1.10	1.10	1.10	1.11	1.11
Ilmenite	0.72	0.70	0.70	0.71	0.71	0.71	0.71	0.72
Pyrophanite	0.00	0.01	0.00	0.00	0.00	0.00	0.00	0.00
Geikielite	0.28	0.29	0.29	0.29	0.29	0.29	0.29	0.28

EPMA point analyses were performed within the ilmenite megacryst and around the perimeter of MI1 of sample ROM 112. EPMA analyses closer to the margin of MI1 show higher X_{Mg} contents (0.39–0.52) in comparison to analyses further from the margin of MI1, within the megacryst interior (X_{Mg} ~0.32) (Table 6). The TiO_2 content of the ilmenite megacryst is also slightly lower near the margin of MI1 (~47–50 wt%) in comparison to the megacryst interior (50–54 wt%) (Table 6). MI1 of sample ROM 112 displays prominent exsolution patterns immediately surrounding the melt inclusion. The exsolution patterns shows compositional variation in BSE signal intensity (Fig 3.8; Chapter 3.4). Due to the small size of the exsolution lamellae, no EPMA data were obtained. However, they show similar BSE signal intensity to Fe-rich ilmenites that form with the melt inclusion (Chapter 4.3.2), epitaxially on the host ilmenite megacryst. This was confirmed by an element map of exsolution patterns surrounding sample S5251 MI2 (discussed below).

Table 6
EPMA analysis of ilmenite megacryst in sample ROM 112. Analyses were performed in the area surrounding MI1 and away from MI1 in more interior positions within the megacryst.

Comment	Ilm interior				Ilm near MI1 margin		
Site	ILM1	ILM2	ILM3	ILM6	ILM4	ILM5	ILM7
SiO_2	0.03	0.04	0.03	0.30	0.04	0.03	0.05
Al_2O_3	0.82	0.43	0.44	0.37	1.07	0.69	1.07
Fe_2O_3	8.21	8.83	8.69	0.00	15.08	11.23	16.84
Cr_2O_3	0.05	0.04	0.08	0.07	0.09	0.07	0.09
TiO_2	51.79	51.61	50.82	54.84	47.87	50.43	48.02
FeO	31.49	31.77	31.28	34.50	26.35	25.98	20.94
MgO	8.45	8.40	8.18	9.05	9.45	10.91	12.60
MnO	0.17	0.16	0.20	0.20	0.26	0.25	0.26
CaO	0.00	0.01	0.02	0.01	0.01	0.01	0.03
NiO	0.10	0.09	0.07	0.06	0.09	0.08	0.14
Total	101.11	101.39	99.79	99.39	100.32	99.66	100.04
Cation proportions calculated for 3 O							
Si	0.00	0.00	0.00	0.01	0.00	0.00	0.00
Al	0.02	0.01	0.01	0.01	0.03	0.02	0.03
Fe^{3+}	0.14	0.16	0.16	0.00	0.27	0.20	0.29
Cr	0.00	0.00	0.00	0.00	0.00	0.00	0.00
Ti	0.91	0.91	0.91	0.98	0.85	0.89	0.83
Fe^{2+}	0.62	0.62	0.62	0.68	0.52	0.51	0.40
Mg	0.30	0.29	0.29	0.32	0.33	0.38	0.43
Mn	0.00	0.00	0.00	0.00	0.01	0.00	0.01
Ca	0.00	0.00	0.00	0.00	0.00	0.00	0.00
Ni	0.00	0.00	0.00	0.00	0.00	0.00	0.00
Total	2.00	2.00	2.00	2.01	2.00	2.00	2.00
X_{Mg}	0.32	0.32	0.32	0.32	0.39	0.43	0.52
Ti	0.91	0.91	0.91	0.98	0.85	0.89	0.83
Fe+Mg+Mn+Cr	1.08	1.09	1.09	1.02	1.15	1.11	1.17
Ilmenite	0.67	0.68	0.68	0.68	0.61	0.57	0.48
Pyrophanite	0.00	0.00	0.00	0.00	0.01	0.01	0.01
Geikielite	0.32	0.32	0.32	0.32	0.39	0.43	0.51

The zones of Mg-rich ilmenite and exsolution lamellae that form with the ilmenite megacryst near the melt inclusion-megacryst interface are also observed in an element map of a section of MI2 within sample S5251 (Fig. 4.2). The ilmenite megacryst immediately surrounding this melt inclusion is enriched in Mg and depleted in Fe in comparison to the interior of the ilmenite megacryst (Fig. 4.2). Although the exsolution lamellae were too small to analyse with the available equipment, the element map confirms that the texture consists of Fe-rich lamellae separated by Fe-poor, Mg-rich zones (Fig. 4.2). At the contact of MI2 and the host ilmenite megacryst of sample S5251 Fe-Ti oxides occur epitaxially on the ilmenite megacryst with a thin (~1 μm) Ca-rich outer reaction seam (Fig. 4.2).

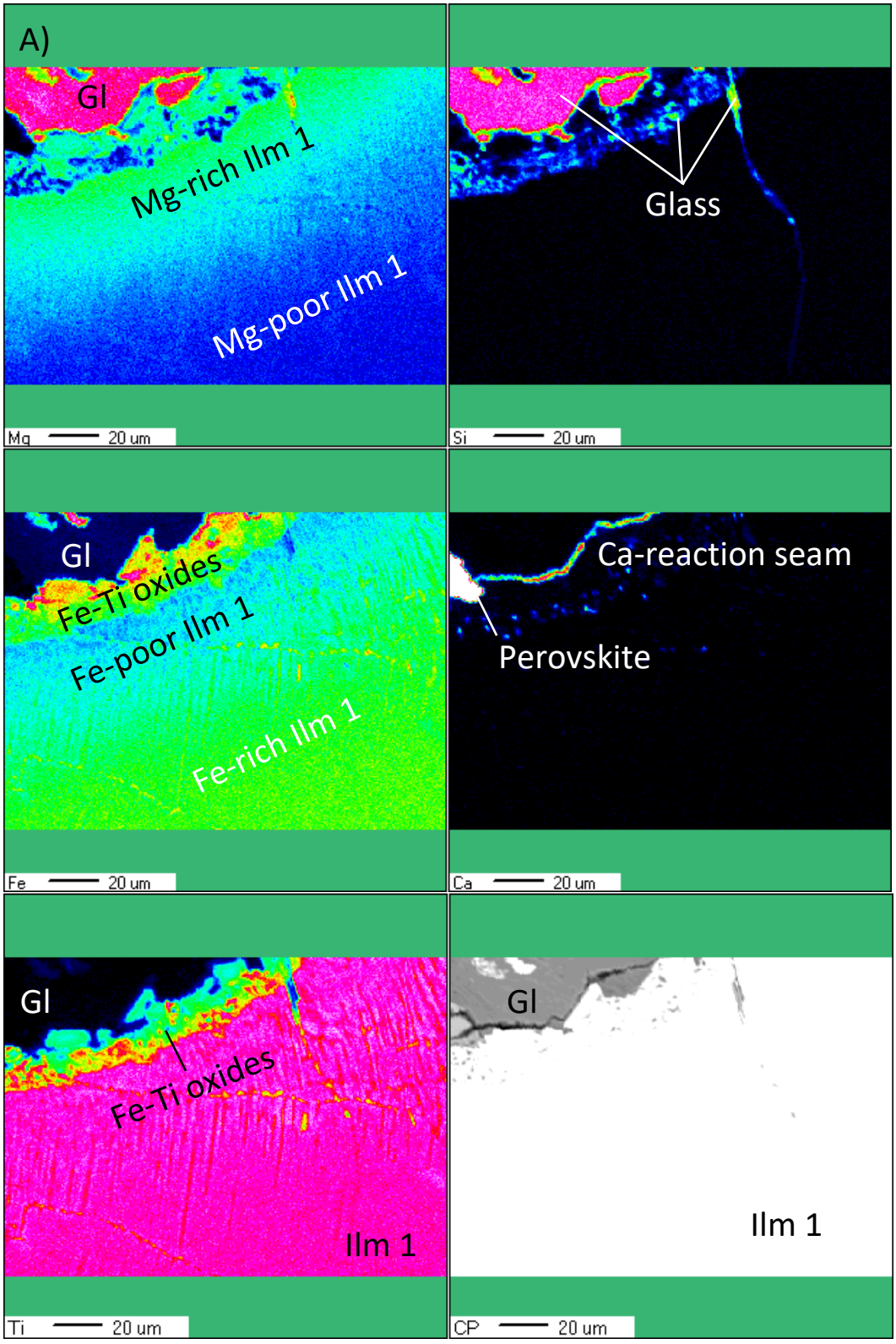
A)
Gl
Mg-rich Ilm 1
Mg-poor Ilm 1
Mg 20 um
Glass
Si 20 um
Gl
Fe-Ti oxides
Fe-poor Ilm 1
Fe-rich Ilm 1
Fe 20 um
Ca-reaction seam
Perovskite
Ca 20 um
Gl
Fe-Ti oxides
Ilm 1
Ti 20 um
Gl
Ilm 1
CP 20 um

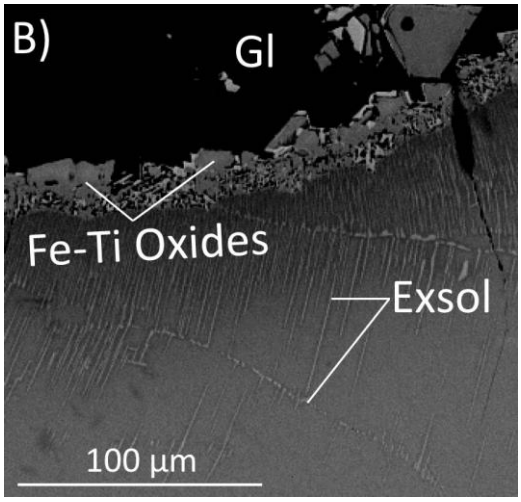

Fig. 4.2. A) Element maps of the reaction seam that forms between MI2 of sample S5251 and the host ilmenite megacryst. The ilmenite megacryst (Ilm 1) varies in Fe-Mg in proximity to the melt inclusion which is mostly composed of glass (Gl). Immediately surrounding the melt inclusion, the ilmenite megacryst shows a zone of Fe-poor Mg-rich ilmenite, in comparison to the megacryst interior which is more Fe-rich. Fe-Ti oxides (spinel, ilmenite, perovskite) form within the melt inclusion epitaxially on the host ilmenite megacryst. A thin Ca-rich reaction seam forms on the epitaxial oxides in contact with the glass. Small (<1 µm) Si-rich domains within the Fe-Ti oxides and within the thin vein are interpreted to represent glass. B) BSE image of the same section of MI2 in sample S5251 showing exsolution lamellae. The lamellae form as BSE-bright domains separated by BSE-dark domains. The element map shows the BSE-bright domains are more Fe-rich.

Chemical modifications are present between the host ilmenite megacryst and the surrounding kimberlite matrix. In sample P015 the ilmenite megacryst in contact with the kimberlite matrix shows a 250 µm Mg-depleted and Fe-enriched zone (0.03 X_{Mg}) (Table 7: ILM-KM reaction) in comparison to the megacryst interior (0.3 X_{Mg}) (Table 7: Ilm megacryst) (Fig. 3.4). Immediately surrounding the Mg-poor reaction zone is a zone of Mg-enriched ilmenite (0.6 X_{Mg}) (Table 7: Mg-rich Ilm megacryst) (Fig. 3.4). The sample also shows exsolution lamellae near the margins of the megacryst and surrounding MI2 (Fig. 3.4). The exsolution lamellae are interpreted to represent Fe-rich lamellae separated by Mg-rich zones.

Table 7
EDS analysis of ilmenite megacryst around MI2 of sample P015 showing chemical modifications associated with kimberlite matrix (Fig. 3.4).

Analysis	Mg-rich ILM1 megacryst	ILM4 megacryst	ILM5 megacryst	ILM2-KM reaction	ILM3-KM reaction	ILM6-KM reaction
SiO_2	0.28	0.13	0.13	0.95	0.41	1.45
Al_2O_3	0.77	0.81	0.70	0.22	0.35	0.29
Fe_2O_3	15.72	13.33	12.45	7.65	0.00	0.00
Cr_2O_3	0.00	0.02	0.06	0.03	0.00	0.10
TiO_2	49.64	47.94	49.31	44.95	49.38	48.12
FeO	18.75	29.36	27.43	42.31	45.60	45.38
MgO	14.94	8.25	9.94	1.48	0.79	1.74
MnO	0.52	0.16	0.35	1.69	1.77	1.84
CaO	0.00	0.04	0.00	0.24	0.80	0.39
NiO	0.00	0.03	0.26	0.17	0.00	0.24
Total	101.30	100.55	100.92	100.13	99.90	99.98
Cation proportions calculated for 3 O						
Si	0.01	0.00	0.00	0.02	0.01	0.04
Al	0.02	0.02	0.02	0.01	0.01	0.01
Fe^{3+}	0.27	0.24	0.22	0.15	0.00	0.00
Cr	0.00	0.00	0.00	0.00	0.00	0.00
Ti	0.84	0.86	0.87	0.86	0.94	0.91
Fe^{2+}	0.35	0.58	0.54	0.90	0.97	0.96
Mg	0.50	0.29	0.35	0.06	0.03	0.07
Mn	0.01	0.00	0.01	0.04	0.04	0.04
Ca	0.00	0.00	0.00	0.01	0.02	0.01
Ni	0.00	0.00	0.00	0.00	0.00	0.00
Total	2.01	2.01	2.01	2.05	2.03	2.04
X_{Mg}	0.59	0.33	0.39	0.06	0.03	0.07
Ti	0.84	0.86	0.87	0.86	0.95	0.92
Fe+Mg+Mn+Cr	1.16	1.14	1.13	1.14	1.06	1.07
Ilmenite	0.41	0.66	0.60	0.91	0.93	0.90
Pyrophanite	0.01	0.00	0.01	0.04	0.04	0.04
Geikielite	0.58	0.33	0.39	0.06	0.03	0.06

4.2 EDS area scans of melt inclusions

The bulk compositions produced by EDS area scans show large variations between MIs, due to large variations in modal proportions (Table 1). This is most notably observed in the CaO contents which may vary between 53.7 wt% in MI2 to 1.0 wt% in MI1 within sample S5628 (Table 9). This reflects large variations in the proportions of calcite exposed in two dimensions (Table 1). The volatile content also varies in accordance with the proportions of calcite, glass, and other mineral phases exposed in two dimensions. The MIs are generally composed of variable SiO_2 (2.9–40.4 wt%) and FeO (1.0–13.7 wt%). The Al_2O_3 content is generally low (<2.4 wt%), as is the K_2O content, reaching no more than 2.9 wt% in MIs rich in phlogopite (Table 8–Table 10). The general composition of the MIs forms a continuum from silicate-rich to carbonate-rich. This trend is observed between MIs from different samples and MIs from a single megacryst sample (Fig. 4.3). In a binary diagram of SiO_2 versus CaO, the MIs plot along an inversely proportional linear trend of decreasing CaO and increasing SiO_2 (Fig. 4.3).

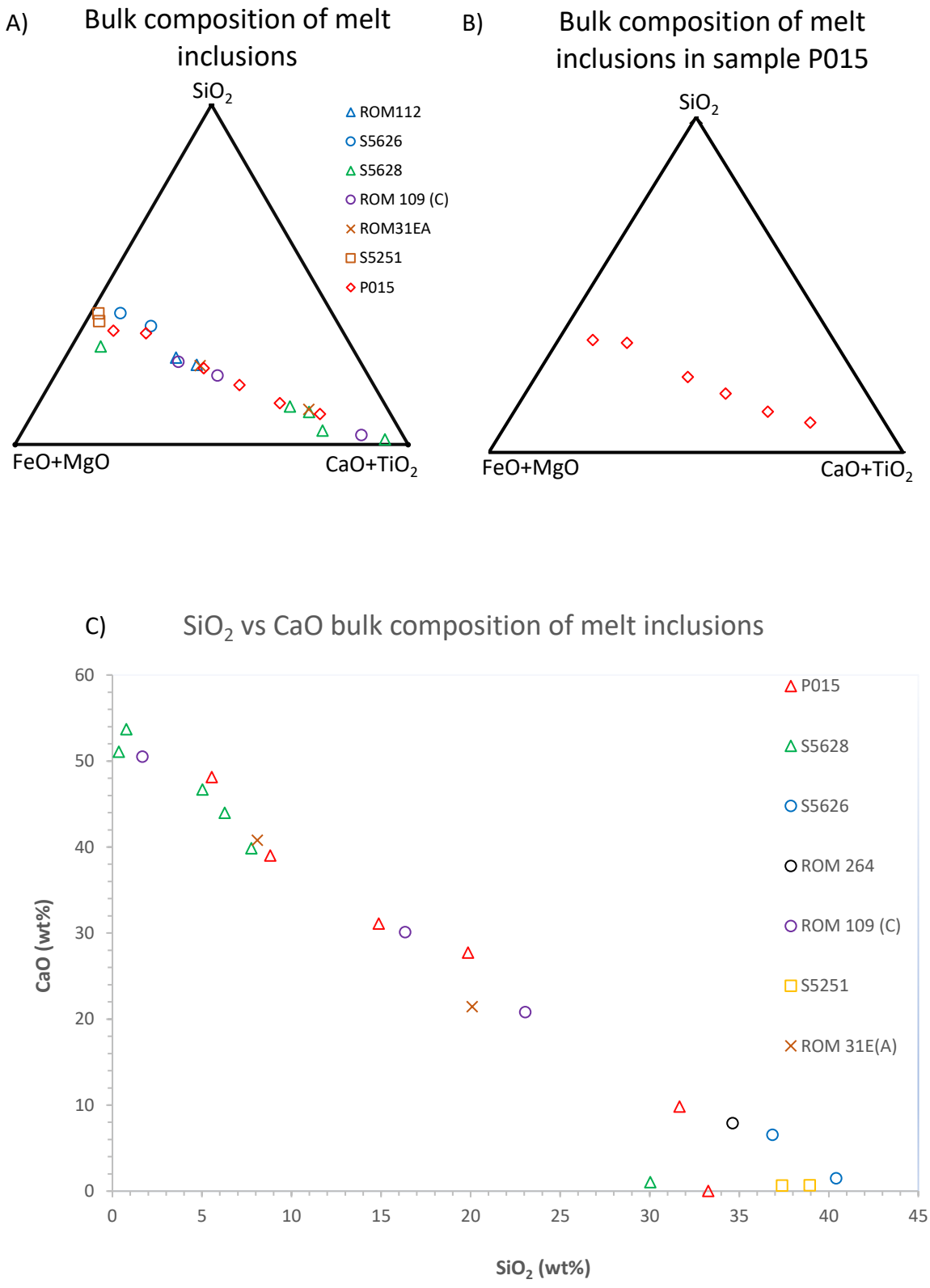

Fig. 4.3. A) Ternary diagram of the bulk compositions (wt%) of melt inclusions from the studied thin sections. The melt inclusions form an array from Si-rich and CaO-poor to CaO-rich and Si-poor. B) Ternary diagrams of the bulk compositions of the melt inclusions in sample P015 demonstrate that this trend may occur within a single sample. C) Binary CaO - SiO_2 diagram of the bulk composition from various samples. The area scans plot along an inversely proportional linear trend of decreasing CaO and increasing SiO_2, correlating with the abundance of calcite in the exposed thin section surface.

Table 8

EDS bulk compositions of melt inclusions (MI) 1 - 6 from sample P015.

Site	MI1	MI2	MI3	MI4	MI5	MI6
SiO_2	19.86	33.27	5.54	31.66	14.87	8.82
Al_2O_3	0.15	0.84	0.04	0.22	0.12	1.02
Fe_2O_3	0.00	0.00	0.00	0.00	0.00	0.00
Cr_2O_3	0.00	0.15	0.00	0.01	0.00	0.00
TiO_2	0.54	8.91	0.11	2.39	3.93	4.70
FeO	3.78	14.09	1.01	7.19	6.02	5.12
MgO	19.64	31.63	5.48	31.10	14.68	7.62
MnO	0.09	0.41	0.03	0.12	0.06	0.03
CaO	27.72	0.00	48.11	9.82	31.10	39.00
Na_2O	0.34	0.08	0.10	0.56	0.28	0.10
K2O	0.05	0.21	0.01	0.08	0.04	0.91
NiO	0.05	0.21	0.01	0.07	0.03	0.02
H_2O*	6.30	10.21	1.87	9.51	4.66	2.13
CO_2*	21.48	0.00	37.68	7.27	24.20	30.53
SO_3	0.00	0.00	0.00	0.00	0.00	0.00
Total	100.00	100.00	100.00	100.00	100.00	100.00

*CO_2 and H_2O contents are estimated from the modal proportions of volatile-bearing phases within the melt inclusions, assuming that calcite is the only CO_2 bearing phase, using the Rock Maker software (Büttner, 2012; see Chapter 2).

Table 9

EDS bulk compositions of MI1 - MI6 from sample S5628.

Site	MI1	MI2	MI3	MI4	MI5	MI6
SiO2	30.04	0.77	0.36	7.76	5.03	6.27
Al_2O_3	2.39	0.18	0.10	1.76	1.14	1.42
Fe_2O_3	0.00	0.00	0.00	0.00	0.00	0.00
Cr_2O_3	0.17	0.00	0.02	0.00	0.00	0.00
TiO_2	5.33	0.95	2.99	3.00	1.02	1.16
FeO	13.68	1.24	3.51	6.78	3.36	4.22
MgO	33.18	0.63	0.49	6.44	4.10	5.24
MnO	0.18	0.00	0.02	0.01	0.01	0.01
CaO	1.03	53.70	51.07	39.85	46.69	43.99
Na_2O	0.68	0.02	0.02	0.15	0.10	0.13
K_2O	2.87	0.00	0.00	0.03	0.02	0.05
NiO	0.01	0.01	0.00	0.04	0.03	0.03
H_2O*	9.69	0.39	1.33	3.08	1.97	3.09
CO_2*	0.76	42.12	40.08	31.07	36.51	34.37
SO_3	0.00	0.00	0.00	0.02	0.01	0.02
Total	100.00	100.00	100.00	100.00	100.00	100.00

*CO_2 and H_2O contents are estimated from the modal proportions of volatile-bearing phases within the melt inclusions, assuming that calcite is the only CO_2 bearing phase using, the Rock Maker software (Büttner, 2012; see Chapter 2).

Table 10
EDS bulk composition of melt inclusions from sample S5626, ROM 264, ROM 109 (C), S5251, and ROM 31E (A).

Sample	S5626		ROM 264	ROM 109 (C)			S5251		ROM 31E (A)	
Site	MI1	MI2	MI1	MI1	MI2	MI3	MI1	MI2	MI1	MI2
SiO_2	36.85	40.41	34.63	16.35	23.05	1.68	38.94	37.39	8.09	20.10
Al_2O_3	0.95	1.20	0.27	0.48	0.16	0.02	0.32	0.30	0.06	0.25
Fe_2O_3	0.00	0.00	0.00	0.00	0.00	0.00	0.00	0.00	0.00	0.00
Cr_2O_3	0.03	0.05	0.00	0.00	0.01	0.00	0.01	0.01	0.00	0.04
TiO_2	1.97	3.68	2.91	3.00	3.07	2.85	1.54	3.38	3.76	5.37
FeO	4.25	5.41	6.29	5.21	6.61	2.86	8.06	9.64	4.70	8.32
MgO	33.44	36.16	31.61	15.77	22.74	1.67	37.95	36.56	7.97	19.56
MnO	0.05	0.08	0.24	0.07	0.08	0.02	0.15	0.15	0.03	0.21
CaO	6.54	1.50	7.90	30.10	20.79	50.51	0.66	0.63	40.79	21.43
Na_2O	0.16	0.40	0.37	0.28	0.43	0.03	0.70	0.68	0.15	0.22
K_2O	0.33	0.24	0.08	0.38	0.06	0.00	0.09	0.09	0.02	0.12
NiO	0.06	0.03	0.04	0.03	0.05	0.00	0.08	0.08	0.02	0.07
H_2O*	10.35	9.77	10.21	5.06	6.98	0.74	11.49	11.09	2.51	7.67
CO_2*	5.01	1.07	5.45	19.47	15.99	39.62	0.00	0.00	31.90	16.66
SO_3	0.00	0.00	0.00	0.00	0.00	0.00	0.00	0.00	0.00	0.00
Total	100.00	100.00	100.00	100.00	100.00	100.00	100.00	100.00	100.00	100.00

*CO_2 and H_2O contents are estimated from the modal proportions of volatile-bearing phases within the melt inclusions, assuming that calcite is the only CO_2 bearing phase using, the Rock Maker software (Büttner, 2012; see Chapter 2).

4.3 Major and minor elemental compositions of glass and crystal phases hosted in melt inclusions

4.3.1 Glass

EPMA analysis of the common variety of glass reveals it is silicate-rich (41.06–42.11 wt% SiO_2) with variable MgO (34.97–39.24 wt%) and FeO (3.16–8.45 wt%) (e.g. Table 14–Table 16). The glass is also composed of minor amounts of Al_2O_3 (0.41–1.65 wt%), TiO_2 (0.1–0.36 wt%), MnO (<0.09 wt%), CaO (<0.48 wt%), NiO (<0.28 wt%), Na_2O (<0.43 wt%), and SO_3 (<0.11 wt%). A volatile component of ~13 wt% is calculated by difference from EPMA oxide totals; this volatile value is assumed for EDS analysis.

Glass is either geochemically homogenous or heterogenous within a melt inclusion or within a coherent glass pool. Glass commonly displays variations in absorption colour (e.g. Fig. 3.5; Fig. 3.10). These optical characteristics correspond to variations in BSE signal intensity (e.g. Fig. 3.5; Fig. 3.10). EPMA and EDS analysis of glass reveals the difference is a result of variations in the Fe-Mg composition of glass. This is the most common form of heterogeneity of glass in the melt inclusions and occurs as patches of Fe-rich glass that have a diffuse boundary with surrounding Fe-poor glass (Chapter 3.5.1). Fe-poor glass generally has a composition of <5 wt% FeO and Fe-rich glass has a composition of 7–12 wt% FeO (Table 11; Table 14). Glass may also be homogenous throughout an inclusion, optically and geochemically. Furthermore, areas of devitrification are geochemically identical to areas which show no devitrification, which is also indicated by the fact that they show a uniform BSE signal intensity (Fig 3.12 A and B).

In addition to the common Fe-Mg variations in glass, several uncommon varieties of glass were also identified. For the remainder of this section specific examples of the glass varieties are discussed.

Glass in sample ROM 264 MI1 forms in five compositional varieties (i–v), several of which are unique to this sample (Chapter 3.5.1; Fig 3.10). The glass shows a concentric distribution within the melt inclusion (glass varieties: i–iii) and also a concentric distribution within globular melt structures on the margins of the inclusion (glass varieties: iv–v) (Chapter 3.3.7).

EPMA and EDS analyses show the glass varieties in MI1 of sample ROM 264 differ in Fe-Mg-Ca-Ti composition. Surrounding the inner calcite grain is a (i) heterogenous zone composed of interconnected veinlets that show a similar BSE signal intensity compared to the inner calcite grain. Point analyses of this heterogenous zone produced a composition of 6.46–22.03 wt% CaO (Table 12). The large variations in composition of this glass are a result of a heterogenous microstructure of highly interconnected veinlets (Fig. 4.4). In an Honours project that includes this sample, Marima (2019) produced high-resolution element maps that show this zone consists of Fe/Mg silicate glass with Ca-rich Si-Mg-Fe-Ti-free veinlets. This suggests the veinlets are carbonatitic. The middle (ii) and outer (iii) layer of glass in the melt inclusion consist of the Fe-poor and Fe-rich varieties of the common Si-Mg-Fe glass, respectively. The Fe-poor glass is composed of 5.14 wt% FeO. The outer Fe-rich layer is composed of 8.45 wt% FeO (Table 11).

Two additional glass varieties (iv–v) form within the globular structures on the margins of the melt inclusion (ROM 264 MI1) (Fig. 3.10). These structures are circular in shape and also exhibit a concentric distribution of phases. The interior consists of kassite (Chapter 4.3.4). The middle layer consists of a Ca-Si glass (iv) and minor amounts of calcite (Fig. 4.4). The outer layer comprises of a Ca-Ti glass (v) (Fig. 4.4). The Ca-Si (iv) glass is composed of 3.76–6.81 wt% SiO_2, 66.75–75.21 wt% CaO, and a minor TiO_2 (1.4–2.9 wt%) and FeO (2.04–4.08 wt%) component. In comparison the Ca-Ti (v) glass is composed of more SiO_2 (24.82–26.92 wt%), TiO_2 (7.33–15.2 wt%), and FeO (14.19–20.88 wt%) with less CaO (32.21–34.15 wt%) (Table 13). The variation in major element composition is also visible in an element map (Fig. 4.4). In a ternary plot of SiO_2, FeO + MgO, and CaO + TiO_2 the composition of the five glass varieties (i–v) form a continuum from silicate-rich to carbonate-rich (Fig. 4.5), similar to the trend observed in bulk compositions (Fig. 4.3). The glass varieties form a trend towards calcite, perovskite and kassite, and not the ilmenite megacryst (Fig. 4.5). A binary plot also reveals an inversely proportional trend between SiO_2 and CaO (Fig. 4.5), similar to that observed for the bulk compositions of the melt inclusions (Fig. 4.3).

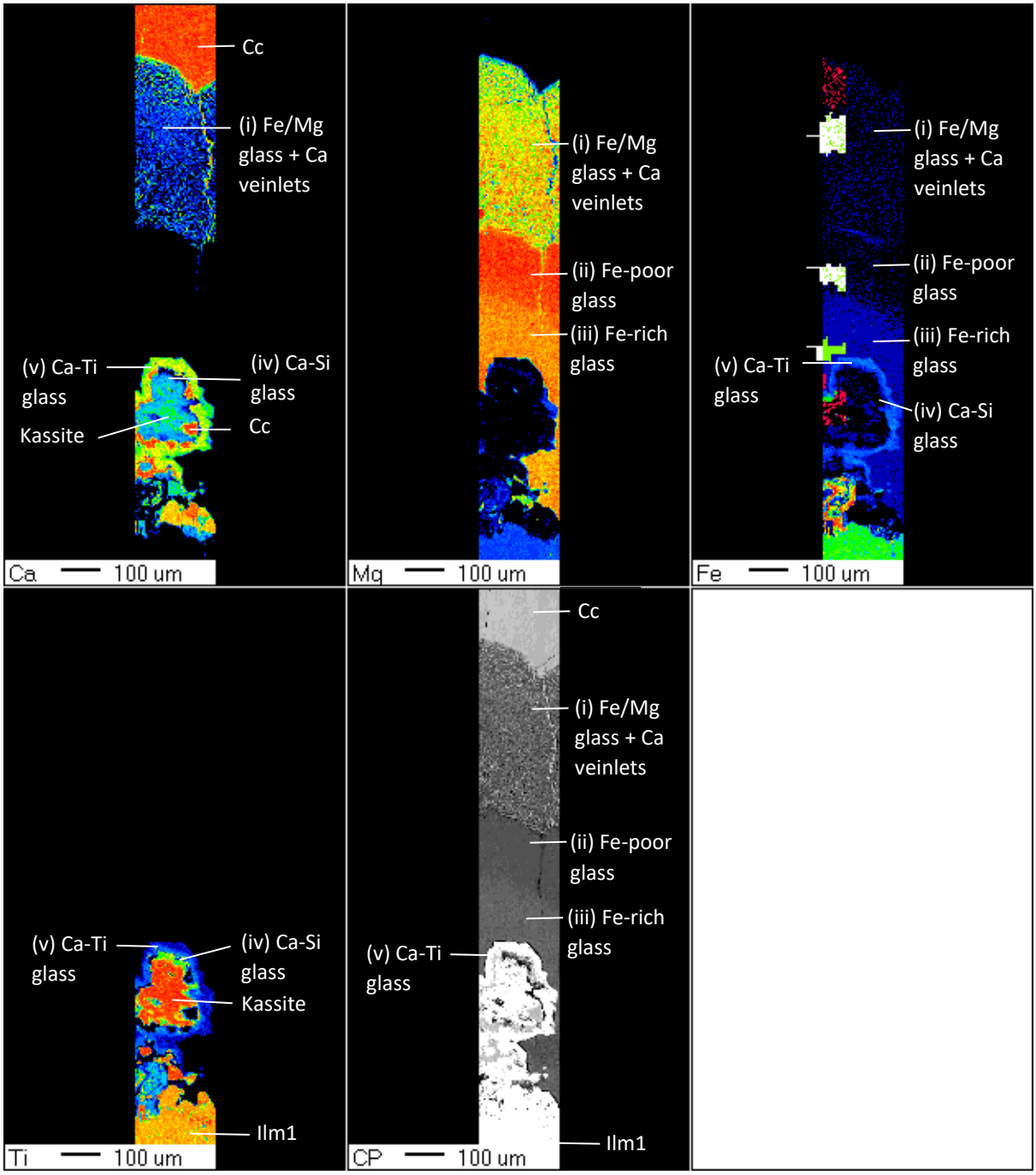

Fig. 4.4. Element map of sample ROM 264 MI1. The glass and mineral phases form a concentric structure within the melt inclusion (Fig. 3.10). The element map was performed from the centre of the MI (composed of calcite (Cc)) to the margins of the MI (Ilm1) showing the compositional variations of the five glass varieties (i–v).

Table 11
EPMA analysis of glass in sample ROM 264 (Fig. 3.10; Fig. 4.4).

Site	ROM 264_MI1_1	ROM 264_MI1_2
Comment	(iii) Fe-rich	(ii) Fe-poor
Al_2O_3	0.41	0.32
SiO_2	42.11	42.03
Cl	0.00	0.00
TiO_2	0.34	0.36
Na_2O	0.00	0.00
MgO	34.97	38.24
SO_3	0.00	0.00
FeO	8.45	5.14
NiO	0.00	0.00
MnO	0.00	0.00
F	0.00	0.48
K_2O	0.00	0.00
CaO	0.00	0.18
Cr_2O_3	0.00	0.00
H_2O	13.54	13.20
Total	100.00	100.00

Table 12
EPMA analysis of the heterogenous zone (i) in sample ROM 264 (Fig. 3.10; Fig. 4.4).

Site	ROM 264 MI1_HZ 1	ROM 264 MI1_ HZ 2	ROM 264 MI1_ HZ 3	ROM 264 MI1_ HZ 4	ROM 264 MI1_ HZ 5	ROM 264 MI1_ HZ 6	ROM 264 MI1_ HZ 7	ROM 264 MI1_ HZ 8	ROM 264 MI1_ HZ 9	ROM 264 MI1_HZ 10
	(i) Fe/Mg glass + Ca	(i) Fe/Mg glass + Ca	(i) Fe/Mg glass + Ca	(i) Fe/Mg glass + Ca	(i) Fe/Mg glass + Ca	(i) Fe/Mg glass + Ca	(i) Fe/Mg glass + Ca	(i) Fe/Mg glass + Ca	(i) Fe/Mg glass + Ca	(i) Fe/Mg glass + Ca
Comment	veinlets	veinlets	veinlets	veinlets	veinlets	veinlets	veinlets	veinlets	veinlets	veinlets
Al_2O_3	0.40	0.38	0.27	2.23	0.91	0.19	1.00	0.29	4.22	0.26
SiO_2	38.40	36.81	27.49	31.20	36.27	19.36	29.83	31.31	33.43	28.60
TiO_2	0.00	0.00	0.00	2.81	1.54	0.22	2.67	0.32	1.45	0.00
Na_2O	0.00	0.00	0.00	0.00	0.00	0.00	0.00	0.00	0.00	0.00
MgO	33.66	32.59	24.91	26.13	30.35	17.86	24.88	25.93	24.56	26.93
FeO	5.06	5.32	3.57	7.01	6.37	2.36	6.81	4.41	6.56	3.84
NiO	0.00	0.00	0.00	0.19	0.00	0.00	0.00	0.00	0.00	0.00
MnO	0.00	0.00	0.00	0.00	0.00	0.00	0.00	0.00	0.00	0.00
CaO	6.46	8.25	22.03	1.58	6.67	32.50	2.78	16.32	3.97	19.85
K_2O	0.00	0.00	0.00	0.00	0.00	0.00	0.00	0.00	0.00	0.00
Cr_2O_3	0.00	0.00	0.00	0.00	0.00	0.00	0.00	0.00	0.00	0.00
H_2O	15.90	16.27	21.63	28.76	17.75	27.27	31.73	21.37	25.53	20.30
Total	100.00	100.00	100.00	100.00	100.00	100.00	100.00	100.00	100.00	100.00

Table 13
EDS analysis of glass varieties (iv) and (v) in sample ROM 264 MI1 (Fig. 3.10; Fig. 4.4).

Analysis	(v) Ca-Ti glass 1	(v) Ca-Ti glass 2	(v) Ca-Ti glass 3	(v) Ca-Ti glass 4	(v) Ca-Ti glass 5	(v) Ca-Ti glass 6	(v) Ca-Ti glass 7	(v) Ca-Ti glass 8	(v) Ca-Ti glass 9	(v) Ca-Ti glass 10	(iv) Ca-Si glass 1	(iv) Ca-Si glass 2
Na_2O	0.04	0.00	0.04	0.04	0.08	0.20	0.02	0.00	0.31	0.00	0.00	0.00
MgO	0.21	0.35	0.15	0.15	0.08	0.29	0.14	0.30	0.15	0.62	7.34	2.61
Al_2O_3	0.04	0.08	0.00	0.30	0.08	0.26	0.25	0.10	0.08	0.02	0.00	0.00
SiO_2	22.22	22.12	22.01	23.40	23.24	22.83	23.39	23.66	23.64	21.80	5.98	3.30
P_2O_5	0.00	0.00	0.00	0.00	0.00	0.21	0.02	0.03	0.05	0.00	0.00	0.00
SO_3	0.07	0.00	0.00	0.00	0.00	0.04	0.01	0.00	0.00	0.01	0.11	0.00
K_2O	0.07	0.00	0.01	0.00	0.01	0.00	0.01	0.00	0.04	0.00	0.00	0.04
CaO	28.84	28.76	28.75	28.31	28.58	28.29	28.33	28.52	28.37	30.00	58.67	66.07
TiO_2	11.46	12.92	13.35	6.60	10.50	9.44	7.03	6.44	7.40	11.25	1.27	2.56
Cr_2O_3	0.00	0.00	0.00	0.01	0.00	0.17	0.06	0.02	0.07	0.00	0.03	0.00
MnO	0.14	0.16	0.01	0.09	0.05	0.06	0.07	0.10	0.08	0.00	0.00	0.34
FeO	13.78	12.46	12.59	18.35	14.52	15.48	17.53	18.03	17.10	13.60	3.58	1.80
NiO	0.09	0.09	0.05	0.00	0.07	0.00	0.09	0.00	0.00	0.00	0.00	0.00
SrO	0.00	0.00	0.00	0.00	0.00	0.00	0.00	0.10	0.00	0.00	0.32	0.33
Volat	22.70	22.70	22.70	22.70	22.70	22.70	22.70	22.70	22.70	22.70	22.70	22.70
Total	100.00	100.00	100.00	100.00	100.00	100.00	100.00	100.00	100.00	100.00	100.00	100.00

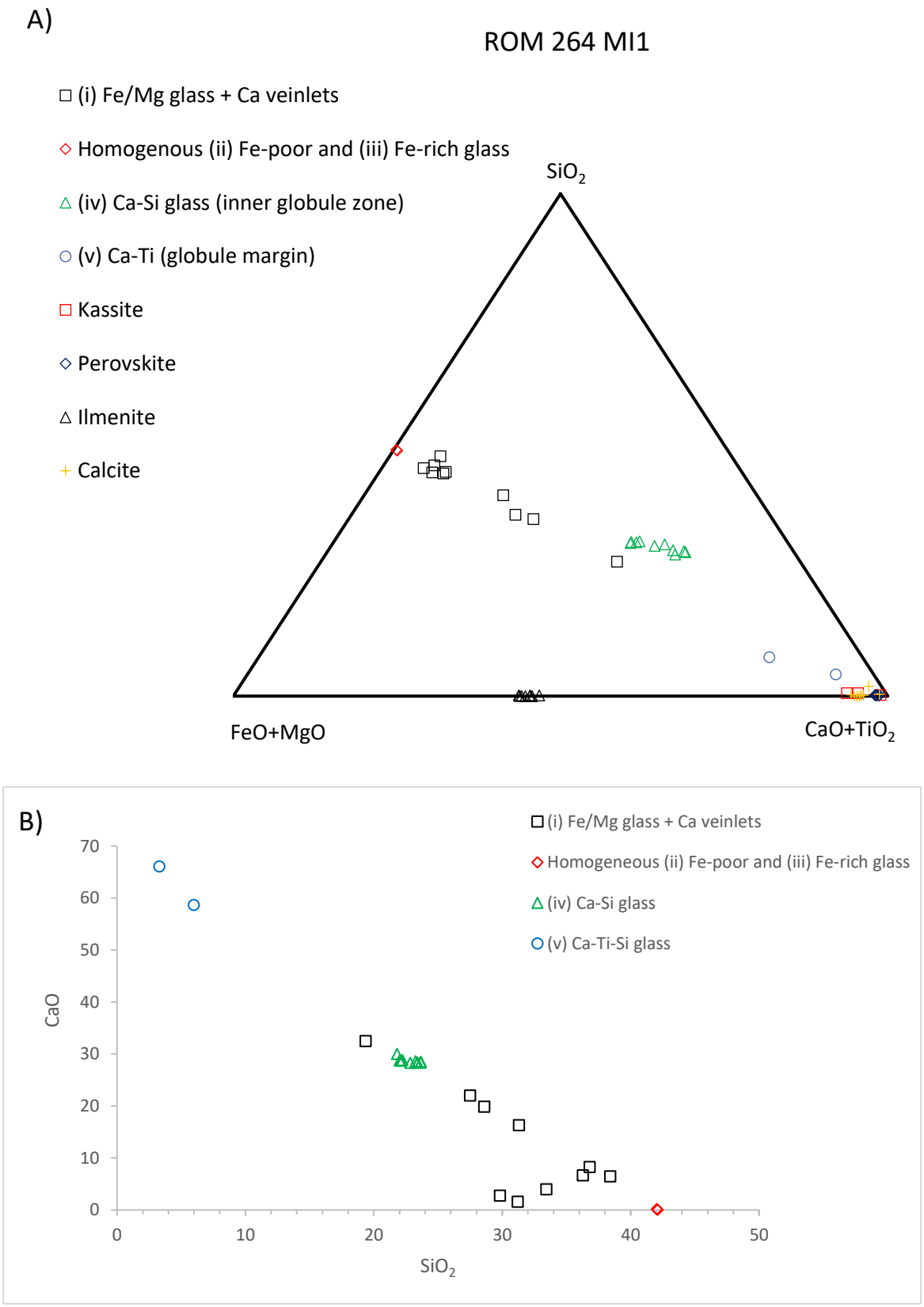

Fig. 4.5. A) Ternary diagram of the five glass varieties (i–v), kassite, perovskite, calcite, and the host ilmenite megacryst in sample ROM 264 MI1 (Fig. 3.10). All analyses, except the host ilmenite megacryst, plot with a linear array from Si-Fe-Mg glass-like compositions to a CaO + TiO_2-rich composition. B) SiO_2 versus CaO binary

diagram of the five glass varieties hosted within MI1 of sample ROM264. The glass varieties form an inversely proportional linear trend in terms of SiO_2 and CaO.

Glass pools in MI1 of sample S5628 show two types: a Fe-rich variety, and an Fe-poor variety of glass. This form of heterogeneity is common throughout all samples. The heterogeneity of glass in this sample is also evident in BSE images (Fig 3.5) which show variations in BSE signal intensity within glass pools. The majority of glass forms the Fe-poor variety, with patches of Fe-rich glass that exhibit a lighter BSE signal intensity (Fig 3.5). The Fe-poor glass has a composition of 4.25–5.67 wt% FeO and the Fe-rich glass has a composition of 7.2–11.2 wt% FeO (Table 14). EPMA of the Fe-poor glass reveals a similar composition of 3.16–3.86 wt% FeO (Table 15). MI2–MI6 of the same inclusion host glass in low modal abundances (Table 1). EDS analysis produced results which have a uniquely Al_2O_3-rich (7.78–9.46 wt% Al_2O_3) and a Fe-rich composition (15.0–17.01 wt% FeO) (Table 16). The texture and composition of glass in MI2–MI6 is homogenous in comparison to MI1.

Table 14
EDS analysis of glass in sample S5628 MI1 (Fig. 3.5).

Site	Det1	Det1	Det1	Det1	Det1	Det1	Det1	Det1	Det1	Det2	Det2	Det2
Comment	Fe-poor	Fe-poor	Fe-rich	Fe-rich	Fe-poor	Fe-rich	Fe-rich	Fe-poor	Fe-rich	Fe-poor	Fe-poor	Fe-poor
Analysis	Gl1	Gl2	Gl3	Gl4	Gl5	Gl6	Gl7	Gl8	Gl10	Gl1	Gl2	Gl3
Na_2O	0.70	1.42	0.80	1.03	1.53	0.87	0.88	1.14	0.38	1.34	0.86	0.75
MgO	41.58	40.39	42.19	42.25	40.55	41.65	42.07	41.03	33.90	39.62	39.79	39.58
Al_2O_3	1.10	1.32	0.95	0.68	1.51	0.98	0.92	1.20	5.41	1.37	1.50	1.18
SiO_2	37.74	37.33	34.75	33.48	37.26	35.18	34.66	38.03	34.75	37.30	37.75	37.99
P_2O_5	0.00	0.02	0.11	0.02	0.00	0.00	0.02	0.04	0.00	0.10	0.00	0.07
SO_3	0.02	0.06	0.00	0.02	0.02	0.04	0.04	0.11	0.00	0.07	0.05	0.06
K_2O	0.00	0.02	0.04	0.06	0.04	0.00	0.02	0.06	0.00	0.03	0.03	0.06
CaO	0.19	0.34	0.07	0.17	0.35	0.12	0.08	0.19	0.20	0.42	0.38	0.45
TiO_2	0.23	0.30	0.48	0.55	0.23	0.33	0.51	0.30	0.16	0.20	0.17	0.17
Cr_2O_3	0.00	0.06	0.02	0.09	0.00	0.00	0.00	0.00	0.02	0.25	0.17	0.46
MnO	0.00	0.00	0.00	0.00	0.00	0.00	0.00	0.00	0.00	0.02	0.00	0.00
FeO	4.52	4.70	6.86	7.92	4.74	6.87	7.04	4.20	10.75	5.33	5.43	5.19
NiO	0.23	0.34	0.02	0.04	0.08	0.27	0.06	0.00	0.73	0.22	0.16	0.22
SrO	0.00	0.00	0.00	0.00	0.00	0.00	0.00	0.00	0.00	0.00	0.00	0.13
Volat*	13.70	13.70	13.70	13.70	13.70	13.70	13.70	13.70	13.70	13.70	13.70	13.70
Total	100.00	100.00	100.00	100.00	100.00	100.00	100.00	100.00	100.00	100.00	100.00	100.00

*volatile values are the average of those produced by EPMA analyses (calculated by difference from oxide totals).

Table 15
EPMA analysis of Fe-poor glass in sample S5628 MI1 (Fig. 3.5).

Site	S5628_MI1_1	S5628_MI1_2	S5628_MI1_3	S5628_MI1_4	S5628_MI1_5	S5628_MI1_6	S5628_MI1_7	S5628_MI1_8
Al_2O_3	1.48	1.65	1.73	1.80	1.70	1.37	1.17	1.51
SiO_2	41.06	42.06	41.96	41.10	41.56	41.30	41.81	41.36
Cl	0.00	0.00	0.00	0.00	0.00	0.00	0.00	0.00
TiO_2	0.00	0.00	0.27	0.00	0.00	0.00	0.00	0.36
Na_2O	0.24	0.43	0.29	0.30	0.00	0.20	0.25	0.35
MgO	38.15	37.99	37.33	37.40	37.23	37.76	37.75	39.24
SO_3	0.00	0.00	0.00	0.00	0.00	0.00	0.00	0.00
FeO	3.65	3.86	3.71	4.00	3.90	3.65	3.74	3.95
NiO	0.00	0.00	0.00	0.28	0.25	0.00	0.00	0.00
MnO	0.00	0.00	0.00	0.00	0.00	0.00	0.00	0.00
F	0.00	0.65	0.00	0.00	0.00	0.00	0.00	0.00
K_2O	0.00	0.00	0.00	0.00	0.00	0.00	0.00	0.00
CaO	0.39	0.31	0.34	0.36	0.27	0.31	0.40	0.48
Cr_2O_3	0.00	0.00	0.00	0.00	0.00	0.00	0.00	0.00
H_2O	14.25	12.64	14.01	13.94	14.20	14.84	14.50	12.20
Total	100.00	100.00	100.00	100.00	100.00	100.00	100.00	100.00

Table 16
EDS analysis of glass in MI2 and MI3 of sample S5628.

Site	MI2	MI2	MI3	MI3
Analysis	Gl1	Gl2	Gl1	Gl2
Na_2O	0.43	0.63	1.25	0.45
MgO	29.36	26.61	28.28	28.55
Al_2O_3	8.17	7.46	9.36	9.07
SiO_2	31.96	32.92	30.54	30.31
P_2O_5	0.10	0.25	0.00	0.16
SO_3	0.03	0.06	0.06	0.04
K_2O	0.13	0.11	0.08	0.09
CaO	0.84	1.16	0.54	0.64
TiO_2	0.46	0.52	0.65	0.60
Cr_2O_3	0.14	0.00	0.09	0.00
MnO	0.09	0.06	0.05	0.19
FeO	14.38	16.35	15.39	15.91
NiO	0.04	0.14	0.02	0.00
SrO	0.16	0.04	0.00	0.29
Volat*	13.70	13.70	13.70	13.70
Total	100.00	100.00	100.00	100.00

*volatile values are the average of those produced by EPMA analyses (calculated by difference from oxide totals).

Sample S5251 MI2 hosts glass which also forms two distinct varieties: (i) a glass matrix and (ii) isometric glass domains. The isometric glass domains are Fe-rich and consist of 8.14–12.28 wt% FeO (Table 17; Fig. 4.7). The glass matrix is Fe-poor and consists of 3.46–6.35 wt% FeO (Table 18). The glass matrix and isometric glass domains are compositional equivalents of the common Fe-poor and Fe-rich varieties of glass, respectively. However, texturally, the isometric glass domains share a sharp contact with the glass matrix, in contrast to the diffuse boundary observed between the common Fe-poor and Fe-rich varieties. The textural features of the isometric glass domains and the glass matrix are observable in PPL (Chapter 3.3.4) and BSE images (Fig 3.7), and the compositional variations are shown in an element map (Fig. 4.6) and a ternary diagram (Fig. 4.7).

Table 17
EDS analysis of Fe-rich glass in sample S5251 MI2 (Fig. 3.7; Fig. 4.6).

Site	Det1	Det1	Det1	Det1	Det1	Det1	Det2	Det2
Analysis	Gl1	Gl2	Gl7	Gl8	Gl16	Gl14	Gl1	Gl2
Na_2O	0.24	0.06	0.19	0.11	0.05	0.25	0.46	0.19
MgO	33.20	34.98	33.26	33.66	32.28	31.98	30.55	31.90
Al_2O_3	1.02	1.14	0.78	0.47	0.60	0.70	0.64	1.15
SiO_2	38.32	40.20	39.56	39.45	38.07	38.27	38.43	38.53
P_2O_5	0.00	0.08	0.07	0.11	0.00	0.01	0.15	0.06
SO_3	0.06	0.02	0.00	0.33	0.02	0.13	0.06	0.27
K_2O	0.14	0.03	0.00	0.04	0.05	0.12	0.02	0.06
CaO	0.20	0.07	0.16	0.09	0.10	0.07	0.39	0.06
TiO_2	0.72	0.83	0.57	0.26	0.49	0.57	1.76	0.64
Cr_2O_3	0.00	0.00	0.07	0.00	0.13	0.07	0.02	0.05
MnO	0.12	0.12	0.13	0.03	0.11	0.04	0.15	0.00
FeO	11.63	7.81	10.93	11.50	14.16	13.87	13.29	13.08
NiO	0.45	0.23	0.13	0.17	0.08	0.17	0.31	0.00
SrO	0.00	0.38	0.03	0.00	0.00	0.00	0.01	0.00
Volat*	13.70	13.70	13.70	13.70	13.70	13.70	13.70	13.70
Total	100.00	100.00	100.00	100.00	100.00	100.00	100.00	100.00

*volatile values are the average of those produced by EPMA analyses (calculated by difference from oxide totals).

Table 17 continued

EDS analysis of Fe-rich glass in sample S5251 MI2 (Fig. 3.7; Fig. 4.6).

Site	Det2	Det2	Det2	Det2	Det2	Det2	Det2	Det2
Analysis	Gl11	Gl12	Gl13	Gl14	Gl15	Gl7	Gl9	Gl17
Na_2O	0.29	0.24	0.21	0.00	0.35	0.61	0.16	0.58
MgO	32.76	34.52	34.68	33.14	32.64	37.01	35.46	31.44
Al_2O_3	0.45	0.04	0.93	0.35	0.96	0.94	0.34	0.81
SiO_2	36.97	39.71	40.24	38.72	38.43	31.74	40.92	39.43
P_2O_5	0.01	0.09	0.14	0.35	0.16	0.39	0.21	0.06
SO_3	0.22	0.14	0.07	0.04	0.14	0.14	0.14	0.07
K_2O	0.00	0.12	0.03	0.00	0.09	0.05	0.07	0.04
CaO	0.20	0.08	0.13	0.01	0.09	0.23	0.01	0.14
TiO_2	0.54	0.17	0.39	0.46	0.41	0.56	0.35	0.42
Cr_2O_3	0.05	0.07	0.00	0.02	0.06	0.00	0.00	0.00
MnO	0.14	0.00	0.01	0.15	0.10	0.23	0.00	0.07
FeO	14.35	11.02	9.27	12.71	12.22	13.05	7.11	13.21
NiO	0.09	0.00	0.15	0.15	0.00	0.23	0.14	0.00
SrO	0.00	0.09	0.00	0.06	0.43	0.64	0.00	0.03
Volat*	13.70	13.70	13.70	13.70	13.70	13.70	13.70	13.70
Total	100.00	100.00	100.00	100.00	100.00	100.00	100.00	100.00

*volatile values are the average of those produced by EPMA analyses (calculated by difference from oxide totals).

Table 18

EDS analysis of Fe-poor glass in sample S5251 MI2 (Fig. 3.7; Fig. 4.6).

	MI2	MI2	MI2	MI2	MI2	MI2	MI2	MI2
Site	Det1	Det1	Det1	Det1	Det1	Det1	Det1	Det1
Analysis	Gl9	Gl10	Gl11	Gl12	Gl13	Gl3	Gl4	Gl5
Na_2O	0.81	0.14	0.79	0.42	0.84	0.66	0.49	0.95
MgO	35.14	36.56	35.83	36.53	35.67	36.16	35.92	35.01
Al_2O_3	0.56	1.31	0.63	0.40	0.59	0.13	0.42	0.79
SiO_2	43.17	39.21	43.52	42.97	44.69	45.52	44.03	44.17
P_2O_5	0.17	0.06	0.08	0.06	0.04	0.05	0.19	0.28
SO_3	0.33	0.17	0.07	0.00	0.05	0.06	0.16	0.03
K_2O	0.08	0.00	0.06	0.04	0.17	0.00	0.00	0.16
CaO	0.11	0.02	0.08	0.05	0.02	0.13	0.15	0.15
TiO_2	0.08	1.95	0.20	0.08	0.03	0.22	0.25	0.21
Cr_2O_3	0.03	0.00	0.00	0.02	0.00	0.05	0.04	0.00
MnO	0.00	0.14	0.00	0.13	0.00	0.00	0.00	0.05
FeO	5.33	6.56	4.68	5.48	4.09	2.99	4.07	4.34
NiO	0.16	0.06	0.00	0.00	0.00	0.16	0.26	0.00
SrO	0.21	0.06	0.05	0.00	0.00	0.17	0.07	0.00
Volat*	13.70	13.70	13.70	13.70	13.70	13.70	13.70	13.70
Total	100.00	100.00	100.00	100.00	100.00	100.00	100.00	100.00

*volatile values are the average of those produced by EPMA analyses (calculated by difference from oxide totals).

Table 18 continued

EDS analysis of Fe-poor glass in sample S5251 MI2 (Fig. 3.7; Fig. 4.6).

	MI2	MI2	MI2	MI2	MI2	MI2	MI2	MI2
Site	Det1	Det2	Det2	Det2	Det2	Det2	Det2	Det2
Analysis	Gl6	Gl3	Gl4	Gl16	Gl5	Gl6	Gl8	Gl10
Na_2O	0.60	0.39	0.41	0.23	0.29	1.09	0.49	0.27
MgO	36.42	35.19	35.42	38.20	36.12	38.74	34.69	37.22
Al_2O_3	0.27	0.63	0.43	1.40	0.36	0.78	1.35	1.39
SiO_2	43.67	43.93	44.15	41.76	43.53	39.81	44.33	41.74
P_2O_5	0.15	0.00	0.00	0.16	0.03	0.00	0.05	0.00
SO_3	0.24	0.20	0.51	0.00	0.11	0.19	0.16	0.11
K_2O	0.01	0.02	0.03	0.02	0.09	0.07	0.11	0.08
CaO	0.10	0.21	0.15	0.01	0.12	0.34	0.26	0.04
TiO_2	0.18	0.29	0.11	0.42	0.40	0.37	0.34	0.39
Cr_2O_3	0.00	0.00	0.18	0.02	0.00	0.11	0.00	0.00
MnO	0.00	0.05	0.00	0.00	0.02	0.14	0.00	0.01
FeO	4.46	5.14	4.82	3.82	4.92	3.98	4.43	4.55
NiO	0.06	0.00	0.04	0.09	0.00	0.15	0.00	0.04
SrO	0.00	0.00	0.00	0.17	0.00	0.00	0.00	0.00
Volat*	13.70	13.70	13.70	13.70	13.70	13.70	13.70	13.70
Total	100.00	100.00	100.00	100.00	100.00	100.00	100.00	100.00

*volatile values are the average of those produced by EPMA analyses (calculated by difference from oxide totals).

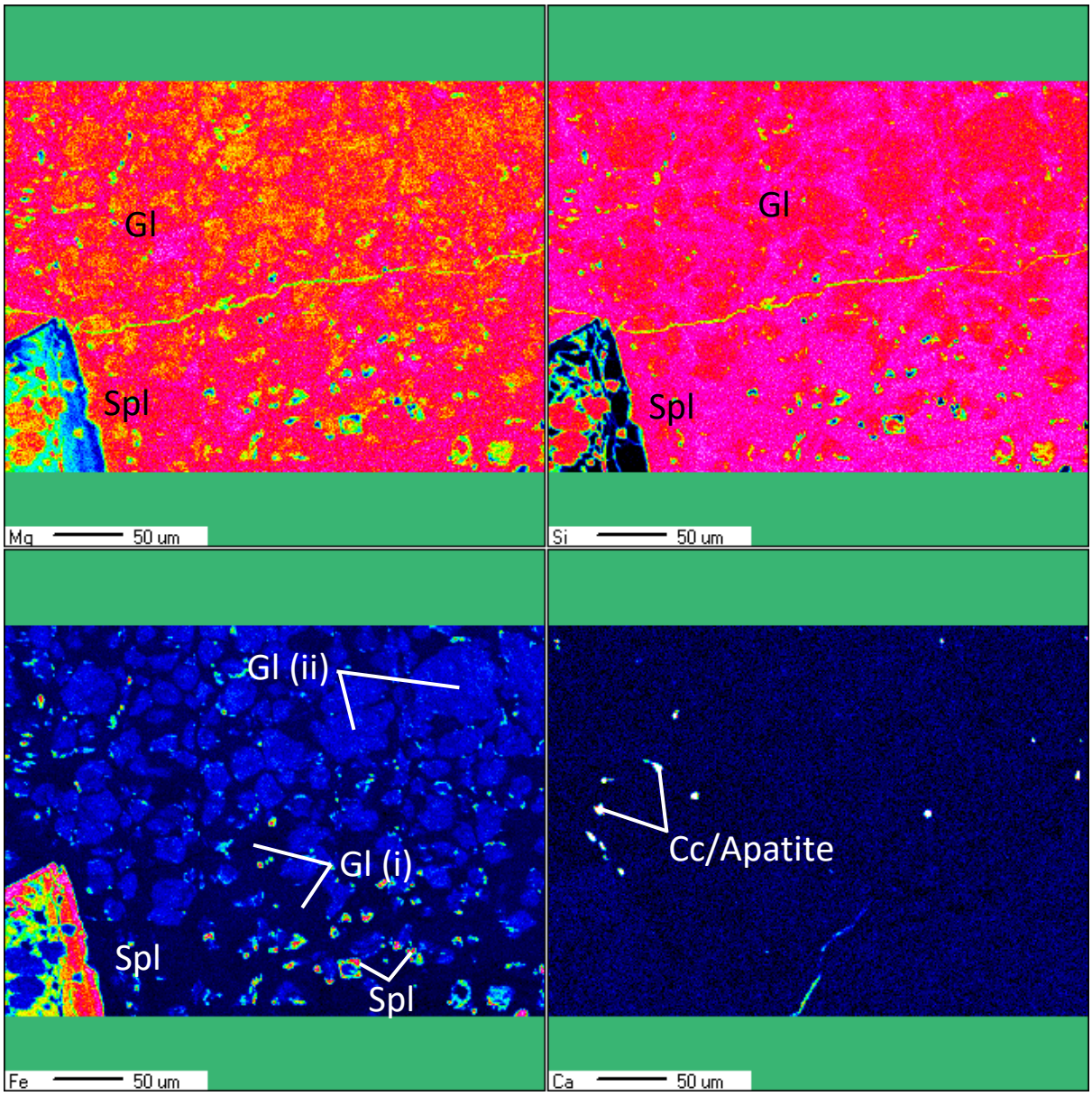
Gl
Spl
Mg 50 um
Gl
Spl
Si 50 um
Gl (ii)
Gl (i)
Spl
Spl
Fe 50 um
Cc/Apatite
Ca 50 um

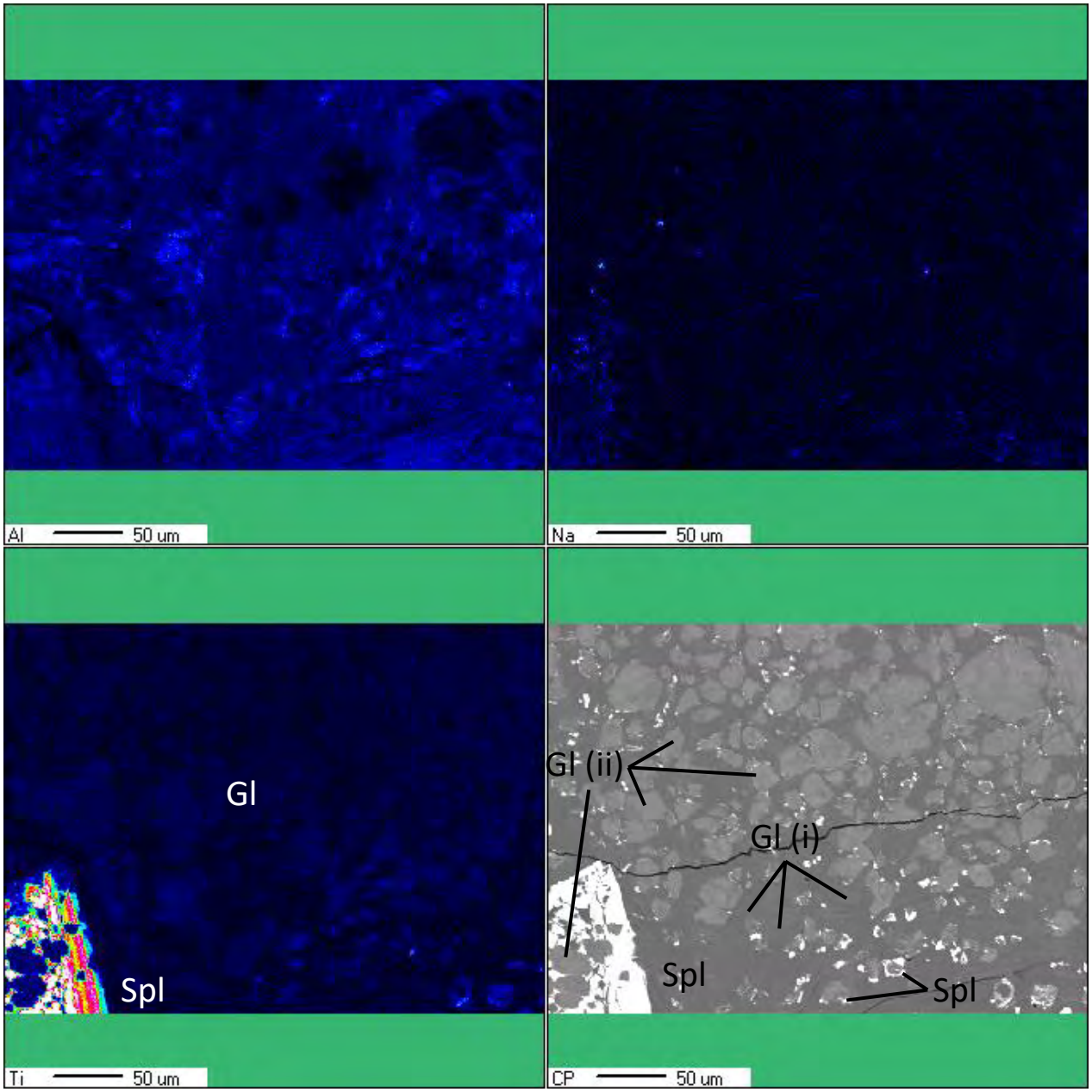

Fig. 4.6. Element maps of glass in sample S5251 MI2. The melt inclusion hosts a large spinel grain (Spl) which varies in Ti, Fe, and Mg from core to rim. Spinel also forms at the interface of two glass varieties (Gl (i) and Gl (ii)) which vary in Fe-Mg-Si. Fine-grained Ca-rich phases possibly represent calcite (Cc) or apatite.

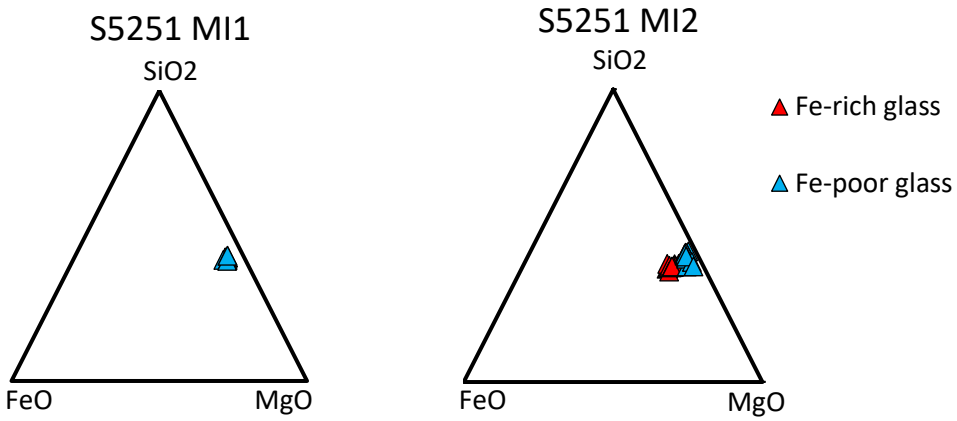

Fig. 4.7. Ternary diagram of glass in sample S5251 MI1 and MI2. Glass is heterogenous in texture in both melt inclusions, forming isometric domains set within a glass matrix. Compositionally, the glass in MI1 is homogenous and the glass in MI2 is heterogenous, forming an Fe-rich and Fe-poor variety. The glass is MI1 is of the Fe-poor variety compared to glass hosted in MI2.

MI1 of the same sample similarly hosts glass which forms isometric glass domains set within a glass matrix (Fig. 3.15). However, the compositional variation between the textural varieties is less discernible. BSE images of the glass show little variation in their BSE signal intensities (Fig 3.6). EDS analysis of the glass reveals a similar composition between the two textural varieties, with FeO contents 6–9 wt% (Table 19; Fig. 4.7).

Table 19
EDS analysis of glass in sample S5251 MI1 (Fig. 3.6).

Analysis	Gl1	Gl2	Gl3	Gl4	Gl5	Gl6	Gl7	Gl8	Gl9	Gl(Ca)
Na_2O	0.27	0.12	0.37	0.57	0.34	0.22	0.30	0.18	0.29	0.75
MgO	34.70	35.20	33.29	33.26	33.80	35.04	34.67	34.91	34.84	33.45
Al_2O_3	1.29	0.92	1.07	1.01	0.82	0.87	0.79	1.08	0.61	1.22
SiO_2	42.22	42.01	41.40	41.30	41.41	41.48	43.20	41.11	43.35	41.42
P_2O_5	0.17	0.15	0.36	0.12	0.02	0.00	0.00	0.22	0.00	0.29
SO_3	0.00	0.00	0.20	0.18	0.12	0.20	0.18	0.11	0.30	0.06
K_2O	0.00	0.00	0.12	0.04	0.07	0.02	0.00	0.07	0.07	0.00
CaO	0.29	0.15	1.65	1.66	0.23	0.11	0.32	0.22	0.19	2.19
TiO_2	0.20	0.18	0.12	0.18	0.24	0.25	0.10	0.30	0.12	0.20
Cr_2O_3	0.08	0.00	0.03	0.01	0.00	0.04	0.03	0.08	0.00	0.16
MnO	0.02	0.11	0.00	0.14	0.00	0.18	0.10	0.07	0.00	0.03
FeO	6.58	7.18	7.37	7.53	8.91	7.34	6.46	7.61	6.43	6.36
NiO	0.10	0.00	0.00	0.24	0.06	0.00	0.05	0.08	0.03	0.06
SrO	0.25	0.14	0.00	0.00	0.00	0.00	0.00	0.02	0.00	0.00
Volat*	13.70	13.70	13.70	13.70	13.70	13.70	13.70	13.70	13.70	13.70
Total	100.00	100.00	100.00	100.00	100.00	100.00	100.00	100.00	100.00	100.00

*volatile values are the average of those produced by EPMA analyses (calculated by difference from oxide totals).

Glass is also observed to be compositionally homogenous within a melt inclusion. For example, EDS analysis of sample S5626 MI1–MI3 reveals the glass is compositionally and texturally (Chapter 3.3.1) homogenous within and between melt inclusions of this sample. This is also observed in BSE images which show little variation in BSE signal intensity within coherent glass pools (Fig 3.2; Fig. 3.3). The glass is similar in composition to the Fe-poor variety of heterogenous glass observed in other melt inclusions (Table 18). The glass is composed of SiO_2 (46.76–47.64 wt%), MgO (37.99–39.88 wt%), FeO (1.35–2.6 wt%), with minor amounts of Al_2O_3 (0.65–2.39 wt%) and TiO_2 (0.09–0.25) (Table 20; Table 21).

Table 20
EDS analysis of glass in sample S5626 MI1 (Fig. 3.2; Fig. 3.3).

	MI1	MI1	MI1	MI1	MI1	MI1	MI1	MI1	MI1	MI1	MI1	MI1
Site	Det1	Det1	Det1	Det1	Det2	Det2	Det2	Det2	Det2	Det2	Det2	Det2
Analysis	Gl1	Gl2	Gl3	Gl4	Gl1	Gl1	Gl2	Gl4	Gl5	Gl6	Gl7	Gl8
Na_2O	0.00	0.00	0.04	0.00	0.05	0.00	0.00	0.00	0.06	0.02	0.05	0.05
MgO	37.34	37.30	36.77	37.13	36.80	37.25	37.34	37.20	37.01	36.43	35.41	38.13
Al_2O_3	0.78	0.92	1.32	0.95	0.97	0.90	0.84	0.90	0.62	0.80	2.15	0.76
SiO_2	45.35	45.54	45.30	45.40	45.35	45.33	45.37	45.40	43.70	45.71	44.42	45.45
P_2O_5	0.03	0.08	0.06	0.00	0.13	0.14	0.17	0.09	0.00	0.04	0.03	0.00
SO_3	0.04	0.10	0.09	0.19	0.16	0.16	0.12	0.36	0.50	0.30	0.31	0.00
K_2O	0.10	0.03	0.29	0.01	0.05	0.03	0.05	0.05	0.00	0.06	0.34	0.03
CaO	0.18	0.06	0.19	0.23	0.56	0.18	0.13	0.33	3.21	0.27	0.37	0.29
TiO_2	0.24	0.22	0.22	0.14	0.13	0.26	0.15	0.19	0.06	0.22	0.31	0.14
Cr_2O_3	0.00	0.16	0.13	0.07	0.09	0.06	0.10	0.19	0.00	0.00	0.18	0.11
MnO	0.00	0.03	0.03	0.00	0.00	0.00	0.00	0.00	0.08	0.03	0.00	0.00
FeO	1.96	1.87	1.78	2.15	1.98	1.99	1.93	1.56	0.99	2.37	2.60	1.35
NiO	0.20	0.00	0.06	0.02	0.02	0.00	0.11	0.02	0.06	0.05	0.13	0.00
SrO	0.10	0.00	0.00	0.00	0.00	0.00	0.00	0.00	0.00	0.00	0.00	0.00
Volat*	13.70	13.70	13.70	13.70	13.70	13.70	13.70	13.70	13.70	13.70	13.70	13.70
Total	100.00	100.00	100.00	100.00	100.00	100.00	100.00	100.00	100.00	100.00	100.00	100.00

*volatile values are the average of those produced by EPMA analyses (calculated by difference from oxide totals).

Table 21
EDS analysis of glass in sample S5626 MI2 and MI3 (Fig. 3.2; Fig. 3.3).

Site	MI2	MI3	MI3	MI3	MI3	MI3	MI3
Analysis	Gl1	Gl1	Gl2	Gl3	Gl4	Gl5	Gl6
Na_2O	0.16	0.07	0.11	0.04	0.01	0.04	0.17
MgO	37.35	38.24	37.34	37.28	37.70	37.43	37.01
Al_2O_3	0.97	0.56	1.07	0.92	0.78	0.92	1.11
SiO_2	45.53	45.44	45.17	45.68	45.57	44.99	44.84
P_2O_5	0.11	0.01	0.12	0.02	0.00	0.06	0.11
SO_3	0.10	0.30	0.29	0.19	0.35	0.10	0.24
K_2O	0.00	0.10	0.04	0.03	0.05	0.06	0.00
CaO	0.11	0.33	0.31	0.20	0.27	0.25	0.66
TiO_2	0.10	0.09	0.18	0.20	0.09	0.19	0.21
Cr_2O_3	0.06	0.02	0.11	0.00	0.00	0.00	0.03
MnO	0.05	0.02	0.00	0.09	0.08	0.08	0.00
FeO	1.68	1.12	1.49	1.66	1.41	2.17	1.76
NiO	0.06	0.00	0.06	0.01	0.00	0.00	0.17
SrO	0.00	0.00	0.00	0.00	0.00	0.00	0.00
Volat*	13.70	13.70	13.70	13.70	13.70	13.70	13.70
Total	100.00	100.00	100.00	100.00	100.00	100.00	100.00

*volatile values are the average of those produced by EPMA analyses (calculated by difference from oxide totals).

4.3.2 Secondary ilmenite

EPMA analysis of secondary ilmenite reveals that it is distinct in composition from the host ilmenite megacryst. Secondary ilmenite has a MgO content of <0.1 wt% (Table 22–Table 25), while megacrystic ilmenite has an MgO content of 7.1–12.6 wt% (Chapter 4.1). This is demonstrated by EPMA and EDS analysis of secondary ilmenite in sample P015 which has a composition of 0.02–0.09 wt% MgO (Table 22–Table 23), while megacrystic ilmenite of the same sample is composed of 7.45–9.93 wt% MgO (Chapter 4.1) (Fig. 4.8; Table 2–Table 4). Secondary ilmenite in this sample also has slightly higher TiO_2 (53.54–54.74 wt%) and similar FeO (45.42–46.56 wt%) (Table 22) content in comparison to megacrystic ilmenite (~50 wt% TiO_2; ~30 wt% FeO; ~12 wt% Fe_2O_3) (Table 2–Table 4). Secondary ilmenite also consists of minor Al_2O_3 (<0.04 wt%), MnO (0.57–0.88 wt%), CaO (<0.18 wt%), NiO (<0.06 wt%), and SiO_2 (<0.12 wt%) components and is Cr-poor (<0.05 wt%). Recalculation for optimal stoichiometric fit suggests that in secondary ilmenite all iron is ferrous. Secondary ilmenite in sample P015 is essentially ilmenite *s.s* (0.98–0.99), with only a minor pyrophanite (0.01–0.02) component (Table 22).

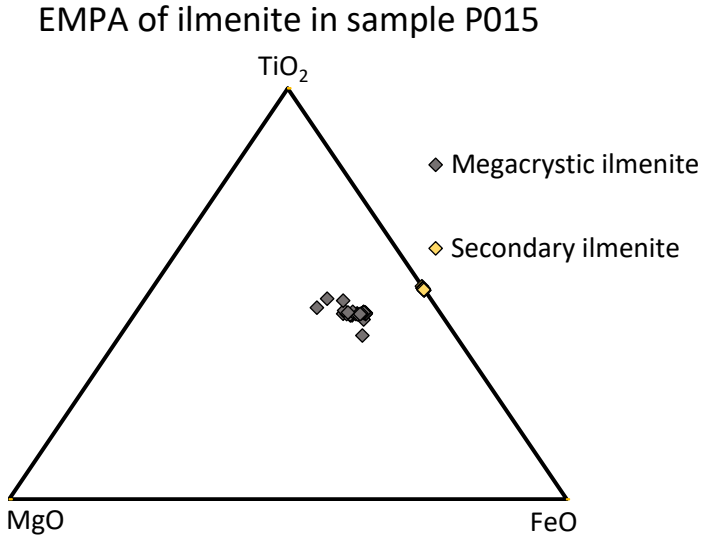

Fig. 4.8. Ternary diagram of secondary ilmenite in comparison to megacrystic ilmenite of sample P015. Note the difference in MgO composition. Secondary ilmenite is MgO-poor and is ilmenite *s.s*. In comparison, megacrystic ilmenite is more MgO-rich and contains of a significant geikielite component.

Table 22

EPMA analysis of secondary ilmenite in sample P015 (Fig. 3.12; Fig. 3.15).

	mi6	mi6	mi6	mi6	mi5	mi5	mi4	mi4	mi4	mi3	mi3	mi1
Site	ilm2	ilm3	ilm4	ilm5	ilm24	ilm25	ilm34	ilm35	ilm36	ilm42	ilm48	ilm54
SiO_2	0.12	0.11	0.05	0.08	0.00	0.09	0.09	0.02	0.00	0.01	0.09	0.22
Al_2O_3	0.01	0.00	0.00	0.00	0.00	0.00	0.03	0.02	0.00	0.00	0.04	0.02
Fe_2O_3	0.00	0.00	0.00	0.00	0.00	0.00	0.00	0.00	0.00	0.00	0.00	0.00
Cr_2O_3	0.05	0.02	0.00	0.03	0.00	0.00	0.03	0.00	0.02	0.00	0.00	0.00
TiO_2	53.78	53.55	54.19	53.99	54.74	54.30	53.86	53.68	54.26	53.62	53.97	52.92
FeO	46.56	46.18	45.97	46.33	45.66	46.17	45.99	45.42	46.08	45.64	46.43	45.88
MgO	0.09	0.07	0.05	0.06	0.04	0.07	0.05	0.02	0.06	0.06	0.07	0.09
MnO	0.56	0.64	0.71	0.78	0.71	0.62	0.88	0.81	0.73	0.68	0.67	0.60
CaO	0.02	0.03	0.07	0.16	0.02	0.01	0.03	0.04	0.14	0.18	0.00	0.02
NiO	0.00	0.06	0.02	0.02	0.00	0.01	0.00	0.00	0.00	0.00	0.00	0.00
Total	101.18	100.65	101.06	101.45	101.17	101.27	100.95	100.01	101.29	100.18	101.27	99.75
Cation proportions calculated for 3 O												
Si	0.00	0.00	0.00	0.00	0.00	0.00	0.00	0.00	0.00	0.00	0.00	0.01
Al	0.00	0.00	0.00	0.00	0.00	0.00	0.00	0.00	0.00	0.00	0.00	0.00
Fe^{3+}	0.00	0.00	0.00	0.00	0.00	0.00	0.00	0.00	0.00	0.00	0.00	0.00
Cr	0.00	0.00	0.00	0.00	0.00	0.00	0.00	0.00	0.00	0.00	0.00	0.00
Ti	1.01	1.01	1.01	1.01	1.02	1.01	1.01	1.01	1.01	1.01	1.01	1.00
Fe^{2+}	0.97	0.96	0.95	0.96	0.95	0.96	0.96	0.95	0.96	0.96	0.96	0.97
Mg	0.00	0.00	0.00	0.00	0.00	0.00	0.00	0.00	0.00	0.00	0.00	0.00
Mn	0.01	0.01	0.01	0.02	0.01	0.01	0.02	0.02	0.02	0.01	0.01	0.01
Ca	0.00	0.00	0.00	0.00	0.00	0.00	0.00	0.00	0.00	0.00	0.00	0.00
Ni	0.00	0.00	0.00	0.00	0.00	0.00	0.00	0.00	0.00	0.00	0.00	0.00
Total	1.99	1.99	1.99	1.99	1.98	1.99	1.99	1.99	1.99	1.99	1.99	1.99
Ti	1.01	1.01	1.01	1.01	1.02	1.01	1.01	1.01	1.01	1.01	1.01	1.00
Fe+Mg+Mn+Cr	0.98	0.98	0.97	0.98	0.96	0.97	0.98	0.97	0.97	0.97	0.98	0.98
Ilmenite	0.98	0.98	0.98	0.98	0.98	0.98	0.98	0.98	0.98	0.98	0.98	0.98
Pyrophanite	0.01	0.01	0.02	0.02	0.02	0.01	0.02	0.02	0.02	0.01	0.01	0.01
Geikielite	0.00	0.00	0.00	0.00	0.00	0.00	0.00	0.00	0.00	0.00	0.00	0.00

Table 23
EDS analysis of secondary ilmenite from sample P015 (Fig. 3.12; Fig. 3.15).

Site	MI1 Det1	MI1 Det1	MI1 Det1	MI1 Det2	MI1 Det2	MI1 Det2	MI3 Det1	MI3 Det1
Analysis	ILM2	ILM3	ILM5	ILM2	ILM3	ILM5	ILM2	ILM4
SiO_2	0.23	0.10	0.19	3.00	0.20	0.13	0.73	0.08
Al_2O_3	0.00	0.00	0.07	0.03	0.00	0.00	0.11	0.26
Fe_2O_3	0.10	0.00	0.00	0.00	0.00	0.00	0.00	0.00
Cr_2O_3	0.09	0.00	0.00	0.00	0.12	0.00	0.12	0.00
TiO_2	50.94	52.10	51.32	51.52	51.96	52.15	51.49	51.51
FeO	46.61	45.76	46.30	44.55	46.23	46.51	45.95	45.31
MgO	0.10	0.05	0.01	0.02	0.15	0.04	0.09	0.00
MnO	0.71	0.79	0.63	0.70	0.62	0.59	0.39	0.85
CaO	0.06	0.03	0.00	0.00	0.09	0.03	0.23	0.23
NiO	0.00	0.00	0.05	0.01	0.07	0.08	0.03	0.20
Total	99.68	99.55	99.51	100.00	99.57	99.66	99.57	99.72
Cation proportions calculated for 3 O								
Si	0.01	0.00	0.00	0.07	0.01	0.00	0.02	0.00
Al	0.00	0.00	0.00	0.00	0.00	0.00	0.00	0.01
Fe^{3+}	0.00	0.00	0.00	0.00	0.00	0.00	0.00	0.00
Cr	0.00	0.00	0.00	0.00	0.00	0.00	0.00	0.00
Ti	0.97	0.99	0.98	0.96	0.99	0.99	0.98	0.98
Fe^{2+}	0.99	0.97	0.99	0.92	0.98	0.99	0.97	0.96
Mg	0.00	0.00	0.00	0.00	0.01	0.00	0.00	0.00
Mn	0.02	0.02	0.01	0.01	0.01	0.01	0.01	0.02
Ca	0.00	0.00	0.00	0.00	0.00	0.00	0.01	0.01
Ni	0.00	0.00	0.00	0.00	0.00	0.00	0.00	0.00
Total	2.01	2.00	2.00	1.97	2.00	2.00	2.00	2.00
Ti	0.98	1.00	0.99	0.96	0.99	0.99	0.98	0.99
Fe+Mg+Mn+Cr	1.02	0.99	1.01	0.94	1.00	1.00	1.00	1.00
Ilmenite	0.98	0.98	0.99	0.98	0.98	0.99	0.99	0.98
Pyrophanite	0.02	0.02	0.01	0.02	0.01	0.01	0.01	0.02
Geikielite	0.00	0.00	0.00	0.00	0.01	0.00	0.00	0.00

Table 23 continued

EDS analysis of secondary ilmenite from sample P015 continued (Fig. 3.12; Fig. 3.15).

	MI3	MI3	MI4	MI4	MI5	MI5	MI6	MI6
Site	Det1	Det2	Det1	Det1	det1	det1	Ov1	Ov1
Analysis	ILM5	ILM2	ILM3	ILM6	ILM3	ILM7	ILM2	ILM3
SiO_2	0.20	0.22	0.05	0.84	0.19	0.12	0.36	0.18
Al_2O_3	0.02	0.08	0.13	0.05	0.14	0.00	0.03	0.00
Fe_2O_3	0.00	0.00	1.03	0.00	0.00	0.00	0.00	0.00
Cr_2O_3	0.00	0.00	0.08	0.06	0.10	0.00	0.04	0.00
TiO_2	52.24	51.01	51.49	49.48	50.62	51.72	51.27	50.77
FeO	45.92	46.29	45.21	45.45	45.82	46.27	46.12	45.47
MgO	0.04	0.00	0.25	0.64	0.00	0.05	0.18	0.10
MnO	0.63	0.81	1.04	0.90	0.81	0.70	0.77	0.92
CaO	0.50	0.00	0.01	0.20	0.00	0.06	0.04	0.14
NiO	0.00	0.00	0.00	0.00	0.03	0.07	0.08	0.18
Total	99.68	99.84	99.82	99.49	99.75	99.71	99.66	99.49
Cation proportions calculated for 3 O								
Si	0.01	0.01	0.00	0.02	0.00	0.00	0.01	0.00
Al	0.00	0.00	0.00	0.00	0.00	0.00	0.00	0.00
Fe^{3+}	0.00	0.00	0.02	0.00	0.00	0.00	0.00	0.00
Cr	0.00	0.00	0.00	0.00	0.00	0.00	0.00	0.00
Ti	0.99	0.97	0.98	0.95	0.97	0.99	0.98	0.97
Fe^{2+}	0.97	0.98	0.96	0.97	0.97	0.98	0.98	0.97
Mg	0.00	0.00	0.01	0.02	0.00	0.00	0.01	0.00
Mn	0.01	0.02	0.02	0.02	0.02	0.01	0.02	0.02
Ca	0.01	0.00	0.00	0.01	0.00	0.00	0.00	0.00
Ni	0.00	0.00	0.00	0.00	0.00	0.00	0.00	0.00
Total	2.00	2.01	2.00	2.01	2.00	2.00	2.01	2.00
Ti	0.99	0.98	0.99	0.96	0.99	0.99	0.98	0.99
Fe+Mg+Mn+Cr	0.99	1.02	1.01	1.02	1.00	1.01	1.01	1.01
Ilmenite	0.98	0.98	0.97	0.96	0.98	0.98	0.98	0.98
Pyrophanite	0.01	0.02	0.02	0.02	0.02	0.01	0.02	0.02
Geikielite	0.00	0.00	0.01	0.02	0.00	0.00	0.01	0.00

EDS analysis of secondary ilmenite in S5628 and ROM 109 (C) also produced a minor MgO composition (<0.32 wt%) (Table 24; Table 25). TiO_2 (44.96–52.35 wt%) and Fe compositions (FeO 41.72–46.49 wt%, Fe_2O_3 4.36–17.12) were similar in comparison to megacrystic ilmenite of the same samples (Table 24; Table 25; Chapter 4.1). The endmember composition of the secondary ilmenite is ilmenite *s.s* (0.954–0.993) with a minor pyrophanite (0.007–0.031) and geikielite (<0.015) component (Table 24; Table 25).

Table 24
EDS analysis of secondary ilmenite in sample S5628 (Fig. 3.5).

Site	MI1 Det2	MI1 Det2	MI2	MI3	MI3	MI3	MI3	MI3	MI3	MI4	MI4	MI6 Ov
Analysis	ILM1	ILM7	ILM3	ILM4	ILM9	ILM14	ILM16	ILM21	ILM23	ILM2	ILM4	ILM2
SiO_2	0.08	0.01	0.03	0.39	0.13	0.07	0.09	0.10	0.06	0.18	0.04	0.22
Al_2O_3	0.08	0.05	0.05	0.09	0.01	0.07	0.04	0.05	0.07	0.04	0.06	0.05
Fe_2O_3	4.35	8.06	10.14	9.80	12.17	12.62	11.70	12.30	11.67	11.09	10.98	12.29
Cr_2O_3	0.07	0.09	0.04	0.08	0.01	0.00	0.00	0.02	0.00	0.00	0.03	0.04
TiO_2	47.48	47.38	46.47	45.92	46.01	45.60	46.20	45.93	46.17	46.04	46.33	44.96
FeO	45.08	43.45	43.04	43.05	41.72	41.46	42.11	41.66	42.01	42.54	42.15	42.36
MgO	0.08	0.17	0.02	0.12	0.01	0.00	0.01	0.00	0.00	0.08	0.09	0.00
MnO	1.46	0.77	0.46	0.70	0.62	0.60	0.63	0.55	0.55	0.49	0.50	0.30
CaO	1.30	0.63	0.44	0.36	0.12	0.18	0.28	0.17	0.27	0.27	0.27	0.41
NiO	0.00	0.09	0.27	0.00	0.00	0.00	0.00	0.00	0.00	0.03	0.05	0.05
Total	100.10	100.78	100.99	100.49	100.84	100.71	101.12	100.83	100.82	100.83	100.59	100.70
Cation proportions calculated for 3 O												
Si	0.00	0.00	0.00	0.01	0.00	0.00	0.00	0.00	0.00	0.00	0.00	0.01
Al	0.00	0.00	0.00	0.00	0.00	0.00	0.00	0.00	0.00	0.00	0.00	0.00
Fe^{3+}	0.08	0.15	0.19	0.19	0.23	0.24	0.22	0.23	0.22	0.21	0.21	0.23
Cr	0.00	0.00	0.00	0.00	0.00	0.00	0.00	0.00	0.00	0.00	0.00	0.00
Ti	0.91	0.90	0.88	0.88	0.87	0.87	0.88	0.87	0.88	0.88	0.88	0.86
Fe^{2+}	0.96	0.92	0.91	0.91	0.88	0.88	0.89	0.88	0.89	0.90	0.89	0.90
Mg	0.00	0.01	0.00	0.00	0.00	0.00	0.00	0.00	0.00	0.00	0.00	0.00
Mn	0.03	0.02	0.01	0.01	0.01	0.01	0.01	0.01	0.01	0.01	0.01	0.01
Ca	0.04	0.02	0.01	0.01	0.00	0.00	0.01	0.00	0.01	0.01	0.01	0.01
Ni	0.00	0.00	0.01	0.00	0.00	0.00	0.00	0.00	0.00	0.00	0.00	0.00
Total	2.04	2.02	2.02	2.02	2.01	2.01	2.01	2.01	2.01	2.02	2.01	2.02
Ti	0.91	0.90	0.88	0.88	0.87	0.87	0.88	0.87	0.88	0.88	0.88	0.86
Fe+Mg+Mn+Cr	1.09	1.10	1.12	1.12	1.13	1.13	1.12	1.13	1.12	1.12	1.12	1.14
Ilmenite	0.97	0.98	0.99	0.98	0.98	0.99	0.98	0.99	0.99	0.99	0.98	0.99
Pyrophanite	0.03	0.02	0.01	0.02	0.01	0.01	0.01	0.01	0.01	0.01	0.01	0.01
Geikielite	0.00	0.01	0.00	0.00	0.00	0.00	0.00	0.00	0.00	0.00	0.00	0.00

Table 25
EDS analysis of secondary ilmenite in sample ROM 109 (C).

	MI1	MI1	MI1	MI1	MI2	MI2	MI2	MI3	MI3	MI3
Site	Det1	Det2	Det2	Det2	Det1	Det1	Det1	Det1	Det2	Det2
Analysis	ILM7	ILM5	ILM6	ILM8	ILM5	ILM6	ILM9	ILM3	ILM4	ILM5
SiO_2	0.00	0.19	0.19	0.27	0.08	0.19	0.53	0.27	0.05	0.19
Al_2O_3	0.18	0.14	0.16	0.19	0.04	0.00	0.20	0.02	0.30	0.09
Fe_2O_3	0.00	0.00	0.00	0.00	0.00	0.00	17.12	0.00	0.00	0.00
Cr_2O_3	0.00	0.00	0.00	0.00	0.00	0.00	0.00	0.00	0.00	0.02
TiO2	51.44	52.23	51.04	50.91	51.63	51.88	41.93	49.46	52.35	51.50
FeO	46.17	45.14	46.56	43.96	46.49	46.09	39.61	46.25	44.64	45.13
MgO	0.18	0.14	0.00	0.16	0.07	0.15	0.32	0.28	0.40	0.00
MnO	1.04	0.80	0.92	1.83	0.67	0.77	0.66	1.01	0.98	1.23
CaO	0.39	0.23	0.09	0.51	0.02	0.29	0.15	0.29	0.30	0.59
NiO	0.00	0.00	0.00	0.08	0.14	0.00	0.00	0.00	0.07	0.00
Total	99.65	99.70	99.80	99.52	99.64	99.93	101.21	99.51	99.70	99.56
Cation proportions calculated for 3 O										
Si	0.00	0.00	0.00	0.01	0.00	0.00	0.01	0.01	0.00	0.00
Al	0.01	0.00	0.00	0.01	0.00	0.00	0.01	0.00	0.01	0.00
Fe^{3+}	0.00	0.00	0.00	0.00	0.00	0.00	0.33	0.00	0.00	0.00
Cr	0.00	0.00	0.00	0.00	0.00	0.00	0.00	0.00	0.00	0.00
Ti	0.98	0.99	0.98	0.97	0.99	0.99	0.80	0.95	0.99	0.98
Fe^{2+}	0.98	0.95	0.99	0.93	0.99	0.97	0.84	0.99	0.94	0.96
Mg	0.01	0.01	0.00	0.01	0.00	0.01	0.01	0.01	0.01	0.00
Mn	0.02	0.02	0.02	0.04	0.01	0.02	0.01	0.02	0.02	0.03
Ca	0.01	0.01	0.00	0.01	0.00	0.01	0.00	0.01	0.01	0.02
Ni	0.00	0.00	0.00	0.00	0.00	0.00	0.00	0.00	0.00	0.00
Total	2.02	2.00	2.01	2.00	2.01	2.00	2.02	2.02	2.00	2.01
Ti	0.98	0.99	0.98	0.98	0.99	0.99	0.80	0.97	0.99	0.99
Fe+Mg+Mn+Cr	1.02	0.99	1.02	1.00	1.01	1.00	1.20	1.03	0.99	0.99
Ilmenite	0.97	0.98	0.98	0.95	0.98	0.98	0.97	0.97	0.96	0.97
Pyrophanite	0.02	0.02	0.02	0.04	0.01	0.02	0.02	0.02	0.02	0.03
Geikielite	0.01	0.01	0.00	0.01	0.00	0.01	0.01	0.01	0.02	0.00

ROM 31E (A) hosts subhedral secondary ilmenite, surrounded by both glass and calcite. The secondary ilmenite grains show a distinct zonation pattern visible as variations in BSE signal intensity (Fig. 3.11). EDS analysis reveals the zonation is due to variations in the Fe-Mg composition. The core of the grain has a MgO composition similar to megacrystic ilmenite, consisting of 12.77–15.43 wt% MgO, while the rim consists of 3.3–3.9 wt% MgO (Table 26). Furthermore, secondary ilmenite that forms on the margins of MI1 in sample ROM 31E (A) is composed of 1–3 wt% MgO (Table 26). However, such Mg-rich secondary ilmenite is rare in the analysed material. Secondary ilmenite analysed in samples S5251, ROM 112, S5626, ROM 264 show low MgO compositions of <0.1 wt% MgO.

Table 26
EDS analysis of secondary ilmenite in sample ROM 31E (A) (Fig. 3.11).

Comment	Core	Middle	Rim	Core	Middle	Rim	megacryst	Megacryst rim	Ilm2 on margins	megacryst	Ilm2 on margins
Analysis	ILM3	ILM4	ILM5	ILM6	ILM8	ILM7	ILM9	ILM10	ILM11	ILM12	ILM13
SiO_2	0.18	0.04	0.13	0.13	0.23	0.43	0.07	0.13	0.20	0.22	0.00
Al_2O_3	0.04	0.02	0.06	0.23	0.10	0.14	0.61	0.00	0.10	0.95	0.01
Fe_2O_3	0.00	0.00	0.00	0.00	0.00	0.00	8.78	0.00	0.00	12.30	0.00
Cr_2O_3	0.00	0.08	0.05	0.00	0.00	0.10	0.12	0.01	0.00	0.02	0.07
TiO2	56.39	58.21	54.45	58.46	55.05	53.59	52.17	56.20	53.48	47.93	52.68
FeO	28.12	26.57	41.02	23.77	35.14	40.85	26.46	34.90	41.64	28.46	44.67
MgO	12.77	13.98	3.30	15.43	8.33	3.39	11.87	8.19	3.34	9.33	1.03
MnO	0.55	0.44	0.39	0.36	0.32	0.50	0.22	0.32	0.37	0.27	0.28
CaO	0.02	0.00	0.00	0.00	0.07	0.07	0.04	0.00	0.00	0.15	0.10
NiO	0.03	0.03	0.00	0.00	0.00	0.00	0.00	0.00	0.14	0.00	0.00
Total	99.42	99.78	99.87	99.13	99.66	99.45	100.55	99.86	99.78	100.89	99.69
Cation proportions calculated for 3 O											
Si	0.00	0.00	0.00	0.00	0.01	0.01	0.00	0.00	0.00	0.01	0.00
Al	0.00	0.00	0.00	0.01	0.00	0.00	0.02	0.00	0.00	0.03	0.00
Fe^{3+}	0.00	0.00	0.00	0.00	0.00	0.00	0.15	0.00	0.00	0.22	0.00
Cr	0.00	0.00	0.00	0.00	0.00	0.00	0.00	0.00	0.00	0.00	0.00
Ti	0.98	1.00	1.00	0.99	0.99	0.99	0.91	1.00	0.99	0.85	1.00
Fe^{2+}	0.54	0.51	0.84	0.45	0.70	0.84	0.51	0.69	0.86	0.56	0.94
Mg	0.44	0.47	0.12	0.52	0.30	0.12	0.41	0.29	0.12	0.33	0.04
Mn	0.01	0.01	0.01	0.01	0.01	0.01	0.00	0.01	0.01	0.01	0.01
Ca	0.00	0.00	0.00	0.00	0.00	0.00	0.00	0.00	0.00	0.00	0.00
Ni	0.00	0.00	0.00	0.00	0.00	0.00	0.00	0.00	0.00	0.00	0.00
Total	2.01	2.00	1.99	2.00	2.00	2.00	2.01	1.99	2.00	2.02	1.99
Ti	0.98	1.00	1.00	0.99	0.99	0.99	0.91	1.00	0.99	0.85	1.00
Fe+Mg+Mn+Cr	1.01	1.00	0.98	0.99	1.00	0.98	1.09	0.99	1.00	1.15	0.99
Ilmenite	0.55	0.51	0.87	0.46	0.70	0.86	0.55	0.70	0.87	0.63	0.95
Pyrophanite	0.01	0.01	0.01	0.01	0.01	0.01	0.00	0.01	0.01	0.01	0.01
Geikielite	0.44	0.48	0.12	0.53	0.30	0.13	0.44	0.29	0.12	0.37	0.04

4.3.3 Spinel

Spinel generally displays a MUM composition typical of Group 1 kimberlites (Fig. 4.9). The spinel composition is in agreement with evolution along Trend 1 identified by Roeder and Schulze (2008) and is characterised by increasing $Fe^{3+}/ (Fe^{3+} + Al + Cr)$ at initially constant $Fe^{2+}/ (Fe^{2+} + Mg)$, followed by increasing $Fe^{2+}/ (Fe^{2+} + Mg)$ (Fig. 4.9).

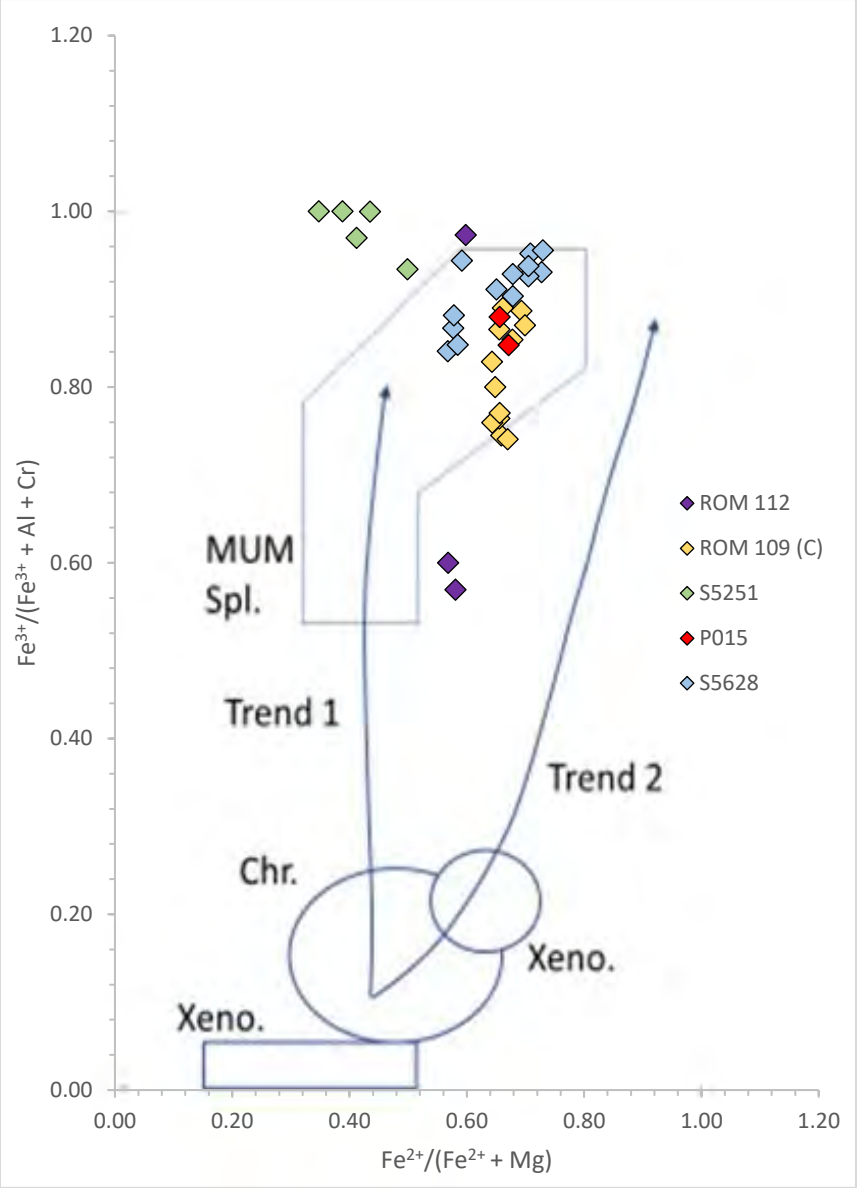

Fig. 4.9. $Fe^{2+}/(Fe^{2+}+Mg)$ versus $Fe^{3+}/(Fe^{3+}+Al+Cr)$ for spinel hosted within melt inclusions from ilmenite megacryst samples S5628; P015; S5251; ROM 109 (C); ROM 112. Spinel paragenetic fields from Roeder and Schulze (2008). The majority of spinel show a MUM composition formed by Trend 1. Xeno. = xenolith; Chr. = chromite; MUM spl. = magnesio-ulvöspinel-magnetite spinel.

A plot of $TiO_2 + MgO + Al_2O_3$ vs $FeO + Fe_2O_3$ shows that the spinel analyses form an inversely proportional linear trend (Fig. 4.10). The spinels form a trend from Ti- and MgO-rich, Fe_2O_3-poor compositions to Fe_2O_3-rich, Ti- and MgO-poor compositions (Fig. 4.10). Spinels occur as grains with a uniform composition or show separate Fe-rich domains in the same spinel crystal.

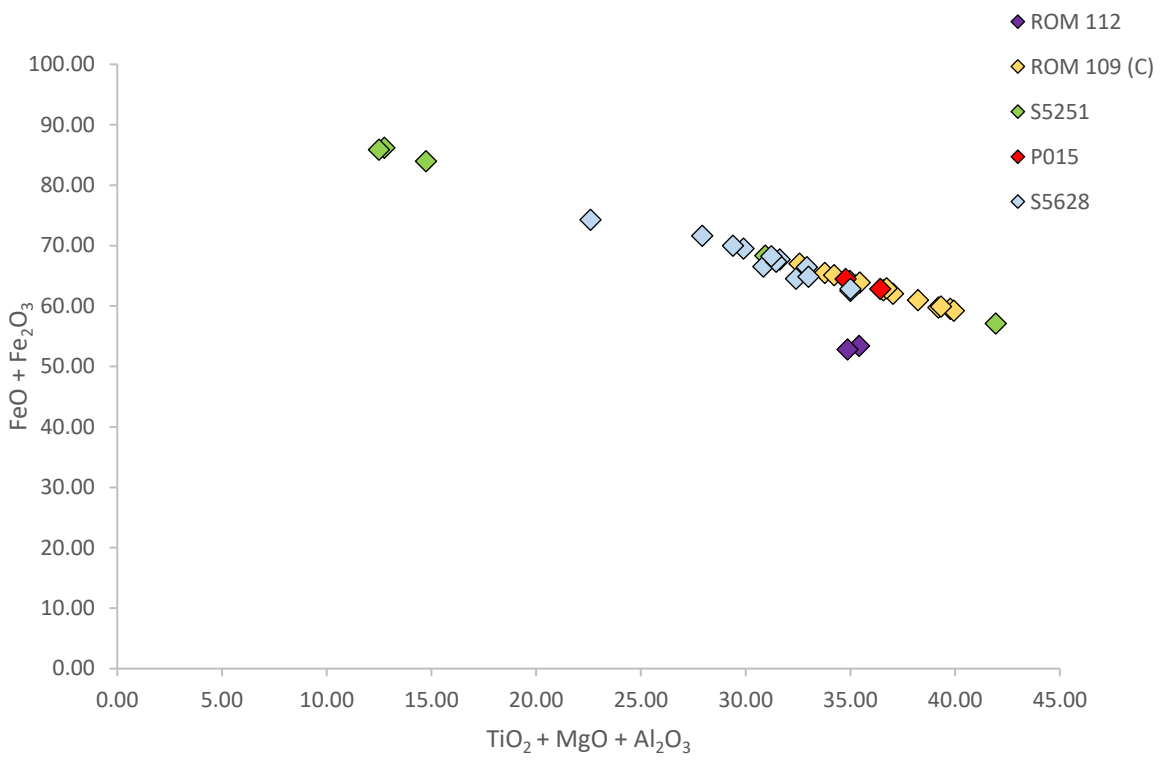

Fig. 4.10. Binary diagram of FeO + Fe_2O_3 (wt%) versus TiO_2 + MgO + Al_2O_3 (wt%). The trend shows a decrease in Ti + Mg + Al with an increase in Fe. Spinel grains are either uniform in composition or may show this trend within a spinel grain.

Spinel in sample ROM 109 (C) and P015 comprise of a TiO_2-rich (~20–23 wt%) and Fe_2O_3-poor (~14–27 wt%) composition, with FeO (~36–44 wt%), MgO (8–12 wt%) and Al_2O_3 (<4 wt%). The endmember composition is mainly composed of ulvöspinel (46–55) and magnesioferrite (37–44) with a minor spinel component (4–13) (Fig. 4.10) (Table 27; Table 28). In comparison, spinel in sample S5628 shows higher Fe_2O_3 contents (~29–48 wt%) and lower TiO_2 (11–21 wt%), FeO (26–38 wt%) and Al_2O_3 contents (1–2 wt%), with similar MgO contents (8–14 wt%). The endmember composition is mainly composed of ulvöspinel (29–53) and magnesioferrite (37–51) with a minor spinel component (1–7) (Fig. 4.10) (Table 29; Table 30).

Table 27
EDS spinel analysis in sample ROM 109 (C) MI1 (Fig. 3.9).

Site	Det1	Det1	Det1	Det1	Det1	Det2	Det2	Det2
Analysis	Spl1	Spl2	Spl3	Spl4	Spl5	Spl1	Spl2	Spl3
Comment	MUM	MUM	MUM	MUM	MUM	MUM	MUM	MUM
SiO_2	0.05	0.12	0.05	0.22	0.09	0.21	0.01	0.33
Al_2O_3	3.64	3.69	3.18	3.43	3.78	3.71	2.28	3.83
Fe_2O_3	16.72	27.94	14.76	17.41	18.70	23.21	20.85	20.30
Cr_2O_3	0.03	0.00	0.18	0.00	0.00	0.00	0.00	0.06
TiO_2	23.65	20.00	24.45	23.29	22.73	21.50	23.15	22.41
FeO	42.83	36.19	44.47	42.36	41.20	38.81	41.78	40.67
MgO	12.48	11.28	12.31	12.49	12.81	11.83	11.15	11.98
MnO	0.44	0.56	0.60	0.58	0.69	0.53	0.65	0.41
ZnO	0.00	0.00	0.00	0.00	0.00	0.00	0.00	0.00
NiO	0.17	0.21	0.00	0.21	0.00	0.20	0.14	0.00
Total	100.00	100.00	100.00	100.00	100.00	100.00	100.00	100.00
Cation proportions calculated for 4 O								
Si	0.00	0.00	0.00	0.01	0.00	0.01	0.00	0.01
Al	0.15	0.15	0.13	0.14	0.15	0.15	0.09	0.16
Fe^{3+}	0.43	0.72	0.39	0.45	0.48	0.60	0.55	0.53
Cr	0.00	0.00	0.00	0.00	0.00	0.00	0.00	0.00
Ti	0.61	0.52	0.64	0.60	0.59	0.56	0.61	0.58
Fe^{2+}	1.24	1.04	1.29	1.22	1.19	1.12	1.22	1.17
Mg	0.64	0.58	0.64	0.64	0.66	0.61	0.58	0.61
Mn	0.01	0.02	0.02	0.02	0.02	0.02	0.02	0.01
Zn	0.00	0.00	0.00	0.00	0.00	0.00	0.00	0.00
Ni	0.00	0.01	0.00	0.01	0.00	0.01	0.00	0.00
Total	3.09	3.04	3.10	3.09	3.09	3.06	3.07	3.07
Endmembers (mol%)								
Ulvöspinel	47.90	46.04	48.82	47.10	46.15	46.82	49.99	47.63
Trevorite	0.35	0.50	0.00	0.45	0.00	0.47	0.31	0.00
Galaxite	0.26	0.25	0.34	0.32	0.37	0.26	0.23	0.22
Jacobsite	0.73	1.19	1.00	1.01	1.18	1.03	1.33	0.76
Gahnite	0.00	0.00	0.00	0.00	0.00	0.00	0.00	0.00
Franklinite	0.00	0.00	0.00	0.00	0.00	0.00	0.00	0.00
Chromite	0.00	0.00	0.00	0.00	0.00	0.00	0.00	0.00
Magnesiochromite	0.02	0.00	0.18	0.00	0.00	0.00	0.00	0.06
Hercynite	0.18	0.10	0.28	0.25	0.18	0.07	0.06	0.21
Magnetite	0.50	0.45	0.84	0.80	0.56	0.27	0.33	0.70
Spinel	12.93	8.93	12.25	12.03	12.40	10.37	7.05	11.50
Magnesioferrite	37.13	42.53	36.29	38.03	39.17	40.70	40.69	38.93

Table 28

EDS spinel analysis in sample P015 MI1 (Fig. 3.12) and sample ROM 109 (C) MI2 and MI3 (Fig. 3.9).

Sample	ROM 109 (C)	ROM 109 (C)	ROM 109 (C)	ROM 109 (C)	ROM 109 (C)	P015	P015
Site	MI3 Det1	MI3 Det1	MI3 Det1	MI3 Det1	MI3 Det2	MI1 Det2	MI1 Det1
Analysis	Spl1	Spl2	Spl3	Spl4	Spl1	Spl1	Spl1
Comment	MUM	MUM	MUM	MUM	MUM	MUM	MUM
SiO_2	0.15	0.08	0.00	0.04	0.00	0.19	0.16
Al_2O_3	2.11	2.13	2.08	2.20	1.89	2.28	2.45
Fe_2O_3	25.85	27.03	21.94	22.26	27.14	26.12	21.58
Cr_2O_3	0.01	0.00	0.01	0.00	0.03	0.00	0.04
TiO_2	21.82	21.15	23.22	22.50	22.03	21.18	22.61
FeO	39.62	38.06	41.97	40.68	39.86	38.35	41.27
MgO	9.85	10.94	10.15	12.02	8.65	11.31	11.36
MnO	0.49	0.40	0.38	0.30	0.40	0.57	0.44
ZnO	0.00	0.00	0.00	0.00	0.00	0.00	0.00
NiO	0.09	0.21	0.24	0.00	0.00	0.00	0.08
Total	100.00	100.00	100.00	100.00	100.00	100.00	100.00
Cation proportions calculated for 4 O							
Si	0.01	0.00	0.00	0.00	0.00	0.01	0.01
Al	0.09	0.09	0.09	0.09	0.08	0.09	0.10
Fe^{3+}	0.68	0.71	0.58	0.58	0.72	0.68	0.57
Cr	0.00	0.00	0.00	0.00	0.00	0.00	0.00
Ti	0.57	0.55	0.61	0.59	0.58	0.55	0.59
Fe^{2+}	1.16	1.11	1.23	1.18	1.17	1.11	1.20
Mg	0.51	0.57	0.53	0.62	0.45	0.59	0.59
Mn	0.01	0.01	0.01	0.01	0.01	0.02	0.01
Zn	0.00	0.00	0.00	0.00	0.00	0.00	0.00
Ni	0.00	0.01	0.01	0.00	0.00	0.00	0.00
Total	3.04	3.05	3.06	3.07	3.02	3.05	3.07
Endmembers (mol%)							
Ulvöspinel	51.46	48.60	52.46	47.97	55.25	47.57	48.76
Trevorite	0.23	0.51	0.59	0.00	0.00	0.00	0.18
Galaxite	0.15	0.12	0.13	0.10	0.11	0.17	0.16
Jacobsite	1.14	0.92	0.84	0.61	1.01	1.26	0.91
Gahnite	0.00	0.00	0.00	0.00	0.00	0.00	0.00
Franklinite	0.00	0.00	0.00	0.00	0.00	0.00	0.00
Chromite	0.00	0.00	0.00	0.00	0.00	0.00	0.00
Magnesiochromite	0.01	0.00	0.01	0.00	0.04	0.00	0.04
Hercynite	0.11	0.00	0.07	0.07	0.06	0.08	0.22
Magnetite	0.87	0.03	0.47	0.45	0.59	0.59	1.23
Spinel	5.24	5.55	6.00	6.82	4.23	6.04	7.36
Magnesioferrite	40.79	44.26	39.44	43.98	38.72	44.29	41.14

Table 29

EDS spinel analysis in sample S5628 MI1 (Fig. 3.5).

Site	Det1	Det1	Det1	Det2	Det2
Analysis	Spl1	Spl2	Spl3	Spl1	Spl2
SiO_2	0.06	0.00	1.00	0.11	0.14
Al_2O_3	1.83	1.98	1.05	2.40	2.39
Fe_2O_3	32.67	36.34	47.88	29.12	28.65
Cr_2O_3	2.05	1.72	1.14	1.68	1.34
TiO_2	17.44	16.49	11.29	18.33	18.98
FeO	31.85	30.19	26.41	33.36	34.18
MgO	13.13	12.38	10.25	14.27	13.63
MnO	0.75	0.51	0.54	0.40	0.51
ZnO	0.00	0.00	0.00	0.00	0.00
NiO	0.22	0.39	0.44	0.32	0.18
Total	100.00	100.00	100.00	100.00	100.00
Cation proportions calculated for 4 O					
Si	0.00	0.00	0.03	0.00	0.00
Al	0.07	0.08	0.04	0.10	0.10
Fe^{3+}	0.85	0.94	1.26	0.75	0.74
Cr	0.06	0.05	0.03	0.05	0.04
Ti	0.45	0.43	0.30	0.47	0.49
Fe^{2+}	0.92	0.87	0.77	0.96	0.98
Mg	0.68	0.64	0.53	0.73	0.70
Mn	0.02	0.02	0.02	0.01	0.01
Zn	0.00	0.00	0.00	0.00	0.00
Ni	0.01	0.01	0.01	0.01	0.00
Total	3.06	3.04	3.00	3.08	3.07
Endmembers (mol%)					
Ulvöspinel	38.68	38.67	28.61	38.31	40.55
Trevorite	0.49	0.97	1.18	0.70	0.39
Galaxite	0.15	0.11	0.05	0.11	0.14
Jacobsite	1.72	1.25	1.47	0.82	1.06
Gahnite	0.00	0.00	0.00	0.00	0.00
Franklinite	0.00	0.00	0.00	0.00	0.00
Chromite	0.05	0.05	0.38	0.03	0.00
Magnesiochromite	2.33	2.05	1.14	1.81	1.50
Hercynite	0.10	0.11	0.57	0.10	0.01
Magnetite	1.08	1.29	16.26	0.79	0.08
Spinel	4.52	4.44	1.71	6.69	6.56
Magnesioferrite	50.89	51.05	48.63	50.63	49.70

Table 30
EDS spinel analysis in MI2, MI3, and MI4 of sample S5628 (Fig. 3.14).

Site	MI2	MI3	MI3	MI3	MI3	MI3	MI3	MI4	MI4
Analysis	Spl1	Spl1	Spl2	Spl3	Spl4	Spl5	Spl6	Spl1	Spl2
SiO_2	0.09	0.13	0.06	1.38	0.05	0.60	0.07	0.04	0.18
Al_2O_3	1.51	1.08	1.89	1.75	1.44	1.21	1.57	1.02	1.36
Fe_2O_3	31.68	33.31	28.27	28.26	29.51	28.65	31.79	34.83	38.91
Cr_2O_3	0.00	0.00	0.06	0.03	0.11	0.00	0.00	0.03	0.12
TiO_2	20.42	19.83	20.87	20.22	21.21	21.17	19.96	19.25	16.51
FeO	37.80	36.64	38.16	36.60	38.22	38.69	36.42	36.80	35.03
MgO	7.96	8.48	10.16	11.03	8.98	9.08	9.70	7.65	7.59
MnO	0.33	0.44	0.47	0.46	0.49	0.52	0.32	0.37	0.29
ZnO	0.00	0.00	0.00	0.00	0.00	0.00	0.00	0.00	0.00
NiO	0.20	0.09	0.07	0.27	0.00	0.09	0.16	0.00	0.01
Total	100.00	100.00	100.00	100.00	100.00	100.00	100.00	100.00	100.00
Cation proportions calculated for 4 O									
Si	0.00	0.00	0.00	0.05	0.00	0.02	0.00	0.00	0.01
Al	0.06	0.04	0.08	0.07	0.06	0.05	0.06	0.04	0.06
Fe^{3+}	0.84	0.89	0.74	0.73	0.78	0.76	0.84	0.93	1.04
Cr	0.00	0.00	0.00	0.00	0.00	0.00	0.00	0.00	0.00
Ti	0.54	0.53	0.55	0.53	0.56	0.56	0.53	0.51	0.44
Fe^{2+}	1.12	1.08	1.12	1.06	1.12	1.14	1.07	1.09	1.04
Mg	0.42	0.45	0.53	0.57	0.47	0.48	0.51	0.40	0.40
Mn	0.01	0.01	0.01	0.01	0.01	0.02	0.01	0.01	0.01
Zn	0.00	0.00	0.00	0.00	0.00	0.00	0.00	0.00	0.00
Ni	0.01	0.00	0.00	0.01	0.00	0.00	0.00	0.00	0.00
Total	3.00	3.00	3.04	3.02	3.02	3.02	3.02	3.00	3.00
Endmembers (mol%)									
Ulvöspinel	53.77	51.77	49.36	46.87	53.51	52.27	49.52	51.67	43.67
Trevorite	0.56	0.25	0.15	0.64	0.00	0.22	0.42	0.00	0.00
Galaxite	0.07	0.06	0.12	0.11	0.10	0.09	0.06	0.05	0.04
Jacobsite	0.88	1.20	1.12	1.09	1.28	1.34	0.82	1.07	0.81
Gahnite	0.00	0.00	0.00	0.00	0.00	0.00	0.00	0.00	0.00
Franklinite	0.00	0.00	0.00	0.00	0.00	0.00	0.00	0.00	0.00
Chromite	0.00	0.00	0.00	0.00	0.00	0.00	0.00	0.00	0.05
Magnesiochromite	0.00	0.00	0.06	0.03	0.14	0.00	0.00	0.03	0.12
Hercynite	0.22	0.14	0.16	0.05	0.02	0.10	0.10	0.28	0.81
Magnetite	2.94	2.72	1.49	0.56	0.20	1.57	1.35	6.23	14.84
Spinel	2.91	2.12	4.53	4.54	3.17	2.78	3.43	1.78	2.05
Magnesioferrite	38.64	41.74	43.01	46.11	41.60	41.63	44.29	38.88	37.61

Spinel in sample S5251 MI2 shows the largest variation in composition. Spinel in this sample comprises two compositional varieties: a Fe_2O_3-poor (~46 wt%) and TiO_2- (~12 wt%) MgO-rich (~17 wt%) variety, with FeO contents of ~22 wt% and Al_2O_3 contents of ~1 wt%. The endmember composition is mainly composed of ulvöspinel (~24) and magnesioferrite (~70) with a minor spinel component (~2). The other variety comprises of a Fe_2O_3-rich (~70 wt%) composition, with lower TiO_2 (~2 wt%), MgO (~11 wt%), Al_2O_3 (<0.1), and FeO (13 wt%) contents. The end member composition is composed of mostly magnetite (26–35) and magnesioferrite (57–56) Fig. 4.10) (Table 31).

In sample S5251 MI2 the Fe_2O_3-rich spinel generally occurs as skeletal grains or the outer rim of euhedral and subhedral grains (Table 31). This is observed in a large spinel grain that hosts circular glass inclusions. The rim of the grain displays a higher BSE signal than to the interior of the grain (Fig. 3.7 B). EDS analysis shows that the BSE-bright domains contain higher Fe_2O_3 and lower MgO and TiO_2 than the interior of the grain (Table 31). This is also observed in an element map of the spinel grain (Fig. 4.8), which shows a decrease in Mg and Ti and an increase in Fe towards the rim of the grain (Fig. 4.10).

Table 31
EDS spinel analysis in MI2 of sample S5251 (Fig. 3.7; Fig. 4.6).

Site	MI2 Det1	MI2 Det1	MI2 Det1	MI2 Det1
Analysis	FeO2	FeO3	FeO5	FeO6
Comment	Skeletal (Mag)	Interior (MUM)	Rim (Mag)	Rim (Mag)
SiO_2	0.42	0.22	0.42	0.53
Al_2O_3	0.00	0.92	0.00	0.01
Fe_2O_3	71.66	46.03	72.79	70.91
Cr_2O_3	0.00	0.00	0.00	0.00
TiO_2	1.77	12.14	0.88	1.57
FeO	12.29	22.31	13.42	14.97
MgO	12.96	17.88	11.88	10.91
MnO	0.85	0.50	0.41	0.94
ZnO	0.00	0.00	0.00	0.00
NiO	0.05	0.00	0.20	0.15
Total	100.00	100.00	100.00	100.00
Cation proportions calculated for 4 O				
Si	0.01	0.01	0.01	0.02
Al	0.00	0.04	0.00	0.00
Fe^{3+}	1.88	1.17	1.93	1.89
Cr	0.00	0.00	0.00	0.00
Ti	0.05	0.31	0.02	0.04
Fe^{2+}	0.36	0.63	0.39	0.44
Mg	0.67	0.90	0.62	0.57
Mn	0.02	0.01	0.01	0.03
Zn	0.00	0.00	0.00	0.00
Ni	0.00	0.00	0.01	0.00
Total	3.00	3.08	3.00	3.00
Endmembers (mol%)				
Ulvöspinel	4.58	24.95	2.27	4.14
Trevorite	0.12	0.00	0.54	0.43
Galaxite	0.00	0.04	0.00	0.00
Jacobsite	2.47	1.13	1.21	2.77
Gahnite	0.00	0.00	0.00	0.00
Franklinite	0.00	0.00	0.00	0.00
Chromite	0.00	0.00	0.00	0.00
Magnesiochromite	0.00	0.00	0.00	0.00
Hercynite	0.00	0.03	0.00	0.01
Magnetite	26.25	1.04	34.46	35.61
Spinel	0.00	2.21	0.00	0.01
Magnesioferrite	66.58	70.61	61.52	57.03

Cr is commonly low in the analysed spinels (<2 wt%). However, some spinel analyses in sample ROM 112 MI1 produced a Cr-rich composition (~11 wt% Cr_2O_3) (Table 32). Both the Cr-rich and Cr-poor spinels in this sample are composed of a TiO_2- (19–20 wt%) and MgO-rich (14–15 wt%) composition, indicating that they formed early in the spinel evolution trend (Table 32). The Cr-rich spinels have lower Fe_2O_3 (~17 wt%) contents in comparison to Cr-poor spinel in the same sample (25 wt% Fe_2O_3) (Table 32). Both the Cr-rich and Cr-poor spinel are present as small (~30 µm) subhedral grains set within aggregates of intergrown serpentine and phlogopite (Chapter 3.5.4; Fig 3.8).

Table 32
EDS spinel analysis in sample ROM 112 (Fig. 3.8).

Site	MI1 Det2	MI1 Det1	MI1 Det1
Analysis	Cr-Spl1	Cr-Spl1	Spl2
SiO_2	0.11	0.14	0.20
Al_2O_3	0.46	0.54	0.30
Fe_2O_3	17.78	17.04	25.68
Cr_2O_3	10.59	11.46	0.23
TiO_2	19.76	19.81	20.70
FeO	35.62	35.78	37.71
MgO	15.19	14.52	14.24
MnO	0.27	0.51	0.61
ZnO	0.00	0.00	0.00
NiO	0.22	0.20	0.33
Total	100.00	100.00	100.00
Cation proportions calculated for 4 O			
Si	0.00	0.00	0.01
Al	0.02	0.02	0.01
Fe^{3+}	0.46	0.44	0.67
Cr	0.29	0.31	0.01
Ti	0.51	0.51	0.54
Fe^{2+}	1.03	1.03	1.10
Mg	0.78	0.75	0.74
Mn	0.01	0.01	0.02
Zn	0.00	0.00	0.00
Ni	0.01	0.01	0.01
Total	3.10	3.09	3.11
Endmembers (mol%)			
Ulvöspinel	39.10	39.98	41.00
Trevorite	0.46	0.43	0.69
Galaxite	0.02	0.05	0.03
Jacobsite	0.58	1.09	1.34
Gahnite	0.00	0.00	0.00
Franklinite	0.00	0.00	0.00
Chromite	0.04	0.07	0.00
Magnesiochromite	10.98	12.08	0.23
Hercynite	0.01	0.01	0.02
Magnetite	0.16	0.27	1.03
Spinel	1.94	2.21	1.03
Magnesioferrite	46.70	43.80	54.63

4.3.4 Serpentine

EDS analysis of euhedral and subhedral fan-shaped serpentine in sample S5626 MI1, MI2, and MI3 (Fig. 3.2; Fig. 3.3) produced a composition of SiO_2 (42.06–44.56 wt%), MgO (36.25–38.04 wt%), FeO (1.51–3.34 wt%), and Fe_2O_3 (<2.22 wt%), with a minor Al_2O_3 (0.76–1.89 wt%), K_2O (0.2–0.82 wt%), and CaO (0.12–0.32 wt%) component (Table 33–Table 34). The serpentine is similar in composition to glass of the same sample (Chapter 4.3.1).

Table 33
EDS analysis of serpentine in MI1 of sample S5626 (Fig. 3.2).

Analysis	Serp1	Serp2	Serp3	Serp4	Serp5	Serp6	Serp7
SiO_2	44.21	43.78	44.03	44.46	44.20	44.26	44.29
Al_2O_3	0.76	1.79	1.23	1.16	1.28	1.03	0.96
Fe_2O_3	1.10	0.00	1.86	1.86	1.88	2.11	2.22
Cr_2O_3	0.00	0.00	0.12	0.06	0.13	0.02	0.07
TiO_2	0.52	0.34	0.47	0.28	0.52	0.30	0.37
FeO	2.96	3.34	1.67	1.67	1.69	1.90	2.00
MgO	37.76	37.48	37.85	37.97	37.75	38.04	37.72
MnO	0.11	0.02	0.08	0.04	0.00	0.00	0.00
CaO	0.18	0.21	0.15	0.17	0.12	0.15	0.17
NiO	0.00	0.00	0.00	0.14	0.01	0.01	0.00
Na_2O	0.16	0.03	0.00	0.00	0.01	0.05	0.06
K_2O	0.20	0.82	0.46	0.28	0.32	0.21	0.13
H_2O	12.94	12.93	13.03	13.03	13.02	13.01	12.99
SO_3	0.14	0.05	0.00	0.00	0.18	0.08	0.23
Total	101.05	100.93	101.22	101.22	101.21	101.22	101.21
Cation proportions calculated for 7 O							
Si	2.05	2.03	2.03	2.05	2.04	2.04	2.05
Al	0.04	0.10	0.07	0.06	0.07	0.06	0.05
Fe^{3+}	0.04	0.00	0.06	0.06	0.07	0.07	0.08
Cr	0.00	0.00	0.00	0.00	0.00	0.00	0.00
Ti	0.02	0.01	0.02	0.01	0.02	0.01	0.01
Fe^{2+}	0.11	0.13	0.06	0.06	0.07	0.07	0.08
Mg	2.61	2.59	2.60	2.60	2.59	2.61	2.60
Mn	0.00	0.00	0.00	0.00	0.00	0.00	0.00
Ca	0.01	0.01	0.01	0.01	0.01	0.01	0.01
Ni	0.00	0.00	0.00	0.01	0.00	0.00	0.00
Na	0.01	0.00	0.00	0.00	0.00	0.00	0.01
K	0.01	0.05	0.03	0.02	0.02	0.01	0.01
OH	4.00	4.00	4.00	4.00	4.00	4.00	4.00
SO_3	0.00	0.00	0.00	0.00	0.01	0.00	0.01
Total	8.91	8.93	8.89	8.89	8.89	8.90	8.89
T	2.05	2.03	2.03	2.05	2.04	2.04	2.05
O	2.86	2.89	2.85	2.84	2.84	2.85	2.84

Table 33 continued

EDS analysis of serpentine in MI1 of sample S5626 continued (Fig. 3.2).

Analysis	Serp1	Serp2	Serp3	Serp4	Serp5	Serp6	Serp7
SiO_2	44.10	43.65	44.23	43.88	44.37	44.36	42.06
Al_2O_3	1.05	1.51	1.24	1.26	1.18	0.86	1.44
Fe_2O_3	1.63	1.97	1.94	1.82	1.67	1.34	1.73
Cr_2O_3	0.05	0.00	0.00	0.04	0.02	0.06	0.13
TiO_2	0.54	0.66	0.49	0.40	0.51	0.49	0.40
FeO	2.21	1.77	1.75	2.00	1.84	2.24	1.56
MgO	37.44	36.46	37.76	37.62	37.84	37.96	36.25
MnO	0.01	0.15	0.00	0.06	0.02	0.05	0.05
CaO	0.35	1.11	0.16	0.18	0.21	0.14	3.72
NiO	0.07	0.00	0.01	0.12	0.04	0.05	0.00
Na_2O	0.22	0.12	0.09	0.09	0.08	0.24	0.01
K_2O	0.25	0.68	0.36	0.39	0.36	0.31	0.29
H_2O	12.97	12.92	13.00	12.96	13.00	12.97	12.75
SO_3	0.06	0.04	0.08	0.11	0.00	0.05	0.52
Total	101.13	101.12	101.19	101.14	101.17	101.10	100.92
Cation proportions calculated for 7 O							
Si	2.04	2.02	2.04	2.03	2.04	2.05	1.98
Al	0.06	0.08	0.07	0.07	0.06	0.05	0.08
Fe^{3+}	0.06	0.07	0.07	0.06	0.06	0.05	0.06
Cr	0.00	0.00	0.00	0.00	0.00	0.00	0.00
Ti	0.02	0.02	0.02	0.01	0.02	0.02	0.01
Fe^{2+}	0.08	0.07	0.07	0.08	0.07	0.09	0.06
Mg	2.58	2.52	2.59	2.59	2.60	2.61	2.54
Mn	0.00	0.01	0.00	0.00	0.00	0.00	0.00
Ca	0.02	0.05	0.01	0.01	0.01	0.01	0.19
Ni	0.00	0.00	0.00	0.00	0.00	0.00	0.00
Na	0.02	0.01	0.01	0.01	0.01	0.02	0.00
K	0.01	0.04	0.02	0.02	0.02	0.02	0.02
OH	4.00	4.00	4.00	4.00	4.00	4.00	4.00
SO_3	0.00	0.00	0.00	0.00	0.00	0.00	0.02
Total	8.89	8.90	8.89	8.90	8.89	8.90	8.96
T	2.04	2.02	2.04	2.03	2.04	2.05	2.00
O	2.85	2.87	2.85	2.86	2.85	2.86	2.95

Table 34
EDS analysis of serpentine in MI2 of sample S5626 (Fig. 3.3).

Analysis	Serp1	Serp2	Serp3	Serp1
SiO_2	43.54	44.31	44.14	44.56
Al_2O_3	1.83	0.96	1.96	0.92
Fe_2O_3	1.98	1.46	1.68	0.00
Cr_2O_3	0.13	0.00	0.09	0.03
TiO_2	0.49	0.56	0.72	0.24
FeO	1.78	2.33	1.51	3.50
MgO	37.52	37.79	36.86	37.78
MnO	0.05	0.08	0.00	0.05
CaO	0.10	0.31	0.42	0.32
NiO	0.00	0.00	0.01	0.01
Na_2O	0.10	0.14	0.20	0.09
K_2O	0.58	0.16	0.34	0.38
H_2O	12.99	12.99	12.36	12.94
SO_3	0.00	0.04	0.16	0.09
Total	101.19	101.14	100.53	100.94
Cation proportions calculated for 7 O				
Si	2.01	2.05	2.03	2.06
Al	0.10	0.05	0.11	0.05
Fe^{3+}	0.07	0.05	0.06	0.00
Cr	0.00	0.00	0.00	0.00
Ti	0.02	0.02	0.03	0.01
Fe^{2+}	0.07	0.09	0.06	0.14
Mg	2.58	2.60	2.53	2.61
Mn	0.00	0.00	0.00	0.00
Ca	0.00	0.01	0.02	0.02
Ni	0.00	0.00	0.00	0.00
Na	0.01	0.01	0.02	0.01
K	0.03	0.01	0.02	0.02
OH	4.00	4.00	3.80	4.00
SO_3	0.00	0.00	0.01	0.00
Total	8.90	8.90	8.68	8.92
T	2.01	2.05	2.03	2.06
O	2.89	2.85	2.84	2.85

EPMA analysis of serpentine in the kimberlite matrix surrounding the ilmenite megacryst in sample ROM 112 2 produced a similar composition of SiO_2 (37.39–39.42 wt%), MgO (36.44–39.1 wt%), FeO (1.51–5.44 wt %), and Fe_2O_3 (3.21–6.23 wt%) as well as minor amounts of Al_2O_3 (1.75–2.38 wt%), TiO_2 (0.03–0.18 wt%) and NiO (0.29–0.59 wt%) with a volatile component of ~12 wt% (Table 35).

Table 35
EPMA analysis of serpentine in the kimberlite matrix of sample ROM 112.

Analysis	ROM 112 MI2_serp 5	ROM 112 MI2_serp 6	ROM 112 MI2_serp 7	ROM 112 MI1_serp 2	ROM 112 MI2_serp 3	ROM 112 MI2_serp 4
SiO_2	38.37	39.16	37.39	39.42	38.96	38.54
Al_2O_3	2.38	1.75	2.72	1.79	2.09	1.94
Fe_2O_3	3.700	4.550	6.230	4.510	3.890	3.210
Cr_2O_3	0.00	0.17	0.14	0.04	0.18	0.00
TiO_2	0.07	0.10	0.18	0.03	0.11	0.04
FeO	5.437	1.513	2.403	2.185	2.867	4.721
MgO	36.44	39.10	37.15	37.70	38.06	36.61
MnO	0.01	0.02	0.19	0.07	0.07	0.11
CaO	0.00	0.08	0.03	0.09	0.06	0.02
NiO	0.40	0.51	0.36	0.59	0.45	0.29
Na_2O	0.00	0.00	0.03	0.01	0.01	0.01
K_2O	0.00	0.06	0.05	0.02	0.00	0.00
H_2O	12.36	12.58	12.41	12.57	12.50	12.25
Total	99.18	99.59	99.29	99.03	99.25	97.73
Cation proportions calculated for 7 O						
Si	1.86	1.87	1.81	1.89	1.87	1.89
Al	0.14	0.10	0.15	0.10	0.12	0.11
Fe^{3+}	0.13	0.16	0.23	0.16	0.14	0.12
Cr	0.00	0.01	0.01	0.00	0.01	0.00
Ti	0.00	0.00	0.01	0.00	0.00	0.00
Fe^{2+}	0.22	0.06	0.10	0.09	0.11	0.19
Mg	2.63	2.78	2.68	2.70	2.72	2.67
Mn	0.00	0.00	0.01	0.00	0.00	0.00
Ca	0.00	0.00	0.00	0.00	0.00	0.00
Ni	0.02	0.02	0.01	0.02	0.02	0.01
Na	0.00	0.00	0.00	0.00	0.00	0.00
K	0.00	0.00	0.00	0.00	0.00	0.00
OH	4.00	4.00	4.00	4.03	4.00	4.00
Total	9.00	9.00	9.00	9.00	9.00	9.00
T	2.00	1.96	1.96	1.99	1.99	2.00
O	3.01	3.03	3.04	2.98	3.01	3.00

EPMA and EDS analysis of subhedral grains in ROM112 MI1 (Fig. 3.8) and S5628 MI1 (Fig. 3.5) produced a similar composition for serpentine (Table 36). However, some analyses of subhedral grains produced a Na_2O-rich composition of ~4–8 wt% (Table 36–Table 38). Stoichiometric calculations for this mineral are incompatible with serpentine due to low SiO_2 and high MgO contents (Table 36–Table 38). There are no apparent textural variations between analyses of serpentine and the Na_2O-rich mineral. This specific mineral was unidentified but possibly represents aenigmatite ($Na_2Fe^{2+}TiSi_6O_{20}$) / ferrikatophorite ($Na_2CaFe^{2+}{}_3MgFe^{3+}Si_7AlO_{22}$ $(OH)_2$). However, the MgO content (~40 wt%) is high for such minerals (Table 36; Table 37; Table 38).

Table 36

EDS analysis of serpentine and an unidentified Na-rich mineral in MI1 of sample ROM 112 (Fig. 3.8). Stoichiometric calculations for serpentine are incompatible with the analysed Na-rich mineral.

Analysis	Serp1	Na phase2	Na phase3	Na phase1
SiO_2	39.62	33.28	34.90	31.90
Al_2O_3	3.45	0.00	0.15	0.02
Fe_2O_3	0.00	0.00	0.00	0.00
Cr_2O_3	0.11	0.09	0.00	0.15
TiO_2	0.24	0.93	0.29	0.86
FeO	9.37	11.02	9.63	12.08
MgO	33.90	40.01	40.92	39.44
MnO	0.11	0.20	0.00	0.06
CaO	0.08	0.11	0.08	0.07
NiO	0.12	0.00	0.19	0.00
Na_2O	0.11	2.23	1.43	3.04
K_2O	0.68	0.05	0.07	0.05
H_2O	12.43	11.95	12.12	11.76
SO_3	0.11	0.00	0.00	0.04
Total	100.43	99.95	99.93	99.47
Cation proportions calculated for 7 O				
Si	1.91	1.67	1.73	1.63
Al	0.20	0.00	0.01	0.00
Fe^{3+}	0.00	0.00	0.00	0.00
Cr	0.00	0.00	0.00	0.01
Ti	0.01	0.03	0.01	0.03
Fe^{2+}	0.38	0.46	0.40	0.52
Mg	2.44	2.99	3.02	3.00
Mn	0.00	0.01	0.00	0.00
Ca	0.00	0.01	0.00	0.00
Ni	0.00	0.00	0.01	0.00
Na	0.01	0.22	0.14	0.30
K	0.04	0.00	0.00	0.00
OH	4.00	4.00	4.00	4.00
SO_3	0.00	0.00	0.00	0.00
Total	9.00	9.40	9.32	9.49
T	2.00	1.67	1.74	1.63
O	3.00	3.73	3.58	3.86

Table 37

EPMA analysis of an unidentified Na-rich mineral in MI1 of sample ROM112 (Fig. 3.8). Stoichiometric calculations for serpentine are incompatible with the analysed Na-rich mineral.

Analysis	MI1c_serp 4	MI1c_serp 5	MI1c_serp 6	MI1c_serp 7	MI1c_serp 8	MI1c_serp 9	MI1c_serp 10
Comment	Na phase	Na phase	Na phase	Na phase	Na phase	Na phase	Na phase
SiO_2	28.39	29.10	24.71	28.57	28.55	28.53	30.23
Al_2O_3	0.16	0.06	0.28	0.00	0.04	0.13	0.06
Fe_2O_3	13.02	12.02	17.95	13.47	11.96	14.70	12.14
Cr_2O_3	0.00	0.00	0.00	0.00	0.00	0.00	0.00
TiO_2	1.16	0.88	0.62	0.80	1.08	0.40	1.02
FeO	0.00	0.00	0.00	0.00	0.00	0.00	0.00
MgO	39.78	40.34	38.07	40.70	40.93	40.04	41.18
MnO	0.12	0.15	0.14	0.08	0.17	0.18	0.23
CaO	0.21	0.33	0.51	0.06	0.08	0.05	0.02
NiO	0.00	0.00	0.00	0.00	0.00	0.00	0.00
Na_2O	4.96	4.70	6.02	5.42	4.24	3.26	2.61
K_2O	0.18	0.10	0.04	0.09	0.07	0.08	0.11
H_2O	13.08	13.19	13.25	12.10	13.88	13.89	13.53
Total	101.04	100.88	101.59	101.28	101.00	101.26	101.14
Cation proportions calculated for 7 O							
Si	1.44	1.47	1.29	1.43	1.45	1.45	1.51
Al	0.01	0.00	0.02	0.00	0.00	0.01	0.00
Fe^{3+}	0.50	0.46	0.70	0.51	0.46	0.56	0.46
Cr	0.00	0.00	0.00	0.00	0.00	0.00	0.00
Ti	0.04	0.03	0.02	0.03	0.04	0.02	0.04
Fe^{2+}	0.00	0.00	0.00	0.00	0.00	0.00	0.00
Mg	3.01	3.04	2.96	3.04	3.10	3.04	3.07
Mn	0.00	0.01	0.01	0.00	0.01	0.01	0.01
Ca	0.01	0.02	0.03	0.00	0.00	0.00	0.00
Ni	0.00	0.00	0.00	0.00	0.00	0.00	0.00
Na	0.49	0.46	0.61	0.53	0.42	0.32	0.25
K	0.01	0.01	0.00	0.00	0.00	0.00	0.01
OH	4.43	4.45	4.61	4.05	4.71	4.72	4.52
Total	9.94	9.95	10.24	9.60	10.20	10.13	9.87
T	1.45	1.48	1.30	1.43	1.45	1.46	1.51
O	4.06	4.02	4.33	4.12	4.03	3.95	3.83

Table 38

EPMA analysis of an unidentified Na-rich mineral in MI1 of sample S5628 (Fig. 3.5).
Stoichiometric calculations for serpentine are incompatible with the analysed Na-rich mineral.

Analysis	Na phase 1	Na phase 2	Na phase 3	Na phase 4	Na phase 6
SiO_2	22.61	29.28	26.46	25.40	26.10
Al_2O_3	0.43	0.78	0.92	0.85	1.12
Fe_2O_3	18.02	16.28	15.37	16.49	16.78
Cr_2O_3	0.00	0.00	0.00	0.00	0.00
TiO_2	0.23	0.39	0.80	0.61	0.54
FeO	0.00	0.00	0.00	0.00	0.00
MgO	38.64	37.36	37.79	38.55	39.07
MnO	0.12	0.09	0.08	0.18	0.21
CaO	0.09	0.00	0.04	0.03	0.00
NiO	0.00	0.00	0.00	0.00	0.00
Na_2O	7.52	4.23	4.30	5.18	4.99
K_2O	0.10	1.58	0.45	0.21	0.17
H_2O	13.96	11.50	15.24	14.15	12.47
Total	101.71	101.48	101.45	101.65	101.44
Cation proportions calculated for 7 O					
Si	1.20	1.47	1.38	1.32	1.33
Al	0.03	0.05	0.06	0.05	0.07
Fe^{3+}	0.72	0.61	0.60	0.65	0.64
Cr	0.00	0.00	0.00	0.00	0.00
Ti	0.01	0.01	0.03	0.02	0.02
Fe^{2+}	0.00	0.00	0.00	0.00	0.00
Mg	3.06	2.79	2.94	2.99	2.97
Mn	0.01	0.00	0.00	0.01	0.01
Ca	0.01	0.00	0.00	0.00	0.00
Ni	0.00	0.00	0.00	0.00	0.00
Na	0.77	0.41	0.44	0.52	0.49
K	0.01	0.10	0.03	0.01	0.01
OH	4.95	3.84	5.31	4.91	4.24
Total	10.76	9.29	10.80	10.49	9.79
T	1.23	1.51	1.44	1.37	1.40
O	4.58	3.93	4.05	4.20	4.15

4.3.5 Perovskite and kassite

Perovskite grains generally show a uniform composition between samples and melt inclusions. Kassite ($CaTi_2O_4(OH)_2$) forms in the same textural positions as perovskite but with a more variable composition (Fig. 4.11).

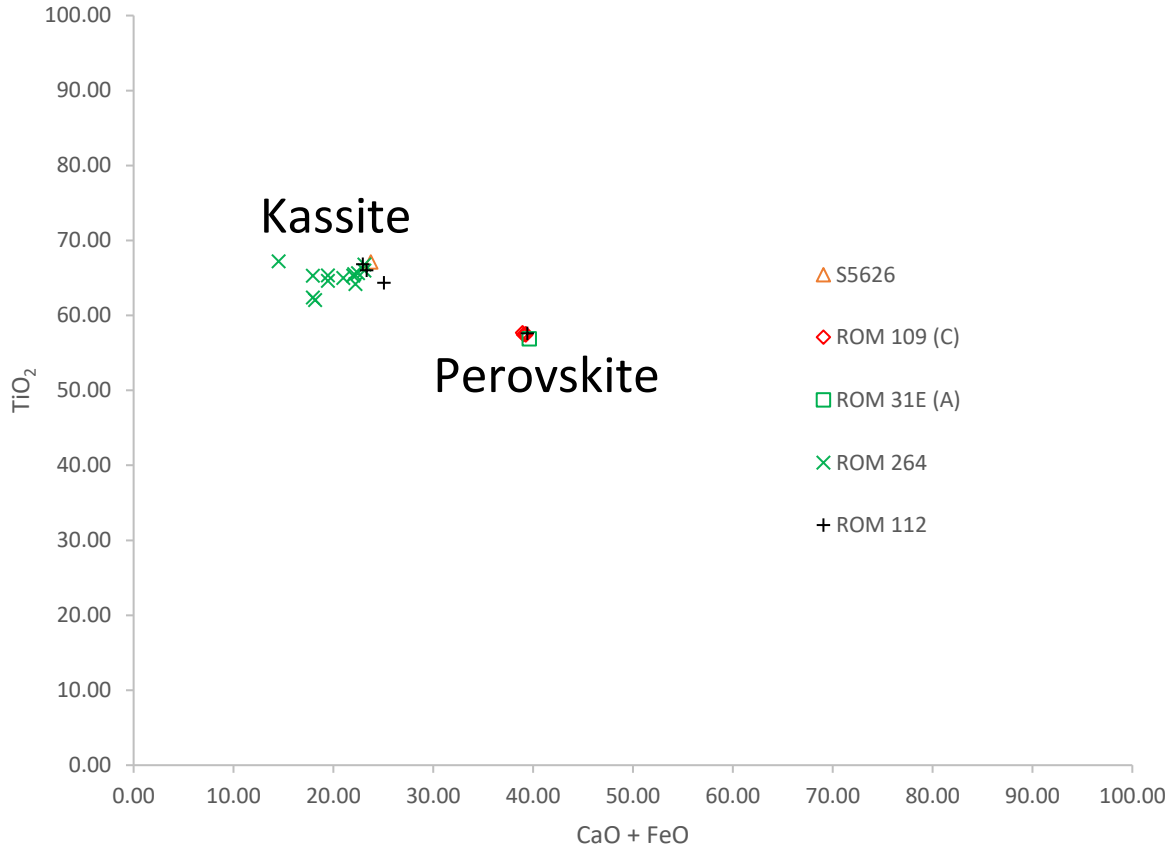

Fig. 4.11. TiO_2 versus CaO + FeO showing the variation in composition between perovskite and kassite. Perovskite comprises a more uniform composition, kassite comprises a more variable CaO + FeO composition.

Sample ROM 109 (C) MI2 and MI3 host perovskite with a uniform composition across both melt inclusions. The perovskite is composed of TiO_2 (57.39–57.68 wt%), FeO (0.19–1.3 wt%), and CaO (38.96–39.28 wt%) (Table 39). This is also consistent with perovskite analysed in ROM 31E A which is composed of similar TiO_2 (56.88 wt%), FeO (0.45 wt%), and CaO (39.62 wt%) contents (Table 39; Fig. 3.11).

Table 39
EDS analysis of perovskite in MI2 and MI3 of sample ROM 109 (C) and ROM 31 E (A) (Fig. 3.9; Fig. 3.11).

Sample	ROM 109 (C)	ROM 109 (C)	ROM 109 (C)	ROM 109 (C)	ROM 31 E(A)
Site	MI2 Det1	MI3 Det2	MI3 Det2	MI3 Det2	MI1 Det1
Analysis	Perov1	Perov1	Perov2	Perov3	Perov1
SiO_2	0.25	0.00	0.03	0.00	0.13
Al_2O_3	0.12	0.23	0.10	0.16	0.18
Fe_2O_3	0.00	0.85	0.69	0.46	1.17
Cr_2O_3	0.00	0.00	0.00	0.00	0.00
TiO_2	57.68	57.39	57.44	57.58	56.88
FeO	1.30	0.19	0.62	0.41	0.45
MgO	0.18	0.16	0.00	0.06	0.24
MnO	0.01	0.11	0.14	0.00	0.08
CaO	38.96	39.27	39.03	39.28	39.62
NiO	0.01	0.00	0.00	0.25	0.02
Na_2O	0.57	0.76	0.59	0.53	0.44
K_2O	0.00	0.05	0.09	0.06	0.00
H_2O	0.00	0.00	0.00	0.00	0.00
SO_3	0.00	0.00	0.14	0.09	0.00
Total	99.08	99.01	98.87	98.89	99.20
Si	0.01	0.00	0.00	0.00	0.00
Al	0.00	0.01	0.00	0.00	0.00
Fe^{3+}	0.00	0.01	0.01	0.01	0.02
Cr	0.00	0.00	0.00	0.00	0.00
Ti	0.99	0.99	0.99	0.99	0.98
Fe^{2+}	0.02	0.00	0.01	0.01	0.01
Mg	0.01	0.01	0.00	0.00	0.01
Mn	0.00	0.00	0.00	0.00	0.00
Ca	0.96	0.96	0.96	0.97	0.97
Ni	0.00	0.00	0.00	0.00	0.00
Na	0.03	0.03	0.03	0.02	0.02
K	0.00	0.00	0.00	0.00	0.00
OH	0.00	0.00	0.00	0.00	0.00
SO_3	0.00	0.00	0.00	0.00	0.00
Total	2.01	2.02	2.02	2.01	2.02
Ti	0.99	0.99	0.99	0.99	0.98
Ca, Fe^{2+}, Na	1.01	1.00	1.00	1.00	1.00
Other	0.02	0.03	0.02	0.02	0.04
XMg	0.20	0.59	0.00	0.20	0.48
XCa	0.97	0.99	0.99	0.99	0.98

Perovskite is often intergrown with kassite. This is seen in sample ROM 112 MI1 which hosts both perovskite and kassite (Fig. 3.8). In this sample, perovskite forms anhedral grains on the margins of the inclusion, which consist of 57.63 wt% TiO_2 and 39.42 wt% CaO (Table 40). These perovskite grains are intergrown with anhedral kassite, a more TiO_2-rich phase. Kassite also forms subhedral grains in interior positions within the melt inclusion (Fig. 3.8). The kassite has a composition of higher TiO_2 (64.38–66.84 wt%) and lower CaO (23.33–25.08 wt%) contents in comparison to perovskite (Table 40).

Table 40
EDS analysis of perovskite and kassite in MI1 of sample ROM 112 (Fig. 3.8).

Analysis	Perov 1	Kassite 1	Kassite 2	Kassite 3
SiO_2	0.09	0.05	0.02	0.04
Al_2O_3	0.21	0.01	0.05	0.02
Fe_2O_3	0.94	0.93	1.06	0.00
Cr_2O_3	0.00	0.00	0.00	0.00
TiO_2	57.62	66.03	64.38	66.84
FeO	0.00	0.09	0.00	0.77
MgO	0.03	0.22	0.46	0.14
MnO	0.01	0.23	0.51	0.92
CaO	39.42	23.33	25.08	22.95
NiO	0.15	0.01	0.00	0.00
Na_2O	0.35	0.07	0.00	0.04
K_2O	0.02	0.00	0.05	0.00
H_2O	0.00	7.56	7.57	7.61
SO_3	0.00	0.00	0.06	0.05
Total	98.87	98.54	99.25	99.37
Cation proportions of perovskite calculated for 3 O. Cation proportions of kassite calculated for 5 O				
Si	0.00	0.00	0.00	0.00
Al	0.01	0.00	0.00	0.00
Fe^{3+}	0.02	0.03	0.03	0.00
Cr	0.00	0.00	0.00	0.00
Ti	0.99	1.97	1.92	1.98
Fe^{2+}	0.00	0.00	0.00	0.03
Mg	0.00	0.01	0.03	0.01
Mn	0.00	0.01	0.02	0.03
Ca	0.97	0.99	1.06	0.97
Ni	0.00	0.00	0.00	0.00
Na	0.02	0.01	0.00	0.00
K	0.00	0.00	0.00	0.00
OH	0.00	2.00	2.00	2.00
SO_3	0.00	0.00	0.00	0.00
Total	2.00	5.02	5.07	5.02
Ti	0.99	1.97	1.92	1.98
Ca, Fe^{2+}, Na	0.98	1.00	1.06	1.00
Other	0.03	0.05	0.08	0.04
XMg	1.00	0.81	1.00	0.24
XCa	1.00	0.98	0.98	0.97

Similarly, ROM 264 MI1 hosts kassite which forms on the margins of the inclusion, intergrown with perovskite. This sample also hosts kassite which occupies the centre of the globular structures on the margins of the inclusions (Fig. 3.10). The perovskite is uniform in composition (Table 41). The kassite is composed of TiO_2 (62.06–65.63 wt%), with variable FeO (0.64–6.15 wt%) and CaO (15.79–25.12 wt%) (Table 42). This is similar in composition to kassite analysed in sample S5626, which forms as subhedral grains within a vein that extends from the MI2 into the host megacryst (Table 43) (Fig. 3.3).

Table 41

EDS analysis of perovskite in ROM 264 MI1 (Fig. 3.10)

Site	MI1 Det1	MI1 Det1	MI1 Det1	MI1 Det2	MI1 Det2
Analysis	Perov1	Perov3	Perov10	Perov2	Perov3
SiO_2	0.17	0.14	0.21	0.12	0.19
Al_2O_3	0.11	0.23	0.30	0.31	0.00
Fe_2O_3	0.42	0.28	0.17	1.63	2.18
Cr_2O_3	0.02	0.00	0.00	0.00	0.15
TiO_2	58.18	57.40	57.49	57.15	56.65
FeO	0.87	1.01	1.34	0.16	0.00
MgO	0.00	0.00	0.09	0.00	0.00
MnO	0.02	0.00	0.00	0.00	0.09
CaO	39.22	38.84	38.85	39.10	39.68
NiO	0.07	0.00	0.07	0.00	0.01
Na_2O	0.64	0.62	0.45	0.45	0.49
K_2O	0.00	0.03	0.15	0.05	0.01
H_2O	0.00	0.00	0.00	0.00	0.00
SO_3	0.00	0.00	0.03	0.07	0.00
Total	99.73	98.55	99.14	99.05	99.41
Cation proportions calculated fro 3 O					
Si	0.00	0.00	0.00	0.00	0.00
Al	0.00	0.01	0.01	0.01	0.00
Fe^{3+}	0.01	0.00	0.00	0.03	0.04
Cr	0.00	0.00	0.00	0.00	0.00
Ti	0.99	0.99	0.99	0.98	0.97
Fe^{2+}	0.02	0.02	0.03	0.00	0.00
Mg	0.00	0.00	0.00	0.00	0.00
Mn	0.00	0.00	0.00	0.00	0.00
Ca	0.96	0.96	0.95	0.96	0.97
Ni	0.00	0.00	0.00	0.00	0.00
Na	0.03	0.03	0.02	0.02	0.02
K	0.00	0.00	0.00	0.00	0.00
OH	0.00	0.00	0.00	0.00	0.00
(SO_3)	0.00	0.00	0.00	0.00	0.00
Total	2.01	2.01	2.01	2.01	2.01
Ti	0.99	0.99	0.99	0.98	0.97
Ca, Fe^{2+}, Na	1.00	1.00	1.00	0.98	0.99
Other	0.02	0.01	0.02	0.04	0.04
XMg	0.00	0.00	0.10	0.00	1.00
XCa	0.98	0.98	0.97	1.00	1.00

Table 42
EDS analysis of kassite in MI1 of sample ROM 264 (Fig. 3.10).

Analysis	Kassite 1	Kassite 2	Kassite 3	Kassite 4	Kassite 5	Kassite 6	Kassite 7	Kassite 8	Kassite 9	Kassite 10	Kassite 11	Kassite 12	Kassite 13
SiO_2	0.20	0.46	0.46	0.15	1.66	0.40	0.28	0.96	0.23	0.33	0.25	0.15	0.64
Al_2O_3	0.03	0.09	0.11	0.13	0.19	0.05	0.13	0.01	0.10	0.00	0.04	0.13	0.00
Fe_2O_3	0.00	0.90	0.62	1.18	1.21	1.24	1.74	2.34	1.08	0.74	0.00	0.87	1.61
Cr_2O_3	0.00	0.00	0.00	0.00	0.20	0.03	0.02	0.11	0.00	0.15	0.11	0.06	0.00
TiO_2	66.79	64.61	65.01	65.30	62.06	65.29	65.63	62.39	65.51	67.22	65.34	65.96	64.18
FeO	0.85	4.24	2.94	5.57	6.15	1.26	0.88	5.41	1.46	5.39	4.96	0.64	1.09
MgO	0.04	0.12	0.16	0.11	1.20	0.04	0.06	0.58	0.14	1.78	0.06	0.25	0.22
MnO	0.05	0.59	0.28	0.44	0.40	0.10	0.09	0.44	0.11	0.30	0.29	0.20	0.17
CaO	23.11	19.46	21.00	17.94	18.16	21.98	22.48	17.94	22.08	14.53	19.45	23.12	22.21
NiO	0.13	0.00	0.00	0.09	0.04	0.10	0.00	0.20	0.08	0.00	0.08	0.00	0.22
Na_2O	0.08	0.28	0.12	0.24	0.28	0.27	0.28	0.59	0.17	0.57	0.15	0.02	0.17
K_2O	0.01	0.09	0.18	0.09	0.18	0.00	0.18	0.07	0.15	0.08	0.18	0.00	0.01
H_2O	7.59	7.45	7.51	7.48	7.53	7.53	7.60	7.45	7.55	7.57	7.47	7.59	7.50
SO_3	0.09	0.04	0.00	0.00	0.00	0.19	0.22	0.00	0.00	0.00	0.22	0.13	0.11
Total	98.95	98.32	98.40	98.71	99.23	98.48	99.58	98.48	98.67	98.66	98.62	99.12	98.12
Cation proportions of calculated for 5 O													
Si	0.01	0.02	0.02	0.01	0.07	0.02	0.01	0.04	0.01	0.01	0.01	0.01	0.03
Al	0.00	0.00	0.01	0.01	0.01	0.00	0.01	0.00	0.00	0.00	0.00	0.01	0.00
Fe^{3+}	0.00	0.03	0.02	0.04	0.04	0.04	0.05	0.07	0.03	0.02	0.00	0.03	0.05
Cr	0.00	0.00	0.00	0.00	0.01	0.00	0.00	0.00	0.00	0.00	0.00	0.00	0.00
Ti	1.98	1.95	1.95	1.97	1.86	1.96	1.95	1.89	1.96	2.00	1.97	1.96	1.93
Fe^{2+}	0.03	0.14	0.10	0.19	0.20	0.04	0.03	0.18	0.05	0.18	0.17	0.02	0.04
Mg	0.00	0.01	0.01	0.01	0.07	0.00	0.00	0.03	0.01	0.10	0.00	0.01	0.01
Mn	0.00	0.02	0.01	0.01	0.01	0.00	0.00	0.01	0.00	0.01	0.01	0.01	0.01
Ca	0.98	0.84	0.90	0.77	0.77	0.94	0.95	0.77	0.94	0.62	0.84	0.98	0.95
Ni	0.00	0.00	0.00	0.00	0.00	0.00	0.00	0.01	0.00	0.00	0.00	0.00	0.01
Na	0.01	0.02	0.01	0.02	0.02	0.02	0.02	0.05	0.01	0.04	0.01	0.00	0.01
K	0.00	0.00	0.01	0.00	0.01	0.00	0.01	0.00	0.01	0.00	0.01	0.00	0.00
OH	2.00	1.99	2.00	2.00	2.00	2.00	2.00	2.00	2.00	2.00	2.00	2.00	2.00
(SO_3)	0.00	0.00	0.00	0.00	0.00	0.01	0.01	0.00	0.00	0.00	0.01	0.00	0.00
Total	5.01	5.02	5.03	5.02	5.07	5.03	5.04	5.06	5.03	5.00	5.03	5.02	5.03
Ti	1.98	1.95	1.95	1.97	1.86	1.96	1.95	1.89	1.96	2.00	1.97	1.96	1.93
Ca, Fe^{2+}, Na	1.01	1.00	1.01	0.97	1.00	1.00	1.00	1.00	1.00	0.84	1.01	1.00	1.00
Other	0.02	0.08	0.07	0.07	0.21	0.06	0.08	0.17	0.07	0.16	0.04	0.06	0.10
XMg	0.07	0.04	0.09	0.03	0.26	0.06	0.11	0.16	0.14	0.37	0.02	0.41	0.26
XCa	0.97	0.85	0.89	0.80	0.74	0.95	0.97	0.78	0.94	0.69	0.83	0.97	0.95

Table 43
EDS analysis of kassite in sample S5626 MI2 (Fig. 3.3)

Analysis	Kassite
SiO_2	0.11
Al_2O_3	0.00
Fe_2O_3	0.57
Cr_2O_3	0.01
TiO_2	66.40
FeO	0.00
MgO	0.27
MnO	0.07
CaO	23.48
NiO	0.00
Na_2O	0.00
K_2O	0.01
H_2O	7.58
SO_3	0.07
Total	98.56
Cation proportions calculated for 5 O	
Si	0.00
Al	0.00
Fe^{3+}	0.02
Cr	0.00
Ti	1.98
Fe^{2+}	0.00
Mg	0.02
Mn	0.00
Ca	1.00
Ni	0.00
Na	0.00
K	0.00
OH	2.00
(SO_3)	0.00
Total	5.01
Ti	1.98
Ca, Fe^{2+}, Na	1.00
Other	0.04
XMg	1.00
XCa	0.98

Variations in the CaO and TiO_2 contents near the margins of the melt inclusions are also observed in a zone of alteration surrounding the melt inclusion-megacryst interface in sample S5628 MI1 (Fig. 3.5). This zone of alteration forms as BSE-bright hemispherical bulges in the host ilmenite megacryst. The centre of these bulges often host a BSE-dark phases, presumably glass or serpentine (Chapter 3.5.5; Fig. 3.5). The TiO_2 of this zone increases inwards from 37.19–53.54 wt%, FeO decreases inward from 30.4–1.16 wt%, and CaO remains fairly consistent (22.95–25.83 wt%) with the exception of the most inner part of the hemispherical bulge which produced 43.93 wt% CaO (Table 44). Stoichiometrically this zone is incompatible with perovskite due to high Fe contents. It is interpreted to form due to the alteration of the ilmenite megacryst by the captured Ca-rich melt. Subhedral kassite also forms in interior positions within the melt inclusion and is composed of 68.5 wt% TiO_2, 4.27 wt% FeO and 24.83 wt% CaO (Table 44).

Table 44
EDS analysis of kassite in MI1 of sample S5628 and a Ca-rich reaction zone that forms along the melt-inclusion megacryst interface, bulging into the host ilmenite megacryst (Fig. 3.5).

Site	MI interior	ILM–MI reaction: outer bulge	ILM–MI reaction: middle bulge	ILM–MI reaction: inner bulge
Analysis	Kassite 1	Ca-Ilm	Ca-Ilm	Ca-Ilm
SiO_2	0.17	1.09	0.08	0.06
Al_2O_3	0.00	0.17	0.11	0.10
Fe_2O_3	0.00	0.00	0.00	0.00
Cr_2O_3	0.99	0.03	0.00	0.01
TiO_2	63.02	37.19	47.54	53.54
FeO	0.00	30.40	26.97	1.16
MgO	0.88	1.34	0.17	0.14
MnO	3.91	0.25	0.21	0.03
CaO	22.85	28.56	22.95	43.93
NiO	0.00	0.00	0.00	0.04
Na_2O	0.00	0.26	0.49	0.49
K_2O	0.00	0.02	0.02	0.05
H_2O	7.52	0.00	0.00	0.00
SO_3	0.00	0.11	0.00	0.00
Total	99.33	99.43	98.55	99.54
Cation proportions of kassite calculated for 5 O				
Si	0.01	0.03	0.00	0.00
Al	0.00	0.01	0.00	0.00
Fe^{3+}	0.00	0.00	0.00	0.00
Cr	0.03	0.00	0.00	0.00
Ti	1.89	0.72	0.89	0.93
Fe^{2+}	0.00	0.65	0.56	0.02
Mg	0.05	0.05	0.01	0.00
Mn	0.13	0.01	0.00	0.00
Ca	0.98	0.79	0.62	1.09
Ni	0.00	0.00	0.00	0.00
Na	0.00	0.01	0.02	0.02
K	0.00	0.00	0.00	0.00
OH	2.00	0.00	0.00	0.00
(SO_3)	0.00	0.00	0.00	0.00
Total	5.09	2.26	2.11	2.08
Ti	1.89	0.72	0.89	0.93
Ca, Fe^{2+}, Na	0.98	1.45	1.20	1.13
Other	0.22	0.09	0.02	0.01
XMg	1.00	0.07	0.01	0.18
XCa	0.95	0.53	0.52	0.98

4.3.6 Phlogopite

Phlogopite compositions are variable but generally show an Al_2O_3-poor composition compared to phlogopites typically observed in Group I kimberlites (< 12 wt %; Fig. 4.12). Phlogopite grains may be uniform in composition within a melt inclusion or display magmatic zoning form core to rim. The zonation of phlogopites forms as a result of a general compositional trend of increasing Fe_2O_3 with decreasing Al_2O_3 and TiO_2, towards tetraferriphlogopite, from core to rim (Fig. 4.13).

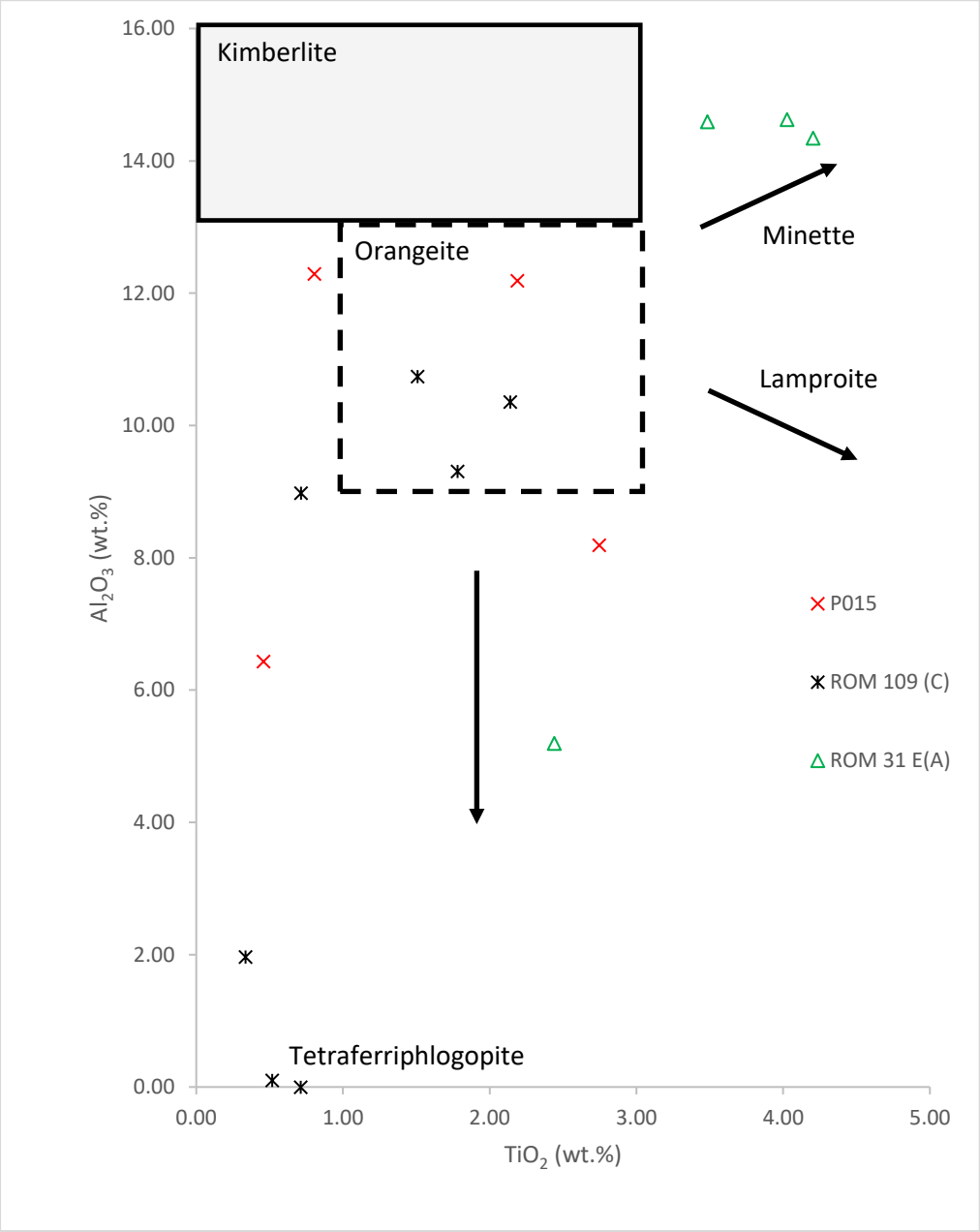

Fig. 4.12. Binary diagram of TiO_2 versus Al_2O_3 for phlogopite. Phlogopite is consistent with phlogopite in Group II kimberlites/orangeite and has a variable Al and Ti composition. Paragenetic fields for phlogopite evolution are from Mitchell (1995b).

Sample ROM 31E (A) MI1 hosts euhedral phlogopite which forms in coherent glass pools (Fig 3.11). The phlogopite grains are compositionally homogenous and composed of an Al_2O_3- and TiO_2-rich, Fe-poor composition of Al_2O_3 (14.34–14.63 wt%), TiO_2 (3.48–4.20 wt%), FeO (5.49–5.76 wt%), and K_2O (9.99–10.40 wt%), with a volatile component of 4.11–4.26 wt% H_2O (Fig. 4.12; Table 45). According to calculations optimising for stoichiometric fit, all Fe is present as Fe^{2+}. MI2 of the same sample comprises less Al_2O_3 (5.2 wt%), and TiO_2 (2.44 wt%) with an Fe_2O_3-rich composition (10.96 wt%; Table 45) indicating the substitution of Al by Fe^{3+}, and hence a large ferrian mica component in the solid solution.

Table 45
EDS analysis of phlogopite in MI1 and MI2 of sample ROM 31E(A) (Fig. 3.11).

Site	MI1 Det1	MI1 Det1	MI1 Det1	MI2 Det1
Analysis	Phlog1	Phlog2	Phlog3	Phlog1
SiO_2	38.98	39.39	39.13	42.38
Al_2O_3	14.63	14.59	14.34	5.20
Fe_2O_3	0.00	0.00	0.00	10.96
Cr_2O_3	0.00	0.07	0.05	0.02
TiO_2	4.03	3.48	4.20	2.44
FeO	5.49	5.68	5.76	0.52
MgO	21.60	22.10	21.73	26.48
MnO	0.17	0.00	0.02	0.10
CaO	0.00	0.02	0.18	0.43
NiO	0.00	0.00	0.00	0.00
Na_2O	0.33	0.32	0.19	0.19
K_2O	10.40	9.99	9.99	8.25
H_2O	4.19	4.21	4.20	4.25
SO_3	0.00	0.22	0.12	0.00
Total	99.82	100.08	99.91	101.22
Cation proportions calculated for 11 O				
Si	2.79	2.81	2.80	2.99
Al	1.23	1.23	1.21	0.43
Fe^{3+}	0.00	0.00	0.00	0.58
Cr	0.00	0.00	0.00	0.00
Ti	0.22	0.19	0.23	0.13
Fe^{2+}	0.33	0.34	0.34	0.03
Mg	2.30	2.35	2.31	2.79
Mn	0.01	0.00	0.00	0.01
Ca	0.00	0.00	0.01	0.03
Ni	0.00	0.00	0.00	0.00
Na	0.04	0.04	0.03	0.03
K	0.95	0.91	0.91	0.74
OH	2.00	2.00	2.00	2.00
(SO_3)	0.00	0.01	0.01	0.00
Total	9.88	9.88	9.85	9.76
Interl: K, Ca,				
Na (1)	0.99	0.95	0.95	0.80
Tet				
Si	2.79	2.81	2.80	2.99
Al IV	1.21	1.19	1.20	0.43
Fe^3 IV	0.00	0.00	0.00	0.58
Tet	4.00	4.00	4.00	4.00
Oct				
Fe^2	0.33	0.34	0.34	0.03
Mg	2.30	2.35	2.31	2.79
Al VI	0.02	0.03	0.00	0.00
Ti	0.22	0.19	0.23	0.13
Fe^3 VI	0.00	0.00	0.00	0.01
Mn	0.01	0.00	0.00	0.01
Cr	0.00	0.00	0.00	0.00
Total Oct	2.88	2.91	2.89	2.96
OH	2.00	2.00	2.00	2.00
XFe	0.12	0.13	0.13	0.01
XFe (tot)	0.12	0.13	0.13	0.18
$Fe^3/(Fe^2+Fe^3)$	0.00	0.00	0.00	0.95

Phlogopite may also exhibit compositional variations in Al_2O_3–Fe_2O_3 within a grain, such as in sample ROM 109 (C) MI1. Phlogopite in this sample forms two large euhedral crystals which show internal compositional variation between the core and rim. This variation is

observable in BSE images (Fig. 3.9). The rim of the phlogopite grains has a lighter BSE signal intensity compared to the interior of the grain (Fig. 3.9). EDS analyses attributed this to variations in Al_2O_3–Fe_2O_3 composition. The rim comprises of tetraferriphlogopite with 14.70–16.61 wt% Fe_2O_3 and <1.97 wt% Al_2O_3. The interior comprises lower Fe_2O_3 (2.90–3.82 wt%) and higher Al_2O_3 (8.89–10.36 wt%) contents (Table 46). The majority of Fe occurs in the form Fe^{3+} calculated stoichiometrically; FeO contents show no variation between rim and core analyses (0.79–2.13 wt%). The phlogopite grains are uniform in other major elements across the grain and consist of SiO_2 (42.47–43.54 wt%), MgO (25.00–26.31 wt%), K_2O (10.18–10.51 wt%), and minor amounts of TiO_2 (0.34–2.14 wt%), Na_2O (<0.56 wt%), and NiO (<0.27 wt%) with a volatile component of 4.11–4.26 H_2O (Table 46). Phlogopite with similar compositional variations was identified in sample P015. The phlogopite is composed of variable Al_2O_3 (6.43–12.29 wt%) and Fe_2O_3 (2.67–10.91 wt%) with uniform FeO (<2.94 wt%) (Table 47). The analysed phlogopites from all melt inclusions therefore show a trend of decreasing Al^{3+} (from values similar to Group II kimberlites; Fig. 4.12) with increasing Fe^{3+} (Fig. 4.13).

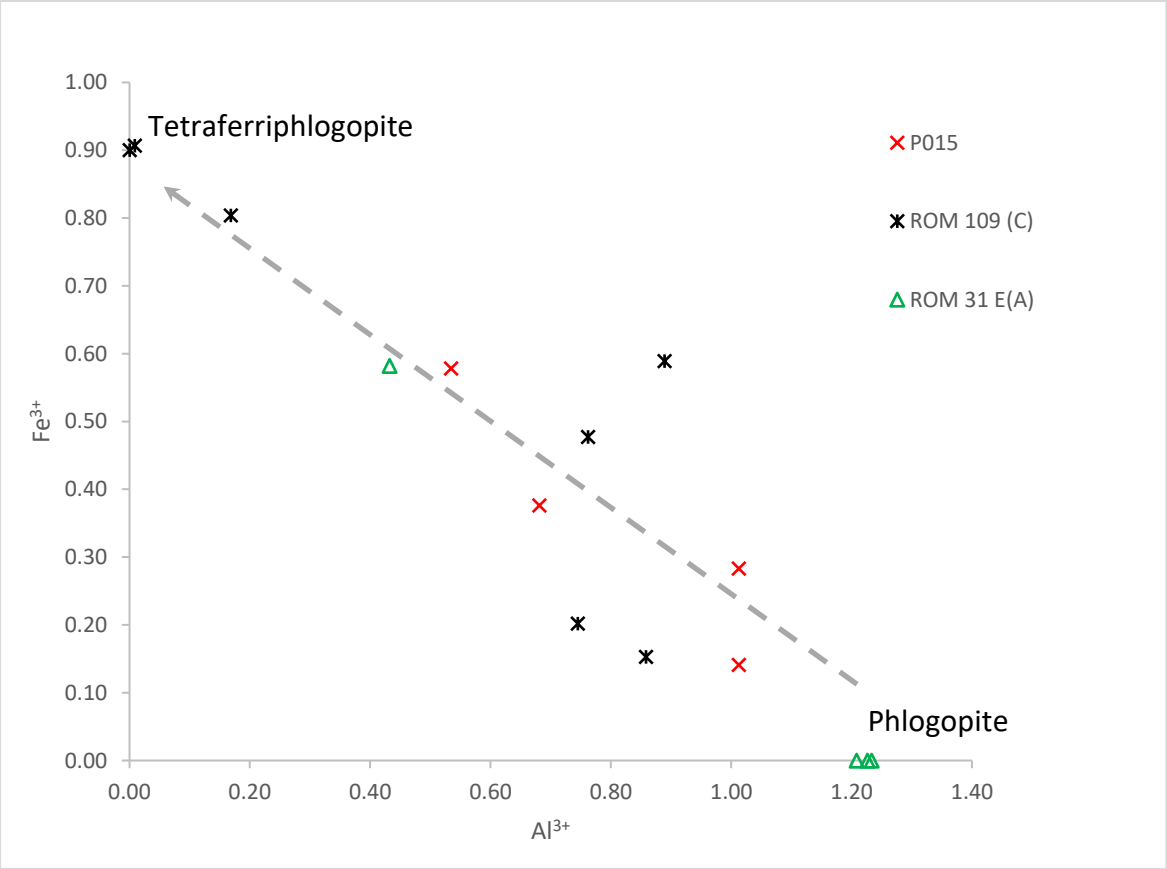

Fig. 4.13. Fe^{3+} versus Al^{3+} showing the trend from phlogopite to tetraferriphlogopite.

Table 46

EDS analysis of phlogopite in MI1 of sample ROM 109 (C) (Fig.3.9).

Comment	Rim	Core	Core	Rim	Rim
Site	MI1 Det1	MI1 Det1	MI1 Det1	MI1 Det2	MI1 Det2
Analysis	Phlog1	Phlog2	Phlog4	Phlog1	Phlog2
SiO_2	43.02	42.47	43.54	42.59	42.75
Al_2O_3	0.10	10.36	8.98	1.97	0.00
Fe_2O_3	16.61	2.90	3.82	14.70	16.41
Cr_2O_3	0.00	0.00	0.00	0.00	0.00
TiO_2	0.52	2.14	0.71	0.34	0.71
FeO	0.79	2.13	2.29	1.47	1.64
MgO	25.65	25.48	26.31	25.00	25.23
MnO	0.03	0.00	0.00	0.00	0.00
CaO	0.05	0.00	0.08	0.13	0.00
NiO	0.00	0.27	0.00	0.00	0.00
Na_2O	0.56	0.13	0.00	0.32	0.22
K_2O	10.18	10.19	10.51	10.37	10.34
H_2O	4.13	4.26	4.26	4.13	4.11
SO_3	0.02	0.02	0.14	0.18	0.00
Total	101.64	100.35	100.64	101.21	101.41
Cation proportions calculated for 11 O					
Si	3.12	2.99	3.07	3.10	3.12
Al	0.01	0.86	0.75	0.17	0.00
Fe^{3+}	0.91	0.15	0.20	0.80	0.90
Cr	0.00	0.00	0.00	0.00	0.00
Ti	0.03	0.11	0.04	0.02	0.04
Fe^{2+}	0.05	0.12	0.13	0.09	0.10
Mg	2.77	2.67	2.76	2.71	2.74
Mn	0.00	0.00	0.00	0.00	0.00
Ca	0.00	0.00	0.01	0.01	0.00
Ni	0.00	0.01	0.00	0.00	0.00
Na	0.08	0.02	0.00	0.05	0.03
K	0.94	0.91	0.94	0.96	0.96
OH	2.00	2.00	2.00	2.00	2.00
(SO_3)	0.00	0.00	0.01	0.01	0.00
Total	9.90	9.86	9.90	9.91	9.89
Interl: K, Ca, Na (1)	1.02	0.93	0.95	1.02	0.99
Tet					
Si	3.12	2.99	3.07	3.10	3.12
Al IV	0.01	0.86	0.75	0.17	0.00
Fe^3 IV	0.87	0.15	0.19	0.73	0.88
Tet	4.00	4.00	4.00	4.00	4.00
Oct					
Fe^2	0.05	0.12	0.13	0.09	0.10
Mg	2.77	2.67	2.76	2.71	2.74
Al VI	0.00	0.00	0.00	0.00	0.00
Ti	0.03	0.11	0.04	0.02	0.04
Fe^3 VI	0.04	0.00	0.01	0.07	0.02
Mn	0.00	0.00	0.00	0.00	0.00
Cr	0.00	0.00	0.00	0.00	0.00
Total Oct	2.88	2.91	2.95	2.89	2.90
OH	2.00	2.00	2.00	2.00	2.00
XFe	0.017	0.045	0.047	0.032	0.035
XFe (tot)	0.256	0.094	0.109	0.248	0.267
$Fe^3/(Fe^2+Fe^3)$	0.95	0.55	0.60	0.90	0.90

Table 47

EDS analysis of phlogopite in MI2 and MI6 of sample P015 (Fig.3.15).

Comment	MI2 det1	MI2 det1	MI2 det1	MI6 Ov1
Analysis	Phlog1	Phlog2	Phlog3	Phlog1
SiO_2	42.27	41.11	40.52	41.53
Al_2O_3	6.43	12.29	12.19	8.19
Fe_2O_3	10.91	5.39	2.67	7.09
Cr_2O_3	0.00	0.13	0.10	0.00
TiO_2	0.46	0.80	2.19	2.75
FeO	0.00	0.54	2.94	0.00
MgO	27.70	26.34	25.53	26.86
MnO	0.12	0.08	0.01	0.20
CaO	0.02	0.05	0.28	0.39
NiO	0.14	0.14	0.00	0.17
Na_2O	0.09	0.00	0.24	0.36
K_2O	8.87	9.56	9.39	8.02
H_2O	4.26	4.29	4.25	4.25
SO_3	0.00	0.02	0.05	0.15
Total	101.26	100.76	100.35	99.96
Cation proportions calculated for 11 O				
Si	2.98	2.87	2.86	2.93
Al	0.53	1.01	1.01	0.68
Fe^{3+}	0.58	0.28	0.14	0.38
Cr	0.00	0.01	0.00	0.00
Ti	0.02	0.04	0.12	0.15
Fe^{2+}	0.00	0.03	0.17	0.00
Mg	2.91	2.74	2.68	2.83
Mn	0.01	0.00	0.00	0.01
Ca	0.00	0.00	0.02	0.03
Ni	0.01	0.01	0.00	0.01
Na	0.01	0.00	0.03	0.05
K	0.80	0.85	0.85	0.72
OH	2.00	2.00	2.00	2.00
(SO_3)	0.00	0.00	0.00	0.01
Total	9.85	9.86	9.89	9.79
Interl: K, Ca, Na (1)	0.81	0.85	0.90	0.80
Tet				
Si	2.98	2.87	2.86	2.93
Al IV	0.53	1.01	1.01	0.68
Fe^3 IV	0.49	0.11	0.13	0.39
Tet	4.00	4.00	4.00	4.00
Oct				
Fe^2	0.00	0.03	0.17	0.00
Mg	2.91	2.74	2.68	2.83
Al VI	0.00	0.00	0.00	0.00
Ti	0.02	0.04	0.12	0.15
Fe^3 VI	0.09	0.17	0.01	-0.01
Mn	0.01	0.00	0.00	0.01
Cr	0.00	0.01	0.00	0.00
Total Oct	3.03	3.00	2.99	2.97
OH	2.00	2.00	2.00	2.00
XFe	0.000	0.011	0.060	0.000
XFe (tot)	0.166	0.103	0.105	0.117
$Fe^3/(Fe^2+Fe^3)$	1.00	0.90	0.45	1.00

A ternary diagram of Al_2O_3-MgO-FeO^T (FeO^T = FeO + Fe_2O_3) of the analysed phlogopites shows that the initial trend of the phlogopites is of decreasing Al_2O_3 with increasing MgO at constant FeO^T (Fig. 4.14). This is followed by a trend of decreasing Al_2O_3 with increasing FeO^T, towards tetraferriphlogopite, at constant MgO, from core to rim (Fig. 4.14).

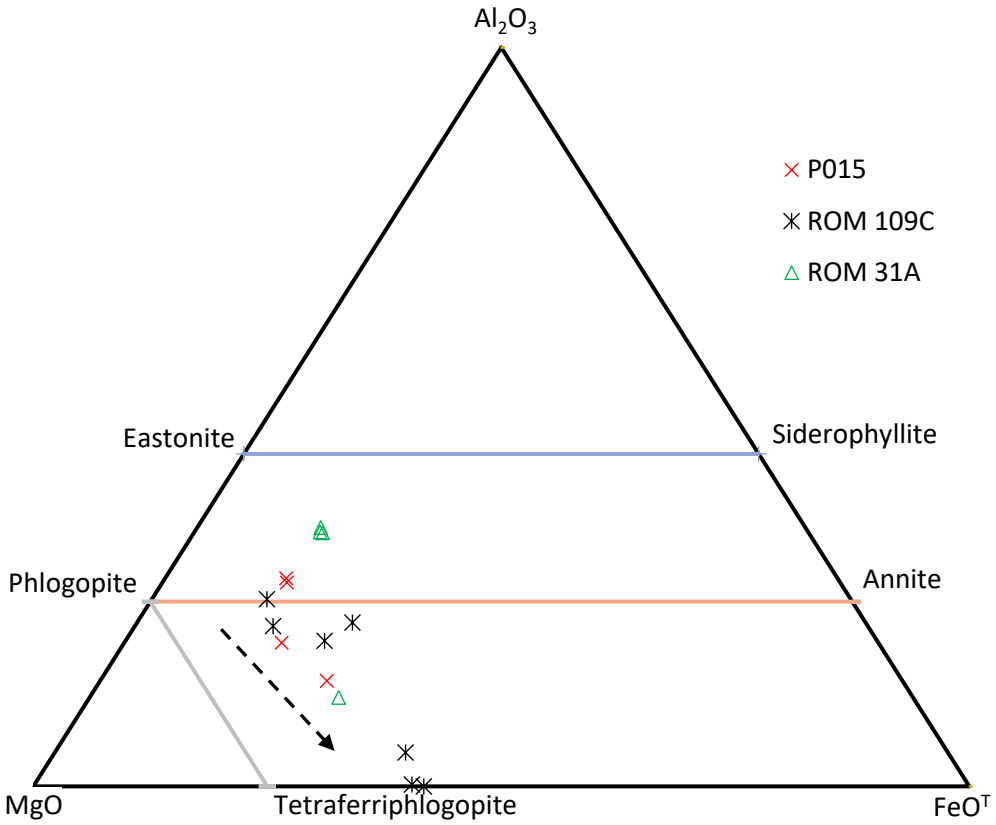

Fig. 4.14. Ternary diagram of Al_2O_3-MgO-FeO^T for phlogopite showing the trend of decreasing Al and increasing Fe (dashed arrow) to tetraferriphlogopite at constant MgO(FeO^T = FeO + Fe_2O_3).

Chapter 5: Trace element analysis

5.1 Ilmenite megacrysts

Trace element analysis transects were performed on the host ilmenite megacryst and around certain melt inclusions in samples P015, ROM 109 (C), and S5628 (Fig. 5.1). Trace element analyses were also performed around certain melt inclusions in samples S5626 and ROM 264 (see Table 50–Table 57 in the appendix). Trace element transects show Zr vs Nb concentrations most consistent with Group 2 ilmenites identified at the Monastery kimberlite by Moore et al. (1992) (Fig. 5.2). Sample ROM 109 (C) shows a range of Zr concentrations with uniform Nb, indicating co-crystallisation with zircon megacrysts.

The primitive mantle-normalised trace element patterns of the transects show uniform characteristic large Nb-Ta and Hf-Zr positive anomalies across all samples, with variable negative Sr and positive Pb anomalies (Fig. 5.3). REE abundances are variable but generally show low concentrations relative to chondrite (0.02–0.2 x chondrite), with a uniform Yb-enrichment (1.3–2 x chondrite) (Fig. 5.3). Variations in the primitive mantle and chondrite-normalised values occur within a particular megacryst (i.e S5628; Fig. 5.3). One analysis in transect 1 (sample P015) produced higher primitive mantle and chondrite-normalised concentrations. This point was performed around MI2 of sample P015 near the margins of the megacryst in contact with kimberlite matrix (Fig. 5.3).

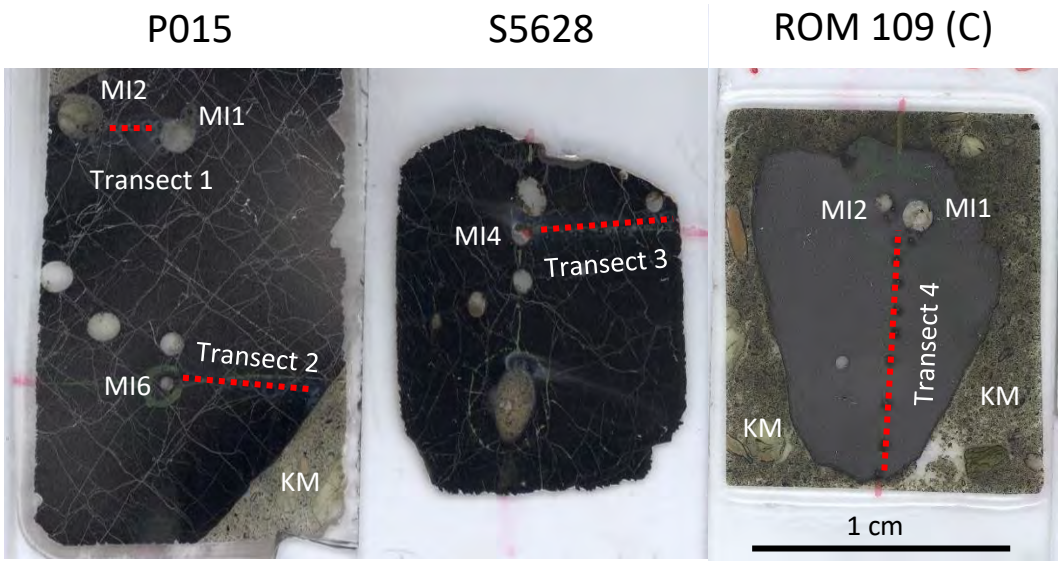

Fig. 5.1. Scans of samples P015, S5628, and ROM 109 (C) showing trace element transects (Fig. 5.2) performed across the ilmenite megacrysts (KM = kimberlite matrix; MI = melt inclusion).

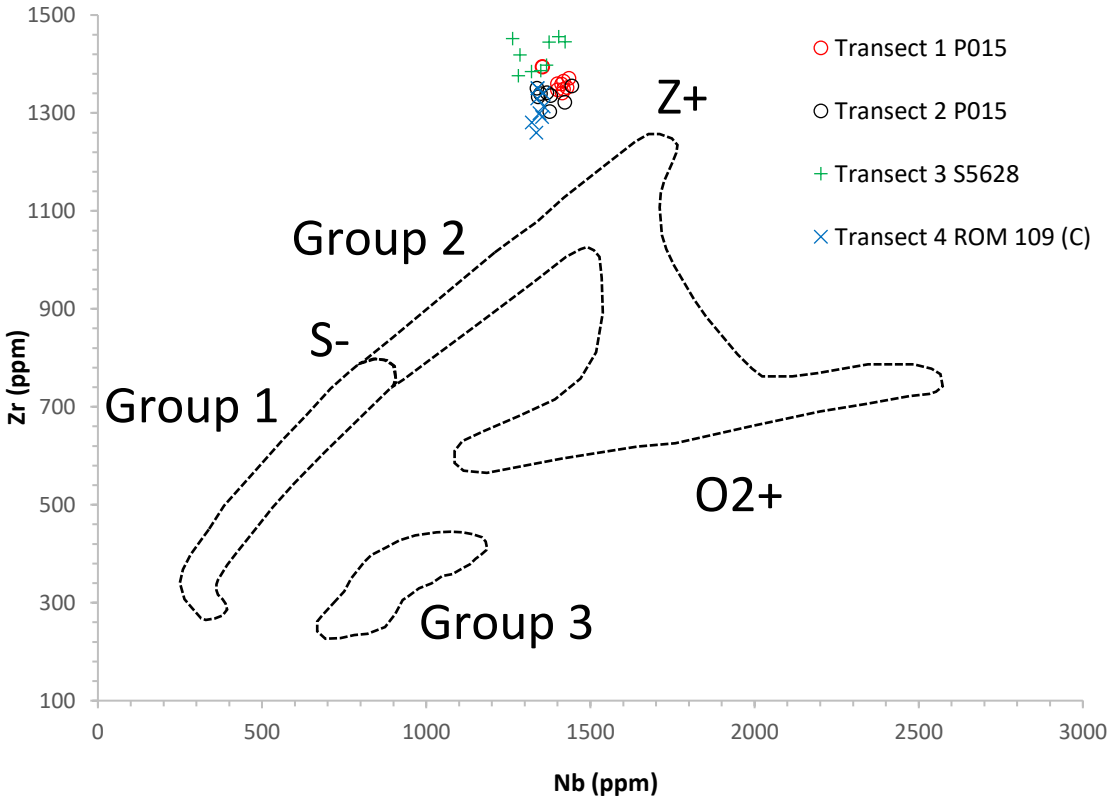

Fig. 5.2. Plot of Zr vs Nb for transects across ilmenite megacrysts of samples P015, ROM 109 (C), and S5628 from the Monastery kimberlite. The idealised compositional trends of Group 1, Group 2 and Group 3 ilmenites identified at the Monastery kimberlite are modified after Moore et al. (1992). The compositional trends are a result of crystallisation of the cumulate megacryst assemblage; S- marks the end of cpx, opx, and garnet crystallisation; Z+ marks the start of zircon crystallisation; O2+ marks the start of Fe-rich olivine crystallisation. Zr vs Nb concentrations in the samples in this study are most consistent with Group 2 ilmenites. Sample ROM 109 (C) shows the lowest Zr concentrations which are variable at constant Nb. Sample S5628 shows the highest Zr concentrations.

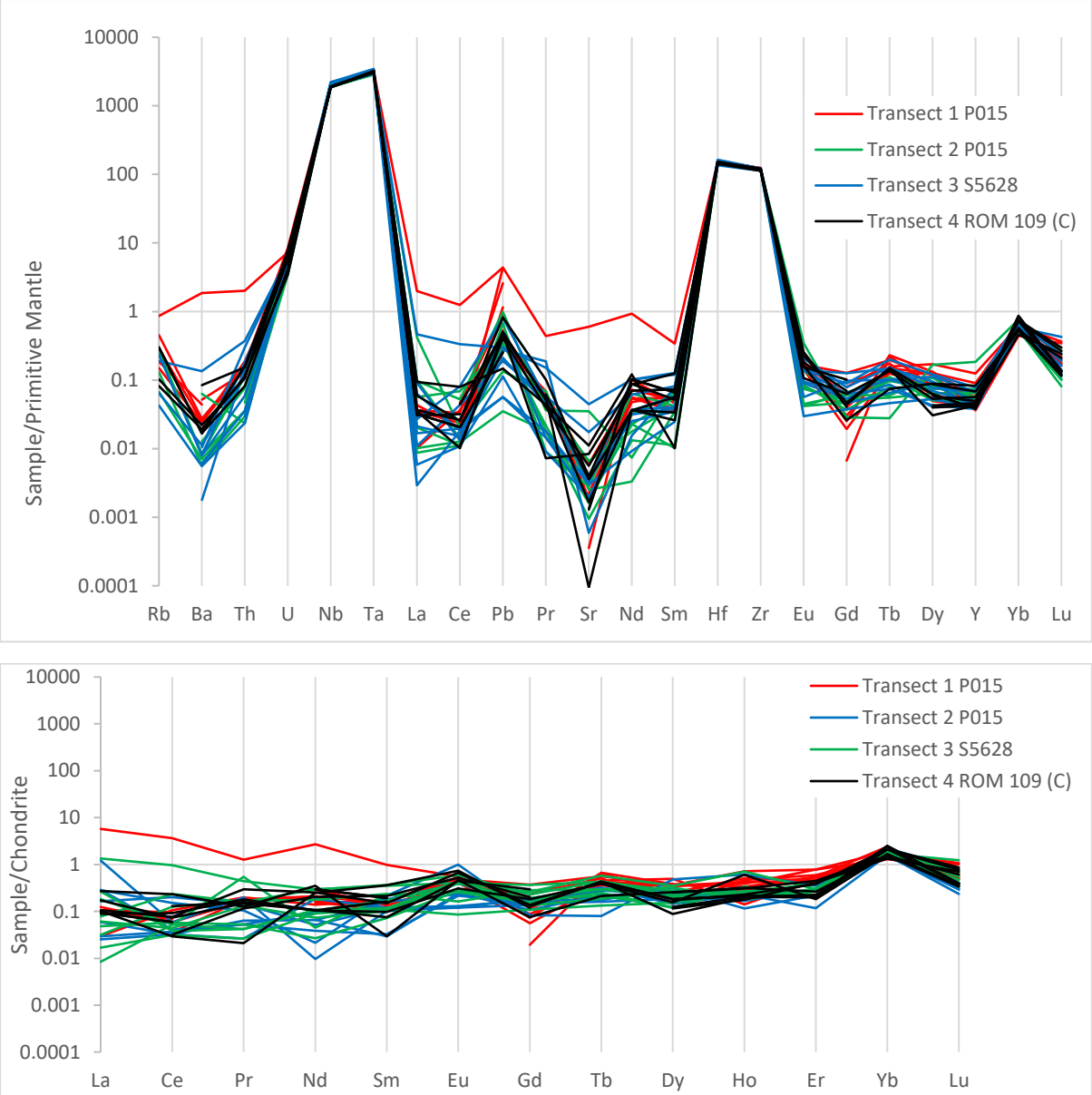

Fig. 5.3. Chondrite-normalised and primitive mantle-normalised (values from Sun and McDonough, 1989) and trace element diagrams for transects across the ilmenite megacrysts of sample P015, S5628, and ROM 109 (C) (Fig. 5.1). The ilmenite megacryst are relatively depleted in comparison to primitive mantle but are characterised by large uniform Nb-Ta and Hf-Zr positive anomalies, with variable positive Pb and variable negative Sr anomalies. Ba is generally depleted with the exception of one analysis in sample P015 that also shows slightly higher trace element and REE concentrations. LREE are variably depleted and appear slightly more depleted than HREE. HREE show more uniform concentrations, with a Yb enrichment (gaps are analyses that were below detection limits).

Trace element point analyses around certain MIs in samples P015, S5628, S5626, ROM 109 (C), and ROM264 show systematic variations in terms of Zr and Nb between samples and within a particular ilmenite megacryst. A plot of all analyses (including transects) within ilmenite megacrysts shows a trend of increasing Zr and Nb, followed by decreasing Zr at constant Nb (Fig. 5.4). The ilmenite megacryst compositions are consistent with trends characteristic of Group 1 and 2 ilmenites (Moore et al., 1992) (Fig. 5.4). The ilmenite megacryst of sample ROM 264 represents the most primitive composition for the data set

for which trace elements are available, followed by ilmenite megacrysts of sample S5626, and finally, samples P015, S5628, and ROM 109 (C) (Fig 5.4). The ilmenite megacrysts are relatively depleted in comparison to primitive mantle but are characterised by variable large Nb-Ta and Hf-Zr positive anomalies (Fig. 5.5). Sample ROM 264 shows the lowest Nb-Ta and Hf-Zr anomalies, followed by S5626. Samples ROM 264 and S5626 also show generally lower primitive mantle-normalised concentrations (particularly Ba, La, Pb, Sr, and Tb) (Fig. 5.5). Samples P015, S5628, and ROM 109 (C) show the largest uniform Nb-Ta and Hf-Zr anomalies (Fig. 5.5). The samples show variable positive Pb and variable negative Sr anomalies (Fig. 5.5). One analysis in sample ROM 109 (C) shows a positive Sr anomaly. REE chondrite-normalised profiles show low REE abundances (0.1–1 x chondrite) with a slight Yb enrichment (~3 x chondrite) (Fig. 5.5).

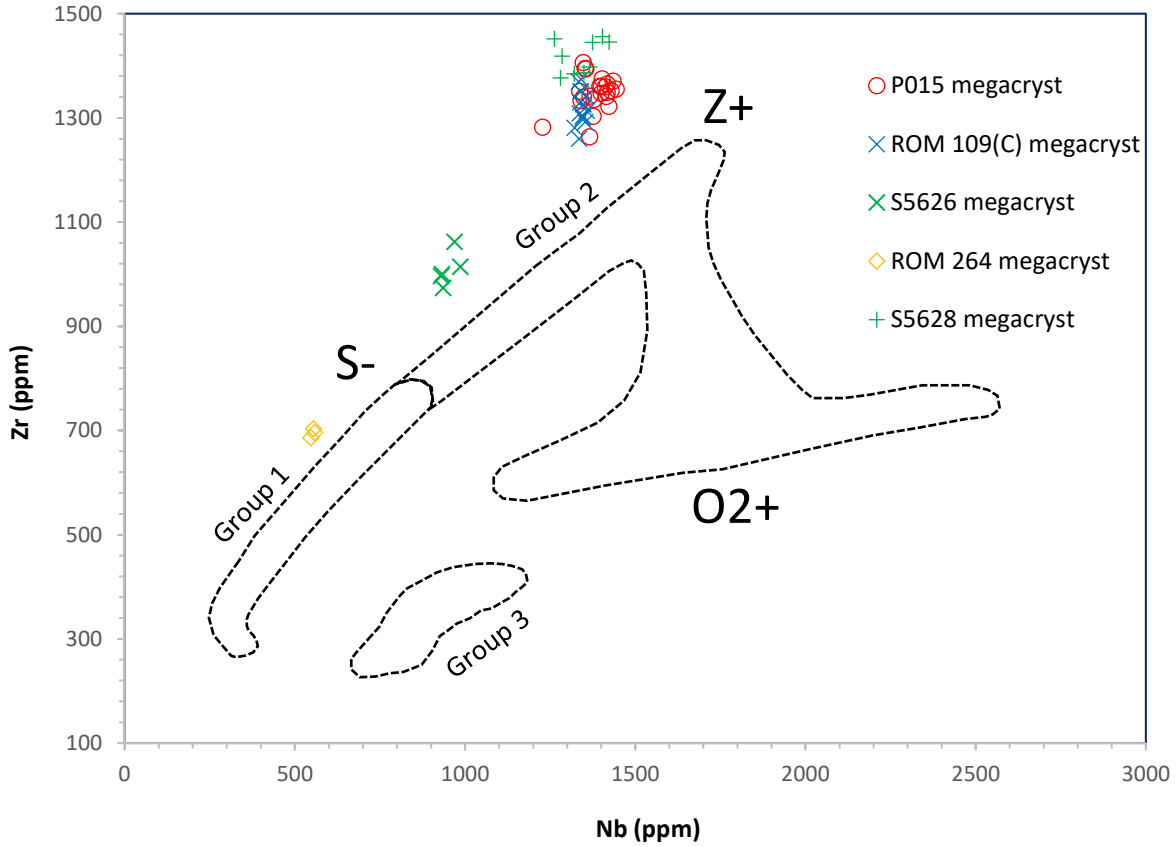

Fig. 5.4. Plot of Zr vs Nb for ilmenite megacrysts from the Monastery kimberlite. The fields are modified after Moore et al. (1992) showing the compositional trends of Group 1, Group 2, and Group 3 ilmenites identified at the Monastery kimberlite. The compositional trends are a result of crystallisation of the cumulate megacryst assemblage; S- marks the end of cpx, opx, and garnet crystallisation; Z+ marks the start of zircon crystallisation; O2+ marks the start of Fe-rich olivine crystallisation. The ilmenite megacrysts define a trend of increasing Zr and Nb, followed by decreasing Zr at constant Nb, consistent with trends characteristic of Group 1 and 2 ilmenites (Moore et al., 1992). The ilmenite megacryst of sample ROM 264 is consistent with Group 1 ilmenites and represents the most primitive composition, followed by ilmenite megacrysts of sample S5626, and finally, samples P015, S5628, and ROM 109 (C), which are consistent with Group 2 ilmenites.

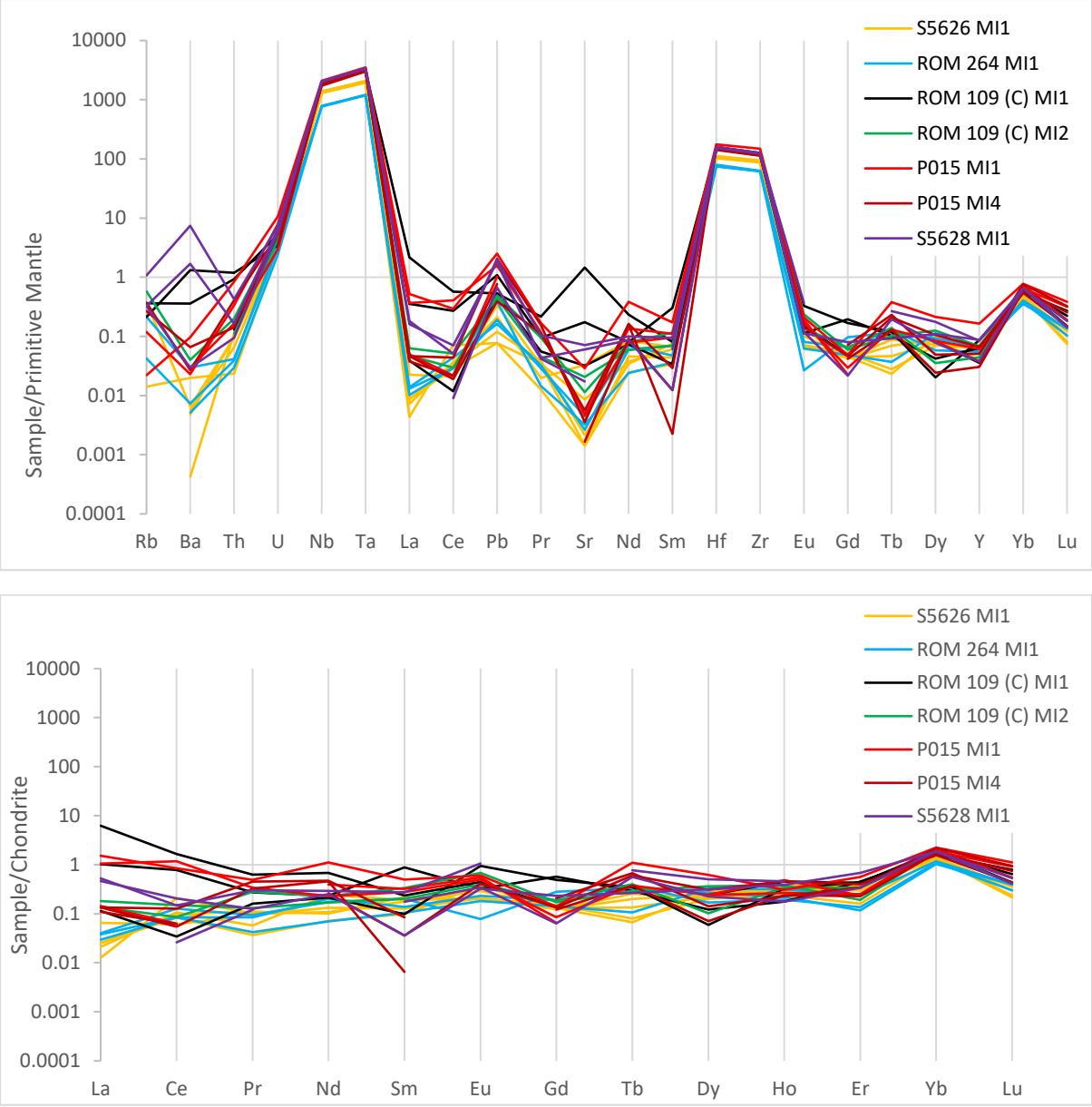

Fig. 5.5. Chondrite-normalised and primitive mantle-normalised (values from Sun and McDonough, 1989) trace element diagrams for point analyses around certain MIs within samples S5626, ROM 264, ROM 109 (C), P015, and S5628. The ilmenite megacrysts are relatively depleted in comparison to primitive mantle but are characterised by large Nb-Ta and Hf-Zr positive anomalies and variable positive Pb and variable negative Sr anomalies. LREE vary from slightly depleted to slightly enriched. HREE show more uniform depleted concentrations, with a Yb enrichment. Sample ROM 264 shows the lowest Nb-Ta and Hf-Zr concentrations. Sample S5626 shows slightly higher Nb-Ta and Hf-Zr anomalies. Sample ROM 264 and S5626 also appear more depleted in Ba, La, Pb, and LREE. Samples ROM 109 (C), P015, and S5628 show the largest Nb-Ta and Hf-Zr anomalies. Ba is generally depleted except for in sample S5628 MI1 and ROM 109 (C) MI2, which shows a positive Ba anomaly. Sample ROM 109 (C) MI2 also shows a positive Sr anomaly (gaps are analyses that were below detection limits).

A binary diagram shows that Nb versus MgO (acquired from corresponding EPMA transect and point analyses; Chapter 4.1) (Fig. 5.6) compositions are consistent with Group 1 ilmenites for sample ROM 264 and Group 2 ilmenites for the ilmenite megacryst of sample P015 and S5628 (Fig. 5.6). Sample ROM 109 (C) has a Nb concentration consistent with

Group 2 ilmenites, but with a higher MgO composition. Indicating it formed later in the megacrystic trend of Group 2 ilmenites (Fig. 5.6).

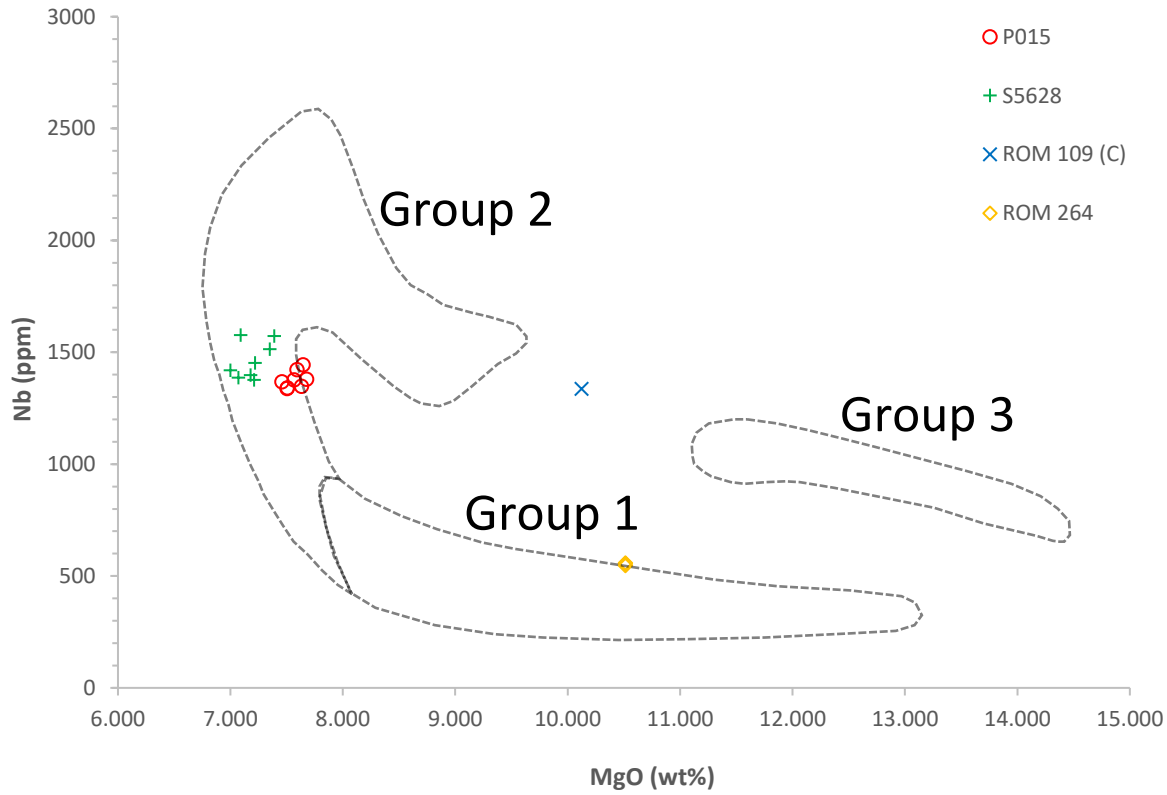

Fig. 5.6. Plot of MgO vs Nb for ilmenite megacrysts of sample P015, S5628, ROM 109 (C), and ROM 264 from the Monastery kimberlite. Fields are modified after Moore et al. (1992) showing the compositional differences between the three groups of ilmenites identified at the Monastery kimberlite. The composition of the ilmenite megacryst in sample ROM 264 is consistent with Group 1 ilmenites. Samples S5628 and P015 show compositions consistent with Group 2 ilmenites, indicating that they crystallised after sample ROM 264. Sample ROM 109 (C) shows Nb concentrations consistent with Group 2 ilmenites, but with larger MgO concentrations.

5.2 Glass and crystal phases hosted in melt inclusions

5.2.1 Glass

Trace element concentrations of glass within the melt inclusions (see Table 58–Table 60 in the appendix) show variations from depleted in REE abundances to LREE-enriched chondrite-normalised patterns. LREE-enriched chondrite-normalised patterns are ~10 x chondrite for LREE with HREE abundance of between 1–4 x chondrite, such as in sample P015 MI1, MI4; ROM 109 (C) MI1, MI2; and S5626 MI1 (Fig. 5.7). Some glass analysis shows no relative REE enrichment compared to chondrite values, such as sample S5628 MI1, which contains consistent REE concentrations between ~0.8–3 x chondrite (Fig. 5.8). In sample ROM 264 MI1, glass shows an LREE-enriched pattern, however, with lower REE concentrations. LREE abundances reach ~4 x chondrite and HREE are depleted, reaching ~0.5 x chondrite (Fig. 5.8).

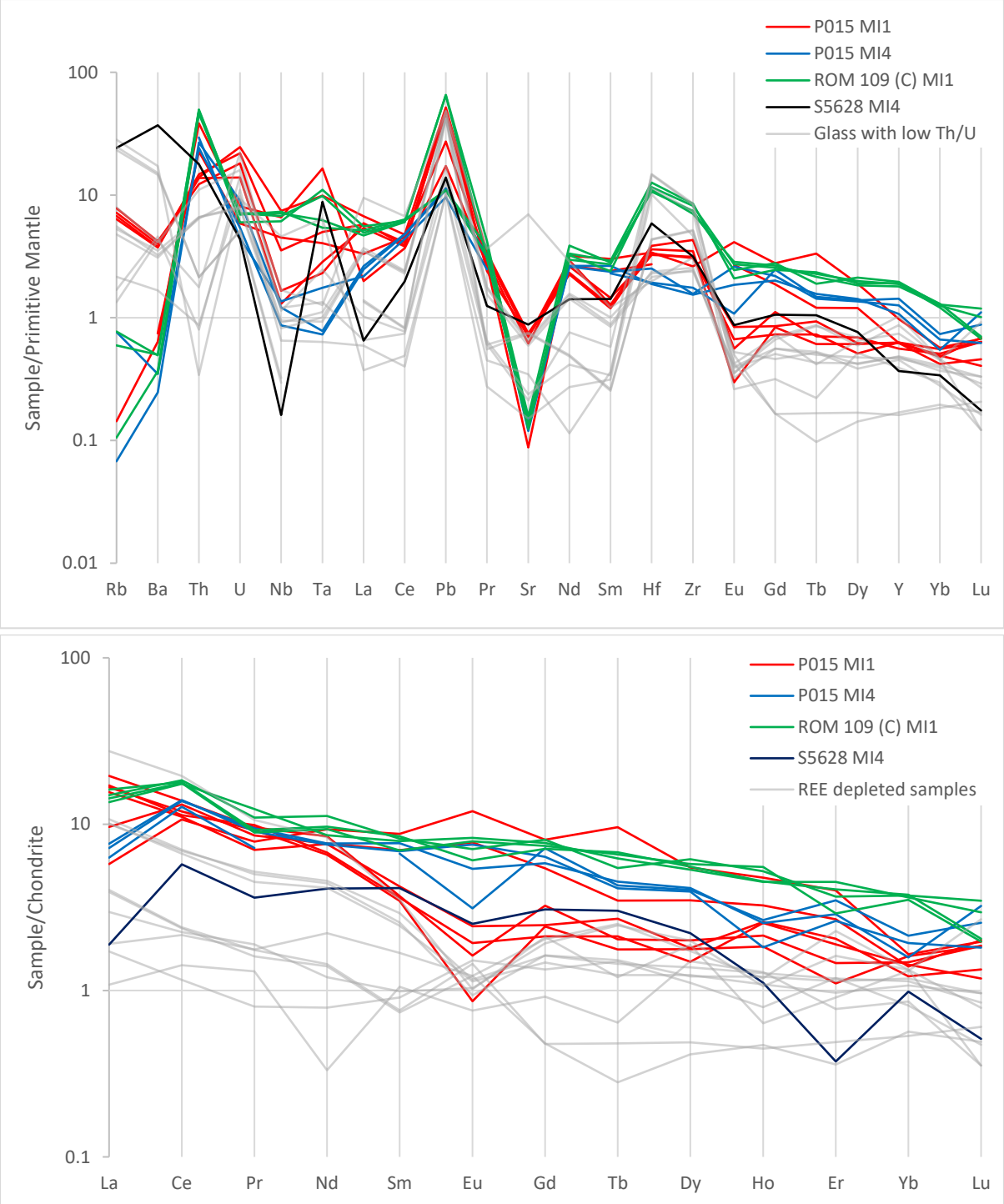

Fig. 5.7. Chondrite-normalised and primitive mantle-normalised (values from Sun and McDonough, 1989) trace element diagrams for glass hosted within sample P015 MI1, MI4; ROM 109 (C) MI1; S5628 MI4. Glass analyses in sample P015 MI1 show variations from high Th/U (4.74) to low Th/U (0.57). REE chondrite-normalised profiles show a general LREE enrichment but vary in abundances (particularly Eu–Er, which vary from 1–10 x chondrite). Glass hosted in ROM 109 (C) MI1, S5628 MI4, and P015 MI4 shows more uniform Th/U and REE abundances. The analyses show high Th/U (4.1–8.01) with LREE-enriched chondrite-normalised patterns (up to 18 x chondrite for LREE). Primitive mantle-normalised profiles show trace element abundances are generally high for glass in sample ROM 109 (C) MI1. Sample MI4 S5628 shows low La values (1.8 x chondrite). Grey lines represent glass analyses in samples ROM 109 (C) MI2, S5628 MI1, S5626 MI1, and ROM 264 which show uniform low Th/U and REE-depleted abundances for comparison (See Fig. 5.8).

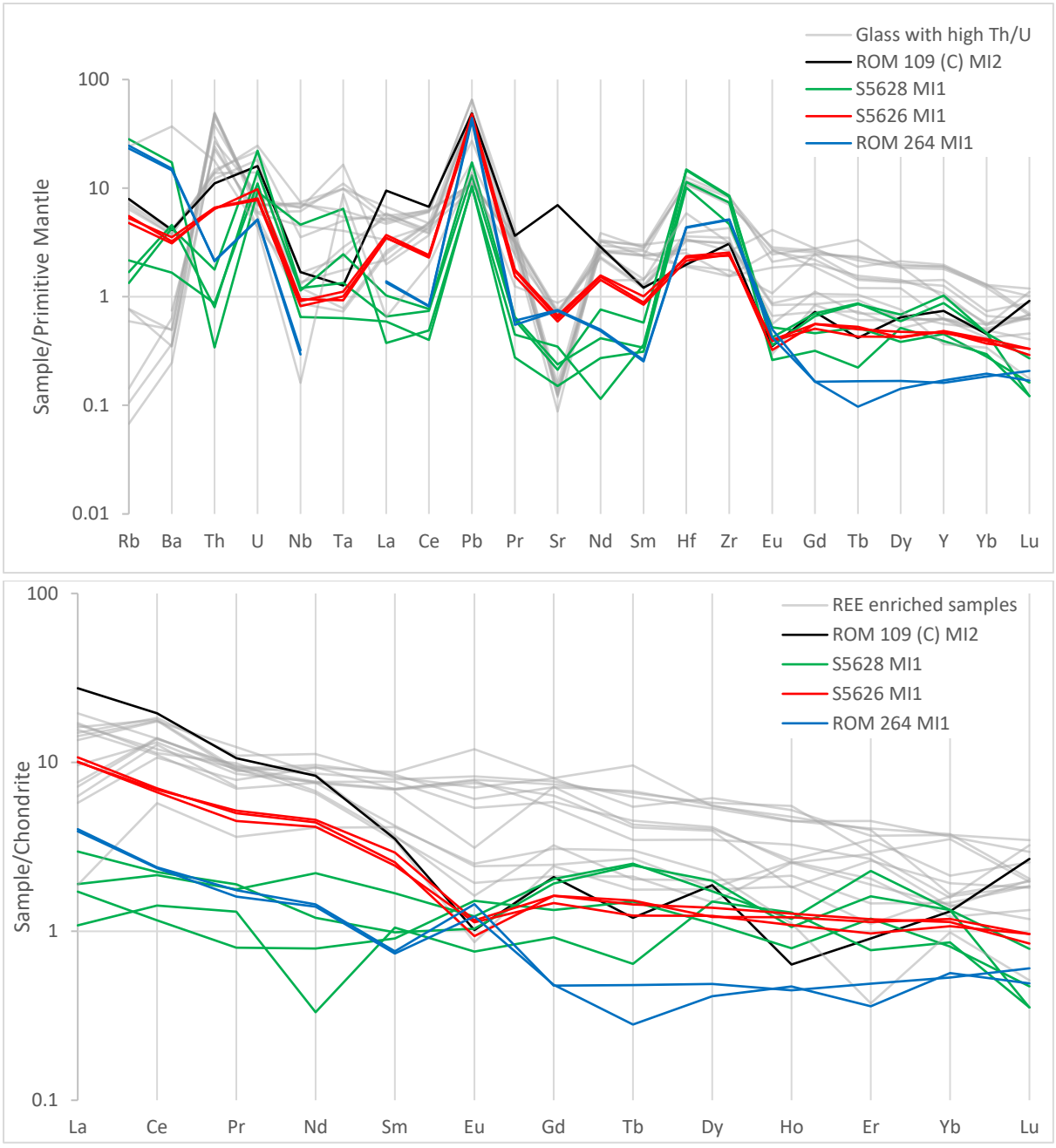

Fig. 5.8. Chondrite-normalised and primitive mantle-normalised (values from Sun and McDonough, 1989) trace element diagrams for glass hosted within samples ROM 109 (C) MI2; S5628 MI1; S5626 MI1; ROM 264 MI1. Glass in these samples shows low Th/U and REE abundances. Glass analyses in these samples show low Th/U (0.03–0.8) with REE abundances that show a slight LREE enrichment or values similar to chondrite values. Glass hosted S5626 MI1, ROM 109 (C) MI2, and ROM 264 MI1 produced an LREE-enriched chondrite-normalised pattern but with low HREE abundances. Glass hosted in ROM 109 (C) MI2 is uniquely enriched in Sr (3.6 x primitive mantle) (Fig. 5.11). Glass hosted in MI1 of S5628 shows REE abundances similar to chondrite values (0.3–2 x chondrite). Grey lines represent glass analyses in samples P015 MI1, MI4; ROM 109 (C) MI1; S5628 MI4 which generally show higher Th/U and REE abundances (except for sample P015 MI1 which shows a wide variation in Th/U and REE abundances) for comparison (Fig. 5.7).

Trace elements in glass show large variations in primitive mantle-normalised profiles. The variations occur between melt inclusions and within glass in individual melt inclusions. The variations in trace element abundances of glass are unrelated to textural and major element variations of glass (as described in Chapter 3 and 4, respectively). Glass generally varies in Th/U, Rb-Ba, Nb-Ta, and Hf-Zr abundances. Glass with high Th/U (up to 8 Th/U) generally shows LREE-enriched chondrite-normalised profiles (Fig. 5.7). Glass with low Th/U (0.04) shows lower REE abundances, with either an LREE-enriched chondrite-normalised pattern or REE abundances similar to chondrite values (Fig. 5.8). The Th/U of glass may be uniform within a melt inclusion (i.e. S5628 MI1, S5626 MI1, Rom 109 (C) MI1; Table 48) or show variation within a melt inclusions (P015 MI1; Fig. 5.7; Table 48).

Glass with high Th/U (>4 Th/U; i.e. samples P015 MI1 and MI4, ROM 109 (C) MI1, S5628 MI4; Fig.5.7) generally show higher trace element concentrations (particularly in terms of Eu–Lu, Nd-Sm, and La-Ce) compared to glass which shows a low Th/U (<1 Th/U; Fig. 5.8). Nb-Ta and Hf-Zr show wide variations in abundances and are similar between glass with low Th/U and high Th/U (Fig. 5.7; Fig. 5.8). Sr is generally depleted in glass, except for sample ROM 264 MI1 which shows an Sr enrichment (Fig. 5.8).

Analyses of glass show large variations in high-field strength elements (HFSE) relative to REE of similar incompatibility ($(Zr/Sm)_n$; $(Hf/Sm)_n$; Table 48). Glasses that are enriched in $(Zr/Sm)_n$ (up to ~25) and $(Hf/Sm)_n$ (up to ~40) generally show depleted Th/U (<0.01) which correspond to REE-poor glass (Fig. 5.9; Fig. 5.10). In contrast, glasses that are more depleted in Zr/Sm (<2) and Hf/Sm (<4) generally show enriched Th/U (up to 8) which correspond to REE-rich glass (Fig. 5.9; Fig. 5.10).

Table 48
Primitive mantle-normalised (n) Th/U, Zr/Sm, and Hf/Sm for glass

Sample	Site name	$(Th/U)_n$	$(Zr/Sm)_n$	$(Hf/Sm)_n$
P015	MI1Gl1	0.57	3.37	3.03
P015	MI1Gl2	0.68	2.93	3.02
P015	MI1Gl3	3.86	0.00	1.13
P015	MI1Gl4	0.67	2.52	2.60
P015	MI1Gl5	0.99	2.10	2.29
P015	MI1Gl6	4.74	0.87	1.13
P015	MI4Gl7	6.65	0.76	0.84
P015	MI4Gl8	2.97	0.66	1.06
P015	MI4Gl9	4.46	0.58	0.71
ROM 109 (C)	MI1Gl1	6.51	3.41	4.85
ROM 109 (C)	MI1Gl2	8.06	2.92	4.34
ROM 109 (C)	MI1Gl3	6.85	2.57	4.05
ROM 109 (C)	MI1Gl4	7.20	2.63	3.78
ROM 109 (C)	MI2Gl4	0.69	2.54	1.63
S5628	MI1Gl1	0.04	20.24	31.44
S5628	MI1Gl2	0.08	14.41	25.19
S5628	MI1Gl3	0.06	25.06	43.61
S5628	MI1Gl4	0.08	14.89	32.31
S5628	MI4Gl5	4.10	2.21	4.12
S5626	MI1Gl1	0.66	2.37	2.28
S5626	MI1Gl2	0.85	2.91	2.54
S5626	MI1Gl3	0.82	2.88	2.68
ROM 264	MIGl1	0.42	19.99	17.00
ROM 264	MIGl2	0.42	19.71	16.65

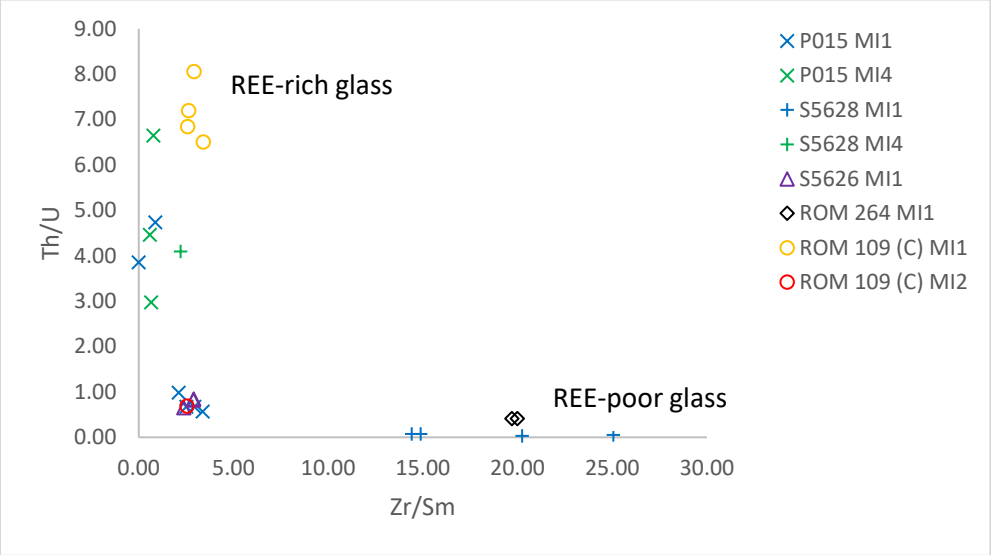

Fig. 5.9. $(Th/U)_n$ versus $(Zr/Sm)_n$ for glass analyses (Table 48). Glass with a high Th/U value shows low Zr/Sm values, which correspond to REE-rich glass. Glass with low Th/U values show high Zr/Sm values, which correspond to REE-poor glass (Fig. 5.8).

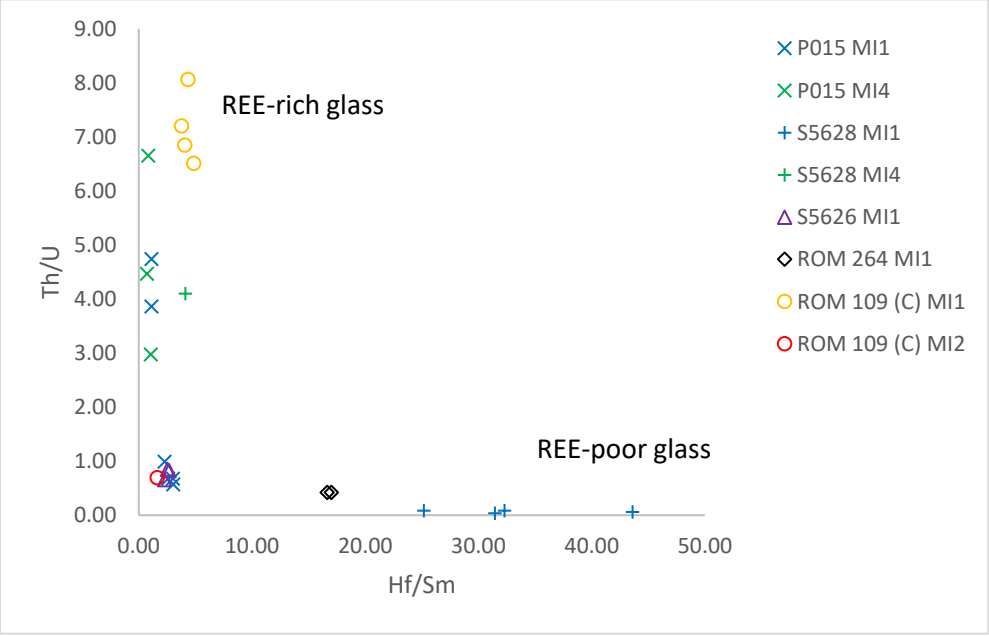

Fig. 5.10. $(Th/U)_n$ versus $(Hf/Sm)_n$ for glass analyses (Table 48). Glass with high Th/U values shows low Zr/Hf values, which correspond to REE-rich glass. Glass with low Th/U values shows high Zr/Hf values, which correspond to REE-poor glass (Fig. 5.7).

5.2.2 Calcite

Trace element analyses of calcite hosted in melt inclusions (see Table 61 and Table 62 in the appendix) show LREE-enriched chondrite-normalised patterns, similar to that of glass, but with a higher concentration of REE (Fig. 5.11). Calcite generally has LREE abundances of ~35–40 x chondrite and HREE abundances of ~2–4 x chondrite, such as in sample P015 MI1, MI4; ROM 109(C) MI1, MI2; S5628 MI4; S5626 MI1; ROM 264 (Fig. 5.11). Sample S5626 MI1 has the highest LREE abundances of up to ~80 x chondrite, with HREE abundances between ~2–4 x chondrite (Fig. 5.11). Primitive mantle-normalised diagrams of calcite are fairly uniform across all samples (Fig. 5.11). However, calcite in sample P015 shows higher Nb-Ta in comparison to other samples and calcite is sample S5626 shows higher La-Ce in comparison to other samples (Fig. 5.11). Calcite grains show uniform HFSE relative to REE of similar incompatibility (Zr/Sm ~2; Hf/Sm ~2) (Table 49).

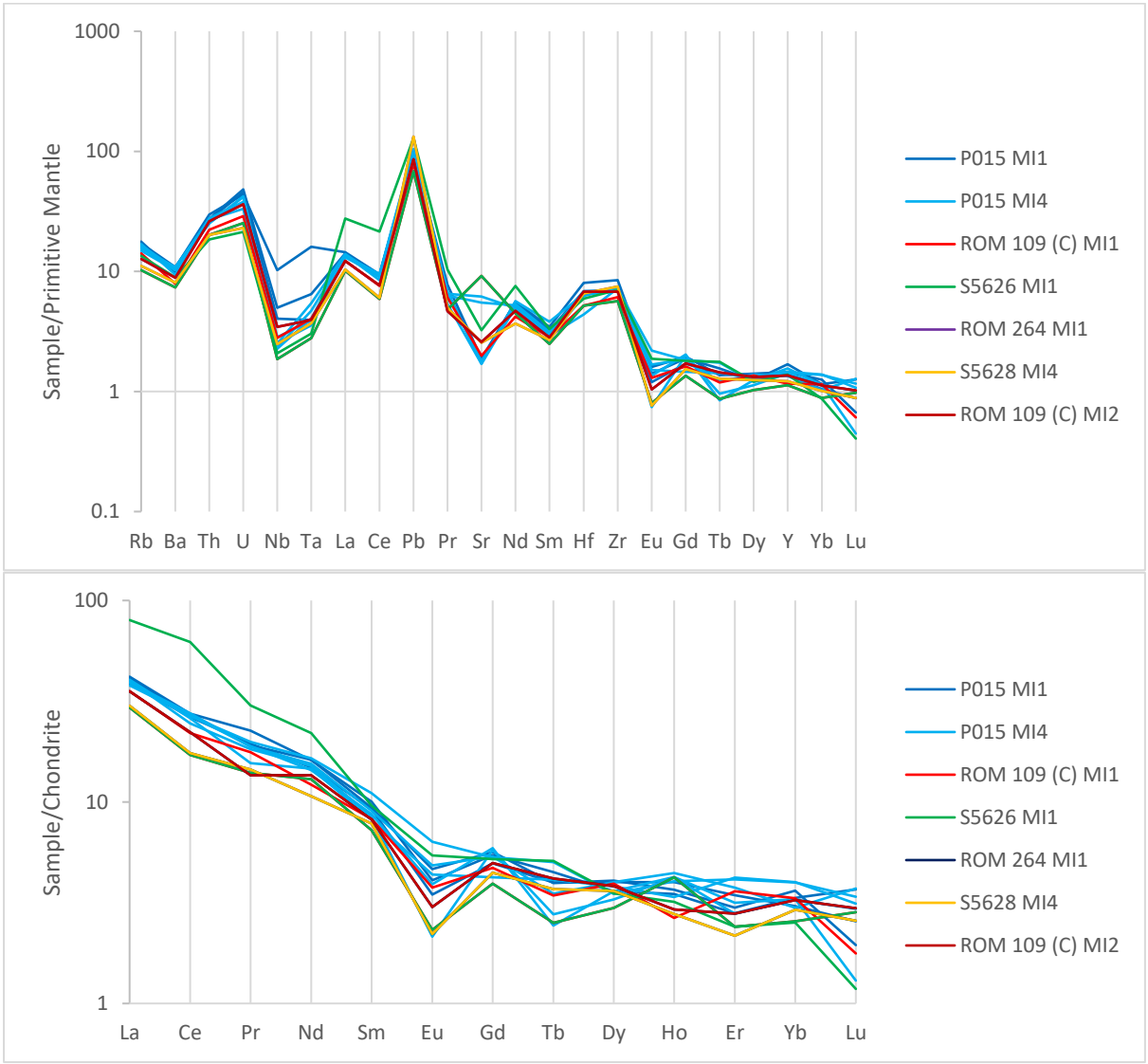

Fig. 5.11. Chondrite-normalised and primitive mantle-normalised (values from Sun and McDonough, 1989) trace element diagrams for calcite hosted in samples P015, ROM 109 (C), S5628, S5626, and ROM 264. Trace

element abundances are uniform across all samples and generally show positive Th-U, Pb, and Hf-Zr anomalies, with variably negative Nb-Ta anomalies. Sr generally shows slight negative anomalies but also varies to slight positive anomalies. Calcite in sample P015 MI1 shows higher Nb-Ta in comparison to other samples. Calcite in sample S5626 shows higher La-Ce in comparison to other samples. Calcite shows a general LREE-enriched chondrite-normalised pattern. Sample S5626 shows slightly higher LREE abundances.

Table 49
Primitive mantle-normalised (n) Zr/Sm and Hf/Sm for calcite

Sample	Site name	Zr/Sm	Hf/Sm
P015	MI1Cal1	2.17	2.13
P015	MI1Cal2	2.25	2.10
P015	MI1Cal3	2.45	2.32
P015	MI4Cal4	2.48	1.50
P015	MI4Cal5	2.29	2.12
P015	MI4Cal6	1.87	1.70
P015	MI4Cal7	2.28	2.14
P015	MI4Cal8	2.61	2.22
ROM 109 (C)	MI1Cal1	2.16	1.83
ROM 109 (C)	MI1Cal2	2.27	2.08
ROM 109 (C)	MI2Cal3	2.40	2.41
S5628	MI4 Cal1	2.78	2.43
S5626	MI1Cal1	2.12	1.80
S5626	MI1Cal2	2.27	2.08
ROM264	MI1Cal1	2.40	2.41
ROM264	MI1Cal2	2.78	2.43

5.2.3 Secondary ilmenite

Due to the small grain size and skeletal crystal shapes of secondary ilmenite, trace element analysis was limited to MI1 and MI4 of sample P015, which host secondary ilmenite with larger grain sizes (Fig. 3.12 A–D). Additionally, a large ilmenite grain hosted in MI2 of the same sample was also analysed (see Table 63 in the appendix). MI2 is not entirely enclosed by the ilmenite megacryst and is therefore connected to the surrounding kimberlite matrix, as such the material hosted within MI2 is identical to the kimberlite matrix (Chapter 3.3.2; Fig. 3.4).

Trace element concentrations of secondary ilmenite in MI1 and MI4 show LREE-enriched chondrite-normalised profiles (~2000 x chondrite for LREE and ~5–20 x chondrite for HREE) (Fig. 5.12). Primitive mantle-normalised profiles for secondary ilmenite in MI1 and MI4 reveal that trace element concentrations are generally higher than the surrounding host ilmenite megacrysts, with the exception of Nb-Ta and Rb abundances (Fig. 5.12). Nb concentrations for secondary ilmenite are identical to the host ilmenite megacryst (~1800–2000 x primitive mantle), Ta concentrations vary from similar to the surrounding host ilmenite megacrysts for MI1 (~3500 x primitive mantle) to slightly lower than the surrounding host ilmenite megacrysts for MI4 (800 x primitive mantle) (Fig. 5.12). Rb abundances of secondary ilmenite in MI1 (0.18 x primitive mantle) and MI4 (0.88 x primitive

mantle) are similar to megacrystic ilmenite (0.02–0.4 x primitive mantle) (Fig. 5.12). Hf-Zr is slightly more enriched (~700 x primitive mantle) than the surrounding host ilmenite megacrysts for MI1 and MI4 (~140 x primitive mantle), Sr shows a negative anomaly (~1.4 x primitive mantle), and Pb also shows a negative anomaly (14–40 x primitive mantle) but is more abundant than the surrounding host ilmenite megacryst which shows a positive anomaly (0.8 x primitive mantle) (Fig. 5.12).

The large ilmenite grain in MI2 produced REE chondrite-normalised profiles and primitive mantle-normalised profiles similar to the surrounding megacryst ilmenite of sample P015, with slightly lower Nb-Ta (1400–8100 x primitive mantle) and Hf-Zr (68–81 x primitive mantle) compared to the ilmenite megacryst (Nb-Ta: 1800–3200 x primitive mantle; Hf-Zr: 120–150 x primitive mantle) (Fig. 5.12).

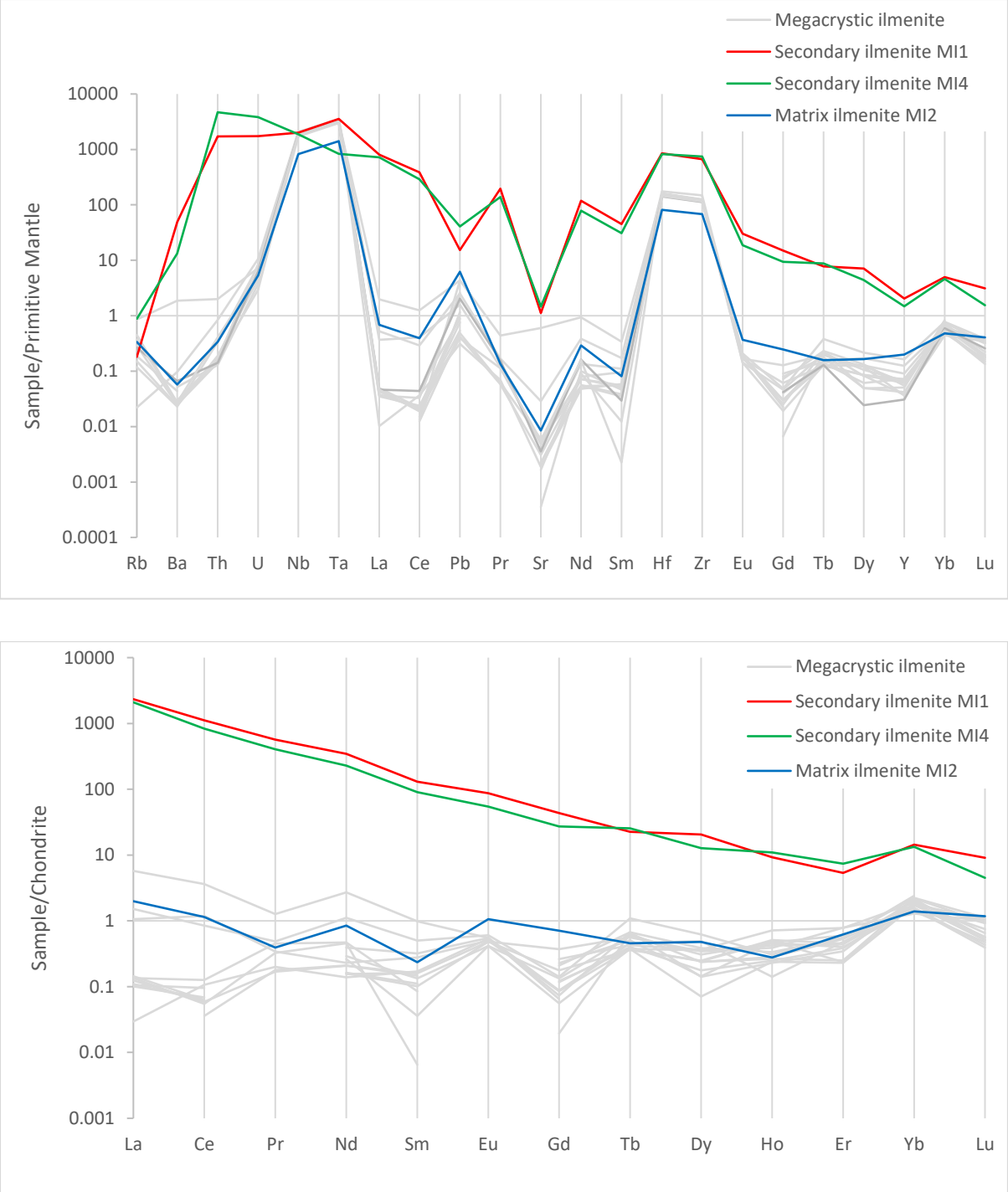

Fig. 5.12. Chondrite-normalised and primitive mantle-normalised (values from Sun and McDonough, 1989) trace element diagrams for secondary ilmenite in MI1 and MI4, and matrix ilmenite in MI2 of sample P015 in comparison to the ilmenite megacryst of the same sample.

Nb vs Zr plots for secondary ilmenite in MI1 and MI4 reveal that Nb abundances are similar to the host ilmenite megacryst of Group 2 ilmenites (1200–1500 ppm), however the Zr abundances are significantly higher (8000 ppm) compared to the host ilmenite megacryst which belongs to Group 2 ilmenites (1000–1500 ppm) (Fig. 5.13). Plots of MgO vs Nb also show that Nb abundances are consistent with Group 2 ilmenites but MgO values for

secondary ilmenite (<0.1 wt%) are significantly lower than megacrystic (Group 2) ilmenites (~6–10 wt%) (Fig. 5.14), as discussed in the previous chapter (Chapter 4.3.2).

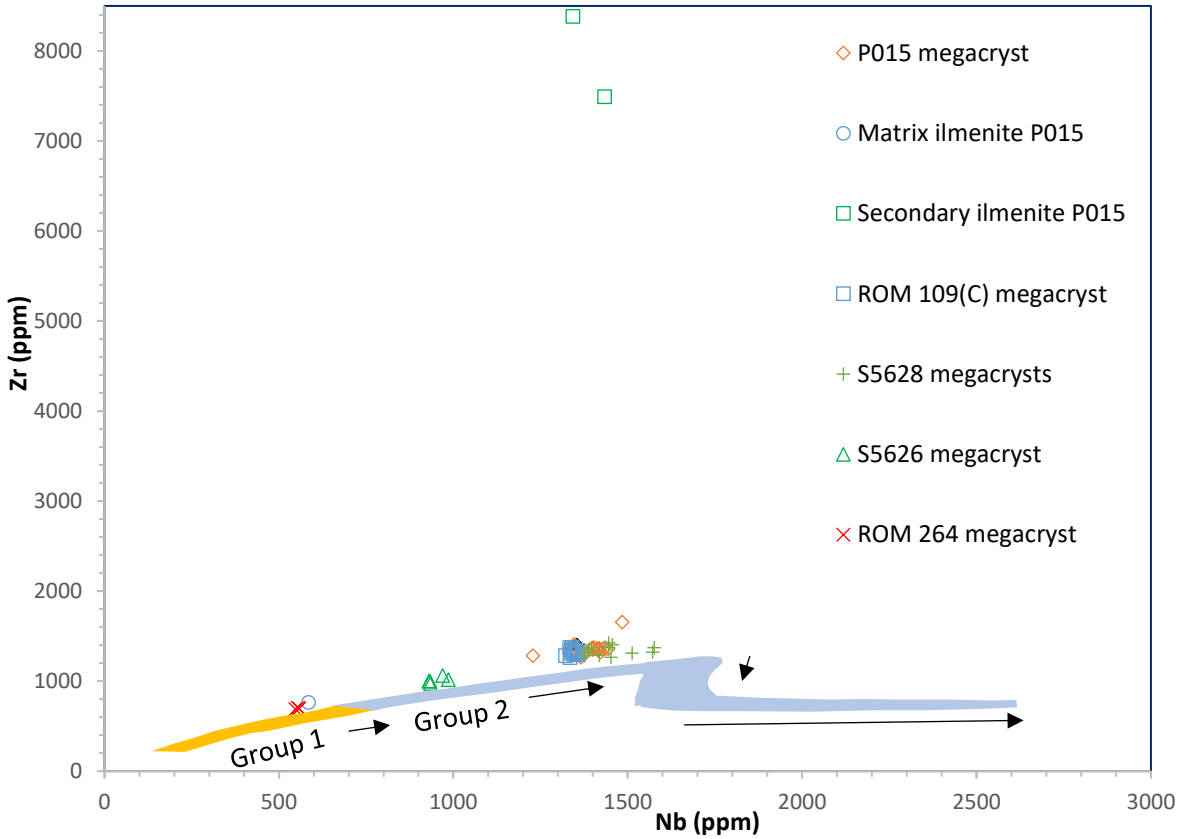

Fig. 5.13. Nb (ppm) versus Zr (ppm) for megacrystic ilmenite, secondary ilmenite, and matrix ilmenite. Fields are modified after Moore et al. (1992) showing the idealised compositional trends of Group 1 (orange) and Group 2 (blue) ilmenites identified at the Monastery ilmenite. The megacrystic and matrix ilmenite plot along a trend of increasing Zr and Nb. The analysed matrix ilmenite in MI2 of sample P015 shows a composition that is more primitive (Group 1) than the ilmenite megacryst of the same sample (Group 2). Secondary ilmenite in P015 MI1 and MI4 show Nb compositions similar to the host megacryst of the same sample, but with higher Zr concentrations.

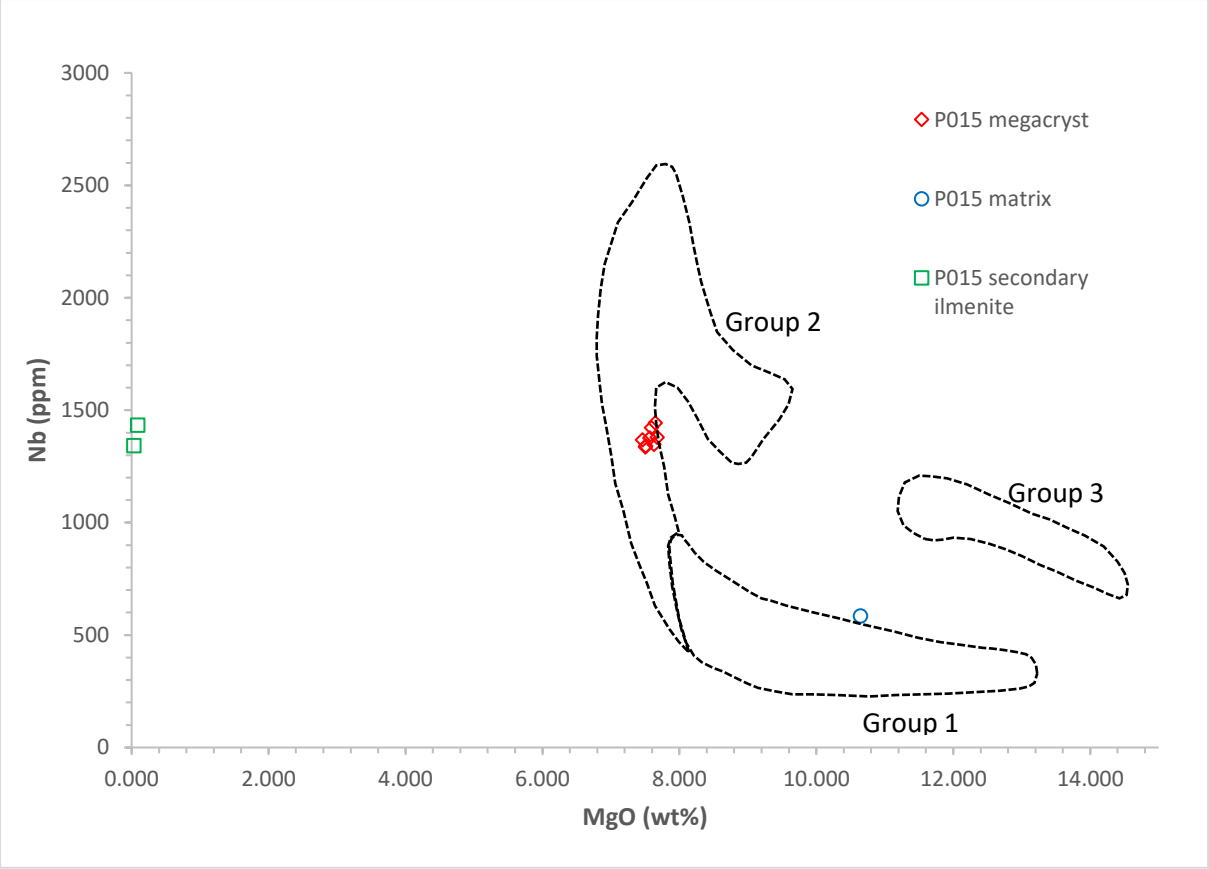

Fig. 5.14. MgO (wt%) versus Nb (ppm) for secondary ilmenite (MI1 and MI4), matrix ilmenite (MI2), and megacrystic ilmenite of sample P015. Matrix ilmenite shows Nb vs MgO composition consistent with Group 1 ilmenites. This suggests it is more primitive in comparison to the host ilmenite megacryst of the same sample which is consistent with Group 2 ilmenites. Secondary ilmenite within the inclusions shows a similar Nb composition compared to megacrystic ilmenite. However, it shows low Mg compositions.

The matrix ilmenite hosted in the partially enclosed MI2 shows lower abundances of Nb and Zr than the surrounding ilmenite megacrysts, which are consistent with Group 2 kimberlites, suggesting that this matrix ilmenite is slightly more primitive in composition (Fig. 5.13). This is also observed in plots of MgO vs Nb for the matrix ilmenite in MI2, which plot as Group 1 ilmenites in comparison to megacrystic ilmenite of the same sample which is consistent with Group 2 ilmenites (Fig. 5.14).

5.2.4 Phlogopite

Phlogopite was analysed in only one sample (S5628; see Table 64 in the appendix). Trace element analysis of phlogopite shows a general LREE-enriched chondrite-normalised pattern. LREE concentrations reach ~19–40 x chondrite with HREE concentrations of ~0.3–1.2 x chondrite. One analysis shows no LREE enrichment with REE abundances of ~0.1–1 x chondrite, similar to REE abundances of phlogopite analysed within olivine megacryst-hosted melt inclusions (Howarth and Büttner, 2019) (Fig. 5.15).

Fig. 5.15. Chondrite-normalised and primitive mantle-normalised (values from Sun and McDonough, 1989) trace element diagrams for phlogopite in MI1 of sample S5628. Grey lines represent phlogopite analysed in olivine-hosted melt inclusions (Howarth and Büttner, 2019). Trace element and REE concentrations range from similar to phlogopite analysed in olivine hosted melt inclusions, to slightly more enriched in trace elements and REE (particularly LREE) (gaps are analyses that were below detection limits).

One phlogopite analysis shows the same primitive mantle-normalised pattern compared to phlogopite analysed within olivine megacryst-hosted melt inclusions from the Monastery kimberlite (Howarth and Büttner, 2019). Two phlogopite analyses show the same primitive mantle-normalised patterns, but with a higher concentration of trace elements (Fig. 5.15). The primitive mantle-normalised profiles for the latter show high Rb and Ba enrichment (1000 x primitive mantle) with low Th concentrations (0.4 x primitive mantle). Nb (19–97 x primitive mantle) and Ta (17–48 x primitive mantle) are variably enriched as well as Pb (52–115 x primitive mantle) and Hf-Zr (13–17 x primitive mantle) (Fig. 5.15).

5.2.5 Serpentine

Trace element analyses of serpentine (see Table 65 in the appendix) within the melt inclusions shows LREE-enriched chondrite-normalised patterns. Serpentine has LREE abundances of ~9-12 x chondrite and HREE abundances of ~1–1.4 x chondrite. Serpentine analyses were limited to sample S5626 due to small grain sizes in other samples (Fig. 5.16). Primitive mantle-normalised profiles of serpentine show positive anomalies for Th-U (6.8–8.7 x primitive mantle), Pb (52–57 x primitive mantle), and Hf-Zr (2.3–2.9 x primitive mantle). Nb-Ta abundances are similar to primitive mantle and Gd to Yb are depleted relative to primitive mantle (0.3–0.6 x primitive mantle) (Fig. 5.16).

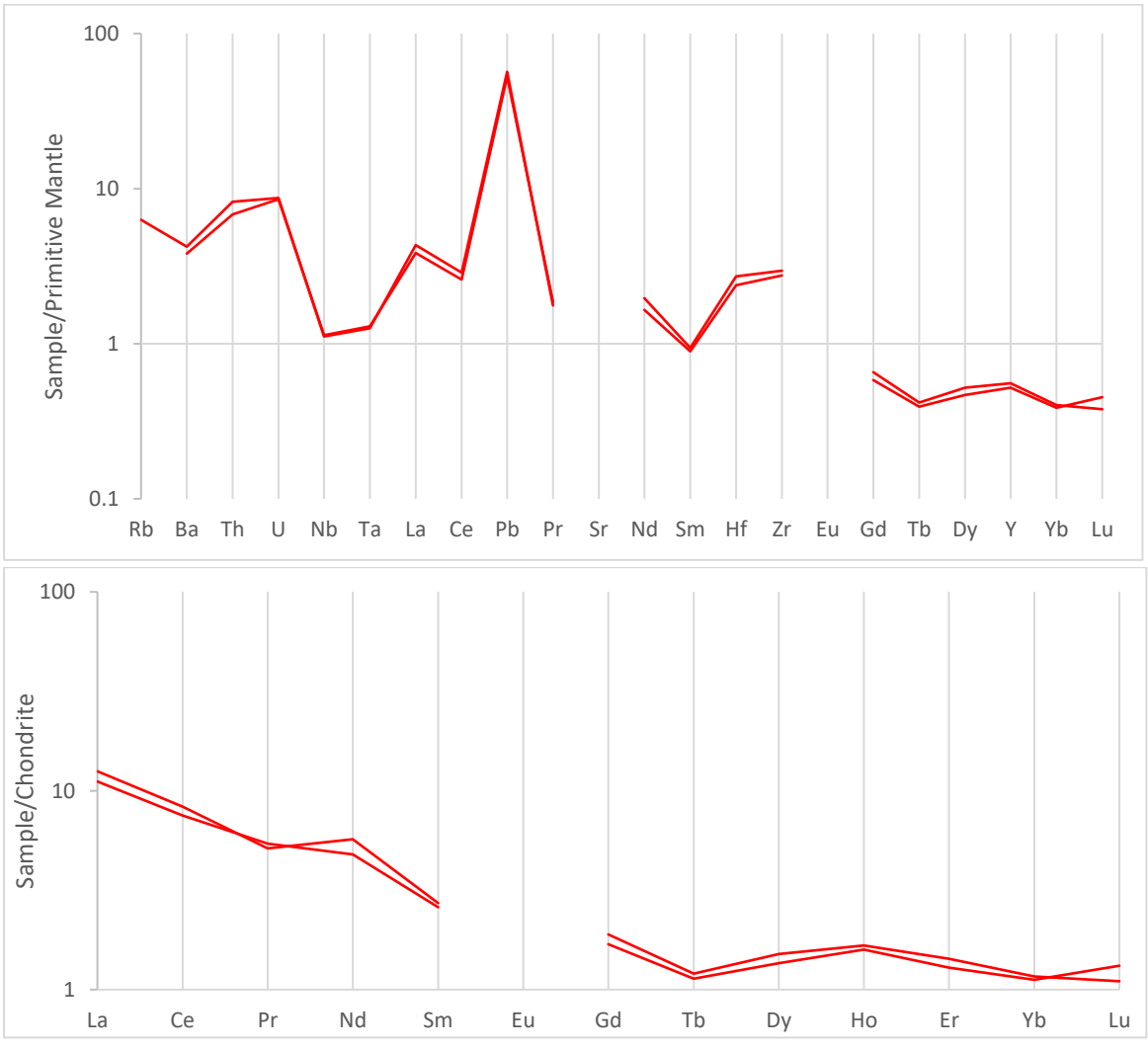

Fig. 5.16. Chondrite-normalised and primitive mantle-normalised (values from Sun and McDonough, 1989) trace element diagrams for serpentine in MI1 of sample S5626. Serpentine shows an LREE-enriched chondrite-normalised pattern. Trace element concentrations are enriched in Th-U, Pb, and Hf-Zr (gaps are analyses that were below detection limits).

Chapter 6: Discussion

6.1 Melt inclusions hosted in ilmenite megacrysts

Polymineralic inclusions hosted within the megacryst assemblage at the Monastery kimberlite are common features that have been reported by various authors (e.g. Nixon and Boyd, 1973; Haggerty and Boyd, 1975; Kirkley et al., 1986; Kamenetsky et al., 2014a; Howarth and Büttner, 2019). Two main mechanisms have been proposed to explain their formation: either from the capture of primary kimberlitic melt during crystallisation of the megacrysts (e.g. Haggerty and Boyd, 1975; Jakob, 1977; Schulze, 1985; Howarth and Büttner, 2019), or from the invasion of melt into already existing megacrysts (e.g. Kamenetsky et al., 2014a). This thesis presents textural and geochemical evidence to constrain the source and mechanism of capture of the melt and its subsequent evolution within ilmenite megacrysts, forming the observed melt inclusions.

The melt inclusions hosted in ilmenite megacrysts are 1–5 mm in size and show circular or oval shapes in thin section. They are randomly distributed within the ilmenite megacrysts (Fig. 3.1). This is consistent with randomly distributed spherical to ellipsoidal melt inclusions seen in 3-D X-ray tomography of ilmenite megacrysts from the Monastery kimberlite (pers. comm., Büttner, 2019).

Melt inclusions hosted in ilmenite megacrysts are smaller in size and more regular in shape than olivine megacryst-hosted melt inclusions (the largest of which are cm-sized). But in the composition and textural features of the daughter phases, the observed melt inclusions are similar to melt inclusions hosted in olivine megacrysts from the Monastery kimberlite (Howarth and Büttner, 2019). This suggests a similar source for the melt captured in olivine and ilmenite megacrysts.

Jakob (1977) noted that the bulk composition of ilmenite megacryst-hosted melt inclusions is similar to the surrounding kimberlite matrix at the Monastery kimberlite. The observed melt inclusions host an assemblage of daughter phases similar to phases that comprise the kimberlitic matrix (Table 1). However, they show larger variations in modal proportions, particularly calcite. EDS area scans of the studied melt inclusions yield a compositional trend that is compatible with kimberlite bulk compositions but may over- or underestimate individual components, likely due to sectioning effects (Fig. 6.1). The melt inclusions plot along a continuous trend from primary kimberlite-like compositions, similar to the estimated primary kimberlite melt (Becker and le Roux, 2006), to carbonate-rich compositions (Fig. 4.3; Fig. 6.1).

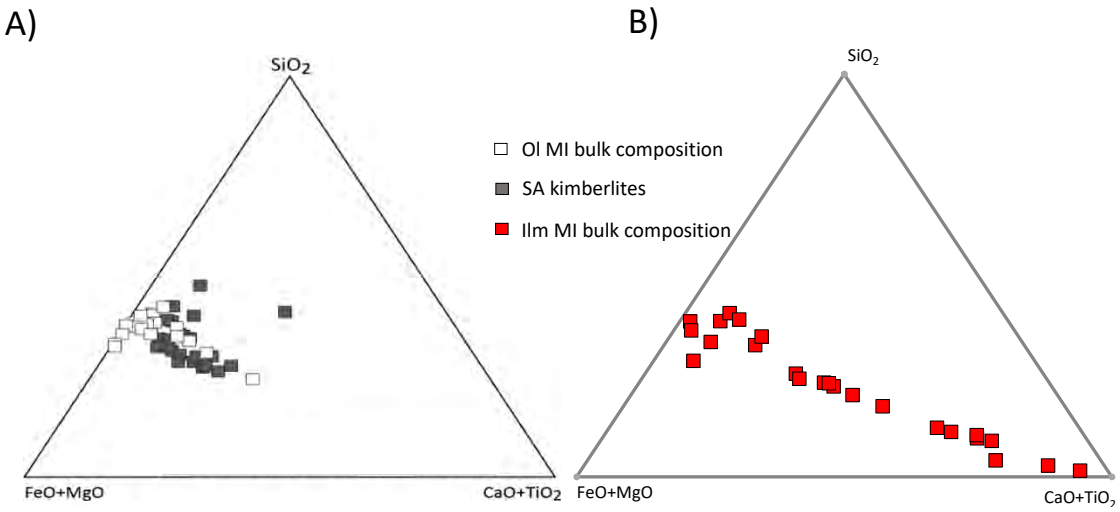

Fig. 6.1. A) Ternary diagram comparing the bulk composition of olivine megacryst-hosted melt inclusions (Ol MI bulk composition; Howarth and Büttner, 2019) to estimated primary kimberlite compositions for South African kimberlites (SA kimberlites; Becker and le Roex, 2006) (left). B) For comparison, 2D EDS area scans of ilmenite megacryst-hosted melt inclusions in this study are shown on the right.

Melt inclusions from various kimberlite localities have previously been classified into silicate-rich endmember inclusions and carbonate-rich endmember inclusions based on the composition and modal proportions of their groundmass (van Achterbergh et al., 2004; Araújo et al., 2009; Bussweiler et al., 2016). Due to the identical compositions of the daughter phases hosted within silicate-rich endmember inclusions compared to carbonate-rich endmember inclusions, the variation in modal proportions were attributed to a sectioning effect (Araújo et al., 2009; Bussweiler et al., 2016). However, more calcite-rich inclusions hosted in ilmenite megacrysts, in comparison to olivine megacryst-hosted melt inclusions from the Monastery kimberlite (Fig. 6.1), suggest that this is related to an overall more carbonate-rich bulk composition, and is not entirely related to a sectioning effect.

Olivine megacrysts from the Monastery kimberlite form two compositional groups: Fe-poor ($Fo_{83.5}$ to $Fo_{87.8}$) and Fe-rich ($Fo_{79.6}$ to $Fo_{81.2}$) megacrysts (Moore, 1986; Howarth, 2018). Howarth and Büttner (2019) described primary melt inclusions hosted in Fe-poor olivine megacrysts (Fo_{84-88}) which crystallised early in the megacryst crystallisation sequence, prior to crystallisation of the observed ilmenite megacrysts (Moore et al., 1992). The differences in the bulk compositions of ilmenite megacryst-hosted melt inclusions and the olivine megacryst-hosted melt inclusions may be due to differences in the timing of crystallisation of their respective host megacrysts and the capture of a kimberlite melt at various stages of its evolution due to the fractional crystallisation of the megacrystic suite.

However, the variation in modal proportions between the melt inclusions is independent of the host ilmenite megacryst sample and spatial distribution within a particular megacryst, as adjacent melt inclusions may show large variations in modal proportions. For example, sample P015 hosts calcite proportions that vary between 20–80 % area exposed in thin section (Fig. 4.3; Table 1). Preliminary 3-D X-ray tomography of ilmenite megacryst and their

inclusions from the Monastery kimberlite suggests that the variations in modal proportions observed in two dimensions persist in three dimensions (pers. comm., Büttner, 2019). This may suggest that the melt was heterogenous at the time of capture and was composed of separate silicate/oxide and Ca-carbonate components of the primary kimberlitic melt. Where olivine megacrysts captured primarily the silicate component, ilmenite megacrysts captured larger abundances of the carbonate component. This suggests that the heterogenous melt began to accumulate into carbonate and silicate-rich domains in the mantle source. This may support petrogenetic links between carbonatites and kimberlites in the mantle source region. Dalton and Presnall (1998) showed that kimberlite forms a continuum from carbonatitic at the solidus to kimberlitic at 70–100°C above the solidus.

Although the modal proportions of daughter phases are highly variable, melt inclusions from the same ilmenite megacryst samples often host similar assemblages of daughter phases which display similar textures. For example, sample S5626 MI1, MI2, and MI3 host a similar assemblage of euhedral serpentine, glass, and calcite (Chapter 3.3.1; Fig. 3.2; Fig. 3.3). Melt inclusions in sample P015 host a similar assemblage of calcite, glass, and skeletal oxides (albeit with varying proportions) (Chapter 3.3.2; Fig. 3.12). Sample S5251 MI1 and MI2 both host large proportions of texturally heterogenous glass and oxides phases (Chapter 3.3.4; Fig. 3.6; Fig. 3.7). The similarity in the daughter phase assemblages and the textures they display in melt inclusions from the same ilmenite megacrysts suggests the capture of a compositionally similar source. This is interpreted to form from the capture of kimberlite melt at various stages of its evolution during the crystallisation of the respective ilmenite megacrysts. Moore et al. (1992) showed that the melt was continuously changing as a result of fractional crystallisation of the megacryst suite. The melt inclusions are, therefore, considered primary in origin.

Jakob (1977) described an amorphous matrix material within ilmenite megacryst-hosted melt inclusions and tentatively interpreted it as possibly representing a devitrified glass. However, the material was not definitively identified or studied in any significant detail. Recently, Howarth and Büttner (2019) identified a glass phase that forms a common component of melt inclusions hosted in olivine megacrysts from the Monastery kimberlite. The authors concluded that this glass phase represents a quenched residual melt produced by the crystallisation of the daughter mineral assemblage within the melt inclusions. The glass-forming melt is interpreted to represent components of primary kimberlite magma captured at mantle depths (4.5–6 GPa). Using the same criteria for glass identification (see Chapter 1.3), this study presents a texturally and compositionally similar glass to that described in olivine megacryst-hosted melt inclusions (Howarth and Büttner, 2019), which is interpreted to form as a result of similar melt capture mechanisms. As the glass represents a residual melt, it records geochemical processes pertaining to the melt evolution prior to quenching of the melt inclusions (Howarth and Büttner, 2019).

6.2 Glass: evidence for phase separation and the evolution of a residual melt within the melt inclusions

The common Si-Mg-Fe-rich glass is largely CaO, Na_2O, Al_2O_3, K_2O, and TiO_2 free (Chapter 4.3.1). Compositionally and texturally, the glass is practically identical to glass described in olivine megacryst-hosted melt inclusions from the Monastery kimberlite by Howarth and Büttner (2019). The glass is homogenous, both optically and geochemically (such as sample S5626; Fig. 3.2; Fig. 3.3), but also commonly displays slight compositional fluctuations seen as Fe-poor (~4 wt%) and Fe-rich domains (~7–12 wt%) within a glass pool (Chapter 4.3.1). This compositional variation is observable as gradational variations in the BSE signal intensity and variations in the absorption colour in PPL images of glass pools (Fig. 3.5; Fig. 3.10). The diffuse separation of chemical components within a glass is indicative of the initial stages of phase separation through spinodal decomposition (between points b and c on Fig. 6.2) (Cahn, 1965; Siggia, 1979). This mechanism for phase separation is the result of sudden temperature changes of a homogenous melt which result in diffusion of chemical components (Cahn, 1965). Similar compositional fluctuations have been described by Howarth and Büttner (2019) in glass within olivine megacryst-hosted melt inclusions. The glass also occasionally displays partially crystallised areas which are optically heterogenous and pleochroic (Fig. 3.12). These areas are interpreted to be the product of devitrification, a common feature of glass in natural systems, that forms due to its metastable nature (Marshall, 1961; Chapter 1.3). In addition to this common glass variety, several uncommon compositional and textural varieties of glass were also identified in the ilmenite megacryst-hosted melt inclusions and are discussed below.

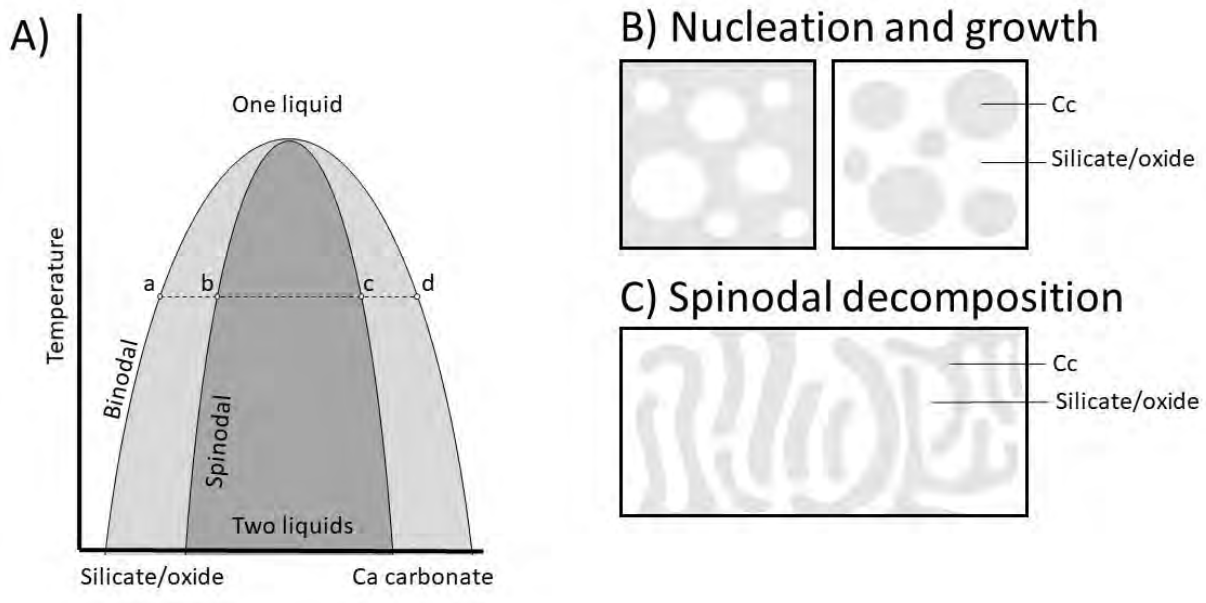

Fig. 6.2. A). Schematic binary phase diagram (Schmalzried, 1981) showing the miscibility gap in a plot of temperature versus composition (silicate/oxide–Ca carbonate). Above the binodal a mixed phase is thermodynamically stable, below the binodal an unmixed state is thermodynamically stable, i.e. mixed phases separate. B). The resultant texture produced by phase separation through nucleation and growth that occurs between the binodal and spinodal (between a and b, or c and d). Nucleation is required to overcome the kinetic barrier in this region. C). The resultant texture is produced by phase separation through spinodal

decomposition that occurs below the spinodal (between b and c). In the majority of samples phase separation of the silicate/oxide and Ca carbonate melts likely occurs between a and b, or c and d (depending on the initial bulk composition) on the phase diagram, resulting in discrete globular calcite segregations (Fig. 3.9 E; Fig. 3.11 B; Fig. 3.12 C and D). In sample ROM 264, a heterogenous zone of interconnected silicate and Ca-rich veinlets suggests that phase separation occurred through spinodal decomposition (between points b and c) in this sample (Fig. 3.10 B; Fig. 4.4). The silicate/oxide melt may have separated into Si-Fe-Mg-Al and Ca-Ti melts, likely between a and b, or c and d on the phase diagram, forming the globular Ca-Ti structures in sample ROM 264 MI1 (Fig. 3.10 B). Furthermore, the residual Si-Fe-Mg melt may have separated into Fe-rich domains and Fe-poor domains. In the majority of samples this forms as separate domains with a diffuse boundary, indicative of spinodal decomposition (between points b and c) (Fig. 3.10 B and D). In sample S5251, Fe-rich glassy globules set within and Fe-poor glass matrix are indicative of phase separation through nucleation and growth (between points a and b, or c and d) (Fig. 3.7; Fig. 3.13; Fig. 4.6). The exact timing of these phase separation events is not entirely evident and may have occurred simultaneously or in overlapping events.

Sample S5251 MI2 hosts glass that forms two distinct textural varieties: globules of Fe-rich (~8–12 wt%) isometric/spherical pale brown to yellow domains set within a Fe-poor (3–6 wt%) glassy matrix (Fig. 3.7). Compositionally, these textural varieties are similar to the diffuse Fe-rich and Fe-poor areas of the common glass variety. However, in contrast, they form sharp boundaries with one another. The texture of glassy globules set within a compositionally distinct glass matrix is indicative of phase separation through nucleation and growth (Cahn, 1965). Phase separation through nucleation and growth occurs above the solidus (between points a and b, or c and d on Fig. 6.2) and is characterised by a tendency of spherical particle shapes of one phase set within a matrix of the other phase (Fig. 3.7; Fig. 4.6; Fig. 6.2 B). The separate phases have low connectivity with sharp interfaces and constant compositions throughout the entire process (Cahn, 1965). The distribution and size of the spherical droplets is random, likely a result of homogenous nucleation of the globules. Between the binodal and spinodal curve (Fig. 6.2), phase separation is kinetically inhibited, requiring large compositional fluctuations to lower the free energy and form nuclei to initiate unmixing (Schmalzried, 1981). Once nucleated, the phases grow in size through diffusion (Cahn, 1965). The composition is unchanged with time at this growth stage. This mechanism of phase separation occurs at relatively constant temperature under equilibrium conditions. Therefore, the phase separation observed in sample S5251 is interpreted to have occurred prior to rapid uplift and cooling during kimberlite ascent, which likely was associated with disequilibrium conditions. The spherical Fe-rich globules are also present as inclusions within a large spinel grain within the melt inclusion (Chapter 3.3.4; Fig 3.7; Fig. 4.6). This indicates that phase separation occurred prior to spinel crystallisation.

The common Si-Mg-Fe-rich glass variety is largely Al_2O_3 and K_2O-poor. This suggests the residual (glass forming) melt was Al and K depleted, likely due to extraction of these elements into phlogopite or (if Al ran out before K) into tetraferriphlogopite. Sample S5628 hosts an Al_2O_3-rich glass (~8–9 wt%) in MI2, MI3, and MI4. This glass variety is rare in the observed data set and was only identified in sample S5628. This suggests that phlogopite crystallisation in these melt inclusions extracted all the K and Al was left over, leaving an Al-rich residual melt that was quenched to form the Al-rich glass.

Sample ROM 264 MI1 hosts several varieties of glass. The general structure of the melt inclusion (MI1) shows a concentric distribution of phases (Fig. 3.10; Fig. 4.4). A large calcite grain occupies the centre of the melt inclusion, surrounded by an isotropic zone with a microstructure of highly interconnected carbonate and silicate veinlets. Surrounding this zone is a layer of the common Si-Mg-Fe glass variety that forms concentric layers of Fe-rich and Fe-poor domains with a diffuse separation commonly observed in other melt inclusions (Fig 3.10; Chapter 3.3.7). The interconnected isotropic zone of carbonate and silicate veinlets in sample ROM 264 MI1 that forms between the central calcite grain and outer silicate glass represents phase separation by spinodal decomposition (between points b and c in Fig. 6.2 A). This mechanism of phase separation occurs spontaneously as no thermodynamic energy barrier is present (Cahn, 1965). The segregation of glassy Mg/Fe silicate components from Si-free Ca components (presumably $CaCO_3$) suggests the segregation of an initially homogenous carbonated silicate melt. The observed features in the melt inclusion are interpreted to form from the immiscibility of a carbonate melt, represented by the central calcite grain, and a silicate melt, represented by the outer layer of glass which has further differentiated into Fe-rich and Fe-poor varieties.

Furthermore, the outer silicate glass component of the melt inclusion (ROM 264 MI1) forms the matrix for Ca- and Ti-rich glassy globules with a concentric internal pattern (Fig. 3.10 B and D). The interior of the spherulitic structures consist of a central kassite grain, surrounded by two concentric layers of compositionally distinct oxidic Ca-Ti-rich glasses (Fig. 3.10; Fig. 4.4). The middle glass layer is Ca-rich (with up to ~75 wt% CaO; ~4 wt% FeO; 3–6 wt% SiO_2; and ~3 wt% TiO_2) with small amounts of calcite. The outer layer of glass is composed of a Ca-Ti-rich composition (with up to 15 wt% TiO_2; ~35 wt% CaO; ~ 22 wt% SiO_2; and ~20 wt% FeO). The glasses display well-defined contacts with one another and with the outer Fe-rich silicate (Si-Mg-Fe) glass matrix (Fig. 3.10; Fig. 4.4). These glassy spherulitic globules set in a silicate glass matrix are interpreted to be the result of phase separation of the silicic/oxidic melt. This stage of phase separation produced a silicic (Si-Fe-Mg) melt and a conjugate oxidic (Ca-Ti) melt that may have crystallised the silicate and oxide minerals of the common daughter assemblage, respectively.

The spherical shape of these spherulites is consistent with phase separation through nucleation and growth, such as is described for glass in sample S5251 (between points a and b, or c and d of Fig. 6.2 A). The spherulites form on the margins of the melt inclusion. The melt inclusion-ilmenite megacryst interface may serve as a nucleation point for these spherulitic domains that occurs hemispherically in the Si-Fe-Mg glass.

The five glass varieties in ROM 264 MI1 plot along a continuum from kimberlitic to carbonatitic in composition (Fig. 4.5). The similar major element compositional patterns for the five glass phases suggests similar underlying processes responsible for their formation and possibly a cogenetic origin. This trend is similar to plots of the bulk composition of all melt inclusions, suggesting the melt inclusions formed from the capture of a compositionally similar melt at various stages of the same phase separation processes.

Howarth and Büttner (2019) concluded that the melt captured within olivine megacrysts underwent several stages of melt segregation. Initially the Ca carbonate melt segregated

from the silicic/oxidic components prior to melt capture. The silicic/oxidic melt then underwent further phase separation into Ca-Ti rich melt (crystallising perovskite, spinel and ilmenite) and SiO_2-MgO-FeO-H_2O rich melt (crystallising serpentine and forming a glass) after melt capture in the megacrysts, producing similar spherulitic Ca-Ti globules. The presence of immiscible globular Ca-Ti glass on the margins of MI1 in sample ROM 264 surrounded by a Si-Fe-Mg glass is consistent with this interpretation. Segregation also likely occurred within the melt inclusion after capture in this particular megacryst. Sample ROM 264 therefore displays the carbonate-silicic/oxidic segregations and oxidic-silicic segregations which have been proposed by Kamenetsky et al. (2014a) and Howarth and Büttner (2019).

6.3 Carbonate–silicate immiscibility

Further evidence for carbonate-silicate liquid immiscibility is preserved in glass textures that are indicative of the co-existence of two immiscible melt phases under equilibrium conditions. These textures are consistent with a variety of textural features from mantle-derived and basaltic melts that have previously been interpreted as resulting from liquid immiscibility in both textural and experimental literature (Kjarsgaard and Peterson, 1991; Macdonald et al., 1993; Chalot-Prat and Arnold, 1999; van Achterbergh al., 2004; Giuliani et al., 2013; Kamenetsky et al., 2014a; Kamenetsky and Yaxley, 2015; Bussweiler et al., 2016; Soltys et al., 2016).

Evidence for carbonate-silicate liquid immiscibility includes: (i) rounded globules/spheres/patches/colloform grains of $CaCO_3$ in a silicate glass matrix (Kjarsgaard and Peterson, 1991; Macdonald et al., 1993; Chalot-Prat and Arnold, 1999; Bussweiler et al., 2016); (ii) a curved meniscus between carbonate and silicate phases (Soltys et al., 2016); (iii) a carbonate groundmass that hosts euhedral oxide and silicate mineral phases (van Achterbergh et al., 2004); and (iv) the coalescence of carbonate spheres, which requires a liquid state prior to quenching (Macdonald et al., 1993).

In the observed inclusions, calcite commonly forms rounded globular grains of varying sizes set within a silicate glass matrix. In sample ROM 109 (C) MI2, calcite forms a colloform-like grain consisting of small, rounded calcite spheres and an adjacent large rounded calcite grain (Fig. 3.9 E). In sample P015 MI4, calcite forms varying sizes (10–300 µm) of globular teardrop-shaped grains (Fig. 3.12 C and D) and in multiple melt inclusions (e.g. MI1; MI3) of the same sample calcite forms large (up to ~2 mm) central anhedral grains surrounded by glass (Fig. 3.12). These rounded calcite grains set within a silicate glass matrix are indicative of the coexistence of an immiscible carbonate and silicate melt (Kjarsgaard and Peterson, 1991; Macdonald et al., 1993; Chalot-Prat and Arnold, 1999; Bussweiler et al., 2016). The variable sizes of the calcite globules indicate coalescence of the immiscible carbonate melt occurred, ultimately resulting in single large calcite grains.

These large anhedral calcite grains most commonly occur towards the centre of the melt inclusions. Even at high calcite modal proportions (Table. 1) the grains are commonly surrounded by a thin film of glass (e.g. P015 MI1, MI3 (Fig. 3.12); ROM 31E (A) MI1 (Fig. 3.11

B)). This occurs because a silicate melt possesses a lower melt-solid interfacial energy in comparison to a carbonate melt (Minarik, 1998). The silicate melt therefore selectively occupies the grain edge, in this case the ilmenite megacryst-melt inclusion interface, while the carbonate component occupies the centre of the melt inclusions (Fig. 6.3). This texture requires the co-existence of mobile immiscible carbonate and silicate melts within the inclusions.

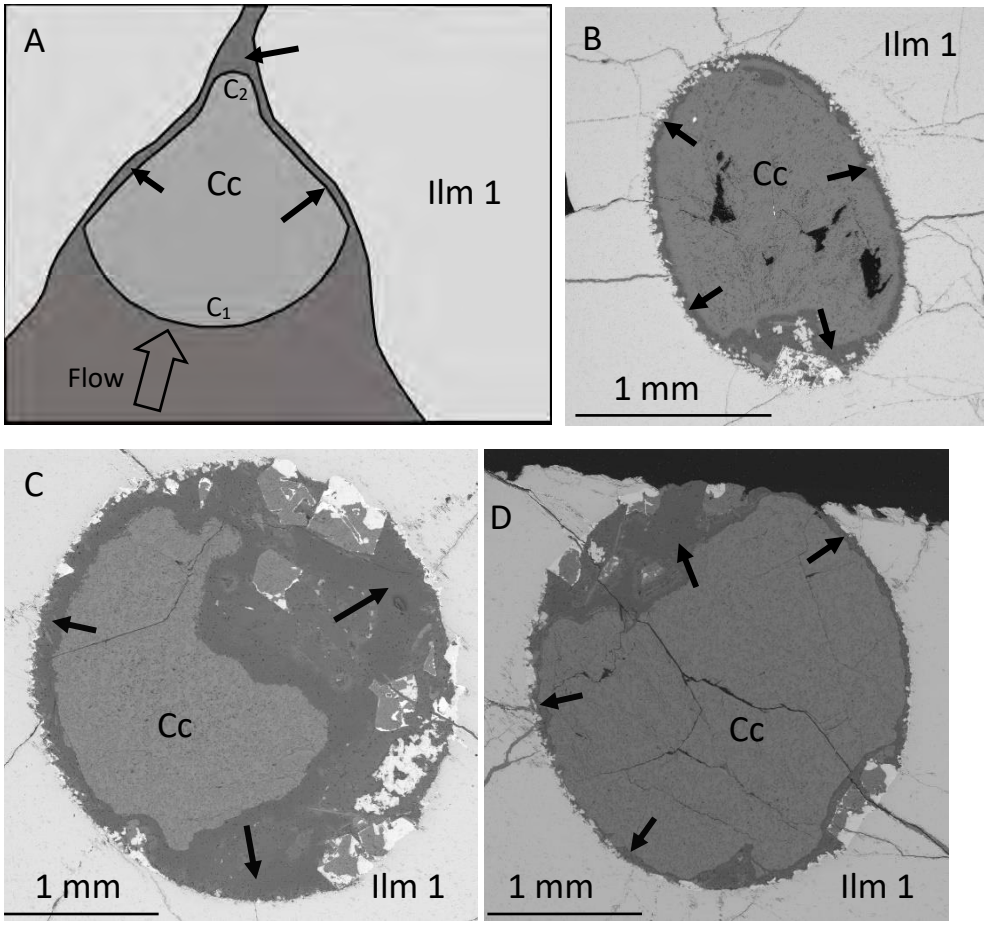

Fig. 6.3. A) Schematic diagram after Minarik (1998) and Bailey (1994) showing how the flow of an immiscible carbonate-silicate melt is restricted as it enters a channel due to the increase in mean curvature of the carbonate-silicate interface (C_1 to C_2). The silicate melt (arrows) preferentially occupies the grain edge with the host ilmenite megacrysts (Ilm 1) and the carbonate melt (Cc) occupies the centre. The interfacial tension of the carbonate and silicate melt counteracts the flow of the carbonate melt, which 'plugs' the channel, thereby restricting the movement of the carbonate melt, and the silicate melt. B) ROM 31E (A) MI1. C) P015 MI1. D) P015 MI3. B-D) BSE images showing how calcite (Cc) occupies the centre of the melt inclusions, surrounded by the silicate glass (arrows) which preferentially occupies the grain edge of the melt inclusions with the host ilmenite megacrysts (Ilm 1).

The calcite grains form a sharp irregular contact with the silicate glass matrix and occasionally form a convex boundary with adjacent glass pools (i.e. ROM 31 E (A) MI1 (Fig. 3.11 A); ROM 109 (C) MI2 (Fig. 3.9E)). The convex shape potentially represents a curved meniscus between the two melt phases (e.g. Soltys et al., 2016). This rounded shape forms

as an immiscible liquid suspended in another liquid will assume a spherical form. In natural systems this is often represented by concave boundaries, a common feature of immiscible silicate and carbonate melts (Bailey, 1994; Soltys et al., 2016).

Other textures are also present in the observed melt inclusions that preserve the co-existence of immiscible silicate and carbonate melts that underwent varying degrees of crystallisation. For example, ROM 112 contains pools of calcite that form the matrix for the well-developed crystal faces of subhedral serpentine and phlogopite crystals that crystallise into the calcite pools (Fig. 3.8). These anhedral calcite pools also share a common extinction angle, suggesting an interconnected nature in 3 dimensions. This is interpreted to form from an interconnected pool of carbonate melt that crystallised into a single calcite crystal after quenching. Prior to quenching, the silicate component crystallised into euhedral serpentine and phlogopite grains. A silicate glass was not identified in this inclusion but may be present elsewhere in the melt inclusion, below or above the exposed thin section.

Similar textural relationships are observed in other melt inclusions, where calcite forms the matrix for euhedral grains of the silicate/oxide minerals of the common daughter assemblage (serpentine (Fig. 3.8), phlogopite (Fig. 3.8), and oxides (Fig. 3.9 B and F; Fig. 3.11 C; Fig. 3.14; Fig. 3.15)). The observed textures are similar to those described by van Achterbergh et al. (2004) for mantle-derived carbonate-rich endmember inclusions in which calcite forms the groundmass for euhedral phlogopite, olivine, spinel, and perovskite.

In sample S5626 MI1, MI2, and MI3 (Fig. 3.2; Fig. 3.3) calcite occurs as thin veinlet structures surrounding, and within, the individual rays of euhedral fan-shaped serpentine set in a glass matrix. This is interpreted to have formed from the carbonate melt occupying the grain-edge of the serpentine. The ability of carbonate melts to form interconnected grain-edge melt at low melt fractions is due to low dihedral angles (Minarik, 1998), which further supports a liquid state of $CaCO_3$ at the time of the quenching of the melts in the melt inclusions.

Calcite also commonly occupies the entire interior void of skeletal oxide grains (secondary ilmenite and spinel) that are set within a glass matrix (Fig. 3.9; Fig. 3.11; Fig. 3.12). This texture is interpreted to form by heterogenous nucleation of Fe-Ti oxides on the interface between the immiscible carbonate and silicate melts, which then grow under disequilibrium conditions, crystallising skeletal shaped grains. Therefore, the silicate and carbonate melts had already segregated at the time of rapid skeletal oxide growth, which likely occurred under disequilibrium conditions during kimberlite ascent. This mode of heterogenous nucleation can also be observed in MI1 and MI2 of sample S5251 where small (>1um) opaque oxides form on the interface of immiscible glass globules set within a glassy matrix (Fig. 3.7; Fig. 3.13; Fig.4.7).

Additionally, calcite also occurs as subhedral crystals, the well-developed crystal faces of these grains are commonly surrounded by glass (Fig. 3.2; Fig. 3.3). This texture requires crystallisation under equilibrium conditions (Shelley, 1993). Calcite and silicate textures therefore preserve both melt and crystalline features. This indicates that the residual silicate

and carbonate melts quenched together, or, in some inclusions, calcite had formed euhedral crystals at the time when the residual silicate melt was quenched.

The calcite-glass textures described above provide evidence that the carbonate-silicate component was immiscible and mobile within the melt inclusions. In summary, this evidence includes: (i) large rounded and poikilitic calcite grains; (ii) calcite pools and/or a calcite matrix for euhedral silicate/oxide grains; (iii) calcite completely occupying the interior of skeletal oxide grains; (iv) highly variable calcite modal proportions. Furthermore, the presence of well-defined faces of subhedral calcite grains indicates that crystallisation of the carbonate melt component into primary magmatic calcite crystals also occurred to some degree prior to quenching and preserves another stage of the magmatic evolution of the captured melt.

Calcite as a daughter phase in polymineralic inclusions has been attributed to secondary infilling because carbonatitic components are more likely to infiltrate megacrysts due to their low viscosity and the wetting property of carbonate melts (Treiman and Schedl, 1983; Bussweiler, 2019). However, in the observed ilmenite megacryst hosted-melt inclusions it is unlikely that the carbonate represents a separate unrelated infiltrating melt due to the abundant evidence of textures indicating or suggesting unmixing of carbonate and silicate melts. The formation of these textures requires the coexistence of immiscible carbonate and silicate melts with sufficiently low viscosity. The bulk migration of such a system would be unlikely (Minarik, 1998; Fig. 6.3). Minarik (1998) showed that silicate melts possess a lower mineral-melt interfacial energy than carbonate melts. Therefore, silicate melts will preferentially wet the grain edge. This is evident as large calcite grains that occupy the centre of melt inclusions, surrounded by a thin layer of glass as described above. Consequently, the bulk migration of immiscible carbonate and silicate melts within a channel will be inhibited as the carbonate globules would theoretically ‘plug’ access to grain-edge channels (Bailey, 1994; Minarik, 1998; Fig. 6.3). Furthermore, no evidence of carbonate has been found along veins in olivine megacrysts that are connected to melt inclusions that contain calcite (Howarth and Büttner, 2019). Therefore, a secondary (infiltrating) origin for calcite is unlikely to explain the observed features and is here interpreted to represent a primary component of the captured melt.

Polymineralic inclusions are thought to represent captured components of early kimberlite melts (e.g. Bussweiler, 2019). The observations of conjugate silicate-carbonate melts in the current study indicate that the primary kimberlite melt was initially a homogenous carbonated-silicate melt (i.e. Nielson and Sand, 2008; Sparks et al., 2009; Howarth and Taylor, 2016; Stamm and Schmidt, 2017; Tappe et al., 2017; Howarth and Büttner, 2019). A carbonated-silicate primary kimberlite melt may undergo phase separation (e.g. Brooker and Kjarsgaard, 2011; Safonov et al., 2011) into conjugate silicate and carbonate components due to coulombic repulsion forces between network formers (SiO_2) and network modifiers (CaO) (Warren and Pincus, 1940; Galakhov and Varshal, 1973; James, 1975; Hudon and Baker, 2002). This is interpreted to have occurred prior to melt capture by the ilmenite megacrysts (with the exception of sample ROM 264 which is interpreted to have captured a homogenous carbonated-silicate melt).

Kamenetsky et al. (2014a) propose that the immiscible phase separation of silicate and carbonate components of the primary kimberlite melt may explain the disparity between evidence for a cognate origin between the ilmenite megacrysts and host kimberlite, such as identical Hf isotope compositions, and their apparent chemical disequilibrium at emplacement level. Kamenetsky et al. (2014a) propose that this phase separation may also account for the common depletion of kimberlites in HFSE relative to REE of similar incompatibility (Price et al., 2000; le Roex et al., 2003; Harris et al., 2004) (i.e. $(Zr/Sm)_n$ < 0.85; $(Hf/Sm)_n$ < 0.70) if the carbonate component forms the major liquid component of kimberlites and the silicate component crystallises the megacrystic suite (Kamenetsky et al., 2014a). Experimental studies indicate that the silicate melt may preferentially accommodate HFSE, Fe, and Ti (Hamilton et al., 1989, Jones et al., 1995; Veksler et al., 1998, 2012). In the current study, the glass shows a wide variation in HFSE abundances ($(Zr/Sm)_n$: 0.6–20; $(Hf/Sm)_n$: 0.6–40). Low HFSE abundances correspond to high Th/U, REE-rich glass, and high HFSE abundances corresponds to low Th/U and REE-poor glass (Fig. 5.9; Fig. 5.10). In comparison, calcite, the major carbonate component, shows relatively uniform HFSE compositions ($(Zr/Sm)_n$: ~2; $(Hf/Sm)_n$: ~2). This indicates that the HFSEs are progressively enriched into the residual silicate melt. REE are partitioned into perovskite and progressively depleted in the residual silicate melt that is quenched to form a glass (Howarth and Büttner, 2019).

The features described in this section support a model of phase separation of the primary kimberlite melt into silicate-oxide and carbonate melts at mantle conditions (e.g. Kamenetsky et al., 2014a). The existence of a carbonate melt at conditions corresponding to the upper mantle is supported by experimental literature (Wallace and Green, 1988; Dasgupta and Hirschmann, 2010). The silicate component may further segregate into oxide-rich and Si-rich liquids (Kamenetsky et al., 2014a; Howarth and Büttner, 2019). The oxide-rich melt may crystallise oxide megacrysts (such as ilmenite) and the Si-rich melt may crystallise the silicate megacrysts (garnet, clinopyroxene, orthopyroxene, olivine, phlogopite, zircon; Gurney et al., 1979). Variable proportions of the coexisting silicate/oxide and carbonate melts were captured by the crystallising ilmenite megacrysts. These immiscible melts underwent varying degrees of crystallisation within the melt inclusion cavities. In the next section the textural and geochemical features of the daughter mineral phases within melt inclusions are discussed.

6.4 Crystallisation of the ilmenite megacrysts and the daughter mineral phases hosted within melt inclusions

The silicic/oxidic component of the conjugate silicic/oxidic-Ca carbonate melts underwent further melt segregation into oxide (Ca-Ti) and silicate (Si-Fe-Mg-Al-K) components (Kamenetsky et al., 2014a; Howarth and Büttner, 2019). These melts may have crystallised the oxide and silicate daughter minerals, respectively. Prior to complete crystallisation, the residual melt of this process was quenched into a glass. In this section the textural and geochemical features of the host ilmenite megacrysts and the daughter mineral assemblage

hosted within the melt inclusions are discussed in order to constrain the post capture evolution of the melt within the melt inclusion cavity.

6.4.1 Phlogopite

Phlogopite has a variable composition but shows low-Al_2O_3 contents that are similar to phlogopite typically observed in Group II kimberlites (Fig. 4.12) (Mitchell, 1995b). The TiO_2 composition of phlogopites varies from titanium rich, similar to kimberlitic phlogopite, to titanium poor, similar to peridotitic phlogopite (Dawson and Smith, 1975). Phlogopite of a similar range in compositions was also reported within melt inclusions hosted in olivine megacrysts from the Monastery kimberlite (Howarth and Büttner, 2019). The variable composition of the analysed phlogopite grains is due to the high potential for substitutions at several structural sites of phlogopite. This phenomenon is dependent on the prevailing physio-chemical conditions of the system (Mitchell, 1995b). As a result, phlogopite is sensitive to changes and records the magmatic evolution of the isolated melt captured by the ilmenite megacryst.

Phlogopite grains often display concentric magmatic zoning, forming along a geochemical trend of a decrease in Al_2O_3 and TiO_2 with an increase in Fe_2O_3 (Fig. 4.12; Fig. 4.13; Fig. 4.14). This trend is common in the analysed phlogopites hosted in various samples (Fig. 4.12; Fig. 4.13; Fig. 15). This trend is not consistent with the two evolutionary trends that have commonly been reported for kimberlitic micas: the primary macrocryst trend (increasing Al and decreasing Mg) (Reguir et al., 2009) and the transitional macrocryst-groundmass trend (characterised by increasing Al and Mg; decreasing Fe, Ti, and Cr) (Mitchell, 1995b). Abersteiner et al. (2019) described phlogopite within melt inclusions hosted in olivine and clinopyroxene megacrysts. The phlogopites displayed similar zoning patterns including a decrease in TiO_2 and Al_2O_3 with an increase in FeO from core to rim, occasionally forming an outer rim of tetraferriphlogopite (Abersteiner et al., 2019).

Fe-rich phlogopites in kimberlites (tetraferriphlogopites; >12 wt% FeO_T) are generally associated with groundmass grains and are confined the outer rims of phlogopite grains (Mitchell, 1995b; Reguir et al., 2009). The abrupt compositional change has previously been attributed to CO_2 degassing or late-stage groundwater influx (Lee et al., 2003). Abersteiner et al. (2019) attribute the outer tetraferriphlogopite rims within olivine and clinopyroxene megacryst-hosted melt inclusions to the progressive depletion of the melt in Al_2O_3 and changes in redox conditions. The observed trend (decrease in Al and Ti), forming outer rims of tetraferriphlogopites, is consistent with the model of fractional crystallisation described by Abersteiner et al. (2019). The phlogopite grains therefore crystallised in a melt progressively depleted in Al and Ti, ultimately producing Fe^{3+}-rich tetraferriphlogopites, indicating more oxidising conditions during the final stages of phlogopite crystallisation. The residual depleted melt of this process formed the Si-Mg-Fe-rich, Al-, K- and Ti-poor glass.

The observed Cr contents of phlogopites are low (<0.1 wt%), similar to primary magmatic megacrystic and groundmass phlogopites that crystallised directly from kimberlite related melts (Dawson and Smith, 1975). Elevated Cr contents of phlogopite within olivine and

clinopyroxene megacrysts have been attributed to interactions with the host megacrysts (Bussweiler et al., 2016; Abersteiner et al., 2019). Bussweiler et al. (2016) noted that the Cr enrichment of phlogopite within polymineralic inclusions correlates with the Cr composition of their respective megacryst hosts. The authors showed that the Cr content of phlogopite within melt inclusions is higher in Cr-pyrope megacrysts (up to 4.5 wt% Cr_2O_3) compared to phlogopite within melt inclusions in Cr-diopside megacrysts (up to 2 wt% Cr_2O_3). The low Cr content (<0.1 wt% Cr_2O_3) of the studied phlogopite grains is interpreted to be a result of the capture of a Cr-poor melt during the crystallisation of the ilmenite megacrysts (a component of the Cr-poor megacryst suite).

6.4.2 The origin of serpentine within the melt inclusions

The origin of serpentine in kimberlites is highly debated (e.g. Fulop et al., 2018; Bussweiler, 2019; Gernon et al., 2019), particularly the origin of the forming fluids and whether serpentine represents a primary or secondary phase. Some studies have identified multiple generations of serpentine representing both a primary and secondary phase (Mitchell, 1986; Giuliani et al., 2017; Howarth and Büttner, 2019). For example, serpentine has been identified as primary magmatic serpentine (or serpophitic serpentine by Mitchell, 1986, 2013) and serpentine has been identified as a product of the alteration of monticellite or olivine, with both generations coexisting in the same sample (Mitchell, 1986; Giuliani et al., 2017).

Serpentine forms a crystalline compositional equivalent to the Si-Fe-Mg glass. However, the Fe contents of serpentine are more variable, extending from compositions isochemical to glass to compositions that are more Fe-rich, even in comparison to the Fe-rich domains of glass (Chapter 3.5.7). Despite their similar composition, serpentine and glass are optically distinct phases (e.g. Fig. 3.2; Fig. 3.3).

Serpentine occurs as discrete euhedral crystals surrounded by a glass matrix (such as in S5626 MI1, MI2, and MI3; Fig. 3.2; Fig. 3.3). This is indicative of a primary magmatic origin, crystallising directly from the entrapped melt under equilibrium conditions. Serpentine may also form as fine-grained aggregates or patches within glass (Fig. 3.5 B and C). This suggests that serpentine also formed from the devitrification of the glass.

Serpentine within melt inclusions hosted in olivine megacrysts from the Monastery kimberlite, similarly, forms as fine-grained clusters within the glass and skeletal grains (Howarth and Büttner, 2019). The authors interpreted the as skeletal grains as possibly representing a primary phase and the fine-grained clusters possibly representing the product of the devitrification of the Si-Mg-Fe glass phase. Skinner and Marsh (2004) suggest that groundmass serpentine in kimberlites may represent the product of devitrification of an unknown kimberlitic glass. Similarily, Willcox et al. (2015) propose that an Al-rich serpentine-like mineral in the Igwisi Hills kimberlites formed by circulating meteoric groundwater that resulted in low-temperature serpentinisation of a reactive residual silicate glass. Howarth and Büttner (2019) suggest that the glass identified within melt inclusions hosted in olivine megacrysts may represent the kimberlitic glass that was inferred by

Skinner and Marsh (2004) and Willcox et al. (2015). The enclosing olivine megacrysts may have protected the glass from pervasive serpentinisation, hence the preservation of fresh glass (Howarth and Büttner, 2019).

Serpentine within the observed ilmenite megacryst-hosted melt inclusions represents formation from two origins: (i) primary magmatic serpentine that forms discrete euhedral and subhedral crystals; (ii) serpentine that forms from the partial crystallisation/devitrification of the isochemical glass phase. The preservation of fresh glass also excludes a significant meteoric origin for serpentinising fluids within the melt inclusions as it would result in pervasive alteration of the fresh glass. Some authors (e.g., Gernon et al., 2019) claim that the volatile content of primary kimberlite magma is too low for primary serpentine crystallisation. However, although the volatile content of primary kimberlite melt has yet to be constrained, the presence of other OH-bearing minerals (i.e. megacrystic and groundmass phlogopite) indicates that to some extent the primary kimberlite melt was H_2O bearing (e.g. Bussweiler, 2019).

An Na_2O-rich (4–7 wt%) serpentine-like mineral was identified in sample ROM 112 MI1 and S5628 MI1 (Chapter 4.3.4). This mineral was unidentified; however, it may represent aenigmatite or ferrikatophorite. Similarly, Giuliani et al. (2017) identified Na_2O-rich (~5.8 wt%) hypabyssal serpentine from the Bultfontein kimberlite (Kimberley, South Africa). The authors attributed Na_2O-rich composition to contributions from carbonate minerals, which form as Na-carbonate inclusions in groundmass serpentine. Kamenetsky et al. (2104b) propose a Na-rich source for the Monastery kimberlite on the basis of Na-rich alteration assemblages surrounding ilmenite and zircon megacrysts (catapleiite, freudenbergite, perovskite, apatite, and phlogopite) and daughter phases hosted in ilmenite melt inclusions (sodalite, nepheline, Na-carbonates, chlorides, and alkali-sulphates). The authors attributed these minerals to contributions from the primary alkali-carbonate kimberlite melt. The analysed Na_2O-rich serpentine-like phase may represent a component of the alkali-rich primary kimberlite melt responsible for the formation of the Monastery kimberlite. However, these Na-rich phases are rare in the observed data set and may have been extracted prior to melt capture. Where present, they may have been preserved from alteration by the enclosing ilmenite megacryst. A more detailed study of these phases may constrain their origin and abundance within the melt inclusions.

6.4.3 Spinel crystallisation

The majority of spinels within the studied melt inclusions are of a MUM (magnesio-ulvöspinel-magnetite) composition, forming along spinel Trend 1 (Roeder and Schulze, 2008) (Fig. 4.9). This composition is typical of spinels in Group I kimberlites (Roeder and Schulze, 2008). Similar MUM spinel compositions were reported within melt inclusions hosted in olivine megacrysts from the Monastery kimberlite (Howarth and Büttner, 2019). Less commonly, spinel in the current study also shows an Fe-rich composition, forming a magnetite-rich endmember composition.

Spinels in the current study form along a range of compositions from TiO_2- and MgO-rich, Fe_2O_3-poor spinel to TiO_2- and MgO-poor, Fe_2O_3-rich spinel (Fig. 4.10). Fe^{3+}-rich spinel compositions are commonly associated with the outer margins of spinel grains and skeletal spinel. This is interpreted as a general compositional trend of decreasing Mg, Ti, and Al with an increase in Fe^{3+} during spinel crystallisation. This is observed in an element map of a large spinel grain in MI2 of sample S5251, which shows a decrease in Ti and Mg with an increase in Fe from core to rim (Fig. 4.6). This is interpreted to form as a result of the progressive depletion of the melt in these components by the crystallisation of the coexisting daughter mineral assemblage (perovskite, serpentine, phlogopite). Therefore, spinel initially form with a MUM composition, followed by spinel a more magnetite-rich composition. The progressive increase of Fe^{3+} in spinel, along with tetraferriphlogopite rims, indicate high fO_2 and more oxidising conditions of the system during the final stages of crystallisation, possibly during ascent.

The presence of Cr-rich spinel (~10.5–11.5 wt% Cr_2O_3) in sample ROM 112 MI1 represents an early product of spinel Trend 1 (Roeder and Schulze, 2008). This is also evident as the Cr-rich spinels comprise of a MgO and TiO_2-rich composition that is associated with spinels that form as early products along spinel Trend 1 (Roeder and Schulze, 2008). Chromite is interpreted to be a primary phase that crystallised from the kimberlitic melt during ascent from the upper mantle (Roeder and Schulze, 2008). However, this Cr-rich composition is only observed in one inclusion. The low Cr contents of the host ilmenite megacrysts in the current study indicates that the Cr-rich composition of these spinel grains is a function of the captured melt and not contamination by the Cr-poor ilmenite megacryst (<0.1 wt% Cr_2O_3). In contrast, spinel within melt inclusions hosted in Cr-diopside and Cr-pyrope megacrysts, shows significant chemical interaction with the captured melt (Bussweiler et al., 2016; Abersteiner et al., 2019). The low-Cr content of the majority of spinel analyses is likely due to the capture of melt that crystallised the Cr-poor ilmenite megacrysts (Gurney et al., 1979).

The textural characteristics of spinel may also provide insight as to the crystallisation conditions. Spinel may occur as large euhedral or subhedral grains with a uniform composition that provide evidence that spinel crystallisation initially occurred under equilibrium conditions (e.g. Fig. 3.9 F). This was followed by the formation of zoned spinel that crystallised in a progressively more depleted melt (e.g. Fig. 4.6). Spinel also commonly occurs as skeletal grains that are indicative of growth under disequilibrium conditions (e.g. Fig. 3.9 E; Fig. 3.12). This occurs due to strong undercooling, most likely as a result of kimberlite ascent. Skeletal crystal shapes are associated with glass formation as they occur in similarly rapidly cooled environments (Shelley, 1993; Vernon, 2004). Skeletal grains form due to slow rates of diffusion relative to fast growth rates, resulting in rapid cruciform growth along the crystal corners in supersaturated conditions. These skeletal crystals form crystallographically orientated hollows or voids, typically filled with groundmass material (Shelley, 1993; Vernon, 2004).

The interior void of skeletal oxide grains (spinel and secondary ilmenite) is commonly comprised entirely of calcite. Sample ROM 31 E(A) MI1 (Fig. 3.11 A) hosts a skeletal grain

that is more similar to the atoll-shaped grains common in Group I kimberlites (Roeder and Schulze, 2008). The inner 'lagoon' of this atoll shaped spinel grain is composed of calcite (ROM 31 E(A) MI1; Fig. 3.11 A). Roeder and Schulze (2008) report that calcite and serpentine (potentially a devitrified glass) commonly occupy interior voids or 'lagoons' of atoll shaped spinel grains in Group I kimberlites. Roeder and Schulze (2008) suggest that the inner lagoon represents a volume of melt that failed to crystallise due to lack of spinel constituents and/or spinel immiscibility. The volume may have been the oxide-silicate melt or a separate immiscible fluid phase (Roeder and Schulze, 2008). We propose that in the analysed material the immiscible carbonate melt occupied the interior void of skeletal oxide grains, which was later quenched to form calcite. Therefore, the interface between the immiscible silicate/oxide and carbonate melts may form the nucleation site for spinel which underwent rapid skeletal/cruciform growth. This explains the common presence of skeletal oxides with voids completely composed of calcite set in a silicate glass matrix. Alternatively, the globular Ca-Ti spherulitic structures hosted in ROM 264 MI1 that comprise a central kassite grain and outer Ti-rich glass may also represent the immiscible silicate-oxide melt proposed by Roeder and Schulze (2008).

Evidence for this mode of heterogenous oxide nucleation is also observed in sample S5251 MI1 and MI2, where small (<1 μm) opaque grains occur along the interface between the glass globules and the glass matrix (Fig. 3.6; Fig. 3.7; Fig. 3.13; Fig. 4.6). Spinel (and secondary ilmenite) also commonly form epitaxially on the host ilmenite megacrysts. Therefore, heterogenous nucleation is likely the most common initiator of oxide mineral crystallisation.

6.4.4 Ilmenite megacrysts

Two distinct geochemical and textural populations of ilmenite were investigated: (i) the monomineralic ilmenite megacrysts and (ii) ilmenite as a daughter phase hosted within the melt inclusions (termed secondary ilmenite in this study).

The ilmenite megacrysts are largely compositionally homogenous across the thin sections with MgO compositions ranging between ~7–12 wt%, classifying them as picro-ilmenites. These major compositions for monomineralic ilmenite megacrysts from the Monastery kimberlite are reported by various authors (Mitchell, 1973; Gurney et al., 1979; Kamenetsky et al., 2014a; Peresetskaya et al., 2018). The trace element abundances of the studied ilmenite megacrysts are consistent with Group 1 and 2 ilmenites identified by Moore et al. (1992) at the Monastery kimberlite (Fig. 5.4; Fig. 5.6). The geochemical trends of Group 1 and 2 ilmenites were attributed to major and trace element fractionation as a result of the crystallisation of the coexisting megacryst suite (Moore et al., 1992).

The investigated ilmenite megacrysts crystallised sequentially in the kimberlite source. This is indicated by the progressive enrichment in incompatible trace elements (i.e. Nb) in the ilmenite megacrysts (Fig. 5.4) (Moore et al., 1992). The sequence of crystallisation of the ilmenite megacrysts of the current data set (for which trace element data are available) is sample ROM 264, followed by sample S5626, and then the co-crystallisation of sample P015,

S5628, and ROM 109 (C). The ilmenite megacryst of sample ROM 264 co-crystallised with garnet, clinopyroxene, and orthopyroxene megacrysts (Fig. 5.4 (S-)). The ilmenite megacrysts of sample S5626, S5628, P015, and ROM 109 (C) crystallised after the cessation of garnet, clinopyroxene, and orthopyroxene megacryst crystallisation. The decrease in the Zr contents of these megacrysts (most notably observed in sample ROM 109 (C)) suggests they may have co-crystallised with zircon megacrysts (Fig. 5.4 (Z+)).

Globular Ca- and Ti-rich spherulites in Fe-poor olivine megacryst-hosted melt inclusions have been interpreted to form as a result of the phase separation of silicic and oxidic components of the melt after capture by the enclosing olivine megacryst (Howarth and Büttner, 2019). Similar Ca-Ti-rich spherulites were observed in one melt inclusion in the current data set, MI1 of sample ROM 264 (Fig. 3.10) (Chapter 3.3.8). The observed spherulites in this melt inclusion are also interpreted to represent melt segregation of silicic and oxidic melts. The ilmenite megacrysts of sample ROM 264, therefore, likely captured a homogenous silicate/oxide melt prior to segregation of the silicate and oxide components. The Zr and Nb composition of the host ilmenite megacryst in this sample (ROM 264) is consistent with Group 1 ilmenites, indicating it crystallised early in the crystallisation history of the observed ilmenite megacrysts (Moore et al., 1992) (Fig. 5.4; Fig. 5.6). The spherulitic textures representing early melt segregation coincide with the more 'primitive' composition of the host ilmenite megacryst and earlier crystallisation of Fe-poor olivine megacrysts in comparison to ilmenite megacrysts (Moore et al., 1992; Howarth and Büttner, 2019). The majority of megacrysts crystallised later as Group 2 ilmenites in the current study (Fig. 5.4; Fig. 5.6) and host variable modal proportions of oxide minerals (ilmenite, spinel, and perovskite) (Table 1). Unlike for sample ROM 264, this suggests that the silicic-oxidic components segregated prior to capture by their respective ilmenite megacrysts. This may tentatively constrain segregation of the silicic and oxidic melts during crystallisation of Group 1 ilmenites (Moore et al., 1992).

6.4.5 Ilmenite as a daughter phase within the melt inclusions

In contrast to the Mg-rich ilmenite megacrysts (7–12 wt% MgO), ilmenite hosted within the melt inclusions are composed of an MgO-poor (<0.1 wt%) composition and consist almost entirely of endmember ilmenite s.s. ($FeTiO_3$) (Fig. 4.8) (Chapter 3.5.3). Low Mg-ilmenite also forms on the rims of ilmenite megacrysts in contact with the kimberlite matrix (~1.5 wt% MgO) (Fig. 3.4; Chapter 4.1).

Ilmenites have been classified into kimberlitic and non-kimberlitic in origin on the basis of MgO-TiO_2 compositions (Sobolev, 1977; Wyatt et al., 2004). An arc defines the reference line between the MgO-rich "kimberlitic" ilmenites and MgO-poor "non-kimberlitic" ilmenites. The position of this reference line changes depending on the particular kimberlite. For on-craton Group I kimberlites from South Africa, such as the Monastery kimberlite, it forms at ~4 wt% MgO and increases to ~16 wt% MgO with increasing TiO_2 (Wyatt et al., 2004). MgO-poor secondary ilmenite (<0.1 wt% MgO) within the melt inclusions and MgO-

poor rims on ilmenite megacrysts (~1.5 wt% MgO) in the current study would, therefore, fall into the non-kimberlite field for South African on-craton kimberlites (Wyatt et al., 2004).

However, Wyatt et al. (2004) noted that some ilmenite analyses from various kimberlites plot into the non-kimberlitic field due to MgO-poor compositions. These MgO-poor grains are generally associated with groundmass ilmenite grains and/or MgO-poor rims of ilmenite megacrysts (Wyatt et al., 2004).

Wyatt et al. (2004) showed that most MgO-poor ilmenites show elevated MnO or Cr_2O_3 compositions (i.e. ~4 wt% MnO; Williams and Robey, 1998). MnO enrichment trends have also been described in some Monastery ilmenites (e.g. Wyatt et al., 2004). These non-kimberlitic compositions have been attributed to incorporated xenoliths, the replacement of Mg^{2+} by Mn^{2+} due to circulating groundwater, or the depletion of Mg in the kimberlitic melt that crystallised late-stage groundmass ilmenites (Wyatt et al., 2004). Semytkivska (2010) note that Mg depletion in ilmenite may be a result of its late crystallisation from a melt that was depleted in Mg by other phases. The authors propose that low MgO (or high SiO_2) compositions may favour crystallisation of Mg-bearing silicates, followed by the crystallisation of ilmenite in a Mg-depleted melt (Semytkivska, 2010). The analysed Mg-poor secondary ilmenites have low MnO contents (<0.2 wt%). Therefore, the low MgO compositions are not as a result of Mg replacement by Mn-bearing circulating groundwater. Furthermore, significant MgO in glass indicates that the residual melt was not depleted in MgO (35–40 wt%). Therefore, the Mg-poor composition of secondary ilmenite is not a result of depletion of Mg in the melt as postulated for some groundmass grains (Wyatt et al., 2004; Semytkivska, 2010).

Alternatively, late-stage ilmenite may be depleted in Mg due to a decrease in the rate of diffusion and activity of Mg^{2+} in the melt as a result of strong undercooling. This is observed in a zoned secondary ilmenite grain in sample ROM 31E (A) which demonstrates a decrease in the MgO composition from core to rim, growing from a Mg-rich melt. The core of the grain has a MgO composition similar to the host ilmenite megacrysts (~12–15 wt%), while the rim has a lower MgO composition (~3.3 wt%) (Chapter 4.3.2; Fig. 3.11 C). However, Mg-rich ilmenite was only identified in one secondary ilmenite grain; the majority occurs as largely MgO-free grains, comprised almost entirely of ilmenite *s.s*.

A trend towards Fe-rich oxide compositions is also observed in spinel grains. This is observed in a large spinel grain in which MgO is progressively depleted towards the margins (Fig. 4.6). Therefore, secondary ilmenite grains crystallised after, or during, spinel, under increasing Mg concentration in the residual melt, but with decreasing Mg^{2+} activities and increasing Fe^{2+}/Fe^{3+} activities in the melt. This is consistent with experimental studies that show that the timing of ilmenite crystallisation in kimberlites is dependent on the initial composition (particularly Mg and Si), oversaturation, activation energies, and diffusion rates of species in the melt (e.g., Semytkivska, 2010). The majority of Fe in secondary ilmenite is composed of Fe^{2+}. However, spinel and tetraferriphlogopite show an increase in ferric Fe components during their crystallisation. The Fe^{2+}-rich composition of secondary ilmenites, which would be expected to be more oxidised, may be a result of their late crystallisation, evident by skeletal crystal shapes, during a decrease in temperature. This may reduce the

solubility of hematite in ilmenite (Deer et al., 2013) and result in the crystallisation of Fe^{2+}-rich secondary ilmenite.

The decrease in the mobility and the rate of diffusion of Mg^{2+} during ilmenite crystallisation is consistent with the skeletal crystal shapes, which are the most common shape of secondary ilmenite grains. Skeletal crystal shapes form as a result of diffusion-controlled growth kinetics under disequilibrium conditions (Vernon, 2004). This supports an interpretation of diffusion-controlled crystallisation of secondary ilmenite to account for the MgO-poor composition.

Ilmenite as a daughter phase hosted within polymineralic inclusions has only previously been reported from olivine megacrysts (Haggerty and Boyd, 1975; Bussweiler, 2019; Howarth and Büttner, 2019). Compositionally, it is enriched in Mg (3–11 wt% MgO; Howarth and Büttner, 2019) in comparison to ilmenite as a daughter phase within ilmenite megacryst-hosted melt inclusions described in this study (<0.1 wt% MgO). As with spinel, Bussweiler (2019) notes that this may be a result of the interaction between the captured melt and the host Mg-rich olivine, although Howarth and Büttner (2019) observed that the interaction between host olivine and melt inclusions is limited. This may suggest that little interaction took place between the Mg-rich ilmenite megacrysts and the captured melt that crystallised the Mg-poor ilmenite grains. Alternatively, the differences in the Mg composition of ilmenite within melt inclusions hosted in ilmenite and olivine megacrysts may be due to differences in the timing of ilmenite crystallisation within the respective megacrysts and disequilibrium conditions during ilmenite crystallisation.

The Cr composition of secondary ilmenite (<0.1 wt%) is similar to the Cr composition of the host ilmenite megacrysts (<0.1 wt%). Gurney et al. (1979) demonstrated that the ilmenite megacrysts are a component of the Cr-poor megacryst suite. The defining composition of the Cr-poor megacrystic suite is due to Cr-depletion by the crystallisation of early Cr-rich megacryst phases (Gurney et al., 1979). In comparison, later crystallising groundmass ilmenite grains are usually Cr-rich (>0.4 wt%) (Boctor and Boyd, 1980; Harte and Gurney, 1981; Apter et al., 1984; Wyatt et al., 2004). Moore et al. (1992) noted that the increase in Cr from Group 1 (<0.4 wt% Cr_2O_3) to Group 2 (>0.5 wt% Cr_2O_3) ilmenites is a result of magma mixing, while Cr-rich Group 3 ilmenites (>0.5 wt% Cr_2O_3) crystallised from a separate unrelated melt. This suggest that secondary ilmenites within the melt inclusions are linked to the Cr-poor megacrystic suite and therefore crystallised from the same batch of magma as the ilmenite megacrysts. This implies a cognate origin between the ilmenite megacrysts and the captured melt that crystallised the secondary ilmenites within the melt inclusions.

A cognate relationship between the ilmenite megacrysts and secondary ilmenite is further reinforced by the similarities in the abundance of incompatible trace elements. The secondary ilmenites are enriched in LREE with higher trace element concentrations in all elements except Nb-Ta, which is similar to the ilmenite megacrysts (Fig. 5.12). Plots of the Zr vs Nb abundances for secondary ilmenites show that the Nb abundances are similar to the host ilmenite megacrysts (Fig. 5.13). Nb is expected to behave as an incompatible element in ilmenites (Moore et al., 1992). Therefore, the similarity in incompatible trace elements (Nb) suggest a genetic relationship between the host megacrystic ilmenite and ilmenite as a

daughter phase within the melt inclusions, which further supports a primary origin for the melt inclusions.

MI2 of sample P015 forms on the margins of the megacryst and is not completely enclosed by the megacryst, thus, it is connected to the kimberlite matrix and hosts material identical to the matrix. This melt inclusion hosts a large ilmenite grain (Fig. 3.4). The ilmenite grain has a similar MgO composition and trace element abundances compared to the host ilmenite megacrysts, however with slightly lower Nb-Ta and Hf-Zr abundances (Fig. 5.12). These geochemical features indicate that it formed earlier than the host ilmenite megacrysts (Fig. 5.13; Fig. 5.14). This suggest that during ascent the kimberlite continued to grow, capturing matrix magma, including ilmenite that was more primitive than the growing ilmenite megacryst.

6.4.6 Trace element evolution of the residual glass forming melt

Trace elements in glass show variations in differentiation where glass with a high Th/U is associated with LREE-enriched chondrite-normalised patterns (Chapter 5.2.1; Fig. 5.7) and glass with a low Th/U is associated with REE-depleted chondrite-normalised patterns (Fig. 5.8). The variations in Th/U and REE abundances are unrelated to Zr vs Nb abundances (Fig. 5.4) as the variations in Th/U and REE abundances of glass occur within the same melt inclusions or glass pool (Fig. 5.7; Fig. 5.8). Therefore, the observed trace element patterns in glass are not a result of the capture of progressively more evolved melt during ilmenite megacryst crystallisation. Trace element variations are, instead, interpreted as the result of partitioning into the daughter mineral assemblage within the melt inclusions, such as described by Howarth and Büttner (2019).

Partitioning of trace elements into the daughter mineral assemblage may also explain the variations in Rb and Ba concentrations of glass (0.1–10 x chondrite) if these trace elements are partitioned into phlogopite. Furthermore, calcite and glass show both Sr-negative and Sr-positive anomalies (Fig. 5.8). In some inclusions BSE-bright irregular grains were identified as strontianite (Fig. 3.11 D). Crystallisation of strontianite may account for the variable depletion in Sr in both calcite and glass in comparison to analyses by Howarth and Büttner (2019) in olivine megacryst-hosted melt inclusions which show Sr partitioning into calcite.

Howarth and Büttner (2019) demonstrated that trace element concentrations of perovskite within olivine megacryst-hosted melt inclusions are identical to that of kimberlitic perovskite, which is the only major carrier of REE and trace elements in kimberlites. The entrapped melt therefore contained similar trace element abundances to the host kimberlite, further reinforcing a kimberlitic source. Trace element analysis of perovskite in the current study was complicated by its small grain size. However, the similarities in trace elements concentrations of glass in ilmenite and olivine megacryst-hosted melt inclusions suggest that perovskite within the studied melt inclusions played a similar role. Perovskite is therefore assumed to be the major host of REE and trace elements that are variably depleted in the glass. The glass is, therefore, interpreted to represent a residual REE-

depleted melt, as a result of trace element partitioning into the common daughter mineral assemblage hosted within melt inclusions.

6.5 Chemical modifications of the ilmenite megacrysts

Previous studies of polymineralic inclusions commonly attributed their formation to the infiltration of kimberlitic melt along fracture networks and cleavage planes of the host megacrysts by dissolution and recrystallisation (Araújo et al., 2009; Bussweiler et al., 2016; Abersteiner et al., 2019). This resulted in the process of 'necking down' (Roedder, 1984) that entrapped the infiltrating melts. Therefore, significant chemical interaction is thought to occur between the entrapped kimberlite melt and their respective megacrystic hosts (e.g. Araújo et al., 2009; Bussweiler et al., 2016; Abersteiner et al., 2019).

The kimberlite melt has been shown to react with a variety of megacrysts species. Bussweiler et al. (2016) reported that the melt inclusion-megacryst interface commonly occurs as 'spongy rims' formed by a halo of abundant micro-melt inclusions (MMIs) in Cr-diopside megacrysts and reaction rims of kelyphite in Cr-pyrope megacrysts. This is interpreted to occur as a result of disequilibrium and hybridisation between the infiltrating kimberlite melt and the host megacrysts (Bussweiler et al., 2016).

Howarth and Büttner (2019), however, noted that the absence of reabsorption textures or compositional variations close to the melt inclusion-megacryst interface suggests little chemical interaction occurred between the content of the melt inclusions and the hosting olivine megacrysts. In addition, the authors showed trace element concentrations in the residual melt evolved by perovskite fractionation and not melt contamination by the olivine megacryst (Howarth and Büttner, 2019).

The interaction between the captured melt and the ilmenite megacrysts is similar to interaction between the ilmenite megacrysts and surrounding kimberlite matrix that has been described by various authors (e.g. Shee, 1984; Gurney et al., 1979; Golubkova et al., 2013; Kamenetsky et al., 2014; Peresetskaya et al., 2018). These reaction rims are primarily composed of perovskite, Mg-depleted ilmenite, and alternating Fe-Mg rich zones that form exsolution lamellae.

For example, in MI2 of sample P015, the interface of the ilmenite megacrysts and kimberlite melt shows a zone that displays a BSE-bright signal intensity (Fig. 3.4). This zone comprises low MgO contents (<1.7 wt%) in comparison to the interior of the ilmenite megacrysts (8–14 wt% MgO). This forms as a result of the interaction between the ilmenite megacrysts and the host kimberlite melt.

Exsolution lamellae form around 10 of the 23 studied melt inclusions (e.g. Fig. 3.2; Fig. 3.3; Fig. 4.2). Therefore, they are common but not ubiquitous. Exsolution lamellae are observed in sample S5251 MI2. An element map shows the exsolution lamellae form up to 40 µm from MI2 (Fig. 4.2). These lamellae consist of crystallographically orientated, BSE-bright, Fe-rich lamellae separated by Mg-rich zones. Haggerty et al. (1977) determined that the formation of exsolution lamellae occurs late in the magmatic trend of ilmenite megacrysts.

Exsolution lamellae comprising of magnetite and magnesian titanohematites in ilmenite megacrysts have been attributed to subsolidus reactions (Jakob, 1977). Ilmenite and hematite form a complete solid solution ($FeTiO_3$–Fe_2O_3) at more than 1050°C, and with decreasing temperature a miscibility gap develops and the solubility of hematite in ilmenite decreases (Deer et al., 2013). The Exsolution of hematite in ilmenite forms when Ti^{4+} and Fe^{2+} are replaced by Fe^{3+} (e.g., Deer et al., 2013). The observed exsolution lamellae are interpreted to form from the interaction of the captured kimberlite melt and the ilmenite megacryst during a decrease in temperature, possibly during ascent, resulting in the exsolution of hematite in ilmenite. This subsolidus reaction may have been triggered by fluid within the inclusions. In sample ROM 112 MI1 the Fe-rich lamellae extend into the melt inclusion; this indicates an interaction between the Mg-rich ilmenite zones and the captured melt occurred to some extent (Fig. 3.8).

This subsolidus reaction may also be expressed in compositional variations of the ilmenite megacrysts immediately surrounding the melt inclusions. These reaction zones also form as variations in the Mg-Fe content of the ilmenite megacryst (Fig. 4.2). Surrounding certain melt inclusions is a zone of Mg-rich ilmenite (0.4 X_{Mg}), which progressively decreases in Mg content with distance from the melt inclusions, after which the ilmenite megacryst composition remains uniform (0.3 X_{Mg}) (Fig. 4.1; Fig. 4.2). This is interpreted to form by the same mechanism that formed exsolution lamellae, due to subsolidus exsolution of hematite in ilmenite. The unmixing of ilmenite in the solid state may result in Mg-rich reaction rims in ilmenite megacrysts immediately surrounding some melt inclusions (Fig. 4.1; Fig. 4.2).

In the observed inclusions, Fe-Mg-Ti oxides (perovskite, secondary ilmenite, and spinel) commonly form a fine-grained reaction zone on the host ilmenite megacrysts within some melt inclusions. For example, in sample S5251 MI2, oxides within the melt inclusions form epitaxially on the host ilmenite megacryst (Fig. 4.2). Similar reaction assemblages of Ti-rich minerals (including Mg-Ti-Fe oxides, perovskite, Mn-ilmenite, magnesian-titanomagnetite) forming along the contact of the host ilmenite megacrysts and kimberlite melt have been reported in previous studies (e.g. Haggerty et al., 1977; Kamenetsky et al., 2014a). These are interpreted to form due to the reaction of the captured melt and the host ilmenite megacrysts, potentially by precipitation and recrystallisation of the ilmenite megacrysts. Some epitaxial oxides may have also crystallised from the Ca-Ti-Fe-rich oxide melt within the melt inclusion.

Perovskite has commonly been reported as a product of the reaction between early Ti-bearing phases and the kimberlite magma (Smirnov, 1959; Boctor and Boyd, 1980; Chakhmouradian and Mitchell, 2000). In sample S5251, epitaxial oxides display a thin (<1 µm) Ca-rich reaction seam (potentially perovskite/kassite) in contact with the glass (Fig. 4.2). These Ca-rich reaction seams likely form due to the interaction of the Fe-Ti-rich oxides with the Ca-rich captured melt, forming perovskite (or an intermediary product of this reaction).

The alteration of Fe-Ti-rich oxides to perovskite also typically manifests as reactions rims on Mg-ilmenite megacrysts (Smirnov 1959; Boctor and Boyd, 1980; Chakhmouradian and Mitchell, 2000). The chemical interaction of the ilmenite megacrysts and surrounding kimberlite melt is characterised by a loss of Ti from ilmenite coupled with an increase in Ca

(Kamenetsky et al., 2014a). This is most notably observed as a Ca-reaction seam on the ilmenite megacryst surrounding MI1 of sample S5628 (Fig. 3.5). This reaction seam is observed as BSE-bright hemispherical bulges that form into the host ilmenite megacryst. The reaction seam is Ca-Ti-Fe-rich. The Ti_2O content of this zone shows an increase inward, towards the melt inclusions, with a decrease in FeO. This is interpreted to form due to the chemical interaction between the captured Ca-rich melt and the ilmenite megacrysts. The melt inclusion hosts low modal abundances of calcite and perovskite (Table 1), therefore, if Ca is not captured by crystallisation of these Ca-bearing phases (calcite, perovskite, and kassite) it may react with the host ilmenite megacryst. Furthermore, since the composition of the melt inclusions appears to be variable, a high Ca-content in the silicic/oxidic melt may result in more pronounce Ca-reaction zones. Anhedral perovskite also commonly forms along the margins of the melt inclusions, often intergrown with kassite (Fig. 3.8 B; Fig. 3.9 F; Fig. 3.10 B). These Ca-rich phases may also represent the product of alteration between the ilmenite megacrysts and the captured melt.

This reaction is also observed due to the interaction between the ilmenite megacrysts and the surrounding kimberlite matrix. For example, in sample P015 MI2 perovskite extends from the host ilmenite megacryst into the channel that connects MI2 with the kimberlite matrix (Fig. 3.4). This is interpreted as due to the reaction of the ilmenite megacryst with the surrounding kimberlitic melt to form perovskite.

Perovskite was therefore identified as forming two distinct generations: (i) as an alteration product formed by the reaction between ilmenite and the captured melt; (ii) as a primary mineral crystallising subhedral and euhedral crystals directly from the entrapped melt. Using perovskite large enough for trace elemental analysis, future studies may investigate the difference in trace element and REE abundances between primary perovskite and secondary perovskite in order to reveal further characteristics in regard to the evolution of the captured melt.

Abersteiner et al. (2019) noted that extensive fracture networks often connect the polymineralic inclusions within clinopyroxene megacrysts to the host kimberlite matrix. The authors interpret this as evidence for a secondary infilling origin for the melt inclusions. The authors therefore consider these secondary inclusions as open systems with regard to the surrounding kimberlite matrix (Abersteiner et al., 2019). The observed ilmenite megacryst-hosted melt inclusions are not connected by an extensive fracture network and display an isolated appearance. This, along with the preservation of fresh glass, indicates that the captured melt evolved as a closed system, remaining isolated from the kimberlite matrix and meteoric fluids. In contrast, sample P015 hosts a melt inclusion on the margins of the megacryst (MI2; Fig. 3.1; Fig. 3.4). This melt inclusion is partially enclosed; thus, it is connected to the surrounding kimberlite matrix and represents an open system in regards to the surround kimberlite matrix. This particular melt inclusion does not host glass or textures commonly associated with the melt inclusions entirely enclosed in the interior of the ilmenite megacrysts. Instead, the material within MI2 is identical to the kimberlite matrix with which it is connected. The contrast between MI2 and melt inclusions within the

same megacryst sample (P015; Chapter 3.3.2; Fig. 3.12) demonstrates the isolated nature of the majority of the observed melt inclusions.

Some melt inclusions are transected by secondary veins, most of which contain only calcite that intersects the solidified glass and crystals of the melt inclusions (Fig. 3.5; Fig. 3.9; Fig. 3.14). Several veins texturally overprint the mineral assemblages within the inclusions (Fig. 3.5). Furthermore, calcite veins are present which are not associated with any melt inclusions. These veins are interpreted as secondary features unrelated to the formation of the melt inclusions, possibly originating from hydrothermal fluids percolating along fractures that formed after emplacement.

Radial apophyses are present surrounding some melt inclusions (e.g. Fig. 3.3; Fig. 3.6). These are interpreted to form prior to complete crystallisation as they host material identical to that observed within the melt inclusion. This indicates that some melt was extracted from the melt inclusions and crystallised within the veins. However, these apophyses are rare in the studied ilmenites. The absence of extensive radial apophyses suggests that at the time of decompression and uplift the ilmenite megacrysts were rheologically more competent than olivine and clinopyroxene megacryst and less susceptible to fracturing.

6.6 Melt capture by the enclosing megacrysts

The random distribution of the melt inclusions within the megacrysts contrasts with a planar arrangement associated with secondary melt inclusions formed along fractures typical of necking down (Roedder, 1979). A more detail study on intact ilmenite megacrysts and their inclusions prior to sectioning would provide important clarity on modal distributions and relationships within and between the melt inclusions.

The random distribution of the melt inclusions, along with the lack of veins associated with the melt inclusions, or evidence that the melt inclusions are arranged along healed veins, suggests that they are primary in origin. This possibly occurs in response to variations in the growth rate of the enclosing megacrysts (e.g. Roedder, 1979). The melt inclusions of the current study are interpreted to represent the capture of a heterogenous, variably differentiated kimberlitic melt during crystallisation of ilmenite megacrysts of the Cr-poor megacryst suite at 4.5–6 GPa (Gurney et al., 1979).

Chapter 7: Conclusions

1. The typically calcite-rich composition of melt inclusions in ilmenite compared to those in olivine megacrysts suggests that this is related to an overall more carbonate-rich bulk composition of the trapped melt, and is not, or not entirely related to sectioning effects. This possibly reflects the differences in the timing of ilmenite megacryst crystallisation compared to olivine megacrysts which captured primitive kimberlitic melt at various stages in its evolution.
2. The coexistence of the carbonate and conjugate silicic/oxidic melts within the melt inclusions is preserved in immiscible melt textures between calcite and silicate glass. These textures include:
    i. Droplet-like globular calcite segregations set within a silicate glass matrix.
    ii. Patches/pools of calcite that form the matrix for euhedral silicate/oxide grains.
    iii. Calcite occupying the internal voids of skeletal oxide grains.
    iv. Interconnected silicate glass and Ca-veinlets indicative of phase separation through spinodal decomposition.

    The variations in the sizes of calcite grains, from small rounded colloform grains to large anhedral grains, suggest that coalescence of the immiscible carbonate melt occurred. These textures are consistent with a complete liquid immiscibility origin under equilibrium conditions.
3. The variations in the bulk compositions of melt inclusions hosted within the same ilmenite megacryst suggest that the melt was heterogenous at the time of capture. The segregation of carbonate and silicic/oxidic components likely occurred prior to the capture of the melt during crystallisation of the ilmenite megacryst in the upper mantle (4.5–6 GPa). The captured melt was therefore initially a homogenous carbonated–silicate melt.
4. The glassy Ca-Ti-Fe spherulites set within a Si-Mg-Fe glass matrix may preserve the segregation of the silicic/oxidic melt into its oxidic (Ca-Ti) and silicic (Si-Mg-Fe) components. The immiscible silicic and oxidic melts may have crystallised the silicate and oxide minerals of the daughter assemblage, respectively.
5. Silicate and oxide minerals of the common daughter assemblage initially crystallised under equilibrium conditions, resulting in euhedral crystal shapes. This was followed by rapid undercooling and disequilibrium growth, resulting in skeletal oxide textures. Prior to complete crystallisation, further strong undercooling during uplift resulted in the quenching of residual melt to form a silicic glass.
6. The Si-Mg-Fe glass is variably depleted in REE, Al_2O_3, K_2O, and TiO_2 due to crystallisation of the common daughter assemblage (phlogopite, spinel, ilmenite, perovskite, and serpentine). Additionally, spinel and phlogopite, often set within a glass matrix, may show progressive depletion in Al and Ti from core to rim. Glass in ilmenite megacryst-hosted melt inclusions, therefore, represents a quenched residual melt.

7. The similarities in the abundances of incompatible trace elements and Cr-poor compositions between the ilmenite megacrysts and ilmenite that crystallised within the melt inclusions suggest that they are cognate in origin. Furthermore, no textural or geochemical evidence supports the infiltration of melt into the megacrysts as a secondary process. This, along with the random distribution of the melt inclusions, suggests that they are primary in origin. The inclusions are interpreted to form from the capture of melt during the crystallisation of the monomineralic ilmenite megacrysts in the SCLM. A primary origin for the melt inclusions implies a cognate relationship between the ilmenite megacrysts and captured kimberlite melt.

References

Abersteiner, A., Kamenetsky, V. S., Goemann, K., Golovin, A. V., Sharygin, I. S., Pearson, D. G., ... & Gornova, M. A. (2019). Polymineralic inclusions in kimberlite-hosted megacrysts: Implications for kimberlite melt evolution. *Lithos*, *336*, 310-325.

Allsopp, H. L., & Barrett, D. R. (1975). Rb–Sr age determinations on South African kimberlite pipes. In *Physics and Chemistry of the Earth* (pp. 605-617). Pergamon.

Apter, D. B., Harper, F.J., Wyatt, B.A. and Smith, B.S. (1984). The geology of the Mayeng kimberlite sill complex, South Africa. In *Developments in Petrology* (Vol. 11, pp. 43-57). Elsevier.

Araújo, D. P., Griffin, W. L., & O'Reilly, S. Y. (2009). Mantle melts, metasomatism and diamond formation: insights from melt inclusions in xenoliths from Diavik, Slave Craton. *Lithos*, *112*, 675-682.

Bailey, R. C. (1994). Fluid trapping in mid-crustal reservoirs by H_2O–CO_2 mixtures. *Nature*, *371*(6494), 238-240.

Banfield, J. F., & Veblen, D. R. (1992). Conversion of perovskite to anatase and TiO_2 (B): A TEM study and the use of fundamental building blocks for understanding relationships among the TiO_2 minerals. *American Mineralogist*, *77*(5-6), 545-557.

Becker, M., & le Roex, A.P.L. (2006). Geochemistry of South African on-and off-craton, group I and group II kimberlites: petrogenesis and source region evolution. *Journal of Petrology 47*, 673–703.

Berg, G. W. (1986). Evidence for carbonate in the mantle. *Nature*, 324(6092), 50-51.

Biellmann, C., Guyot, F., Gillet, P., & Reynard, B. (1993). High-pressure stability of carbonates; quenching of calcite-II, high-pressure polymorph of $CaCO_3$. *European Journal of Mineralogy*, *5*(3), 503-510.

Boctor, N. Z., & Boyd, F. R. (1980). Oxide minerals in the Liqhobong kimberlite, Lesotho. *American Mineralogist*, *65*(7-8), 631-638.

Boyd, F. R., & Nixon, P. H. (1975). Origins of the ultramafic nodules from some kimberlites of northern Lesotho and the Monastery Mine, South Africa. In *Physics and Chemistry of the Earth*, *9*, 431-454.

Brooker, R. A., & Kjarsgaard, B. A. (2011). Silicate–carbonate liquid immiscibility and phase relations in the system SiO_2–Na_2O–Al_2O_3–CaO–CO_2 at 0.1–2.5 GPa with applications to carbonatite genesis. *Journal of Petrology*, *52*(7-8), 1281-1305.

Bussweiler, Y. (2019). Polymineralic Inclusions in Megacrysts as Proxies for Kimberlite Melt Evolution—A Review. *Minerals*, *9*(9), 530.

Bussweiler, Y., Stone, R. S., Pearson, D. G., Luth, R. W., Stachel, T., Kjarsgaard, B. A., & Menzies, A. (2016). The evolution of calcite-bearing kimberlites by melt-rock reaction:

evidence from polymineralic inclusions within clinopyroxene and garnet megacrysts from Lac de Gras kimberlites, Canada. *Contributions to Mineralogy and Petrology*, *171*(7), 65.

Büttner, S.H. (2012). Rock Maker: an MS Excel spreadsheet for the calculation of rock compositions from proportional whole rock analyses, mineral compositions, and modal abundance. *Mineralogy and Petrology*, 104, 129-13.

Cahn, J. W. (1965). Phase separation by spinodal decomposition in isotropic systems. *The Journal of Chemical Physics*, *42*(1), 93-99.

Chakhmouradian, A. R., & Mitchell, R. H. (2000). Occurrence, alteration patterns and compositional variation of perovskite in kimberlites. *The Canadian Mineralogist*, *38*(4), 975-994.

Chalot-Prat, F., & Arnold, M. (1999). Immiscibility between calcio carbonatitic and silicate melts and related wall rock reactions in the upper mantle: a natural case study from Romanian mantle xenoliths. *Lithos*, *46*(4), 627-659.

Dalton, J. A., & Presnall, D. C. (1998). The continuum of primary carbonatitic–kimberlitic melt compositions in equilibrium with lherzolite: data from the system $CaO–MgO–Al_2O_3–SiO_2–CO_2$ at 6 GPa. *Journal of Petrology*, *39*(11-12), 1953-1964.

Dasgupta, R., & Hirschmann, M. M. (2010). The deep carbon cycle and melting in Earth's interior. *Earth and Planetary Science Letters*, *298*(1-2), 1-13.

Davies, G. R., Spriggs, A. J., & Nixon, P. H. (2001). A non-cognate origin for the Gibeon kimberlite megacryst suite, Namibia: implications for the origin of Namibian kimberlites. *Journal of Petrology*, *42*(1), 159-172.

Davis, G. L., Krogh, T. E., & Erlank, A. J. (1976). The ages of zircons from kimberlites from South Africa. *Year Book Carnegie Institution of Washington*, *75*, 821-824.

Dawson, J. B. (1971). Advances in kimberlite geology. *Earth-Science Reviews*, *7*(4), 187-214.

Dawson, J. B., & Hawthorne, J. B. (1973). Magmatic sedimentation and carbonatitic differentiation in kimberlite sills at Benfontein, South Africa. *Journal of the Geological Society*, *129*(1), 61-85.

Dawson, J. B., & Smith, J. V. (1975). Chemistry and origin of phlogopite megacrysts in kimberlite. *Nature, 253(5490)*, 336–338. doi:10.1038/253336b0.

Deer, W., Howie, R. A., & Zussman, J. (2013). *An introduction to the rock-forming minerals* (p. 696). Longman.

Dongre, A., & Tappe, S. (2019). Kimberlite and carbonatite dykes within the Premier diatreme root (Cullinan Diamond Mine, South Africa): New insights to mineralogical-genetic classifications and magma CO_2 degassing. *Lithos*, *338*, 155-173.

Eggler, D. H., McCallum, M. E. H., & Smith, C. B. (1979). Megacryst Assemblages in Kimberlite from Northern Colorado and Southern Wyoming: Petrology, Geothermometry-

Barometry, and Areal Distribution. *The Mantle Sample: Inclusion in Kimberlites and Other Volcanics*, *16*, 213-226.

Fulop, A., Kopylova, M., Kurszlaukis, S., Hilchie, L., Ellemers, P., & Squibb, C. (2018). Petrography of Snap Lake kimberlite dyke (Northwest Territories, Canada) and its interaction with country rock granitoids. *Journal of Petrology*, *59*(12), 2493-2518.

Galakhov, F. Y., & Varshal, B. G. (1973). Causes of phase separation in simple silicate systems. In *Phase-Separation Phenomena in Glasses/Likvatsionnye Yavleniya v Steklakh/Ликвационные Явления в Стеклах* (pp. 7-11). Springer, Boston, MA.

Gernon, T. M., Sparks, R. S. J., Field, M., Ogilvie-Harris, R., Schumacher, J. C., & Brooker, R. (2019). Comment on: 'Petrography of the Snap Lake Kimberlite Dyke (Northwest Territories, Canada) and its Interaction with Country Rock Granitoids' by Fulop et al. (2018), Journal of Petrology, doi: 10.1093/petrology/egy025. *Journal of Petrology*, *60*(3), 649-660.

Girnis, A. V., Brey, G. P., & Ryabchikov, I. D. (1995). Origin of group 1A kimberlites: fluid-saturated melting experiments at 45–55 kbar. *Earth and Planetary Science Letters*, *134*(3-4), 283-296.

Girnis, A. V., Bulatov, V. K., & Brey, G. P. (2011). Formation of primary kimberlite melts–Constraints from experiments at 6–12 GPa and variable CO_2/H_2O. *Lithos*, *127*(3-4), 401-413.

Giuliani, A., Kamenetsky, V. S., Kendrick, M. A., Phillips, D., Wyatt, B. A., & Maas, R. (2013). Oxide, sulphide and carbonate minerals in a mantle polymict breccia: Metasomatism by proto-kimberlite magmas, and relationship to the kimberlite megacrystic suite. *Chemical Geology, 353*, 4-18

Giuliani, A., Soltys, A., Phillips, D., Kamenetsky, V. S., Maas, R., Goemann, K., ... & Griffin, W. L. (2017). The final stages of kimberlite petrogenesis: petrography, mineral chemistry, melt inclusions and Sr-CO isotope geochemistry of the Bultfontein kimberlite (Kimberley, South Africa). *Chemical Geology*, *455*, 342-356.

Golubkova, A. B., Nosova, A. A., & Larionova, Y. O. (2013). Mg-ilmenite megacrysts from the Arkhangelsk kimberlites, Russia: genesis and interaction with kimberlite melt and postkimberlite fluid. *Geochemistry International*, *51*(5), 353-381.

Gornitz, V. (1981). Skeletal crystals. *Encyclopedia of Earth Sciences–Mineralogy: New York, Springer*, 469-473.

Gurney, J. J., Jakob, W. R. O., & Dawson, J. B. (1979). Megacrysts from the Monastery kimberlite pipe, South Africa. *The Mantle Sample: Inclusion in Kimberlites and Other Volcanics*, *16*, 227-243.

Haggerty, S. E., Hardie, R. B., & McMahon, B. M. (1977, September). The mineral chemistry of ilmenite nodule associations from the Monastery diatreme. In *International Kimberlite Conference: Extended Abstracts* (Vol. 2, pp. 132-134).

Haggerty, S.E., and Boyd, F.R. (1975). Kimberlite inclusions in an olivine megacryst from Monastery. Long abstracts. *Kimberlite Symposium*, London, July 1975.

Hamilton D. L., Bedson P., & Esson J. (1989). The behaviour of trace elements in the evolution of carbonatites. *In Carbonatites: Genesis and Evolution* (ed. K. Bell). Unwin Hyman, London, pp. 405–427.

Harker, A. (1909). *The natural history of igneous rocks*. Macmillam.

Harris, M., Le Roex, A., & Class, C. (2004). Geochemistry of the Uintjiesberg kimberlite, South Africa: petrogenesis of an off-craton, group I, kimberlite. *Lithos, 74(3-4)*, 149-165.

Harte, B., & Gurney, J. J. (1981). The mode of formation of chromium-poor megacryst suites from kimberlites. *The Journal of Geology*, *89*(6), 749-753.

Hawkes, D. D. (1967). Order of Abundant Crystal Nucleation in a Natural Magma. *Geological Magazine, 104(05),* 473-486.

Hops, J. J., Gurney, J. J., & Harte, B. (1992). The Jagersfontein Cr-poor megacryst suite—towards a model for megacryst petrogenesis. *Journal of Volcanology and Geothermal Research*, *50*(1-2), 143-160.

Howarth, G. H. (2018). Olivine megacryst chemistry, Monastery kimberlite: Constraints on the mineralogy of the HIMU mantle reservoir in southern Africa. *Lithos*, *314*, 658-668.

Howarth, G. H., & Büttner, S. H. (2019). New constraints on archetypal South African kimberlite petrogenesis from quenched glass-rich melt inclusions in olivine megacrysts. *Gondwana Research*, *68*, 116-126.

Howarth, G. H., & Taylor, L. A. (2016). Multi-stage kimberlite evolution tracked in zoned olivine from the Benfontein sill, South Africa. *Lithos*, *262*, 384-397.

Hudon, P., & Baker, D. R. (2002). The nature of phase separation in binary oxide melts and glasses. I. Silicate systems. *Journal of Non-Crystalline Solids*, *303*(3), 299-345.

Jakob, W. R. O. (1977) Geochemical aspects of the megacryst suite from the Monastery kimberlite pipe. (MSc thesis, University of Cape Town).

James, P. F. (1975). Liquid-phase separation in glass-forming systems. *Journal of Materials Science*, *10*(10), 1802-1825.

Jones, J. H., Walker, D., Pickett, D. A., Murrell, M. T., & Beattie, P. (1995). Experimental investigations of the partitioning of Nb, Mo, Ba, Ce, Pb, Ra, Th, Pa, and U between immiscible carbonate and silicate liquids. *Geochimica et Cosmochimica Acta*, *59*(7), 1307-1320.

Kamenetsky, M. B., Sobolev, A. V., Kamenetsky, V. S., Maas, R., Danyushevsky, L. V., Thomas, R., ... & Sobolev, N. V. (2004). Kimberlite melts rich in alkali chlorides and carbonates: a potent metasomatic agent in the mantle. *Geology*, *32*(10), 845-848.

Kamenetsky, V. S., & Yaxley, G. M. (2015). Carbonate–silicate liquid immiscibility in the mantle propels kimberlite magma ascent. *Geochimica et Cosmochimica Acta*, 158, 48-56.

Kamenetsky, V. S., Belousova, E. A., Giuliani, A., Kamenetsky, M. B., Goemann, K., & Griffin, W. L. (2014a). Chemical abrasion of zircon and ilmenite megacrysts in the Monastery kimberlite: Implications for the composition of kimberlite melts. *Chemical Geology*, 383, 76-8.

Kamenetsky, V. S., Golovin, A. V., Maas, R., Giuliani, A., Kamenetsky, M. B., & Weiss, Y. (2014b). Towards a new model for kimberlite petrogenesis: Evidence from unaltered kimberlites and mantle minerals. *Earth-Science Reviews*, *139*, 145-167.

Kamenetsky, V. S., Kamenetsky, M. B., Golovin, A. V., Sharygin, V. V., & Maas, R. (2012). Ultrafresh salty kimberlite of the Udachnaya–East pipe (Yakutia, Russia): a petrological oddity or fortuitous discovery? *Lithos*, *152*, 173-186.

Kirkley, M. D., Smith, H. S., & Gurney, J. J. (1986). Kimberlite carbonates: A carbon-oxygen stable isotope study. In *International Kimberlite Conference: Extended Abstracts* (Vol. 4, pp. 57-59).

Kjarsgaard, B., & Hamilton, D. L. (1989). Carbonatite origin and diversity. *Nature*, *338*(6216), 547-548.

Kjarsgaard, B., & Peterson, T. (1991). Nephelinite-carbonatite liquid immiscibility at Shombole volcano, East Africa: petrographic and experimental evidence. *Mineralogy and Petrology*, *43*(4), 293-314.

Kopylova, M. G., Kostrovitsky, S. I. and Egorov, K. N. (2013). Salts in southern Yakutian kimberlites and the problem of primary alkali kimberlite melts. *Earth-Science Reviews*, *119*, 1-16.

Kopylova, M. G., Nowell, G. M., Pearson, D. G., & Markovic, G. (2009). Crystallization of megacrysts from protokimberlitic fluids: geochemical evidence from high-Cr megacrysts in the Jericho kimberlite. *Lithos*, *112*, 284-295.

Le Roex, A. P., Bell, D. R., & Davis, P. (2003). Petrogenesis of group I kimberlites from Kimberley, South Africa: evidence from bulk-rock geochemistry. *Journal of Petrology*, *44*(12), 2261-2286.

Lee, M. J., Garcia, D., Moutte, J., & Lee, J. I. (2003). Phlogopite and tetraferriphlogopite from phoscorite and carbonatite associations in the Sokli massif, Northern Finland. *Geosciences Journal*, *7*(1), 9.

Marima, E. (2019). Segregation and crystallisation in megacryst-hosted melt inclusions from the Monastery kimberlite. (Honours thesis, Rhodes University).

Marshall, R. R. (1961). Devitrification of natural glass. *Geological Society of America Bulletin*, *72*(10), 1493-1520.

Martins, T., Chakhmouradian, A. R., & Medici, L. (2014). Perovskite alteration in kimberlites and carbonatites: the role of kassite, $CaTi_2O_4(OH)_2$. *Physics and Chemistry of Minerals*, *41*(6), 473-484.

Macdonald, R., Kjarsgaard, B. A., Skilling, I. P., Davies, G. R., Hamilton, D. L., & Black, S. (1993). Liquid immiscibility between trachyte and carbonate in ash flow tuffs from Kenya. *Contributions to Mineralogy and Petrology*, *114*(2), 276-287.

Merry, M., & le Roex, A. (2007). Megacryst suites from the Lekkerfontein and Uintjiesberg kimberlites, southern Africa: evidence for a non-cognate origin. *South African Journal of Geology*, *110*(4), 597-610.

Minarik, W. G. (1998). Complications to carbonate melt mobility due to the presence of an immiscible silicate melt. *Journal of Petrology*, *39*(11-12), 1965-1973.

Mitchell, R. H. (1973). Magnesian ilmenite and its role in kimberlite petrogenesis. *The Journal of Geology*, *81*(3), 301-311.

Mitchell, R. H. (1986). The nature of kimberlites. In *International Kimberlite Conference: Extended Abstracts* (Vol. 4, pp. 9-11).

Mitchell, R. H. (1995a). Kimberlites and orangeites. In *Kimberlites, Orangeites, and Related Rocks* (pp. 1-90). Springer, Boston, MA.

Mitchell, R. H. (1995b). Compositional variation of micas in kimberlites, orangeites, lamproites and lamprophyres. In *International Kimberlite Conference: Extended Abstracts* (Vol. 6, pp. 390-392).

Mitchell, R. H. (2008). Petrology of hypabyssal kimberlites: relevance to primary magma compositions. *Journal of Volcanology and Geothermal Research*, *174*(1-3), 1-8.

Mitchell, R. H. (2013). Paragenesis and oxygen isotopic studies of serpentine in kimberlite. In *Proceedings of 10th International Kimberlite Conference* (pp. 1-12). Springer, New Delhi.

Mitchell, R. H., & Chakhmouradian, A. R. (1998). Instability of perovskite in a CO_2-rich environment; examples from carbonatite and kimberlite. *The Canadian Mineralogist*, *36*(4), 939-951.

Moore, A. E. (1981). Unusual perovskite textural relationships in olivine melilitites from Namaqualand-Bushmanland, South Africa. *Mineralogical Magazine*, *44*(334), 147-150.

Moore, A. E. (1987). A model for the origin of ilmenite in kimberlite and diamond: implications for the genesis of the discrete nodule (megacryst) suite. *Contributions to Mineralogy and Petrology*, *95*(2), 245-253.

Moore, A., & Belousova, E. (2005). Crystallization of Cr-poor and Cr-rich megacryst suites from the host kimberlite magma: implications for mantle structure and the generation of kimberlite magmas. *Contributions to Mineralogy and Petrology*, *149*(4), 462-481.

Moore, R. O. (1986). A Study of the Kimberlites, Diamonds and Associated Rocks and Minerals from the Monastery Mine, South Africa. (Doctoral dissertation, University of Cape Town).

Moore, R. O., Griffin, W. L., Gurney, J. J., Ryan, C. G., Cousens, D. R., Sie, S. H., & Suter, G. F. (1992). Trace element geochemistry of ilmenite megacrysts from the Monastery kimberlite, South Africa. *Lithos*, *29*(1-2), 1-18.

Moussallam, Y., Morizet, Y., & Gaillard, F. (2016). H_2O–CO_2 solubility in low SiO_2-melts and the unique mode of kimberlite degassing and emplacement. *Earth and Planetary Science Letters*, *447*, 151-160.

Mullin, J. W. (1993). *Crystallization*, Butter-Worth.

Nielsen, A. E. (1964). *Kinetics of precipitation* (Vol. 18). Pergamon.

Nielsen, T. F., & Sand, K. K. (2008). The Majuagaa kimberlite dike, Maniitsoq region, West Greenland: constraints on an Mg-rich silicocarbonatitic melt composition from groundmass mineralogy and bulk compositions. *The Canadian Mineralogist*, *46*(4), 1043-1061.

Nixon, P. H., & Boyd, F. R. (1973). The discrete nodule association in kimberlites from northern Lesotho. *Lesotho kimberlites*, 67-75.

Nowell, G. M., Pearson, D. G., Bell, D. R., Carlson, R. W., Smith, C. B., Kempton, P. D., & Noble, S. R. (2004). Hf isotope systematics of kimberlites and their megacrysts: new constraints on their source regions. *Journal of Petrology*, *45*(8), 1583-1612.

Pasteris, J. D., Boyd, F. R., & Nixon, P. H. (1979). The ilmenite association at the Frank Smith Mine, RSA. *The Mantle Sample: Inclusion in Kimberlites and Other Volcanics*, *16*, 265-278.

Peresetskaya, E., Kargin, A., Nosova, A., Sazonova, L., & Lebedeva, N. (2018). Mg-rich ilmenite from the Grib kimberlite (Arkhangelsk region, Russia): composition and origin. In *EGU General Assembly Conference Abstracts* (Vol. 20, p. 342).

Pivin, M., Femenias, O., & Demaiffe, D. (2009). Metasomatic mantle origin for Mbuji-Mayi and Kundelungu garnet and clinopyroxene megacrysts (Democratic Republic of Congo). *Lithos*, *112*, 951-960.

Powers, H. E. C. (1963). Nucleation and early crystal growth. *Industrial Chemist*, *39*, 351-355.

Price, S. E., Russell, J. K., & Kopylova, M. G. (2000). Primitive magma from the Jericho Pipe, NWT, Canada: constraints on primary kimberlite melt chemistry. *Journal of Petrology*, *41*(6), 789-808.

Reguir, E. P., Chakhmouradian, A. R., Halden, N. M., Malkovets, V. G., & Yang, P. (2009). Major-and trace-element compositional variation of phlogopite from kimberlites and carbonatites as a petrogenetic indicator. *Lithos*, *112*, 372-384.

Roedder, E. (1979). Origin and significance of magmatic inclusions. *Bulletin de Mineralogie*, *102*(5), 487-510.

Roedder, E. (1984). *Volume 12: Fluid inclusions*. Mineralogical Society of America.

Roeder, P. L., & Schulze, D. J. (2008). Crystallization of groundmass spinel in kimberlite. *Journal of Petrology*, *49*(8), 1473-1495.

Russell, J. K., Porritt, L. A., Lavallée, Y., & Dingwell, D. B. (2012). Kimberlite ascent by assimilation-fuelled buoyancy. *Nature*, *481*(7381), 352-356.

Safonov, O. G., Kamenetsky, V. S., & Perchuk, L. L. (2011). Links between carbonatite and kimberlite melts in chloride–carbonate–silicate systems: experiments and application to natural assemblages. *Journal of Petrology*, *52*(7-8), 1307-1331.

Schulze, D. J. (1985). Evidence for primary kimberlitic liquids in megacrysts from kimberlites in Kentucky, USA. *The Journal of Geology*, *93*(1), 75-79.

Schulze, D. J., Anderson, P. F., Hearn Jr, B. C., & Hetman, C. M. (1995). Origin and significance of ilmenite megacrysts and macrocrysts from kimberlite. *International Geology Review*, *37*(9), 780-812.

Schmalzried, H. (1981). Solid state reactions. (2nd edition), *Verlag Chemie, Weinheim, Florida, Basel*.

Semytkivska, N. (2010). *Picro-ilmenites: An experimental study in simple and complex systems to investigate PT-fO_2-composition relations at high pressure* (Doctoral dissertation, ETH Zurich).

Sha, L. K. (2012). Concurrent fractional and equilibrium crystallisation. *Geochimica et Cosmochimica Acta*, *86*, 52-75.

Shee, S. R. (1984). The oxide minerals of the Wesselton mine kimberlite, Kimberley, South Africa. *Unknown Journal*, 59-73.

Shelley, D. (1993). *Igneous and Metamorphic Rocks under the Microscope*. Chapman & Hall, London, 445 p.

Siggia, E. D. (1979). Late stages of spinodal decomposition in binary mixtures. *Physical review A*, *20*(2), 595.

Skinner, E.M.W. (1989) Contrasting Group I and Group II kimberlite petrology: towards a genetic model for kimberlites. *In Kimberlites and Related Rocks, Vol 1 Their Composition, Occurrence Origin and Emplacement*. Blackwell Scientific Publications, 528-544.

Skinner, E.M.W., Marsh, J.S. (2004). Distinct kimberlite pipe classes with contrasting eruption processes. *Lithos 76*, 183–200.

Smirnov, G. I. (1959). Mineralogy of Siberian kimberlites. *International Geology Review*, *1*(12), 21-39.

Smith, C. B., Gurney, J. J., Ebrahim, N., Skinner, E. M. W., & Clement, C. R. (1985). Geochemical character of southern African kimberlites: a new approach based on isotopic constraints. *Transactions of the Geological Society of South Africa*, *88*(2), 267-280.

Smith, C.B. (1983). Pb, Sr and Nd isotopic evidence for sources of southern African Cretaceous kimberlites. *Nature, 304*, 51-54.

Sobolev, N. V., & Brown, D. A. (1977). *Deep-seated inclusions in kimberlites and the problem of the composition of the upper mantle*. Amer Geophysical Union.

Soltys, A., Giuliani, A., Phillips, D., Kamenetsky, V. S., Maas, R., Woodhead, J., & Rodemann, T. (2016). In-situ assimilation of mantle minerals by kimberlitic magmas—Direct evidence from a garnet wehrlite xenolith entrained in the Bultfontein kimberlite (Kimberley, South Africa). *Lithos, 256*, 182-196.

Sparks, R. S. J. (2013). Kimberlite volcanism. *Annual Review of Earth and Planetary Sciences*, *41*, 497-528.

Sparks, R. S. J., Brooker, R. A., Field, M., Kavanagh, J., Schumacher, J. C., Walter, M. J., & White, J. (2009). The nature of erupting kimberlite melts. *Lithos*, *112*, 429-438.

Stamm, N., & Schmidt, M. W. (2017). Asthenospheric kimberlites: volatile contents and bulk compositions at 7 GPa. *Earth and Planetary Science Letters*, *474*, 309-321.

Stamm, N., Schmidt, M. W., Szymanowski, D., von Quadt, A., Mohapi, T., & Fourie, A. (2018). Primary petrology, mineralogy and age of the Letšeng-la-Terae kimberlite (Lesotho, Southern Africa) and parental magmas of Group-I kimberlites. *Contributions to Mineralogy and Petrology*, *173*(9), 76.

Sun, S. S., & McDonough, W. F. (1989). Chemical and isotopic systematics of oceanic basalts: implications for mantle composition and processes. *Geological Society, London, Special Publications*, *42*(1), 313-345.

Swanson, S. E., Naney, M. T., Westrich, H. R., & Eichelberger, J. C. (1989). Crystallization history of Obsidian dome, Inyo domes, California. *Bulletin of Volcanology*, *51*(3), 161-176.

Tappe, S., Romer, R. L., Stracke, A., Steenfelt, A., Smart, K. A., Muehlenbachs, K., & Torsvik, T. H. (2017). Sources and mobility of carbonate melts beneath cratons, with implications for deep carbon cycling, metasomatism and rift initiation. *Earth and Planetary Science Letters*, *466*, 152-167.

Ting, H. H., & McCabe, W. L. (1934). Supersaturation and crystal formation in seeded solutions. *Industrial & Engineering Chemistry*, *26*(11), 1201-1207.

Treiman, A. H., & Schedl, A. (1983). Properties of carbonatite magma and processes in carbonatite magma chambers. *The Journal of Geology*, *91*(4), 437-447.

Tröger, W. E., Bambauer, H. U., Taborszky, F., & Trochim, H. D. (1982). *Optische Bestimmung der gesteinsbildenden Minerale*. 5th revised edition. Schweitzerbart'sche Verlagsbuchhandlung, Stuttgart, p. 188.

van Achterbergh, E., Griffin, W. L., Ryan, C. G., O'Reilly, S. Y., Pearson, N. J., Kivi, K., & Doyle, B. J. (2004). Melt inclusions from the deep Slave lithosphere: implications for the origin and evolution of mantle-derived carbonatite and kimberlite. *Lithos*, *76*(1-4), 461-474.

van Achterbergh, E., Griffin, W. L., Ryan, C. G., O'Reilly, S. Y., Pearson, N. J., Kivi, K., & Doyle, B. J. (2002). Subduction signature for quenched carbonatites from the deep lithosphere. *Geology*, *30*(8), 743-746.

Veksler, I. V., Dorfman, A. M., Dulski, P., Kamenetsky, V. S., Danyushevsky, L. V., Jeffries, T., & Dingwell, D. B. (2012). Partitioning of elements between silicate melt and immiscible fluoride, chloride, carbonate, phosphate and sulfate melts, with implications to the origin of natrocarbonatite. *Geochimica et Cosmochimica Acta*, *79*, 20-40.

Veksler, I. V., Petibon, C., Jenner, G. A., Dorfman, A. M., & Dingwell, D. B. (1998). Trace element partitioning in immiscible silicate–carbonate liquid systems: an initial experimental study using a centrifuge autoclave. *Journal of Petrology*, *39*(11-12), 2095-2104.

Vernon, R. H. (2004). *A practical guide to rock microstructure*. Cambridge University Press.

Wagner, P. A. (1914). *The diamond fields of southern Africa*. The Transvaal Leader.

Wallace, M. E., & Green, D. H. (1988). An experimental determination of primary carbonatite magma composition. *Nature*, *335*(6188), 343-346.

Warren, B. E., & Pincus, A. G. (1940). Atomic consideration of immiscibility in glass systems. *Journal of the American Ceramic Society*, *23*(10), 301-304.

Wartho, J. A., & Kelley, S. P. (2003). $^{40}Ar/^{39}Ar$ ages in mantle xenolith phlogopites: determining the ages of multiple lithospheric mantle events and diatreme ascent rates in southern Africa and Malaita, Solomon Islands. *Geological Society, London, Special Publications*, *220*(1), 231-248.

Weiss, Y., McNeill, J., Pearson, D. G., Nowell, G. M., & Ottley, C. J. (2015). Highly saline fluids from a subducting slab as the source for fluid-rich diamonds. *Nature*, *524*(7565), 339-342.

Willcox, A., Buisman, I., Sparks, R. S. J., Brown, R. J., Manya, S., Schumacher, J. C., & Tuffen, H. (2015). Petrology, geochemistry and low-temperature alteration of lavas and pyroclastic rocks of the kimberlitic Igwisi Hills volcanoes, Tanzania. *Chemical Geology*, *405*, 82-101.

Williams, C. M., Robey, J. V. A., & Abson, J. P. (1998). Petrography and mineral chemistry of the Mwenezi-01 kimberlites, Zimbabwe. In *International Kimberlite Conference: Extended Abstracts* (Vol. 7, pp. 955-957).

Winter, J. D. (2013). *Principles of igneous and metamorphic petrology*. Pearson Education.

Wyatt, B. A., Baumgartner, M., Anckar, E., & Grutter, H. (2004). Compositional classification of “kimberlitic” and “non-kimberlitic” ilmenite. *Lithos*, *77*(1-4), 819-840.

Xu, J., Melgarejo, J. C., & Castillo-Oliver, M. (2018). Styles of alteration of Ti oxides of the kimberlite groundmass: implications on the petrogenesis and classification of kimberlites and similar rocks. *Minerals*, *8*(2), 51.

Yaxley, G. M., Crawford, A. J., & Green, D. H. (1991). Evidence for carbonatite metasomatism in spinel peridotite xenoliths from western Victoria, Australia. *Earth and Planetary Science Letters*, *107*(2), 305-317.

Yaxley, G. M., Ghosh, S., Kiseeva, E. S., Mallik, A., Spandler, C., Thomson, A. R., & Walter, M. J. (2019). CO_2-rich melts in Earth. In *Deep Carbon: Past to Present* (pp. 129-162). Cambridge University Press.